

POLARISATION SHIFT KEYING MODULATED FREE-SPACE OPTICAL COMMUNICATION SYSTEMS

XUAN TANG

A thesis submitted in partial fulfilment
of the requirements of the
University of Northumbria at Newcastle
for the degree of
Doctor of Philosophy

Research undertaken in the
School of Computing, Engineering and
Information Sciences

February 2012

Abstract

The data transmission rate, range, and reliability of free-space optical communication (FSO) systems are affected by a number of atmospheric phenomena, such as rain, haze, fog, snow, and scintillation. Thick fog with over 300 dB/km of attenuation limits the link length to around 100 m. Even under clear air conditions with no atmospheric scattering, the FSO communication link still suffers from fading due to scintillation. Scintillation fade margins are 2 to 5 dB for FSO links of 500 metres or less, which is well below margins for the atmospheric attenuation. For the link range beyond 1 km, scintillation may severely impact the performance of FSO links, thus resulting in the link deterioration, i.e., higher outage probability and ultimately complete link failure. In this thesis the performance of terrestrial FSO system based on the polarization shift keying modulation (POLSK) scheme under a turbulence channel is being investigated and analysed. The results are theoretically compared with on-off keying (OOK) and phase shift keying (PSK) modulated FSO systems in an atmospheric turbulence channel based on the bit error rate (BER) and the outage probability metrics. Results presented show that the binary POLSK (BPOLSK) offers the highest immunity to the phase noise in the atmospheric turbulence against OOK (with fixed and adaptive threshold levels) modulated FSO systems, primarily because it does not exhibit a BER floor. For BPOLSK under a moderate turbulence regime and for a BER of 10^{-9} the signal to noise ratio (SNR) requirement is ~ 39.5 dB. For the moderate turbulence regime OOK suffers from higher BER floor level. Heterodyne BPSK-FSO systems using an electrical phase locked loop (PLL) suffer from the PLL induced phase noise penalty. The power penalties due to the atmospheric turbulence must be compensated for to guarantee a reliable communication link. To mitigate the energy loss due to the atmospheric attenuation, the transmitted optical power could be increased sufficiently but it must meet eye safety requirements. Simply increasing the transmission power cannot improve the link performance limited by the atmospheric turbulence induced fading. Convolutional coding and the spatial diversity scheme have been applied in POLSK-FSO systems to circumvent scintillation, which is assumed to obey the gamma-gamma distribution. A relatively simple equal gain combining (EGC) and the optimal but complex maximum ratio combining (MRC) techniques are considered. The system performance and the error probabilities based on the convolutional coding together with EGC and MRC techniques are investigated and compared under different atmospheric turbulence regimes. For example, to achieve a symbol error probability (SEP) of 10^{-9} in a weak turbulence regime, the SNR requirements are ~ 28.5 dB and ~ 13 dB for uncoded and coded coherent heterodyne 8-POLSK schemes, respectively. With four detectors and using the MRC technique, the achievable power gains are ~ 6 dB, ~ 17.5 dB and ~ 15.5 dB in weak, moderate and strong turbulence regimes, respectively. Increasing the number of detectors to ten, results in ~ 24 dB of power gain a strong turbulence regime. Results presented also show that the spatial diversity offers an increased link margin as the scintillation level rises. The performance of a linear BPOLSK scheme using the direct detection has also been experimentally investigated. The obtained results are compared with OOK under the same operating conditions at the same data rate. Two transmission links of 6 m and 27 m are considered. An external interferometer is replaced by two intensity modulated laser sources with orthogonal states of polarisation (SOPs). This new scheme is less complex compared to the existing techniques. As a result of the underlying assumptions in the derivation, there is a close match between the experimental and predicted Q -factors for the weak turbulence regimes for BPOLSK-FSO system.

Table of Content

Abstract	i
List of Figures	v
List of Tables	viii
Glossary of Abbreviations	ix
Glossary of Symbol	xi
Dedication	xvi
Acknowledgements	xvii
Declaration	xviii
 Chapter One — Introduction	 1
1.1 Background	1
1.2 Research Motivation and Justification	6
1.3 Research Objectives	15
1.4 Original Contributions	17
1.5 Thesis Organization	20
1.6 List of Publications and Awards	22
 Chapter Two — Fundamentals of FSO	 26
2.1 Overview of FSO Technology	27
2.2 Features of FSO	30
2.3 Applications	31
2.4 System Configuration	32
2.5 Optical Detection Methods	34
2.6 Atmospheric Channel	36
2.6.1 Atmospheric Attenuation	37
2.6.2 Atmospheric Turbulence	38
2.7 Noise in Optical Detector	40
2.7.1 Thermal Noise	40
2.7.2 Dark Current Shot Noise	41
2.7.3 Photon Fluctuation Noise	41
2.7.4 Background Radiation	42
2.8 Eye Safety and Standards	43
2.9 Summary	46
 Chapter Three — Atmospheric Turbulence Models	 47
3.1 Optical Turbulence	48
3.2 Lognormal Turbulence Model	51
3.2.1 Spatial Coherence in Weak Turbulence	56
3.3 Gamma-Gamma Turbulence Model	58
3.4 Negative Exponential Turbulence Model	63
3.5 Summary	64
 Chapter Four — Coherent Polarisation Shift Keying Systems	 66
4.1 Digital Modulation Schemes	67

4.2	Optical Coherent Receiver	69
4.2.1	Optical Heterodyne Detection Receiver	70
4.2.2	Optical Homodyne Detection Receiver	72
4.2.3	Comparisons between Optical Coherent and Direct Detection Receivers	73
4.3	Polarisation Modulation	75
4.3.1	Polarised Wave	76
4.3.2	Polarisation Shift Keying Signals	80
4.3.3	Polarisation Modulator	82
4.4	Polarisation Fluctuations in a Turbulence Channel	84
4.5	Outage Probability in a Lognormal Turbulence Channel	85
4.6	Outage Probability in a Negative Exponential Turbulence Channel	87
4.7	Summary	88

Chapter Five — BPOLSK-FSO Systems in an Atmospheric Turbulence Channel

		90
5.1	POLSK-FSO Using the Square-Law Demodulation	92
5.1.1	System Configuration	92
5.1.2	Error Probabilities Analysis	97
5.1.3	Power Penalty Caused by Non-Ideal PBS	100
5.2	BPOLSK-FSO with a Reference Carrier	104
5.2.1	System Configuration	104
5.2.2	Error Probabilities Analysis	107
5.3	Differential Circular Polarisation Shift Keying	108
5.3.1	System Configuration	108
5.3.2	Error Probabilities Analysis	111
5.4	Comparison of BPOLSK, OOK and BPSK Based FSO Links	112
5.5	Summary	119

Chapter Six — BPOLSK-FSO with Receiver Diversity Techniques

6.1	Receiver Diversity Techniques	122
6.1.1	Maximum Ration Combining (MRC)	126
6.1.2	Equal Gain Combining (EGC)	127
6.1.3	Results and Discussions	128
6.2	Performance of Received Signal Correlation and Outage Probability	132
6.3	Summary	137

Chapter Seven — Multilevel POLSK FSO in the Gamma-Gamma Turbulence

	Channel	138
7.1	Coherent Heterodyne 8-Polsk System	140
7.1.1	System Configuration	140
7.1.2	Error Probability Analysis	144
7.1.3	Maximum Likelihood Sequence Detection	145
7.1.4	Receiver Diversity Technique	148
7.1.5	Results and Discussion	149
7.2	Coherent Heterodyne MPOLSK System	152
7.2.1	System Configuration	152
7.2.2	Symbol Error Probability with Ideal PLL	157

7.2.3	Performance Degradation due to Phase Tracking Error and Atmosphere Turbulence	158
7.2.4	Receiver Diversity Techniques	159
7.2.5	Results and Discussion	160
7.3	Summary	164
Chapter Eight — The Link Budget Analysis		166
8.1	Atmospheric Transmission	167
8.1.1	Rayleigh Scattering	168
8.1.2	Mie Scattering	169
8.2	Beam Diverging Loss	170
8.3	Losses due to Optical Components, Windows and Pointing	172
8.4	Link Budget Analysis	172
8.5	Summary	175
Chapter Nine — Experimental Investigation of BPOLSK-FSO in a Turbulence Channel		176
9.1	BPOLSK-FSO Link Using an Indoor Simulated Chamber	177
9.1.1	Transmitter	180
9.1.2	Turbulence Channel	181
9.1.3	Receiver	182
9.1.4	Results	186
9.2	BPOLSK-FSO using DD with Reflecting Mirrors	187
9.2.1	Experimental Set-up	188
9.2.2	Results	194
9.3	Summary	193
Chapter Ten — Conclusions and Future Work		199
10.1	Conclusions	199
10.2	Future Work	204
References		207

List of Figures

Fig. 1-1	Outline of thesis contributions
Fig. 2-1	Block diagram of a terrestrial FSO link.
Fig. 2-2	A direct detection receiver.
Fig. 3-1	Kolmogorov cascade theory of turbulence and eddies between scale size L_0 and l_0 form the inertial subrange. (L_0 : the outer scale; l_0 : the inner scale).
Fig. 3-2	Lognormal PDF with $E[I] = 1$ for various values of turbulence variance σ_I^2 .
Fig. 3-3	The transverse coherence distance ρ_0 against the link range with a range of C_n^2 for the plane wave at the wavelengths of $\lambda = 850$ nm and 1550 nm.
Fig. 3-4	Gamma-gamma PDF with respect to the turbulence regimes from weak to strong.
Fig. 3-5	$S.I.$ against the turbulence variance σ_I^2 with $C_n^2 = 10^{-15} \text{ m}^{-2/3}$ and $\lambda = 850$ nm.
Fig. 3-6	The range of values for α and β in the whole turbulence regime.
Fig. 3-7	Negative exponential PDF for various values of P_0 .
Fig. 4-2	A heterodyne detection receiver.
Fig. 4-3	A homodyne detection receiver.
Fig. 4-4	A snapshot at a fixed time t of the electrical field vector of linear polarised light.
Fig. 4-5	Snapshots at a fixed time t of the electrical field vector of right-hand (a) and left hand (b) circular polarised light.
Fig. 4-6	A snapshot of the trajectory of the endpoint of the electric field vector at a fixed time t of elliptical polarised light. a , major axis; b , minor axis; ϵ , ellipticity; η , azimuth.
Fig. 4-7	Poincare sphere. RHC (right-hand circular); LHC (left-hand circular); ϵ (ellipticity); η (azimuth).
Fig. 4-8	Schematic of POLSK modulator.
Fig. 4-9	Outage probability against the power margin for a lognormal turbulent atmospheric channel for $\sigma_I^2 = [0.1, 0.3, 0.5, 1]$.
Fig. 4-10	The outage probability, P_{out} , against the power margin, m , in the saturation and weak turbulence regimes for $\sigma_I^2 = 0.5$.
Fig. 5-1	System block diagram of the BPOLSK-FSO using square-law demodulation: (a) the transmitter, and (b) the receiver.
Fig. 5-2	SOPs at the output of the BPOLSK receiver.
Fig. 5-3	An offset angle θ relatives to one of the transmission axes \vec{x} of the linear polarised light.
Fig. 5-4	An offset angle relative to one of the transmission axes of the linear polarised light: (a) A non-orthogonal deviation of the transmission axes, and (b) An orthogonality-preserving deviation of the transmission axes from the SOPs of the incoming light.
Fig. 5-5	Receiver sensitivity power penalty against the offset angle θ at a BER of 10^{-9} using (5.24), (5.28) and (5.32).

- Fig. 5-6 Coherent BPOLSK-FSO transceiver with the reference carrier PM modulator: (a) the transmitter, and (b) the receiver.
- Fig. 5-7 Coherent DCPOLSK-FSO transceiver: (a) the transmitter, and (b) the receiver.
- Fig. 5-8 Comparisons of BER performances of various schemes against the normalized electric SNR $E[\Re P_r P_{lo}] = 1$ in the absence of turbulence.
- Fig. 5-9 BER against the SNR for coherent BPSK for a range of phase error variance $\sigma_\Delta = [0, 0.1, 0.2, 0.3, 0.5]$.
- Fig. 5-10 Comparisons of BER performances of various schemes against the normalized electric SNR $E[\Re P_r P_{lo}] = 1$ in (a) weak, (b) moderate and (c) strong turbulence regimes.
- Fig. 6-1 Receiver diversity with \mathcal{N} - PDs.
- Fig. 6-2 Error probability of BPOLSK-FSO diversity with the EGC and MRC against the normalised SNR $E[\Re P_r P_{lo}] = 1$ in the gamma-gamma channel for: (a) $\mathcal{N} = 1, 2$, and (b) $\mathcal{N} = 1, 3$.
- Fig. 6-3 Spatial diversity gain $m_{\mathcal{N}, \sigma_l}$ for the BPOLSK scheme employing MRC technique to achieve a BER of 10^{-9} against the number of photodetectors \mathcal{N} with the normalised electric SNR $E[\Re P_r P_{lo}] = 1$ under all turbulence scenarios from weak to strong regimes.
- Fig. 6-4 Correlation coefficient $\rho(\xi)$ as a function of the transverse separation ξ in a weak turbulent field.
- Fig. 6-5 Error probability of the BPOLSK-FSO with EGC at a range of correlation coefficients for $\mathcal{N} = 2$ and $\sigma_l^2 = 0.3$.
- Fig. 6-6 The upper bound of the outage probability (6.20) and the exact solution (6.19) against the power margin with EGC spatial diversity in a weak turbulent atmospheric channel for $\sigma_l = [0.1, 0.3]$ and $\mathcal{N} = [1, 2]$.
- Fig. 6-7 EGC diversity gain against the number of photodetector at P_{out} of 10^{-9} in a lognormal atmospheric channel with $\sigma_l^2 = [0.1^2, 0.3^2, 0.5^2, 0.7^2]$.
- Fig 7-1 Coherent 8-POLSK-FSO transceiver: (a) the transmitter, and (b) the receiver.
- Fig. 7-2 Convolutional encoder.
- Fig. 7-3 State diagram for rate 1/3 ($k = 1$) convolutional encoder.
- Fig. 7-4 Comparisons of SEP performances of coded 8-POLSK and uncoded BPOLSK (5.40), (7.13), (7.17) and (7.18) against the normalized electric SNR $E[\Re P_r P_{lo}] = 1$ in various turbulence levels.
- Fig. 7-5 Power gain for the 8-POLSK scheme employing MRC technique to achieve a SEP of 10^{-9} against the number of detectors with the normalized electric SNR $E[\Re P_r P_{lo}] = 1$ under all turbulence scenarios from weak to strong regimes.
- Fig. 7-6 Block diagram of the MPOLSK coherent heterodyne optical communication system: (a) the transmitter, and (b) the receiver. COD (encoder), P/S (parallel to serial converter).
- Fig. 7-7 SEP performances of 8POLSK (with the phase noise variance $\sigma_\Delta = [0.1, 0.3, 0.5]$), 16POLSK and 32POLSK schemes against the electrical SNR using a single detector in a non-turbulent channel.
- Fig. 7-8 The SEP performance of 8POLSK, 16POLSK and 32POLSK modulation schemes against the electrical SNR using a single detector and an ideal PLL in an atmospheric turbulence channel.
- Fig. 7-9 The spatial diversity gain against the number of detector (\mathcal{N}) for 16POLSK employing MRC in a turbulence channel to achieve a SEP of 10^{-9} .

- Fig. 8-1 AN FSO link showing beam divergence.
- Fig. 8-2 Link range against the link margin for OOK and BPOLSK to achieve a BER of 10^{-9} in a non-turbulent FSO channel with visibility values $V = 2, 20$ and 50 km.
- Fig. 9-1 BPOLSK-FSO experimental system block diagram to measure the atmospheric turbulence effect.
- Fig. 9-2 BPOLSK-FSO link set-up (a) channel, (b) transmitter and (c) receiver.
- Fig. 9-3 The schematic diagram of the BPOLSK transmitter.
- Fig. 9-4 The schematic of the optical receiver module. LPF (lowpass filter).
- Fig. 9-5 AD8015 TIA based detector circuit schematic diagram.
- Fig. 9-6 AD8042 rail-to-rail amplifier based subtractor schematic diagram.
- Fig. 9-7 Measured (Ex.) and predicted (Th.) Q -factors for the BPOLSK and OOK (using peak power) modulation schemes with two transmit optical power levels (-16.8 dBm/ -12.5 dBm) against the turbulence variances (σ_t^2).
- Fig. 9-8 BPOLSK-FSO with the link length of 27 m schematic picture.
- Fig. 9-9 BPOLSK-FSO with the link length of 27 m set-up diagram.
- Fig. 9-10 Principle of the beam reflections between the convex and concave mirrors.
- Fig. 9-11 Pictures of the first five reflection spots showing the laser beam divergence effects.
- Fig. 9-12 Structure of the PBS.
- Fig. 9-13 Experimental (Ex.) and theoretical (Th.) Q -factors for the BPOLSK and OOK modulation schemes with the link length of 27 m against the turbulence variances (σ_t^2).
- Fig. 9-14 Eye diagrams for the BPOLSK (a) without turbulence and (b) $\sigma_t^2 = 0.06$; and OOK (c) without turbulence and (d) $\sigma_t^2 = 0.06$.
- Fig. 9-15 Received signal distributions with turbulence variance of $\sigma_t^2 = 0.06$ for (a) BPOLSK and (b) OOK.

List of Tables

Table 5.1	Turbulence parameters with respect to weak, moderate and strong regimes.
Table 8.1	Atmospheric scatters with their radius and the scattering process at $\lambda = 850$ nm.
Table 8.2	Specifications for the FSO link budget.
Table 8.3	Receiver sensitivity to achieve a BER of 10^{-9} based on OOK and BPOLSK.
Table 9.1	Parameters of BPOLSK-FSO communication system.
Table 9.2	Experimental parameters for BPOLSK-FSO with the link length of 27 m.

Glossary of Abbreviations

3-D	Three-dimensional
AFC	Automatic frequency control circuit
AM	Amplitude modulation
AM-SIM	Amplitude modulation subcarrier intensity modulation
ANSI	American National Standards Institute
ASK	Amplitude shift keying
PSK	Phase shift keying
AWGN	Additive white Gaussian noise
BER	Bit error rate
BFSK	Binary frequency shift keying
BPF	Electric bandpass filter
BPOLSK	Binary polarisation shift keying
CDMA	Code division multiple access
CDRH	Center for Devices and Radiological Health
CENELEC	European Committee for Electrotechnical Standardization
CO ₂	Carbon dioxide
COD	Encoder
CPOLSK	Circular polarisation shift keying
DCPOLSK	Differential circular polarisation shift keying
DD-BPOLSK	BPOLSK with direct detection
DPIM	Digital pulse interval modulation
DPSK	Differential phase shift keying
DSL	Digital subscriber loop
EGC	Equal gain combining
EMI	Electromagnetic interference
ESA	European Space Agency
FCC	Federal Communications Commission
FM-SIM	Frequency modulation subcarrier intensity modulation
FOV	Field of view
FSK	Frequency shift keying
FSO	Free-space optical communication
FTTH	Fibre to the home
Ge	Germanium
HDTV	High definition television
i.i.d.	Independent and identically distributed
IEC	International Electro-technical Commission
IF	Intermediate frequency
IM/DD	Intensity modulation/direct detection
InGaAs	Indium gallium arsenide
ISI	Inter-symbol interference
LDPC	Low density parity codes
LHC	Left-hand circular
LIA	Laser Institute of America
LiNbO ₃	Lithium Niobate
LMDS	Local multipoint distribution service
LO	Local oscillator

LOS	Line-of-sight
LPF	Low pass filter
MPOLSK	Multilevel polarisation shift keying
MF	Matched filter
MRC	Maximum ratio combining
MSM	Multiple subcarrier modulation
MZI	Mach-Zehnder interferometer
NASA	National Aeronautics and Space Administration
NEC	Nippon Electric Company
NRZ-OOK	Non-return-to-zero on-off keying
OBBF	Optical bandpass filter
Ofcom	Office of Communications
OFDM	Orthogonal frequency division multiplexing
OOK	On-off keying
P/S	Parallel to serial converter
PLC	Power-line communication
PAM	Pulse amplitude modulation
PAPR	Peak-to-average power ratio
PBC	Polarisation beam combiner
PBS	Polarisation beam splitter
PD	Photodiode
PDF	Probability density function
PFM	Pulse frequency modulation
PLL	Phase locked loop
PM	Phase modulation
POLSK	Polarisation shift keying
PPM	Pulse position modulation
PRBS	Pseudo random binary sequence
PSD	Power spectral density
PSK	Phase shift keying
PSK-SIM	Phase shift keying subcarrier intensity modulation
PAPR	Peak to average power ratio
PWM	Pulse width modulation
QAM	Quadrature amplitude modulation
QW	Quarter wave retarder
RF	Radio frequency
RHC	Right-hand circular
RMS	Root mean square
RZ-OOK	Return-to-zero on-off keying
S.I.	Scintillation index
SeIC	Selection combining
SEP	Symbol error probability
SIM	Subcarrier intensity modulation
SNR	Signal-to-noise ratio
SOP	State of polarisation
THz	Terahertz
TIA	Trans-impedance amplifier
TL	Transmitting laser
UWB	Ultra-wide band
WDM	Wavelength division multiplexing

Glossary of Symbols

\hat{A}	A normal value of $C_n^2(0)$ at the ground level ($\text{m}^{-2/3}$)
A	Amplitude of the electric field in a terrestrial channel
A_r	Field amplitude in the turbulence channel
A_0	Field amplitude in the ideal channel
A_x	Amplitude of the electromagnetic field in \vec{x} axis
A_y	Amplitude of the electromagnetic field in \vec{y} axis
A_T	Aperture areas of the transmitter
A_D	Aperture areas of the receiver
A_s	Aperture areas of the source
A_{im}	Size of the diffraction pattern
A_p	Cross-sectional area of a scattering particle
(a, b)	Major and minor axes of the elliptical polarised light
α_c	Coefficient of the waveguide
$a_{x,y}(t)$	Amplitude modulation functions
b_k	Transmitted bit
B	Bandwidth in Hz
B_L	Linewidth of the laser sources
B_{bp}	Bandwidth of the bandpass filter
$c(t)$	Electric current at the output of the photodetector
$c_{lp}(t)$	Electric current after the lowpass filter
$c_{IF}(t)$	Intermediate electric currents
$c_x(t)$	Output electric currents from the photodetector in \vec{x} branch
$c_y(t)$	Output electric currents from the photodetector in \vec{y} branch
$c_{xm}(t), c_{ym}(t)$	Electric currents at the output of the square-law demodulation
$c_{xb}(t), c_{yb}(t)$	Electric current at the output of BPFs
C_n^2	Index of refraction structure parameter ($\text{m}^{-2/3}$)
$C_R(t)$	Optical power of right circular polarised light
$C_L(t)$	Optical power of left circular polarised light
D	Diameter of the receiver aperture
D^k	Hamming distance between the sequence of output bits corresponding to each branch and the sequence of output bits corresponding to the all-zero branch
d_s	Length of the splitter
d	Half the distance between the adjacent symbols in one polarisation axis
d_T	Transmitter aperture diameter
d_R	Receiver aperture diameter
$\vec{E}_0(t)$	Electromagnetic field of the laser beam traversing through a terrestrial channel without turbulence
$\vec{E}_{lo}(t)$	Electromagnetic field from an optical local oscillator
\vec{E}_x	Electromagnetic field in the horizontal axis \vec{x}
\vec{E}_y	Electromagnetic field in the vertical axis \vec{y}

$\vec{E}_{\text{out}}(t)$	Output electromagnetic field from the Mach-Zehnder interferometer
$\vec{E}_s(t)$	Modulated electromagnetic field
$E[\chi]$	Expectation of variable χ
$\{G_i\}_{i=1}^N$	Spatial diversity gain factor
\mathbf{g}_k	Function generators of the convolutional encoder
h	Altitude (m)
$h_{\text{MF}}(t)$	Impulse response of the matched filter
I_{sky}	Radiation from the extended source (sky)
I_{sun}	Radiation from the sun
I_0	Zero order modified Bessel function of the first kind
$\langle i \rangle$	Mean generated electric current over a given period of time
i_{th}	Threshold signal level
i	Detected current with the receiver aperture size normalised to unity
K	Optical wave number
$K_n(\cdot)$	Modified Bessel function of the 2 nd kind of order n
K_{PL}	Constant dependent upon the modulation mechanism
k	Number of information bits per transmission
κ	Boltzmann constant
k_F	A constant parameter
l_0	Inner scale size of turbulent air
l	Log-amplitude
ℓ	Path length in the waveguide.
$\Delta\ell$	Difference path length in the waveguide
L_0	Outer scale size of turbulent air
L_t	Largest inhomogeneities of the turbulent medium
L	Link length between transmitter and receiver (m)
L_{Atmosp}	Atmospheric transmission loss
L_{Geom}	Geometric loss
L_{op}	Optical loss
L_p	Pointing loss
L_M	Link margin
$m(t)$	Information signal
m	Power margin
m_{EGC}	Power margin for equal gain combining
\mathcal{M}	Indicator taking into account the number of bits in error
M	Number of points in the constellation
$\mathbf{M}_{\text{coupler}}$	Propagation matrix of waveguide
$\mathbf{M}_{\Delta\phi_c}$	Propagation matrix of phase shifter
\mathbf{M}	Matrix of the Mach-Zehnder Interferometer
n	Index-of-refraction
$\{n_1, n_2\}$	Refractive index of the waveguide
$n^I(t)$	In-phase component of the noise $n(t)$
$n^Q(t)$	Quadrature component of the noise $n(t)$
$n(t)$	Additive white Gaussian noise
$n_{xb,yb}$	Additive white Gaussian noise variance after the bandpass filter
$n_{lp}(t)$	Additive white Gaussian noise after the lowpass filter
$[\Delta n]^2$	Mean square change in refractive index due to thermal

	variations
\mathcal{N}	Number of photodetector
N_p	Amount of particles per unit volume in the transmission link
Ω	Ohm
P	Atmospheric pressure (millibars)
P_r	Optical power of the received optical carrier
P_0	Optical power of the optical carrier operating over an ideal channel
P_x	Large-scale atmospheric effects
P_y	Small-scale atmospheric effects
P_{lo}	Optical power of the local oscillator
P_t	Emitted optical power from the light
P_e	Unconditional probability
P_e^*	Predetermined threshold BER
P_{ec}	Conditional error probability
P_{eEGC}	Conditional bit error rate for the receiver using equal gain combining scheme
P_{out}	Outage probability
P_{av}	Average power per bit
$P_r(\lambda, L)$	Received optical power
$p(e 0)$	Error probability of the transmission of a ‘0’
$p(e 1)$	Error probability of the transmission of a ‘1’
$p(\vec{P}_r)$	Joint PDF for \mathcal{N} -photodetector receiving uncorrelated signals
Q_0	Q -factor in the absence of turbulence
q	Electronic charge of an electron
R_s	Symbol rate
R_b	Bit rate
$\text{Re}[\]$	Real part of a complex number
R_L	Load resistance
\Re	Responsivity of the photodetector
$\text{rect}_T(t)$	Rectangular pulse of width T
T	Symbol period
T_e	Temperature in Kelvin
$T(D(\theta), \mathcal{M})$	Transfer function
(u, v)	A coordinate system elliptical polarised light
v	Root mean square wind speed (m/s)
V_1	Driving voltage to control the value of the length d in the waveguide
V_2	Driving voltage to control the value of the phase shift $\Delta\phi_c$ in the phase shifter
V_0	DC bias current
$V_j(t)$	Electric signal at the output of a matched filter
V_j	Output signal from the sampler
V_i	Threshold output
V	Visibility range
\vec{x}	Unit vector denoting the horizontal direction where the field is polarised
\vec{y}	Unit vector denoting the vertical direction where the field is polarised
σ_l^2	Rytov variance

σ_{Th}^2	Variance of thermal noise
σ_{Bg}^2	Variance of background radiation
σ_{Qtm}^2	Variance of quantum noise
σ_{χ}^2	Variance of variable χ
σ_N^2	Scintillation index
σ_n^2	Noise variance
σ_T^2	Additive white Gaussian noise variance
σ_{Δ}^2	Phase noise variance
ω	Angular frequency of the received optical carrier
ω_{lo}	Angular frequency of the local oscillator
ω_{IF}	Frequency of the intermediate signal
ω	Angular frequency of the optical carrier signal
ω_m	Angular frequency of a sine wave
φ_r	Phase noise of the received optical carrier
$\varphi(t)$	Phase noise of the transmitted optical carrier
$\varphi_{lo}(t)$	Phase noise of the local oscillator
$\varphi_{IF}(t)$	Phase noise of the intermediate signal
$\Delta\varphi(t)$	Phase tracking error due to the phase locked loop
$\varphi_{PLL}(t)$	Phase signal of the carrier from phase locked loop
ϕ	Phase difference between the electrical fields in \hat{x} and \hat{y} axes
$\Delta\phi_c$	Phase difference between two signals in the waveguide in Mach-Zehnder Interferometer
θ	An offset angle from the transmission axes of the linear polarised light
θ_s	Optical source divergence angle
ϑ	Field phase
$\Phi_n(K)$	Power spectral density of refractive index fluctuation
ρ_0	Transverse coherence length
$\rho(s)$	Correlation coefficient
α	Effective number of atmospheric turbulence large scale eddies
$\alpha_a(\lambda)$	Absorption coefficient
β	Effective number of atmospheric turbulence small scale eddies
$\beta_{x,y}(t)$	Phase modulation functions
$\beta_T(\lambda)$	Attenuation coefficient/ extinction coefficient
$\beta_s(\lambda)$	Scattering coefficient
$\beta_{Rayleigh}(\lambda)$	Attenuation coefficient
$\beta_s(\lambda)$	Mie scattering coefficient
Ξ	Polarisation angle between the electrical fields in \hat{x} and \hat{y} axes without turbulence
$\Delta\Xi$	Change of polarisation angle in the presence of turbulence
$\gamma(P_r)$	Signal to noise ratio in the atmospheric turbulence for a given noise level
γ^*	Average signal to noise ratio in the absence of atmospheric turbulence
γ	Electrical signal to noise ratio at the input of the coherent demodulator
γ_l	Signal to noise ratio of the phase locked loop
γ_{MRC}	Optimum post detection electrical signal to noise ratio of a

γ_{EGC}	maximum ratio combining receiver
γ_T	Optimum post detection electrical signal to noise ratio of a equal gain combining receiver
γ_{N,σ_l}	Optimum post detection electrical signal to noise ratio
δ_{Kim}	Spatial diversity gain
δ_{Kruse}	Kim model function
μ	Kruse model function
μ_{no}	Mean received signal with turbulence
s	Means received signal without turbulence
s_{ij}	Spatial separation
$\Gamma(\cdot)$	Spatial separation between photodetectors i and j
$\Gamma_x(\rho)$	Gamma function
$\vec{\Psi}$	Spatial coherence of a travelling optical field
$\vec{\Psi}_0$	Rytov transformation variable
$\vec{\Psi}_1$	Absence-of-turbulence part of $\vec{\Psi}$
λ	Turbulence induced deviation of $\vec{\Psi}$
ς	Wavelength (microns)
χ	Gaussian distributed phase fluctuation of the field
η	Gaussian distributed log-amplitude fluctuation
ϵ	Azimuth angle
r	Ellipticity of the elliptical polarised light
ε	Radius of the atmospheric particles
τ_0	Amplitude modulation function
$*$	Coherence time of the atmospheric fluctuation
Λ	Convolution operation
\mathcal{T}_{th}	Likelihood function of on-off keying
\mathcal{C}_x	Transmittance threshold
\mathbb{X}	Covariance matrix
\mathcal{U}	Row matrix
\mathcal{X}_0	Normally distributed with mean μ_u and variance σ_u^2
	Size parameter

Dedication

To my parents

Acknowledgements

This thesis was carried out in the Optical Communications Research Group, School of Computing, Engineering and Information Science at Northumbria University, Newcastle upon Tyne, United Kingdom.

I wish to acknowledge my Director of Studies, Professor Z. Ghassemlooy, for his support, guidance, encouragements and proof reading of this thesis. Also, I wish to express my appreciation to him for giving me the valuable opportunity to undertake my research within his research group.

Sincere thanks also go to Dr. S. Rajbhandari and Dr. W. O. Popoola, for providing invaluable help and advices throughout this work. I am also greatly indebted to Dr. G. Brooks, Dr. D. Johnson and the entire Northumbria Communication Research Laboratory for helping me work out my problems during the last three years.

Last thanks would go to all the colleagues in the Optical Communications Research Group for listening to me and sharing the laughs all through these years.

I specially thank my parents for their constant support, understanding, encouragement and patience.

Declaration

I declare that the work contained in this thesis is entirely mine and that no portion of it has been submitted in support of an application for another degree or qualification in this, or any other university, or institute of learning, or industrial organisation.

Xuan Tang

February 2012

Chapter One

Introduction

1.1 Background

Free-space optical communication (FSO) has, since the beginning of history, been accomplished through the transmission of information loaded optical radiation from a transmitter to a receiver separated by the atmosphere. In a military situation as long ago as around 800 BC, optical communication in the form of beacons was used to enable messages to reach the receiver without a time delay [1, 2]. The disadvantage of this method was that only a limited number of predetermined messages could be transferred, resulting in low information capacity [3].

During the years 1790—1794 an optical telegraph based on a chain of semaphores was used by French naval navigators. Alexander Graham Bell constructed and received a patent for a 'photo-phone' in 1880, which is considered as the re-birth of optical wireless communication [4-6]. The transmitted telephone signals were generated by modulating the sun's radiation with voice signals which propagated over an unguided channel of 200 meters. The restrictions on this work were the crudity of the devices and the intermittent nature of the sun's radiation.

A number of communication experiments have been carried out using modulated electric light sources by the Australian, German and Japanese armies around 1935-40. The techniques used in these experiments were obtained from the recording of optical sound tracks on the motion picture film. In the early 1930s Mr Sony, who established the Sony Corporation in Japan, carried out a research that involved prototyping a modulated light communication system. These systems provided the military with the high directivity and a high security before the microwave hardware became available [5, 7]. During the Second World War, an infrared optical telegraph was developed to ensure a secure data transmission link. However, difficulties in inserting the technology in operational systems were greater than envisioned by the early pioneers due to: 1) accurate pointing and tracking systems were not available; and 2) the optical components were unreliable and needed improving [8]. Additionally the laser beam propagating over the atmospheric channel is always susceptible to the energy losses due to the atmospheric attenuation and turbulence. Such components included laser sources, detectors, high speed modulators/demodulators, high accuracy pointing components, high stability mechanical

structures, high quality interface and high speed electronics that typically needed to drive high voltages due to the bulk nature of the electro-optical elements.

With the maturity of optoelectronic devices in the market as well as the expanding demand for larger bandwidth we have seen a growing research activity in FSO technology that was installed in the early 1960s. Some of these FSO technologies are: transmission of television signals using a GaAs light emitting diode over a 30 mile distance performed in the MIT Lincoln laboratory in 1962 [8]; a He-Ne laser modulated by voice signals transmitted over a distance of 118 miles between Panamint Ridge and San Gabriel Mountain, USA, in May 1963, the same year in which the first TV-over-laser was demonstrated in North American Aviation [8]; in 1970 the Nippon Electric Company (NEC) in Japan built the first full duplex FSO using a 0.6328 μm He-Ne laser between Yokohama and Tamagawa, a distance of 14 km [8]. In the same year the demonstration of the first semiconductor laser that required no cooling, but could be operated at the room temperature, was reported by Hayashi *et al.* [1]. From here onwards, FSO communications we have seen a rapid development in FSO communication in both commercial and military operations.

Additionally, FSO has also found applications in deep space. The National Aeronautics and Space Administration (NASA) and the European Space Agency (ESA) have successfully applied FSO technology between satellites with a data rate of 10 Gbps [9]. The volume of fund to stimulate growth in the field of laser communications increased dramatically in the United States and Europe in 1980. The USA Government Agencies

had played an important role in the development of laser communications. Europe via ESA initiated the project on developing the next generation of communication technologies [10].

In the early 90's an interesting boost to laser communications came from the commercial side of satellite communications. A handful of companies in the USA were engaged in laser communications. Meanwhile, Europe started a program on the semiconductor inter-satellite laser communications [10]. Japan also showed increased interests in the laser communication and organised the program of the flight demonstration [10].

At the present time, as a method of exploiting more bandwidth and utilizing the broad array of new services, FSO technology is seen as a cost-effective method to solve the high-bandwidth bridge (the "last mile") [11-13]. FSO applications, in both military and civilian fields in particular the access network, have been reported in the last few years in various parts of the world [14-21]. For example, the FSO technology was successfully used to continually transmit the image between the Waterhouse Centre and the studio during the Sydney Olympic Games in 2000 [22]. As a commercially complementary technology to the radio frequency (RF) (in the range of about 3 kHz to 30 GHz) and the millimeter-wave (30 GHz to 300 GHz) wireless systems, the FSO has now emerged as a reliable communication technology with rapid deployment of voice, data, and video within the access networks [23-25]. Data rates offered by wireless networks based on RF and millimetre wave can be from a few megabits per second up to several hundred

megabits per second according to the system configurations of point-to-multipoint and point-to-point, respectively [23, 26-28].

The limitations of RF and millimeter-wave technologies in market penetration include interference from unlicensed bands, spectrum congestion, and licensing issues [25, 29]. Though the future emerging license-free bands are promising [30], RF and millimeter-wave still have certain limitations in the offered bandwidth and the range compared with the FSO technology [23-25]. Integrated hybrid FSO/fibre systems and wavelength division multiplexing (WDM) based FSO systems can be utilised to increase the link span as well as the transmission capacity [31-35].

The previous perception on FSO's dwindling acceptability, efficiency, and slow market penetration are now rapidly fading away. A number of service providers, organizations, government, and private establishments are now incorporating the FSO technology into their network infrastructure [15, 36, 37]. Today the terrestrial FSO technology is regarded as the complementary scheme in handling modern communication challenges, typically the requirements from end users for access to a high bandwidth/data rate at an affordable cost [25, 38]. The integration of the FSO technology into existing access networks is far more rapid since it is transparent to the traffic type and the data protocol. In spite of this, the biggest challenges, such as the atmospheric attenuation and the turbulence and the attainment of 99.999% link availability, still have to be circumvented in order to increase the link range and link availability in terrestrial FSO systems [1, 37, 39].

1.2 Research Motivation and Justification

In order to deal with the important emerging optical-access market segment, several optical access technologies are now being developed. FSO is one of the most promising new access technologies as the laser beams emitted from the robust optical transceivers propagate directly through the atmosphere to form point-to-point communications [3, 40].

For a number of applications, the FSO technology presents many advantages over its counterparts, for instance RF spectrum. Such an advantage is the immunity of FSO to the electromagnetic interference (EMI), thus making it the preferred option in certain applications where there is a requirement for a very low level of interference or no interference at all [41-43]. In addition, FSO is not affected or influenced by RF [13, 42, 44]. Another advantage offered by FSO over RF is the increased security owing to the laser's narrow beam, which makes detection, interception and jamming very difficult. Further advantages offered by FSO over RF include the possibility of rapid deployment and the flexibility of establishing temporary communication links, much higher data rates, low cost, small size, and limited power consumption [42, 44, 45].

On the other hand, the high bandwidth requirement in the present communication systems is the motivating force behind research and development in today's market. The access network bandwidth bottleneck mainly due to the limitations of the copper wire technology which connects the end users to the high-speed link limits the data rate/download rate [23, 25, 44]. The RF spectrum is becoming more congested every

year and the allocation of the RF spectrum is progressively more expensive and difficult as the regulations on allocation of the RF spectrum vary from one county to another [24, 25, 42, 44]. Optical wireless communication offers a potentially abundant bandwidth that is currently unregulated worldwide that could be used to overcome the bandwidth bottleneck.

Further methods proposed to tackle this bottleneck consist of the power-line communication (PLC) [46, 47], digital subscriber loop (DSL) or cable modems [48-51], fibre to the home (FTTH) [52, 53], local multipoint distribution service (LMDS) [54, 55], and ultra-wide band (UWB) technologies [1, 56, 57]. PLC systems and DSL are copper-based, which means potential disruption to the network operation because copper wires are susceptible to damage. In addition, it is more expensive, time-consuming and complicated to maintain and to reconfigure the wired networks [36, 58].

FTTH offers a considerably higher data rate — 10 Gbps can be easily delivered to the end users and up to 10 Tbps is feasible for the implementation of FTTH combined with WDM [5, 32, 33]. As from the point of view of deployment and penetration rates of the FTTH technology, South Korea and Japan are the pioneers at the global level [52, 53, 59]. However, its prohibitive cost of implementation is the most prominent obstacle inhibiting a wider deployment. LMDS was conceived as a fixed wireless, point-to-multipoint technology originally designed for the digital television transmission operating at microwave frequencies bands of 27.5 – 31.3 GHz and 40.5 – 42.5 GHz in the US and Europe, respectively [55, 60]. The fact that its throughput capacity and link

reliability depends on a common radio link makes the scheme more susceptible to severe signal attenuation and outage during rainfall [54, 60]. Additionally the carrier frequencies within the licensed bands constrains its applications [27].

The UWB technology uses the unlicensed radio spectrum in the 3.1 – 10.6 GHz band for short-range communications [30, 57]. It is also a copper wire based solution and its potential data rate is at odds with several Gbps available in the backbone. The interference of UWB signals with other systems operating within the same frequency spectrum is another drawback [56, 61].

Wireless FSO technology offers comparable capacity to that of optical fibre with significant reduction in cost and time [38, 39, 62, 63]. The integration of FSO into the access network can be done relatively cheaply and quickly as it is transparent to the traffic type and protocols. Therefore, it is desirable to analyse the performance of an optical wireless system [43, 64]. The data transmission rate, range, and reliability of an optical wireless communication system are affected by a variety of atmospheric phenomena, such as rain, haze, fog, snow, and scintillation [2, 63, 65-71]. Although rain and snow affect the link performance of microwave and radio systems at longer wavelengths, they generate inconsequential attenuation effects on the traversing infrared laser signal. For instance, the attenuation of approximately 6 dB/km due to the heavy rain is far less than the maximum attenuation values caused by fog [2, 42, 70, 72].

Snow and dust present an attenuation value of around 60 dB/km [2, 71, 73, 74], which is negligible for short transmission links. From all of these phenomena the most significant

atmospheric scatters are fog and haze. Experimental results have recorded atmospheric attenuation of over 100 dB/km due to the fog in Prague, Graz, Italy, the United Kingdom, America, and other parts of the world [17, 27, 75-78]. The attenuation due to thick fog is over 300 dB/km which restricts the link length to 100 m [42].

To mitigate the energy loss due to the atmospheric attenuation, the additional optical power would be needed but not exceeding the safety regulation [27]. Views have been expressed that an FSO link in excess of 500 metres in a heavy fog is unachievable unless the transmitted optical power is well above the regulatory limits [27, 70, 71, 76]. However, the fact that thick fog is localized and only exists for a short time makes FSO links of greater than 1 km achievable. Furthermore, an FSO-RF hybrid system is capable of offering 99.999% availability in all weather conditions at the expense of reduced data rate, loss of data during switch over from FSO to RF or vice versa and/or loss of real time operation due to temporary storage of data when switching [23, 24, 27, 29, 44, 76].

Even under clear air conditions where no atmospheric scattering exists, the propagating laser beam still suffers losses. Scintillation, referring to the fluctuation in the refractive index of the atmosphere caused by the atmospheric turbulence, depends on the wind speed, altitude and temperature [45, 65-67, 79, 80]. Scintillation is the origin of signal fading resulting from constructive and destructive interference in the optical beam propagating over the atmospheric channel. For short optical links scintillation produces insignificant variation in the received optical power. For example, scintillation fade margins are 2 to 5 dB for FSO links of 500 metres or less, which is well below the

margins for the atmospheric attenuation [81, 82]. In comparison, when the link range is beyond 1 km, scintillation may severely impact the performance of FSO communication systems resulting in communication link deterioration, i.e., an increase in the error probability in the received signal [66, 68, 83-85].

The bit error rate (BER) characterizes the performance of the communication system, which depends on both electronic-circuit induced short-term errors and long-term random breaks of up to tens of milliseconds in communication data traffic caused by signal fading [13, 41, 43, 85, 86]. As the consequence of deep signal fading represents a unique and significantly more challenging problem and consequently conventional data coding techniques cannot be used as the solution without compromising on the system efficiency, i.e., the data throughput [44, 45, 85, 87].

Analysis of atmospheric turbulence has been carried out by a number of researchers and several theoretical models have been developed to characterize its behaviour. The simplest and most widely reported model is the lognormal turbulence, which is mathematically convenient and tractable [64, 66, 88-92]. The lognormal model is based on the Rytov approximation, which requires the unperturbed phase gradient to be large compared to the magnitude of the scattering field wave [88, 89, 92, 93]. However, the lognormal model only covers the weak turbulence regime with a single scattering event. For turbulence in the saturation regime with multiple scatterings, the lognormal model becomes invalid [67, 91, 94, 95]. The strength of turbulence can be described by the log intensity variance σ_I^2 and the lognormal model is only valid for $\sigma_I^2 < 1.2$ [91-93].

Another important parameter for describing the turbulence strength is the scintillation index ($S.I.$), which is the log intensity variance normalized by the square of the mean irradiance. The experimental results have indicated that the scintillation index does not only saturate, but also decreases after it reaches the maximum value while the strength of turbulence continues rising [67]. The gamma-gamma model first proposed by Andrews *et al* [96] is valid for all turbulence regimes from weak to strong regimes. It is based on the assumption that the fluctuation of the laser beam propagating through the turbulent medium consists of refraction and scattering effects. The negative exponential model is used to describe the signal fluctuations under atmospheric turbulence conditions within the saturation regime [67, 94, 96, 97].

The performance impairments due to scintillation can be mitigated by adopting several approaches such as: aperture averaging and diversity techniques [88, 94, 98], adaptive optics [85], saturated optical amplifiers [99], modulation techniques and error control coding [88, 94]. The performance of coded FSO links for the lognormal and gamma-gamma channel models under atmospheric turbulence have been investigated [88, 94, 100]. This work also presents the upper bounds on the BER using the transfer function technique for the coded FSO links with intensity modulation/direct detection (IM/DD).

The diversity techniques comprising space, time, or frequency (wavelength) have been adapted to improve impairments in performance due to the scintillation. With the spatial diversity technique, where a single receiver with a large field of view (FOV) is replaced by a group of detectors with a narrow FOV, the probability of all the detectors suffering

simultaneously from deep fade is much reduced. Moreover, the spatial diversity scheme limits the amount of background light from unwanted sources that impinges on the specific detector, which otherwise could be received by the single receiver with a wide FOV [98]. Applying adaptive optics to mitigate the wave-front deformation resulting from atmospheric turbulence has been investigated [101], but this technique is very expensive and complex to implement on terrestrial FSO systems.

The types of modulation schemes in FSO systems are crucial to ensure the maximum power efficiency. Amplitude shift keying (ASK), phase shift keying (PSK), differential phase shift keying (DPSK) and frequency shift keying (FSK) are the most common bandpass modulation formats adopted for optical and non-optical communication systems. On-off keying (OOK) format is the simplest and most widely used scheme but it is highly sensitive to the channel turbulence [1, 36, 66, 88, 94, 102]. The threshold level is fixed midway between the expected levels of data bits one and zero in a standard OOK-FSO system [101].

Operating the OOK-FSO system with a fixed threshold level without considering the signal fluctuation will increase detection error [103]. In this case, the optimum decision point must be determined by tracking this fluctuation [1]. Since the threshold detector needs to continually track the channel noise and fading, detection of the optimum threshold creates great design challenges. The PSK based subcarrier intensity modulation (SIM) requires no adaptive thresholding scheme, thereby offering superior performance compared to the OOK in the presence of the atmospheric turbulence induced fading

channels [42, 104, 105]. However, there is a power penalty in PSK systems due to the phase noise of the semiconductor laser sources [106, 107]. The phase noise not only reduces the power of the desired signal component, but also induces crosstalk interference from the in-phase and quadrature components. Hence, the PSK modulation technique requires a complex transceiver design due to tight synchronisation [106, 108]. The performance analysis of PSK schemes will be further discussed in Chapter Five. The SIM also requires no adaptive thresholding scheme but suffers from a high peak to average power ratio (PAPR), which translates into poor power efficiency [1, 109].

Choosing a modulation scheme for a particular application therefore entails trade-offs among these listed factors. The frequency offset in DPSK leads to the additional power penalty owing to delayed and undelayed bits not being in phase [110]. FSK scheme is bandwidth inefficient and offers inferior BER performance compared to PSK and DPSK in the additive white Gaussian noise (AWGN) channel [110].

Polarisation shift keying (POLSK) is proposed as an alternative modulation technique to both envelop- and phase- based modulation schemes. The digital information is encoded in the state of polarisation (SOP) of the laser source [111, 112]. Stokes parameters are used to represent the SOP so the symbol constellation is scattered over a three-dimensional (3-D) space [112]. The POLSK scheme was considerably insensitive to the laser phase noise at the receiver, provided that the intermediate frequency (IF) filter bandwidth was large enough to avoid the phase-to-amplitude noise conversion [110, 112]; and the SOPs can be maintained over a long propagation link [113, 114]. In

comparison to DPSK and FSK modulation techniques, POLSK signal does not suffer from the excess frequency chirp generated by the all-optical processing devices [110]. Additionally, POLSK is a constant envelope modulation which is especially attractive for the peak power limited systems [113, 115].

A variant of POLSK schemes using external modulations have been adopted in [116-118], where the SOPs of a fully polarised propagating optical beam were considered to exploit the two orthogonal channels in an FSO system. [119]. A polarisation modulated direct detection system to extract the Stokes parameters of the transmitted light for the binary and multilevel transmissions was proposed in [117]. A binary POLSK scheme with direct detection offers 3 dB lower peak optical power compared to the OOK modulated IM/DD system [118]. A 4-level polarisation modulated direct detection system (with phase modulation) was reported in [116], whereas a digital coherent optical polarisation modulation scheme was outlined in [120]. The experimental results showed that the SOPs for a optical beam propagating over a long turbulence channel were maintained, which proved that the SOPs were the most stable properties compared with the amplitude and phase [112, 113]. The POLSK scheme improves performance in terms of the peak optical power by 3 dB but at the cost of increased system complexity compared to the OOK scheme [121]. Circular polarisation shift keying (CPOLSK) also has been adopted in FSO systems because it does not require phase tracking, therefore it is not applicable to mobile systems and it is more complex compared with the linear polarisation schemes [113].

This research investigates the POLSK pre-modulated optical coherent heterodyne system in weak, moderate, strong and saturation turbulence regimes. In order to address the symbol detection challenges associated with OOK-FSO in the atmospheric turbulence induced channel and the phase tracking error generated penalty of BPSK-FSO, the system performance will be compared with OOK-FSO and coherent BPSK-FSO in terms of the average BER. The error control coding and the spatial diversity technique will be also considered to improve the fading effect of atmospheric turbulence channels on POLSK-FSO systems. The noise, comprising of both the background radiation and the thermal noise, is modelled as the AWGN. We also assume that the transmitter and the receiver have a perfect link alignment. The FSO link under consideration is line-of-sight (LOS), thus no inter-symbol interference (ISI) will be considered. The power penalty caused by the non-ideal polarisation beam splitter (PBS) will also be discussed. For the purpose of achieving these goals the succeeding research objectives have been formulated.

1.3 Research Objectives

This research work is aimed at investigating the performance of a coherent POLSK pre-modulated FSO system in an atmospheric turbulence channel with the view to understanding its benefits and limitations. Additionally, it is also aimed at comparing the system performance of POLSK-FSO with that of OOK-FSO and BPSK-FSO. Detailed analysis has been carried out to determine the transmitted power required to achieve a

desired performance and accordingly, the possible link margin and the achievable link range. A list of research objectives has been outlined in order to accomplish these aims:

- Review the fundamental theory of a terrestrial FSO system and the challenges imposed on the system performance.
- Review the characteristic properties of the atmospheric channel, and understand the limits and range of validity of each model for describing the channel fading induced by turbulence.
- Review the performance of OOK, BPSK and DPSK pre-modulated terrestrial FSO in an atmospheric turbulence channel.
- Review the state of art for POLSK systems.
- Review the theory of the Poincare sphere, the Stokes polarisation parameters and the methods of using optical components to do the measurements.
- Investigate the performance of coherent POLSK-FSO communication systems in terms of the BER probability across all turbulence regimes using the following atmospheric turbulence models: (i) lognormal, (ii) gamma-gamma, and (iii) negative exponential.
- Investigate the coherent heterodyne receiver combined with the spatial diversity technique for mitigating the fading effect due to atmospheric turbulence on the terrestrial POLSK-FSO systems.

- Investigate the convolutional coded POLSK for improving the performance of the optical systems operating over the atmospheric turbulence channel.
- Develop an experimental test-bed to validate the atmospheric turbulence fading effect on a POLSK-FSO system. Verify experimentally the turbulence induced fading effect on OOK-FSO and compare with POLSK-FSO. Compare experimental data with the predicted and simulated data.

1.4 Original Contributions

As a result of the study, the following original contributions have been made:

- The analytical and simulation results for the error performance and fading penalty of various coherent optical binary polarisation shift keying (BPOLSK) systems operating over the turbulent atmosphere across the whole turbulence regimes have been detailed in **Chapter Five**. The conditional and unconditional BER expressions of the BPOLSK-FSO system in a turbulence channel have been derived. The analysis of power penalty caused by the non-ideal PBS is also carried out. The error performance of BPOLSK has been compared with other modulation schemes in the presence of turbulence and the phase noise under the same channel conditions.
- Coherent differential circular polarisation shift keying (DCPOLSK) scheme for FSO communication system in a turbulence induced fading channel is proposed

and analysed in **Chapter Five**. The closed form expression for unconditional BER of DCPOLSK has been derived, and its performance is compared with the OOK-FSO and coherent BPSK-FSO based SIM.

- The error performances of an OOK-FSO and BPSK-FSO systems is analysed in a turbulence channel and the difficulty of estimating the optimum threshold level is highlighted in **Chapter Five**.
- The error probabilities of POLSK combined with the spatial diversity technique to ameliorate the effect of atmospheric turbulence are reported in **Chapters Six and Seven**.
- The performance of a coherent multilevel POLSK (MPOLSK) based FSO communication system operating over the turbulence channel is analysed in **Chapter Seven**. To mitigate the turbulence induced fading, convolutional coding and spatial diversity techniques are employed. The symbol error probability (SEP) is derived using the transfer function technique.
- The performance of a BPOLSK with direct detection (DD-BPOLSK) operating over the atmospheric turbulence channel is experimentally investigated. The values of Q-factors obtained for the DD-BPOLSK system are verified in conjunction with the theoretical results to confirm the validity of the proposed scheme. The analytical error probabilities for DD-BPOLSK and non-return-to-zero OOK (NRZ-OOK) modulated FSO systems have been presented and compared in **Chapter Nine**.

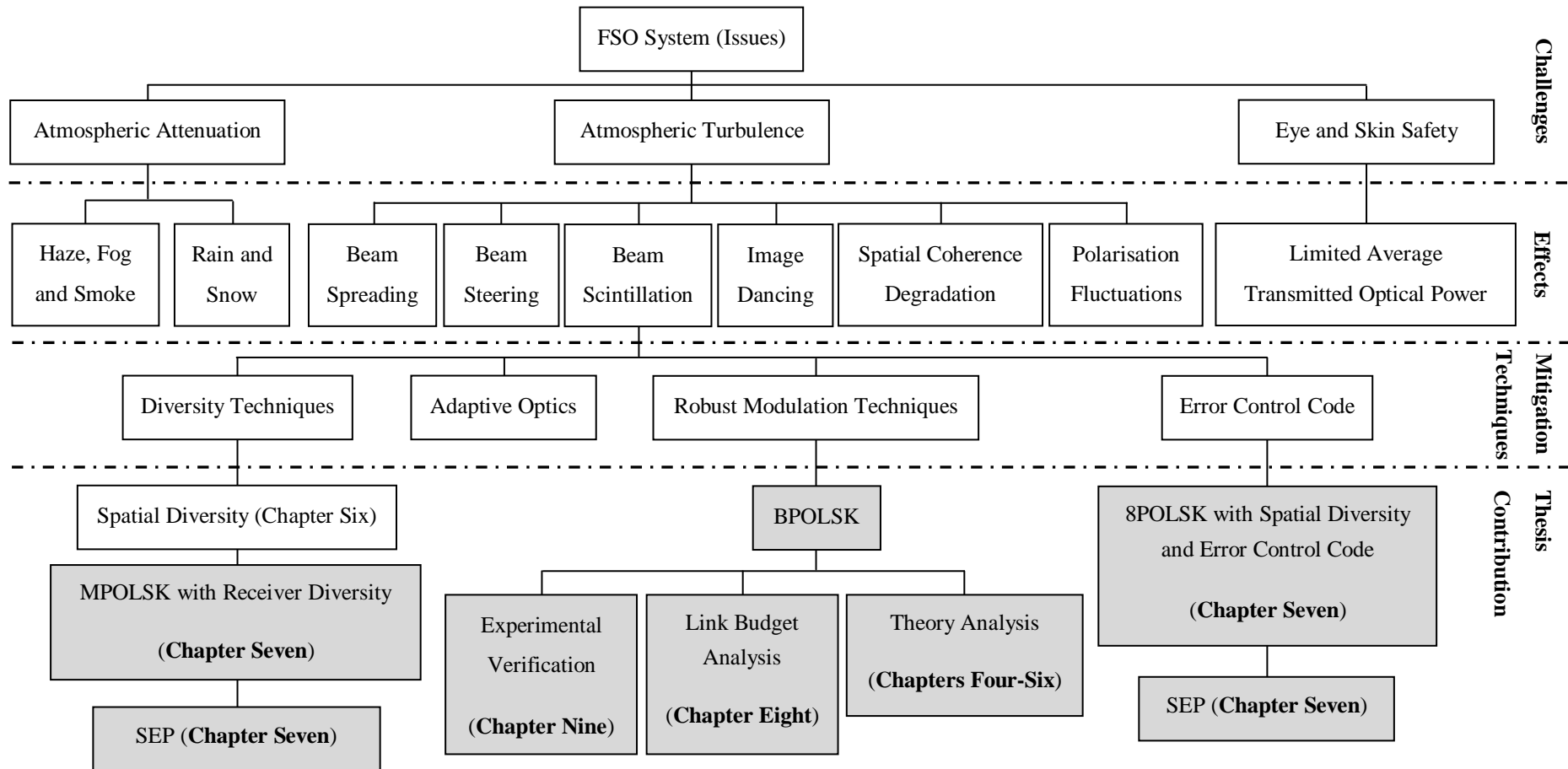


Fig. 1.1: Outlines the research road map and the original contributions.

1.5 Thesis Organization

This thesis contains ten chapters in total, which are outlined below:

Chapter One — Introduction: The fundamental theory of optical wireless communication technology is presented. Additionally, the advantages and challenges of optical wireless transmission are examined and compared with RF systems. It also consists of aims and objectives of the research as well as the original contributions.

Chapter Two — Fundamentals of FSO: The overview of the FSO technology is presented together with its distinctive features and applications. The general block diagram for an FSO communication system is introduced, and the functions of individual parts are highlighted. The atmospheric channel and the noise sources that limit the data transmission are described. Eye safety issues are discussed in the remainder of the chapter.

Chapter Three — Atmospheric Turbulence Models: Three different atmospheric turbulence channels are investigated. The discussion of these models is vital because they will be used to describe the statistical distributions of the received irradiance fluctuation which are detailed from Chapters Five to Nine.

Chapter Four — Coherent Polarisation Shift Keying Systems: The digital modulation schemes are assessed followed by the general coherent optical system structure. The POLSK scheme is introduced. The polarisation fluctuations in a turbulence channel are

examined. The outage probabilities in a lognormal channel and a negative exponential channel are analysed.

Chapter Five — BPOLSK-FSO Systems in an Atmospheric Turbulence Channel:

This chapter discusses several coherent BPOLSK modulated FSO schemes in an atmospheric turbulence channel. Some of the main constraints affecting the coherent BPOLSK-FSO systems are also considered. The designs of BPOLSK-FSO systems are analysed and performances are evaluated across all turbulence regimes to provide a comparison with other modulation schemes.

Chapter Six — BPOLSK-FSO with Receiver Diversity Techniques: Regarding propagation over the turbulence channel, the spatial diversity techniques are applied to improve the performance of BPOLSK-FSO systems. The spatial diversity techniques are described, and the error probabilities of BPOLSK-FSO systems employing spatial diversity are evaluated.

Chapter Seven — Multilevel POLSK FSO in the Gamma-Gamma Turbulence

Channel: This chapter studies the performance of the MPOLSK scheme in the presence of atmospheric turbulence for different modulation levels. The analytical SEP of the coherent heterodyne MPOLSK is carried out for a direct LOS FSO system. To mitigate the turbulence induced fading, convolutional coding and spatial diversity techniques will be also employed for the improvement in overall system performance. The upper SEP bounds are derived using the transfer function technique. The spatial diversity gain for a number of detectors is also determined for different turbulence levels.

Chapter Eight — The Link Budget Analysis: This chapter deals with different aspects of loss mechanisms faced in the design of a BPOLSK modulated FSO system, including the channel absorption and scattering. The link budget expression has been derived as well as the estimation of an achievable link ranges and margins.

Chapter Nine — Experimental Investigation of BPOLSK-FSO in a Turbulence

Channel: This chapter presents the experimental details of BPOLSK-FSO system using DD in the presence of atmospheric turbulence. For comparison purpose the performance of OOK-FSO system is investigated under the same channel conditions and the corresponding results are explained. The experiment to assess the BPOLSK-FSO system performance is performed using the indoor atmospheric chamber (5.5 m in length). After that, the transmission distance is increased to 27 metres by using multiple reflections of the laser beams between mirrors.

Chapter Ten — Conclusions and Future Work: Finally, the summary of keys findings is presented in this chapter. The conclusion as well as the future work is outlined.

1.6 List of Publications and Awards

Refereed Journals

1. Z. Ghassemlooy, X. Tang, S. Rajbhandari, “Experimental Investigation of Binary Polarisation Modulated Free Space Optical Communication with Direct Detection in Turbulence Channel”, *accepted by Journal of IET Communications*, 2012.

2. X. Tang, Z. Ghassemlooy, S. Rajbhandari, W. O. Popoola, and C. G. Lee, "Coherent polarisation shift keying modulated free space optical links over a gamma-gamma turbulence channel," *American Journal of Engineering and Applied Sciences*, vol. 4, pp. 520-530, January 2012.
3. X. Tang, Z. Ghassemlooy, S. Rajbhandari, W. O. Popoola, and C. G. Lee, "Coherent optical binary polarisation shift keying heterodyne system in the free-space optical turbulence channel," *IET Microwaves, Antennas & Propagation*, vol. 5, pp. 1031-1038, June 2011.

Conference Papers

4. X. Tang, Z. Ghassemlooy, S. Rajbhandari, W. O. Popoola, C. G. Lee, "Differential Circle Polarisation Shift Keying with Heterodyne Detection in Free Space Optical Turbulence Channel", *16th European Conference on Networks and Optical Communications 2011 (NOC 2011)* in Newcastle, UK, pp. 149-152, July 2011.
5. X. Tang, Z. Ghassemlooy, S. Rajbhandari, W. O. Popoola, C. G. Lee, E. Leitgeb, and V. Ahmadi, "Free-space optical communication employing polarisation shift keying coherent modulation in atmospheric turbulence channel," *Proceeding of the 7th Symposium on Communication Systems, Networks and Digital Signal Processing 2010 (CSNDSP 2010)*, in Newcastle upon Tyne, UK, pp. 663-668, July 2010.
(Invited paper)

6. X. Tang, S. Rajbhandari, W. O. Popoola, Z. Ghassemlooy, E. Leitgeb, S. S. Muhammad, and G. Kandus, "Performance of BPSK Subcarrier Intensity Modulation Free-Space Optical Communications using a Log-normal Atmospheric Turbulence Model," *2010 Symposium on Photonics and Optoelectronic (SOPO)*, Chengdu, China, pp. 1-4, 19-21 June 2010.
7. X. Tang, Z. Ghassemlooy, S. Rajbhandari, and W. O. Popoola, "Performance of the coherent optical binary polarisation-shift-keying heterodyne system in free space optical communications using a lognormal atmospheric turbulence model," *Mosharaka International Conference on Communications, Propagation, and Electronics (MIC-CPE 2010)*, Amman, Jordan, pp. 30-35, 5-7 March 2010. (**Invited paper**)

Posters

8. X. Tang, Z. Ghassemlooy, S. Rajbhandari, W. O. Popoola, "Performance of the Coherent Optical Binary Polarisation-Shift-Keying Heterodyne System in Free Space Optical Communications using a Lognormal Atmospheric Turbulence Model", The Northumbria Research Conference 2011, Newcastle, UK, 5-6 May 2011. (Poster)
9. X. Tang, Z. Ghassemlooy, S. Rajbhandari, W. O. Popoola, "Performance of BPSK Subcarrier Intensity Modulation Free-Space Optical Communications using a Log-normal Atmospheric Turbulence Model", The Northumbria Research Conference 2010, Newcastle, 2010. (Poster)

Research Related Awards

The best performing student over one hundred international PhD students for two consecutive academic sessions, 2008/2009 and 2009/2010.

Chapter Two

Fundamentals of FSO

This chapter provides a brief overview of the FSO technology, which will be helpful in understanding work carried out. The fundamentals of FSO technology, such as its applications, features, and terminology have been reviewed. The optical detection methods are described and the noise sources at the receiver are examined for their influence on the performance of the systems. With regard to the atmospheric channel, both atmospheric attenuation and turbulence are introduced. This chapter concludes with a discussion of the eye/skin safety of optical radiation.

2.1 Overview of FSO Technology

Research in the field of FSO communication has grown exponentially since 1970 and a large number of commercial products based on FSO technology are now readily available. FSO is proposed as a complementary technology to the RF technology [13, 25, 122, 123]. It offers an unregulated bandwidth in excess of terahertz technology (THz) and very high speeds, which makes this an extremely attractive means of meeting the ever-increasing demand for broadband traffic, mostly driven by the last-mile access network and high definition television (HDTV) broadcasting services [42]. FSO systems based on the WDM technology can reach up to 1 Terabit/s capacity or even beyond [5, 37, 39]. Further advantages include smaller and more compact transceivers, reduced installation and development costs and immunity to electromagnetic interference [13, 42, 124]. Long term evolution (LTE) is introduced as a new order mobile communication standard and is specified by the 3rd generation partnership project (3GPP) within the Release 8 version, following widely used standards such as UMTS/HSPA and GSM/EDGE. LTE supports a bandwidth ranges from 1.4 MHz to 20 MHz. The technologies used in the downlink and uplink are the orthogonal frequency – division multiple access (OFDMA) and the single-carrier frequency – division multiple access (SC-FDMA), respectively. Favourable features are offered by LTE, for example, are a high speed and a high spectral efficiency under a frequency selective channel condition. The LTE technology mainly sustains voice over the IP and packet switched traffic (IP traffic). It permits both time division duplex (TDD) and full duplex and half duplex (FDD) communication configurations. Additionally, LTE also supports the multiple-input-multiple-output (MIMO) communications system [125, 126].

In addition, the FSO link, with its inherent low probability of intercept and anti-jamming characteristics, is among the most secure of all wide-area connectivity solutions. Unlike many RF systems that radiate signals in all directions, thus making the signal available to

all within the receiving range, the FSO transceivers use a highly-directional and cone-shaped laser beam normally installed high above street level with a LOS propagation path [37, 64, 124].

The interception of a laser beam is extraordinarily difficult and anyone tapping into the systems can easily be detected as the intercept equipment must be placed within the very narrow optical footprint. Even if a portion of the beam is intercepted, an anomalous power loss at the receiver could cause an alarm via the management software. To protect the overshoot energy against being intercepted at the receiver, a window or a wall can be set up directly behind the receiver [42]. Based on these features, FSO communication systems developed for voice, video and broadband data communications are used by security organizations such as governments and the military [1, 5].

In terrestrial FSO links, the data/information is transferred between two points through optical radiation propagating over unguided channels. The transported data could be embedded into the intensity, phase, frequency or SOP of the optical carrier. In general, to ensure a successful exchange of information, the configuration of the FSO link is based on LOS where the transmitter and the receiver can directly ‘see’ one another without any obstructions in between [39, 124, 127]. Currently, many diverse applications of FSO are tailored to offer low- and very-high-speed wireless links effectively. FSO technology has numerous applications, spanning from very short-range (mm range) optical interconnects within integrated circuits for clock distribution, to outdoor intra-building links of a few kilometres to inter-satellite links [39, 122, 123, 128, 129].

Wireless communications using optical pipes together with lenses had been examined in detail by Bell Laboratories before fibre optics were developed as the most successful optical waveguide [128]. The growth and development of cheap fibre optic components had allowed accelerated development of FSO technology with the use of fibre-optic links. Outdoor terrestrial FSO systems with a link length of a few kilometers have been applied at multi-Gbps data rates [13, 64, 124]. The terrestrial channel is subject to severe weather fluctuations due to haze, fog, and snow via light scattering, attenuation, and absorption which significantly affect the power budget [70, 123, 127, 129, 130]. The FSO links are also influenced by the sun, which is within the receivers' field of view. To attain 99.999% link availability during thick fog is still a challenge in FSO technology. One solution is to use the hybrid FSO/RF system where an RF link as the back-up at a reduced data rate [25, 70, 129].

The optimisation of links can be achieved by using fixed locations. Fresnel lenses or other high-gain and directly 'optical antennas' are applied to obtain high receiver sensitivity [64, 122, 123, 131]. The techniques to enlarge the FSO link include placing fibre-optic amplifiers at transmitters and receivers, in conjunction with an external optical Mach-Zehnder interferometer (MZI), the forward-error correction, advanced power-efficient encoding techniques, and coherent receivers [64, 122, 127, 128]. The following sections outline the basic features, the field of applications and the functions of each block in the FSO system.

2.2 Features of FSO

Several typical features of FSO technology are:

- i. Huge modulation bandwidth* — The frequency range of an optical carrier spans from $10^{12} - 10^{16}$ Hz to 2000 THz data bandwidth. Since the amount of data transmitted is directly related to the bandwidth of the carrier, optical communication allows a far greater information capacity compared to the RF technology with a usable frequency bandwidth comparatively lower by a factor of 10^5 [13, 64, 124].
- ii. Narrow beam size* — A typical laser beam has a diffraction limited divergence in between $0.01 - 0.1$ mrad [4], which concentrates the optical power within an extremely narrow area that provides the FSO system adequate spatial isolation from potential interference. Therefore, independent FSO communication systems exist with virtually unlimited degrees of frequency reuse and data interception by unintended users becomes extremely difficult. However, a precise alignment for FSO links is required at the expense of tight beam size [1, 122, 127, 129].
- iii. Unlicensed spectrum* — It is becoming increasingly expensive and difficult to allocate additional RF frequencies because of the congested spectrum and the variations in the regulatory authorities in different countries, such as the Office of Communications (Ofcom) in the UK and the Federal Communications Commission (FCC) in the USA. In contrast, FSO technology offers license-free spectrum, low-cost initial set-up, and shorter deployment time [70, 123, 130].

- iv. *Cost-effective* — The development of FSO links is cheaper than that of an RF system with a similar data rate. No additional cost of trenching and right of way is required for FSO to deliver a comparable bandwidth to optical fibre [1, 25, 37, 39].
- v. *Quick to deploy and redeploy* — FSO technology offers portability and quick deployment. It also only takes a short time to redeploy the FSO link easily to another location [39, 64, 85, 123].
- vi. *Weather dependent* — The performance of a terrestrial FSO communication link can be degraded due to the atmospheric absorption and scattering of the propagating laser beam. Another challenge limiting FSO communication is the requirement for a direct LOS link between the optical transmitter and the receiver, as laser beams cannot penetrate buildings, hills, trees and other opaque obstacles [39, 70, 123, 127, 130].

2.3 Applications

Below are a number of typical applications where the FSO technology could successfully be applied [42, 132, 133]:

- i. *Last mile access* — The bandwidth gap (last mile bottleneck) that exists between the end users and the fibre optics backbone can be bridged by using the FSO technology. In today's market, products are readily available with links spanning from 50 m up to a few km and data rates covering from 1 Mbps to 10 Gbps [13, 36, 64, 124].

- ii. *Back up to optical fibre link* — In circumstances where the communication link is down or unavailable [36, 123, 127, 129, 130].
- iii. *Cellular communication back-haul* — To carry traffic between base station and switching centres in 3G/4G networks. It can also transport the IS-95 code division multiple access (CDMA) signals from micro- and macro- cell sites to the base stations [36].
- iv. *Disaster recovery/temporary links* [85, 122, 127, 129].
- v. *Multi-campus communication network* — Providing back-up links at Gigabit- or Fast- Ethernet speeds [39, 70, 85, 123, 130].
- vi. *Difficult terrains* — Where the right of way is unavailable or too expensive such as across rivers, in the inner city and across rail tracks, etc [25, 37].
- vii. *HDTV* — For broadcasting live high definition signals in remote locations to the central office [1, 13, 64, 124].

2.4 System Configuration

A physical model of a laser communication system is depicted in Fig. 2-1. The data/information is coded to the modulation format, such as pulse-position modulation, pulse-code modulation, etc., which is then fed into the modulator driver. The types of modulator are classified as internal and external. Generally speaking, the internal

modulator offers the advantages of compactness, cost effectiveness, and simplicity, while the external modulator can generate optical pulses of higher bit rates and higher quality. For polarisation modulation schemes, which are the subject of this thesis, external modulators will only be used. For more discussions on internal modulation the readers are referred to [42, 69, 134].

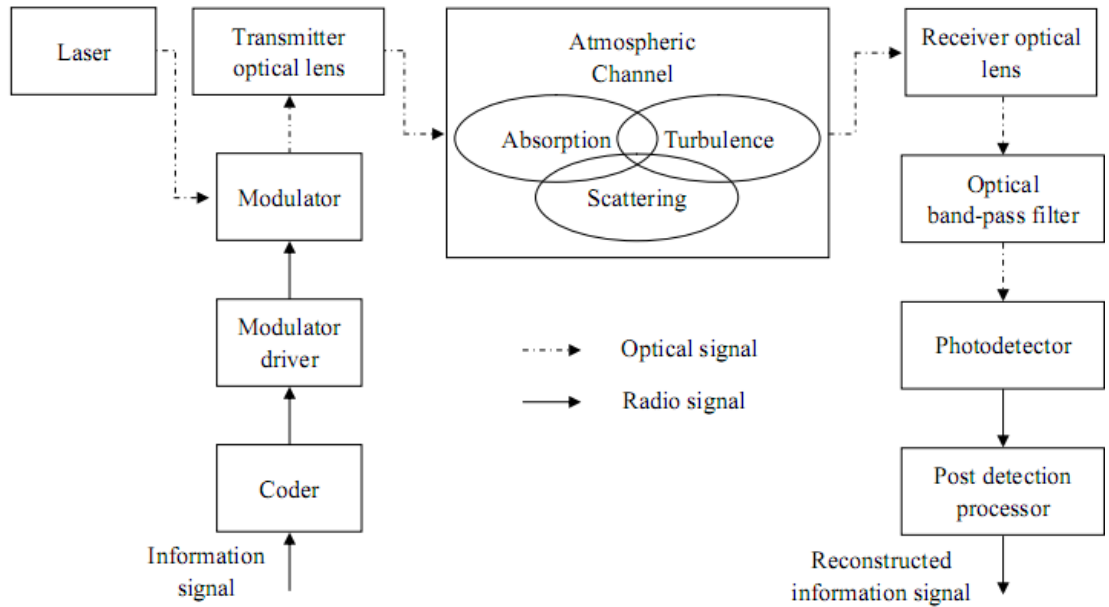


Fig. 2-1: Block diagram of a terrestrial FSO link using an external modulator.

The optical carrier could be modulated in its intensity, frequency, phase, or the SOP, and then collimated by the transmitter optical lens. The FSO system is essentially based on LOS without any obstructions in the propagation path. The unguided channel could be any or a combination of space, sea-water, or the atmosphere [13, 124]. In this thesis only the atmospheric channel will be considered. After traversing through the atmospheric

channel, the optical energy is gathered by a receiver optical concentrator and transferred into an electrical signal by the photodetector. The electrical current passes through the post detection processor for the final demodulation. Optical communication systems can be divided into two main classes: IM/DD and coherent systems. The operating principles are briefly described in the following sections.

2.5 Optical Detection Methods

Optical demodulation operations include transformations that detect amplitude, intensity, frequency, phase, or polarisation states of the carrier and reconstruct the information signal which has modulated the carrier. The two basic types of optical demodulation methods are: direct detection and coherent detection. Coherent detection can be classified into two subgroups: heterodyne detection and homodyne detection, which will be discussed in Chapter 4.

The direct or coherent homodyne detection optical receivers are used in the baseband demodulation systems. The modulation spectrum is shifted from the carrier frequency to the baseband. The frequency conversion is achieved in an optical heterodyne receiver where the information signal spectrum is translated from the optical carrier frequency to a lower radio frequency. Since this research is mainly focused on the optical coherent POLSK systems, the details of the coherent system and its performance in the presence of noise and atmospheric turbulence will be investigated in Chapters 4 to 9.

Comparison will also be made with FSO systems based on the direct detection receiver. The direct detection receiver is analysed with its block diagram depicted in Fig. 2-2. The photodetector may be regarded as a linear intensity-to-current converter or a quadratic (square-law) converter of optical electric field-to-detector current, which generates an output current proportional to the instantaneous intensity of the carrier.

The baseband electrical current is filtered by an electrical lowpass filter (LPF) with a bandwidth of the symbol rate which is sufficient to pass the information signal without any distortion and limits the amount of photodetector noise [42, 69, 135]. The direct detection receiver is only useful for amplitude modulation or IM because the photodetector response is insensitive to the frequency, phase, or polarisation states of the carrier over its operating regime [69, 135].

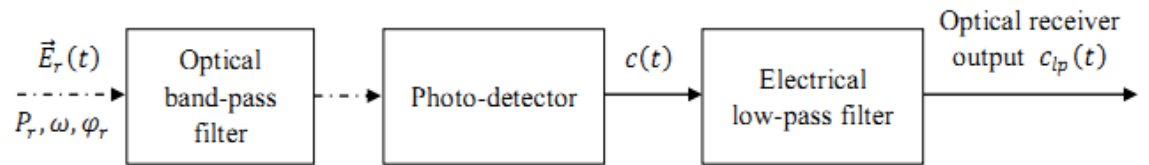


Fig. 2-2: A direct detection receiver.

For an intensity modulated transmitting laser beam, the received electric field (as shown in Fig. 2-2) is expressed as [69, 135]:

$$\vec{E}_r(t) = \sqrt{P_r} \sqrt{m(t)} e^{i(\omega t + \varphi_r)} \vec{x}, \quad (2.1)$$

where P_r , ω and φ_r are the optical power, angular frequency and the phase noise of the received optical carrier, respectively; \vec{x} represents the unit vector denoting the direction along which the field is polarised.

The modulation function $m(t)$ is given by [135]:

$$m(t) = \sum_{k=-\infty}^{\infty} b_k \text{rect}_T(t - kT), \quad (2.2)$$

where $b_k \in [0, 1]$ is the transmitted bit, T is the bit duration, and $\text{rect}_T(t)$ is the rectangular pulse of width T , which is equal to one for $T \in (0, T]$ and zero elsewhere.

The electric current $c(t)$ at the output of the photodetector is proportional to the time average of the instantaneous optical carrier power P_r over the carrier period and is expressed as [69, 135]:

$$c(t) = \Re \left| \sqrt{P_r} m(t) \right|^2, \quad (2.3)$$

where \Re is the responsivity of the photodetector which is dependent upon the type of photodetector employed.

2.6 Atmospheric Channel

An optical radiation propagating through the atmospheric channel is subject to atmospheric attenuation due to the photons' absorption by the molecular constituents (ozone, fog, carbon dioxide (CO₂), and water vapour, etc.) [70, 123, 127, 129, 130]. For

this reason part of the optical energy is converted into heat. The optical radiation also experiences scattering, which changes the initial propagating direction, shape, and electromagnetic properties of the laser. Furthermore, the beam also spreads out while propagating over the channel, thus enlarging the received power footprint which becomes larger than the detector aperture area [136]. A complete parametric description of the intertwining effects of the atmosphere on the laser signal propagation for all weather conditions is not within the scope of this section. The aim here is to provide a theoretical basis for the laser propagation in atmosphere, pertinent examples, and references for further analysis.

2.6.1 Atmospheric Attenuation

The optical radiation propagating through the atmosphere is subject to the atmospheric attenuation due to the absorption of radiation and to the scattering by atmospheric constituents. The atmospheric absorption is caused due to the interaction between the photon and the atmospheric molecules along the transmission path such as ozone, water vapour, and CO₂. When some of the photons are extinguished, their energies turn into heat [1, 69]. The atmospheric molecular concentration depends on the pressure and temperature that vary with weather, altitude, and geographical locations. Absorption varies as the function of wavelength. The four absorption windows along the spectral regions corresponding to the visible and the near-infrared radiations are approximately 900 to 980 nm, 1.1 to 1.6 μm , 1.3 to 1.5 μm , and 1.8 to 2 μm . The wavelengths used in

outdoor wireless systems are selected to coincide with the absorption windows, such as 780 to 800 nm, 1.2 to 1.3 μm , and 1.5 to 1.7 μm [42, 86, 137].

Atmospheric scattering causes the angular fluctuations. The optical radiation is scattered due to the molecular size particles and this process is called Rayleigh scattering. When particle (fog and smoke) size is large compared with the transmission wavelength, the process is called Mie scattering. Mie scattering is much less wavelength dependent while Rayleigh scattering is predominant at the shorter wavelengths [34, 138, 139]. More details will be discussed in the link budget analysis in Chapter 8.

2.6.2 Atmospheric Turbulence

Apart from the atmospheric attenuation, the laser beam traversing the atmospheric channel also experiences the atmospheric turbulence [123, 127, 131]. Some of the sun radiation strikes the earth's surface is absorbed, which heats the surface air layer. Heated air rises over the land and mix turbulently with the cooler air, thus causing a random variation in the atmospheric temperature along the propagation path. The temperature fluctuations depend on the wind speed and the altitude [4].

The temperature inhomogeneities of the atmosphere result in fluctuations in the refractive index, which causes the variations in the sizes of air packets from ~ 0.1 cm to ~ 10 m. The optical radiation traversing these air packets is partially or totally deviated, depending upon the relative sizes of the beam and the temperature inhomogeneity. This is because

the air packets act like prisms of varying refractive indices. Consequently, this interaction of the laser beam with the turbulent medium leads to random variation/fading in the irradiance (scintillation) and the phase of the laser carrier [4, 123, 127, 131]. The atmospheric turbulence depends on the wind speed, the atmospheric altitude/pressure, and the variation of refractive index.

The influences of atmospheric turbulence on the laser communications include [69]:

- i. *Beam steering* - Angular deviation of the beam from its initial LOS target leading to the beam being out of the receiver aperture range.
- ii. *Image dancing* - The focus of the received beam moves randomly in the image plane caused by the variations of the arrival-angle of the laser.
- iii. *Beam spreading* - The beam divergence is increased due to scattering, which causes a reduction in the received power density.
- iv. *Beam scintillation* - The spatial power density fluctuates at the receiver plane which is the result of small scale destructive interference within the optical beam cross-section.
- v. *Spatial coherence degradation* - The phase coherence across the beam phase fronts suffers losses due to the turbulence [95].
- vi. *Polarisation fluctuation* - This is negligible for the horizontally travelling optical radiation [67].

The statistical behavior of the received irradiance traversing a turbulent atmosphere will be detailed in Chapter Three.

2.7 Noise in Optical Detection

To accurately characterize the system performance, a good understanding of origins of noise is required. It is also useful to consider the electrical signal-to-noise ratio (SNR) as the limit to the system performance. A number of noise sources are associated with the optical communication systems, mainly arising from the background radiation and from the internally generated noise [69, 135]. A summary of the dominant sources of noise is presented next.

2.7.1 Thermal Noise

This is also known as the Johnson noise, which is the spontaneous fluctuation especially prevalent in resistors operating at room temperature. It is caused by thermal interaction between the free electrons and the vibrating ions in a conducting medium [42, 69, 135]. The thermal noise can be regarded as ‘white’ noise since the power spectral density (PSD) is independent of frequency. The Gaussian distribution is used to characterize the statistical behaviour of the thermal noise with zero mean and variance of [140]:

$$\sigma_{Th}^2 = \frac{4\kappa T_e B}{R_L}, \quad (2.4)$$

where κ is the Boltzmann's constant ($1.3806503 \times 10^{-23} \text{ m}^2 \text{ kg s}^{-2} \text{ K}^{-1}$), T_e is the temperature in Kelvin, B is the bandwidth in Hz and R_L is the equivalent load resistance in Ohm (Ω) is normalised to 1Ω .

2.7.2 Dark Current Shot Noise

In a photoemissive or photovoltaic detector, the dark current flowing in the absence of any photons impinging on the photodetector causes shot noise. The dark current, arising from the transition of electrons from the valence to the conduction band, includes tunnel, leakage, diffusion currents and generation-recombination taking place in the space-charge region and is proportional to the volume of the depletion region [135]. The amount of dark current is significantly dependent upon the energy band-gap of the photodetector materials. The shot noise variance is given as [1]:

$$\sigma_{Dk}^2 = 2q\langle i \rangle B, \quad (2.5)$$

where q represents the electronic charge, and $\langle i \rangle$ is the mean generated electric current over a given period of time

2.7.3 Photon Fluctuation Noise

The significant noise affecting all types of photodetectors is interrelated with the quantum nature of light itself, which is due to the varying number of photons emitted by a coherent optical source whereas the mean radiation intensity is constant. The photon fluctuation noise is also known as generation-recombination noise for a solid-state

detector or as the shot noise for a photoemissive detector [69, 135]. The variance of quantum noise can be expressed as [1, 42]:

$$\sigma_{Qtm}^2 = 2q\langle i \rangle B. \quad (2.6)$$

2.7.4 Background Radiation

It is the result of the photons generated by the environment. The background radiation is dominated by two major sources: extended sources (e.g. the sky) and localised point sources (e.g. the sun). The radiation from other sources (stars and reflected background radiation) is presumed to be too weak to affect the terrestrial FSO systems, whereas its effects are significant on the performance of the deep space FSO.

However, the impact of background noise can be mostly decreased by using an optical bandpass filter (OBPF) and a receiver with a very narrow FOV. The OBPFs coated onto the receiver with bandwidth less than 1 nm are available in the market. The background radiation considered as the shot noise has a variance [69]:

$$\sigma_{Bg}^2 = 2qB\Re(I_{sky} + I_{sun}), \quad (2.7)$$

where I_{sky} and I_{sun} represent the radiation from the sky and the sun. In general, the background radiation is greater than other noise processes [1, 69] so that it dominates the total shot noise which is the summation of all type of noises.

2.8 Eye Safety and Standards

Some of the data transmission limitations faced by the FSO technology can be alleviated by increasing the optical power. For instance, the optical signal propagating through the atmospheric channel is subject to a high attenuation, which can be compensated by using a high emitted optical power to improve the link range and SNR. A smaller and faster low-capacitance photodetector can also be used for a high power level transmission system.

Meanwhile, the safety of the optical radiation has to be ensured. The optical power at their respective wavelengths (infrared, visible, and ultraviolet) must not exceed the specific safety levels and cause any damage to both the eye and skin that might come into contact with it [42, 141-143]. Injury to the eye can be far more serious due to the eye's ability to focus and concentrate the optical energy.

The optical power covering the wavelengths from 400–1400 nm can be focused on the retina, whereas other wavelengths are more likely to be absorbed by the cornea before the energy is focused. A high-energy spot can be created by this focused energy. As the area of the spot reduces, the temperature of the retina rises, and the damage becomes worse [144]. In fact, the use of a 1550 nm wavelength optical carrier has been proposed because the cornea is opaque to infrared radiation beyond 1400 nm [1].

The infrared radiation at 1550 nm wavelength can be almost completely absorbed by the cornea and aqueous humour [145]. Additionally, in spite of the sensitivity of germanium (Ge) and indium gallium arsenide (InGaAs) photodetectors to electromagnetic energy at

around 1550 nm, these detectors are more expensive and present higher capacitances [146]. Apart from the transmission optical power, other issues that have to be considered are the flux density (the power per unit area), the wavelength of operation, and the length of time that the eye is exposed to the optical radiation [143].

Several international organizations provide standards on the safety issue of laser beams, among which the leading ones are [68]: American National Standards Institute (ANSI), International Electrotechnical Commission (IEC), European Committee for Electrotechnical Standardization (CENELEC), Laser Institute of America (LIA), and Center for Devices and Radiological Health (CDRH).

As specified by the revised IEC 60825-1 standard, the classification of systems according to their significant characteristics and requirements is presented in Table 2.1 [145].

Table 2.1: Classification of laser beams on eye safety issue.

Class	Comments
Class 1	Radiation from a low power device at a wavelength range 302.5–4000 nm. Lasers belonging to Class 1 are intrinsically safe due to their technical design under all reasonably conceivable usage conditions, when viewing through optical instruments (monocular, binoculars, microscope);
Class 1M	Similar to Class 1 and providing beams that are divergent, or large-diameter beams. The danger can be considerably heightened when using it with optical instruments, including binoculars, telescope, etc.
Class 2	A Class 2 laser is safe as it is limited to a 1 mW continuous wave, or the light with high optical power is not spatially coherent, or the emission time is less than 0.25 seconds. It covers the visible-light range 400–700 nm. Defensive reflexes ensure eyes are protected, for example, the palpebral

	reflex (closing of the eyelid) provides effective protection under all reasonably foreseeable usage conditions, when using optical instruments (binoculars, microscope, monocular).
Class 2M	Visible radiation from a low power device covering the band 400 - 700 nm. Class 2M provides beams that are divergent or large-diameter beams. The danger can be considerably heightened when using it with optical instruments, including binoculars, telescope, etc. The radiation of light emitted from the pupil must not exceed the limits of Class2.
Class 3R	Potentially dangerous for direct vision. The amount of radiation from a Class 3R laser is limited to 5 mW and it is in the band 302.5 - 4000 nm.
Class 3B	It is hazardous for direct vision whereas the diffuse reflection is not harmful. The average power is limited to 30 mW. The Class 3B laser operates in the band 302.5–4000 nm. Protective eyewear and specific training are typically required before the maintenance or installation is carried out.
Class 4	Class 4 lasers are high power devices, which can burn the skin and cause potentially permanent eye damage for both direct and diffuse beam viewing. They have to be fitted with a key switch and a safety interlock. Protective eyewear and specific training are required before carrying out the maintenance or installation.

The transmission optical power emitted from a Class 1 laser operating at 1550 nm could be approximately 50 times more than that emitted from a laser working in the shorter infrared wavelength (850 nm), provided the sizes of the aperture lens are same. It is also important to note that the determinant of the laser classification is the output power which is in front of the transmit aperture instead of the absolute power created by a laser diode inside the equipment. Therefore, it is theoretically possible to design an eye-safe FSO system operating at any wavelength. In fact, the FSO system can be considered as Class 1 or 1M even if the inner laser diode is actually Class 3B. In such a case, the light

is spread out to pass through the large-diameter lens aperture before it enters the space or multiple large transmission apertures are used to maintain the Class 1 or 1M safety classifications [68].

2.9 Summary

This chapter outlined the introductory discussion to optical wireless communication systems. The features and usage which make FSO technology suitable for the access network were highlighted. The challenges faced by the optical beam propagating over the atmospheric channel also were discussed with the aim of having a complete overview of the technology and the possibility to compare it to radio as a medium for wireless communication. It has to be noted that optical wireless will not replace radio as the only technology to transmit information wirelessly but operates in a complementary way. One technology is preferred over the other depending on a particular system as requested. Various areas of FSO applications were mentioned as well as the issue of eye safety and laser classifications. Descriptions of the operating principles of IM/DD were given to provide a background for the subsequent chapters. Furthermore, the various noise sources were analysed.

Chapter Three

Atmospheric Turbulence Models

Understanding of the statistical distribution of the received irradiance in the atmospheric turbulence is necessary to predict the reliability of an optical system operating in such an environment. Several mathematical models for the random fading irradiance signals have been developed; however, a valid probability density function (PDF) for all the turbulence regimes does not currently exist [1, 95]. The three most reported models for irradiance fluctuation will be discussed in this chapter, which are the lognormal, the gamma-gamma, and the negative exponential models corresponding to weak, weak-to-strong and saturation regimes, respectively [13, 67, 95-97, 131, 147]. Since the gamma-

gamma model covers all atmospheric turbulence regimes, it will be applied to evaluate the performance of FSO link in the subsequent chapters.

3.1 Optical Turbulence

The turbulent air can be regarded as a set of eddies with various temperatures, acting like refractive prisms with different sizes and refractive indices. The ‘Taylor hypothesis’ will be discussed here as it is widely used for a turbulent atmospheric channel [67, 86]. In the ‘Taylor hypothesis’, the turbulent eddies are assumed to be frozen or fixed and only move with the transverse component of the wind. The statistical properties or the temporal variations in the beam pattern result from the direction from which the wind blows perpendicular to the direction the light is travelling. Additionally, the temporal coherence time τ_0 is approximately milliseconds, which is greater than the duration of a typical data symbol [95]. Therefore, an atmospheric turbulence channel is called a ‘slow fading channel’ as it is static during the symbol period.

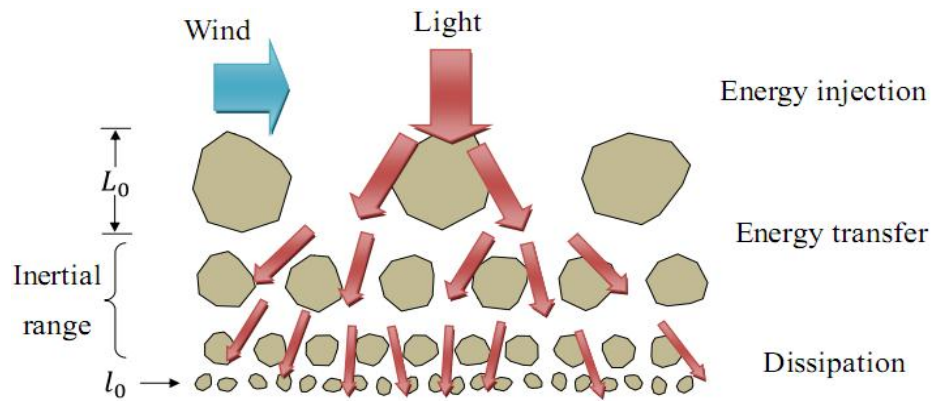


Fig. 3-1: Kolmogorov cascade theory of turbulence eddies between scale size L_0 and l_0 form the inertial subrange. (L_0 : the outer scale; l_0 : the inner scale).

The turbulent eddies have various scale sizes extending from the inner scale size l_0 to the outer scale size L_0 of turbulent air as shown in Fig. 3-1. More specifically, the outer scale L_0 grows linearly with the height of the observation point above ground in the surface layer of approximately 100 m, whereas the inner scale l_0 near the ground is typically around 3 to 10 mm and extends to several centimetres with higher altitude h [66, 96]. Due to the influence of inertial forces, the large eddy splits into smaller pieces to form an incessant cascade of scale sizes between l_0 and L_0 , which is known as the inertial range as illustrated in Fig. 3-1. Those scale sizes that are smaller than the inner scale are part of the dissipation range [96].

The turbulent air is due to the index-of-refraction (n) inhomogeneities caused almost exclusively by the atmospheric temperature fluctuation along the link range of the optical radiation propagating over the atmosphere [69]. The variation of temperature is a function of the wind speed, atmospheric pressure, and altitude [1].

The relationship between the temperature and refractive index of the atmosphere n is given as [148]:

$$n = 1 + 77.6(1 + 7.52 \times 10^{-3}\lambda^{-2}) \frac{P}{T_e} \times 10^{-6}, \quad (3.1)$$

where P is the atmospheric pressure (millibars) and λ is the wavelength (microns).

And the rate of change in the refractive index with respect to the atmospheric temperature is given as [67]:

$$-dn/dT_e = 77.6(1 + 7.52 \times 10^{-3}\lambda^{-2}) \frac{P}{T_e^2} \times 10^{-6}, \quad (3.2)$$

The effects of humidity on the refractive index fluctuation are assumed negligible at optical wavelength [95].

The Rytov variance σ_l^2 for a plane wave is used as a measure of turbulence strength and is derived as [1, 44, 149]:

$$\sigma_l^2 = 1.23C_n^2 K^{7/6} L^{11/6}, \quad (3.3)$$

where C_n^2 ($\text{m}^{-2/3}$) denotes the index of refraction structure parameter, $K = 2\pi/\lambda$ is the optical wave number, and $L(\text{m})$ is the link length between transmitter and receiver.

The parameter C_n^2 is given as [1, 42, 45, 149]:

$$C_n^2(h) = 0.00594(\nu/27)^2(10^{-5}\hbar)^{10}\exp(-\hbar/1000) + 2.7 \times 10^{-16}\exp(-\hbar/1500) \\ + \hat{A}\exp(-\hbar/100), \quad (3.4)$$

where \hbar is the altitude in metres (m), \hat{A} is a normal value of $C_n^2(0)$ at the ground level in $\text{m}^{-2/3}$, and ν is the root mean square (RMS) wind speed (pseudowind) in metres per second (m/s). The value of C_n^2 varies with the altitude \hbar , but it is assumed to be constant for a horizontally propagating field. The typical average value of C_n^2 is $10^{-15} \text{ m}^{-2/3}$ and a range from $10^{-17} \text{ m}^{-2/3}$ to $10^{-12} \text{ m}^{-2/3}$ corresponds to turbulence regimes from weak to strong, respectively [147, 149].

The PSD of refractive index fluctuation is closely related to C_n^2 with the following equation [123, 150, 151]:

$$\Phi_n(K) = 0.033C_n^2 K^{-11/3}, \quad 2\pi/L_0 \ll K \ll 2\pi/l_0 \quad (3.5)$$

However, the modified expression for a wider range of K is derived by Tatarski and Von Karman [147, 152, 153].

To mathematically describe the turbulent air is extremely difficult, because the observable atmospheric quantities are mixed non-linearly [96]. Therefore, the following assumptions have been made to simplify the mathematics [95]:

- i.* The terrestrial FSO channel is non-dispersive. Specific to radiation and absorption of the optical beam, this assumption is still valid as the heat generated is unimportant in comparison with diurnal contributions.
- ii.* The optical beam doesn't suffer from any energy loss due to the atmospheric scattering, which leads to a constant mean energy in the absence or presence of turbulence. This assumption is made with regard to the spherical and plane waves. The laser beam propagating over a long link span is generally considered as a plane wave [95, 154].

3.2 Lognormal Turbulence Model

The weak turbulence regime is characterized by the single scattering event based on the Rytov approach [67, 155, 156]. The Rytov transformation variable $\vec{\Psi}$ is defined to represent the natural logarithm of the transmission field \vec{E}_r , $\vec{\Psi} = \ln[\vec{E}_r]$ [152]. By invoking the smooth perturbing method [95], the Gaussian complex variable $\vec{\Psi}$ can be written as:

$$\vec{\Psi} = \vec{\Psi}_0 + \vec{\Psi}_1, \quad (3.6)$$

where $\vec{\Psi}_0$ and $\vec{\Psi}_1$ correspond to the absence-of-turbulence part and turbulence induced deviation, respectively. Both variables are Gaussian processes.

To find out the statistical distribution of irradiance fluctuation in a weak turbulence regime, the amplitude fluctuation is obtained as:

$$\vec{\Psi}_1 = \vec{\Psi} - \vec{\Psi}_0 = \ln[\vec{E}_r] - \ln[\vec{E}_0] = \ln[\vec{E}_r/\vec{E}_0], \quad (3.7)$$

where \vec{E}_r and \vec{E}_0 stand for electric fields representing the laser beam traversing through a terrestrial channel in the presence and absence of turbulence, respectively. The electric field \vec{E}_0 of the optical beam is defined as [1]:

$$\vec{E}_0 = A \exp\{i[\varphi]\}, \quad (3.8)$$

where A and φ represent the amplitude and phase of the electric field in a terrestrial channel, respectively. Thus, (3.7) can be rewritten as [157]:

$$\vec{\Psi}_1 = \ln[A_r/A_0] + i[\varphi_r - \varphi_0] = \chi + i\varsigma, \quad (3.9)$$

where χ denotes the Gaussian distributed log-amplitude fluctuation, and ς is the Gaussian distributed phase fluctuation of the field.

As the POLSK signals can be viewed as orthogonally amplitude modulated signals which are highly insensitive to the phase noise, only the irradiance fluctuation will be presented.

The PDF of the amplitude fluctuation χ is derived [44, 95, 123, 147, 149]:

$$p(\chi) = \frac{1}{\sqrt{2\pi\sigma_\chi^2}} \exp\left\{-\frac{(\chi - E[\chi])^2}{2\sigma_\chi^2}\right\}, \quad (3.10)$$

where $E[\chi]$ and σ_χ^2 correspond to the expectation and variance of variable χ , respectively. The variance σ_χ^2 is related to the refractive index structure parameter C_n^2 and expressed as [67]:

$$\sigma_\chi^2 = \begin{cases} 0.56k^{7/6} \int_0^L C_n^2(x)(L-x)^{5/6} dx & \text{for a plane wave,} \\ 0.563k^{7/6} \int_0^L C_n^2(x)(x/L)^{5/6}(L-x)^{5/6} dx & \text{for a spherical wave,} \end{cases} \quad (3.11)$$

where L is the horizontal distance that the optical field/radiation travelled through.

The field irradiances (optical powers) operating in the presence and absence of a turbulence channel are $P_r = |A_r|^2$ and $P_0 = |A_0|^2$, respectively. The log-amplitude is given as [123]:

$$l = \ln|P_r/P_0| = \ln|A_r/A_0|^2 = 2\chi, \quad (3.12)$$

where A_r and A_0 represent the amplitude in the presence and absence of a turbulence channel, respectively. And

$$P_r = P_0 \exp(l). \quad (3.13)$$

The statistics of the irradiance fluctuation of the laser travelling through the weak turbulence channel has been experimentally verified to obey the lognormal distribution [158].

Invoking the variable transformation, $p(P_r) = p(\chi)|d\chi/dl|$, the lognormal PDF is obtained as [44, 123, 149]:

$$p(P_r) = \frac{1}{\sqrt{2\pi}\sigma_l} \frac{1}{P_r} \exp\left[-\frac{(\ln(P_r/P_0) - E[l])^2}{2\sigma_l^2}\right] \quad P_r \geq 0, \quad (3.14)$$

where the Rytov variance, is $\sigma_l^2 = 4\sigma_\chi^2$ which is only valid for the spherical wave. The expression for σ_l^2 is given in (3.3). The mean log-amplitude is $E[l] = 2E[\chi]$ [123].

As the experimental results reported in [95], the lognormal model can only predict the irradiance fluctuation in a weak turbulence channel for $\sigma_\chi^2 < 0.3$. Beyond this range, the lognormal turbulence model becomes invalid caused by the multiple scattering due to a combination of increased link range and/or C_n^2 [67, 96]. Based on the second assumption in Section 3.2, the amount of energy is counted as the same during the scattering process, which means $E[\exp(l)] = E[P_r/P_0] = 1$ and $E[P_r] = P_0$. Applying the standard relation (3.15) (valid for the Gaussian random variable with real values) [147], the expression for $E[\exp(l)]$ is given as [123]:

$$E[\exp(az)] = \exp(aE[z] + 0.5a^2\sigma_z^2), \quad (3.15)$$

$$1 = \exp(E[l] + 0.5\sigma_l^2), \quad (3.16)$$

$$E[l] = -\sigma_l^2/2, \quad (3.17)$$

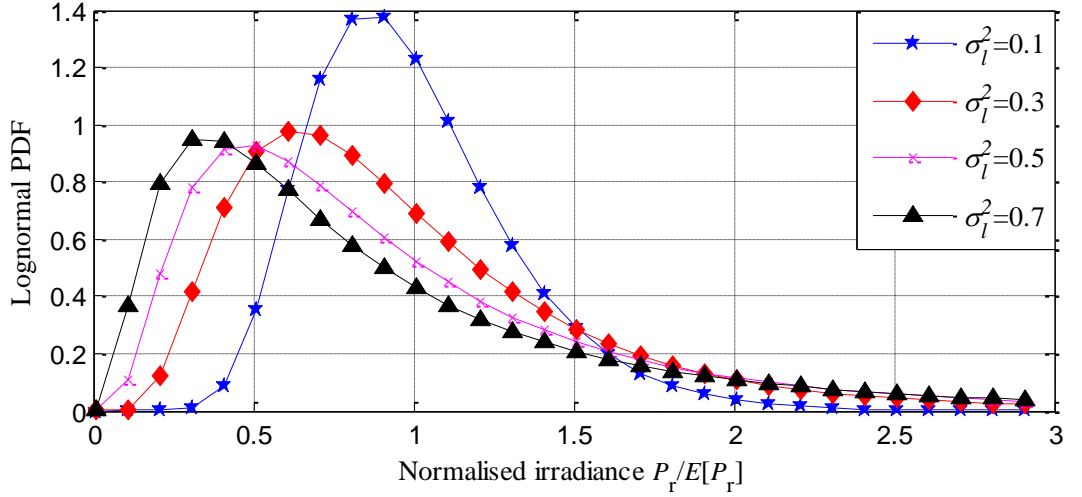


Fig. 3-2: Lognormal PDF with $E[P_r] = 1$ for various values of turbulence variance σ_l^2 .

The lognormal PDF expressed by (3.14) is shown in Fig. 3-2 for a range of σ_l^2 . The distribution is skewed right. Increasing the value of turbulence variance σ_l^2 will increase the skewness. Meanwhile, the tail becomes longer in the positive infinity direction, which indicates the extent of the irradiance fluctuation as the channel inhomogeneity increases. The normalized variance of the irradiance fluctuations, also known as scintillation index $S.I.$, is considered as the most crucial parameter in characterising the effects of the atmospheric turbulence, as given by [96]:

$$S.I. = \exp(\sigma_l^2) - 1, \quad (3.18)$$

When the scintillation index increases linearly with σ_l^2 (Rytov parameter) until it reaches a maximum value greater than unity, the scintillation enters into the strong turbulence regime characterized by the random focusing due to the large-scale inhomogeneities [67, 95]. Continuously raising the inhomogeneity strength or the link range will decrease the focusing effect and the peak fluctuations as the result of multiple self interferences. In

such case the turbulence enters into the saturation regime at which the scintillation index approaches unity from above. Saturation is induced by the increasingly lower (spatial) coherence of the propagating optical wave due to the multiple self interferences. Saturation can be viewed as extended independent multiple sources, each of which radiates with a distinct random phase [95].

3.2.1 Spatial Coherence in Weak Turbulence

The optical beam suffers a decrease in its spatial coherence while propagating through a turbulent atmospheric channel. The degree of the coherence degradation is related to the turbulence strength and the transmission link range as the coherence radiation is split due to the turbulent air. The reduced spatial coherence distance can be measured using the diameter of the fragmental coherence radiation.

The spatial coherence of a travelling optical field can be derived based on the Rytov approach [67]:

$$\Gamma_x(\rho) = A^2 \exp[-(\rho/\rho_0)^{5/3}], \quad (3.19)$$

where ρ_0 denotes the transverse coherence length at which the coherence of the optical field is $\Gamma_x(\rho) = e^{-1}$.

The transverse distance ρ_0 for plane and spherical waves is defined by following equations [67], respectively:

$$\rho_0 = \left[1.45k^2 \int_0^L C_n^2(x) dx \right]^{-3/5}, \quad (3.20a)$$

$$\rho_0 = \left[1.45k^2 \int_0^L C_n^2(x) (x/L)^{5/3} dx \right]^{-3/5}. \quad (3.20b)$$

The coherence distance is important in the aperture averaging which is the technique to determine the size of the receiver aperture in order to collect the propagating optical field. In a multi-receiver optical system the minimum separation distance of the detector array is determined by the coherence length ρ_0 in order to receive uncorrelated signals [1, 123].

The transverse coherence length for a plane wave at two wavelengths, $\lambda = 850$ nm and 1550 nm, for various values of C_n^2 ($\text{m}^{-2/3}$) is depicted in Fig. 3-3. The coherence length is higher at longer wavelengths. For example, when the link range is 1 km and $C_n^2 = 10^{-15} \text{ m}^{-2/3}$, the coherence lengths are ~ 0.07 m and ~ 0.15 m for the plane wave at the wavelengths of 850 nm and 1550 nm, respectively. The coherence length reduces as the link range or the turbulence level rises. For instance, when C_n^2 increases to $10^{-12} \text{ m}^{-2/3}$, the corresponding coherence length decrease to ~ 0.001 m and ~ 0.002 m.

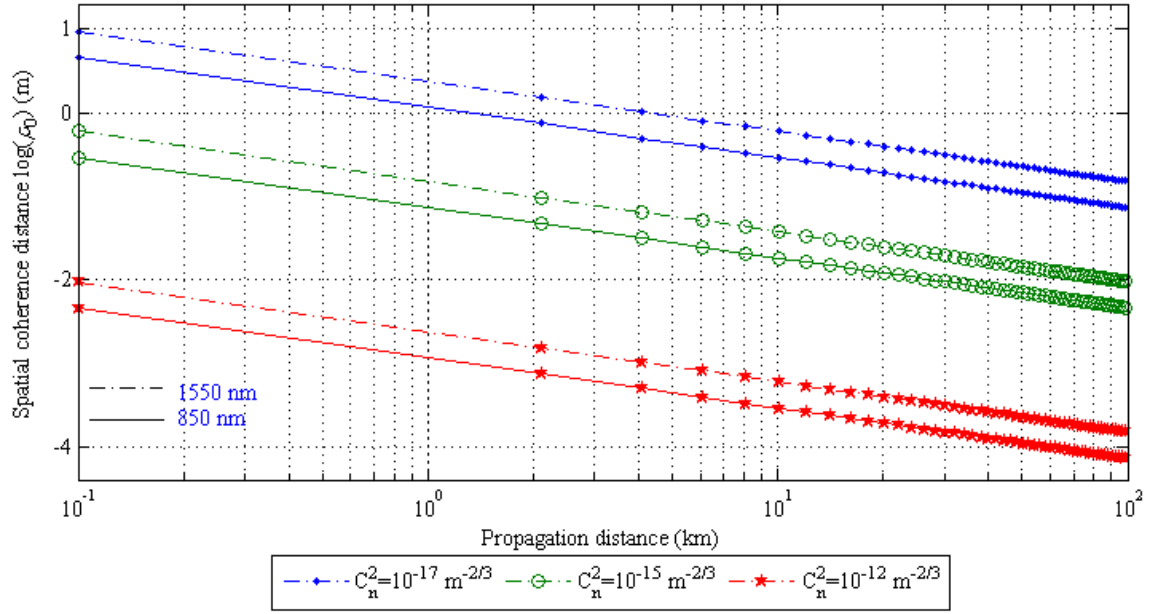


Fig. 3-3: The transverse coherence distance ρ_0 (m) against the link range with a range of C_n^2 ($\text{m}^{-2/3}$) for the plane wave at the wavelengths of $\lambda = 850$ nm and 1550 nm.

3.3 Gamma-Gamma Turbulence Model

The gamma-gamma model is proposed by Andrews *et al* [96, 131, 149]. The irradiance fluctuation of an optical beam propagating over the turbulent air can be viewed as the modulation process comprising small scale (scattering) and large scale (refraction) effects. The small scale effect is caused by the eddies/cells smaller than the Fresnel zone or the coherence radius, while the large scale is due to the turbulent eddies larger than the first Fresnel zone or the scattering disk. Assuming the small scale eddies are modulated by the large scale eddies, the irradiance can be described by $P_r = P_x P_y$, where P_x and P_y arise from large-scale and small-scale atmospheric effects, respectively. In addition, both

are two statistically independent random processes and governed by gamma distributions [13, 45, 79, 96, 97]:

$$p_x(P_x) = \frac{\alpha(\alpha P_x)^{\alpha-1}}{\Gamma(\alpha)} \exp(-\alpha P_x) \quad P_x > 0, \alpha > 0, \quad (3.21a)$$

$$p_y(P_y) = \frac{\beta(\beta P_y)^{\beta-1}}{\Gamma(\beta)} \exp(-\beta P_y) \quad P_y > 0, \beta > 0. \quad (3.21b)$$

The effective numbers of large- and small-scale eddies of the scattering process respectively are represented by α and β which characterise the irradiance fluctuation PDF. The conditional PDF is obtained by first fixing P_x and writing $P_y = P_r/P_x$ [13, 45, 127, 149],

$$p_y(P_r|P_x) = \frac{\beta(\beta P_r/P_x)^{\beta-1}}{P_x \Gamma(\beta)} \exp(-\beta P_r/P_x) \quad P_r > 0, \quad (3.22)$$

where P_x denotes the (conditional) mean value of P_r .

The unconditional irradiance fluctuation is derived by forming the average of (3.22) over the gamma distribution [1, 13, 45, 96, 149]:

$$\begin{aligned} p(P_r) &= \int_0^\infty p_y(P_r|P_x) p_x(P_x) dP_x, \\ &= \frac{2(\alpha\beta)^{(\alpha+\beta)/2}}{\Gamma(\alpha)\Gamma(\beta)} P_r^{\frac{\alpha+\beta}{2}-1} K_{\alpha-\beta}(2\sqrt{\alpha\beta P_r}) \quad P_r > 0, \end{aligned} \quad (3.23)$$

where $K_n(\cdot)$ denotes the modified Bessel function of the 2nd kind of order n , and $\Gamma(\cdot)$ represents the Gamma function.

Assuming the optical beam at the receiver is a plane wave, the two parameters α and β are related to atmospheric conditions through models for large-scale and small-scale scintillations by [1, 149]:

$$\alpha = \left[\exp \left(\frac{0.49\sigma_l^2}{(1 + 1.11\sigma_l^{12/5})^{7/6}} \right) - 1 \right]^{-1}, \quad (3.24a)$$

$$\beta = \left[\exp \left(\frac{0.51\sigma_l^2}{(1 + 0.69\sigma_l^{12/5})^{5/6}} \right) - 1 \right]^{-1}. \quad (3.24b)$$

Provided (3.23) and (3.24), the gamma-gamma PDF $p(P_r)$ is plotted against the irradiance P_r for various values of α and β corresponding to weak, moderate, and strong turbulence regimes as shown in Fig. 3-4. As the turbulence level increases from weak to strong, the distribution spreads out more and the tail becomes longer, which raises the extent of irradiance. The gamma-gamma PDF model is verified by Andrews [96]. The gamma-gamma channel is particularly attractive in predicting the statistical distribution of the irradiance fluctuation in a turbulent atmospheric channel because it is valid for all turbulence scenarios from weak to strong.

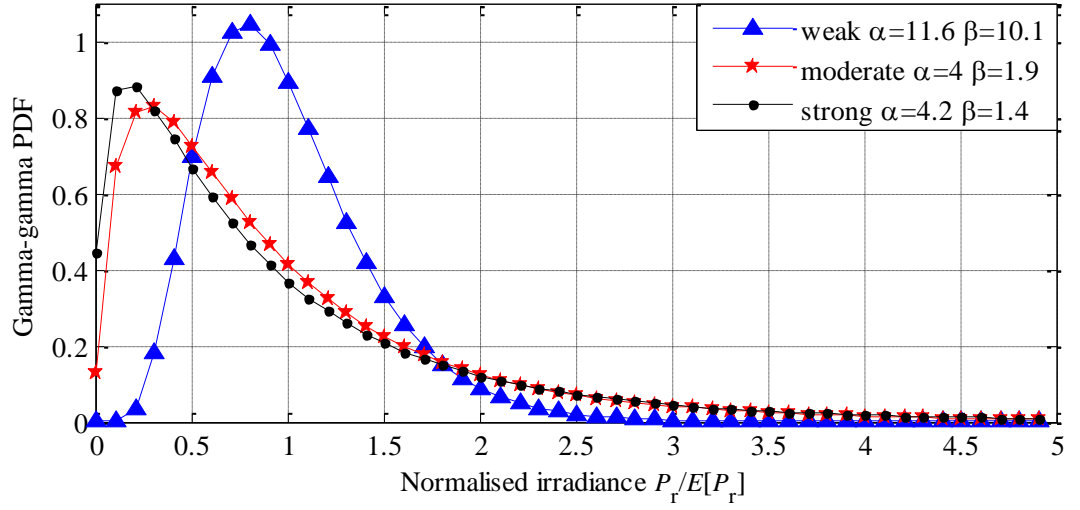


Fig. 3-4: Gamma-gamma PDF with respect to the turbulence regimes from weak to strong.

The *S.I.* as a function of the lognormal turbulence variance σ_l^2 in a gamma-gamma turbulence channel is obtained as [1]:

$$\sigma_N^2 = \exp \left[\frac{0.49\sigma_l^2}{(1 + 1.11\sigma_l^{12/5})^{7/6}} + \frac{0.51\sigma_l^2}{(1 + 0.69\sigma_l^{12/5})^{5/6}} \right] - 1. \quad (3.25)$$

The value of *S.I.* against the turbulence variance σ_l^2 is plotted in Fig. 3-5 using (3.25). As σ_l^2 increases, the *S.I.* increases to the maximum value and then it tends to be flat as the turbulence induced fading approaches the saturation regime.

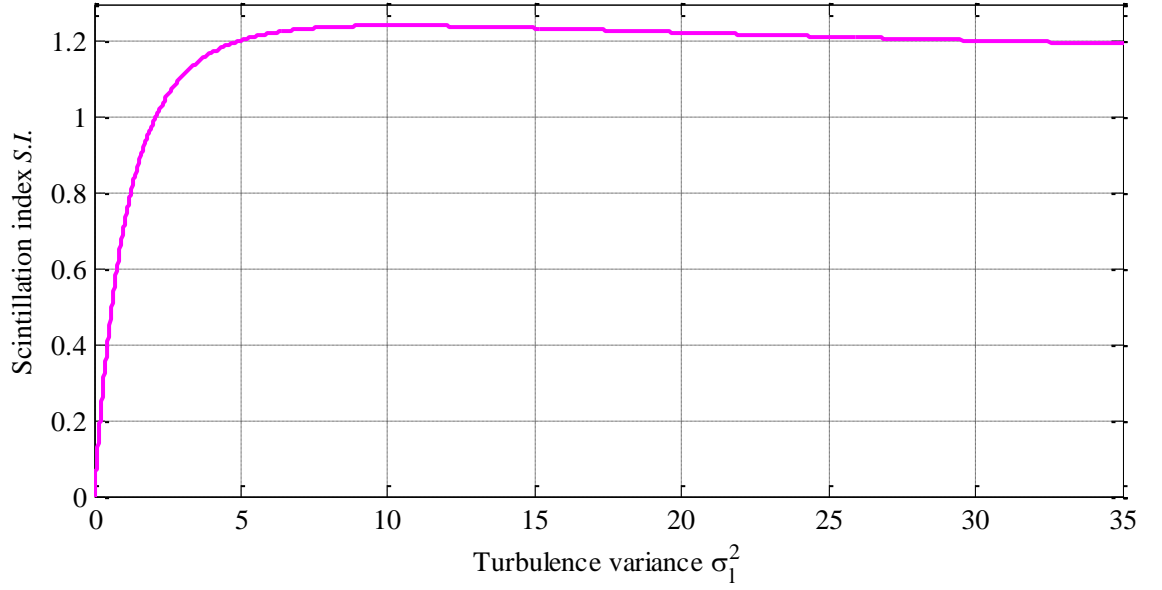


Fig. 3-5: $S.I.$ against the turbulence variance σ_l^2 with $C_n^2 = 10^{-15} \text{ m}^{-2/3}$ and $\lambda = 850 \text{ nm}$.

The range of values for α and β across the turbulence regimes from weak to strong are shown in Fig. 3-6. The weak turbulence regime is characterized by a large effective number of large and small scale eddies. As the irradiance fluctuation increases until $\sigma_l^2 > 0.2$, the turbulence enters into the focusing regime, where the values of α and β drop noticeably. Continuously increasing σ_l^2 results in the saturation regime where α and $\beta \rightarrow 1$. According to [79], the transverse spatial coherence radius of the optical wave determines the effective number of small scale eddies. Increasing the turbulence variance σ_l^2 increases the effective number of discrete refractive scatters α which ultimately turns into unbounded in the saturation regime as illustrated in Fig. 3-6. In such a case the distribution of irradiance fluctuation is modelled as the negative exponential distribution.

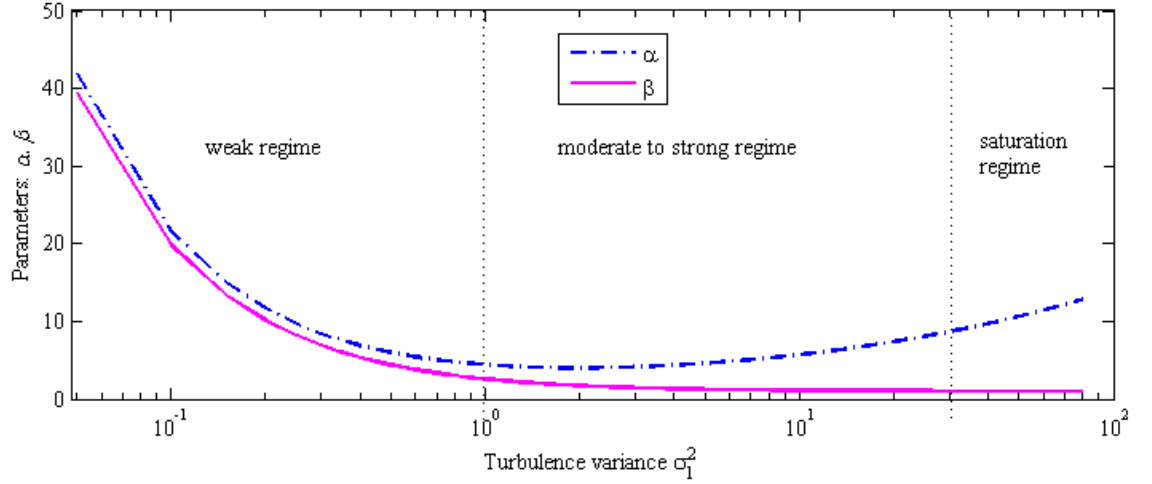


Fig. 3-6: The range of values for α and β in the whole turbulence regime.

3.4 Negative Exponential Turbulence Model

The multiple scattering effects must be taken into account as the strength of turbulence increases [96]. Beyond the saturation regime, the turbulence approaches the limits, also known as the fully developed speckle regime where the link range extends several kilometres and the number of independent scatterings becomes large [10, 159]. The irradiance fluctuation of the optical field propagating over a turbulence channel in the saturation regime is governed by the Rayleigh distribution implying negative exponential statistics which is expressed as [95, 160, 161]:

$$p(P_r) = \frac{1}{P_0} \exp\left(-\frac{P_r}{P_0}\right) \quad P_0 > 0, \quad (3.26)$$

where P_0 denotes the mean received irradiance.

The value of the scintillation index is approaching unity, $S.I. \rightarrow 1$, in the saturation regime. The negative exponential turbulence model is depicted in Fig. 3-7. In addition,

other turbulence models proposed are also valid from weak to strong turbulence regime. Both the lognormal-Rician [162] and the I-K [163] turbulence models cover the entire turbulence regimes from weak to strong. The K-model [157, 164, 165] is only applied for the strong turbulence regime.

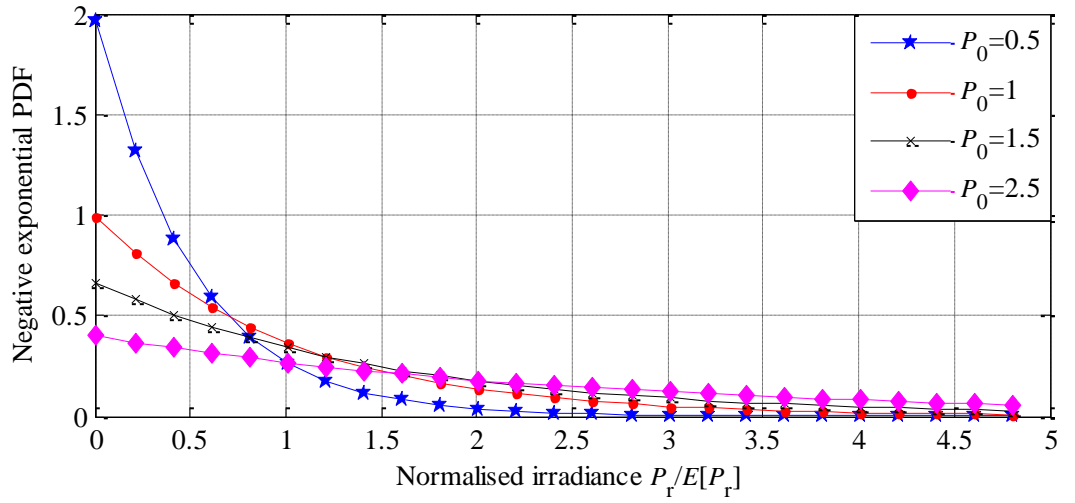


Fig. 3-7: Negative exponential PDF against the normalised irradiance for various values of P_0 .

3.5 Summary

This chapter gives a complete parametric description of the optical beam propagation over a turbulence channel. A theoretical basis of the atmospheric propagation characteristics, pertinent examples, and references for further data are provided. A number of definitions introduced in this chapter are important for a better comprehension of the atmospheric phenomena and the effects on a propagating laser beam. Additionally, different atmospheric turbulence models have been outlined. The lognormal is

mathematically tractable but only valid in the weak regime. Beyond the weak regime, where multiple scattering needs to be taken into account, the gamma-gamma model is more suitable but lacks the mathematical convenience. The negative exponential model is used in the saturation regime. The gamma-gamma turbulence model will be applied in the subsequent chapters to characterise the statistical behaviour of the received optical signal and derive error rate expressions of FSO links.

Chapter Four

Coherent Polarisation Shift Keying Systems

To design an optical wireless system, selecting the right modulation scheme is of paramount importance. The bandwidth, the power efficiency and the design complexity of the transmitter and receiver, which affect the overall performance of the system, are defined by the modulation technique adopted [45, 66]. The coherent POLSK modulation scheme will be introduced in this chapter, and will be used in the following chapters to compare the error probabilities with other modulation schemes in the presence of channel impairments, such as noise and turbulence. The chapter is organised as follows. Discussions on digital modulation schemes will be outlined in Section 4.1;

followed by the general coherent optical system structure in Section 4.2; the POLSK scheme will be introduced in Section 4.3; the polarisation fluctuations in a turbulence channel will be discussed in Section 4.4; the outage probabilities in a lognormal channel and a negative exponential channel are analysed in Sections 4.5 and 4.6, respectively; finally, the will be presented in Section 4.7.

4.1 Digital Modulation Schemes

Digital modulation schemes are favoured in optical transmission for a number of reasons including the performance, the compatibility with the digital world, the ability to introduce coding, encryption, compression, and the hard and soft signal processing [45, 80, 157, 166-168]. The modulation tree is illustrated in Fig. 4-1 in which the highlighted modulation techniques will be introduced in the following chapters. In order to present the advantages of polarisation modulation schemes with regard to the error performance in the atmospheric turbulence channel, comparisons of the POLSK, NRZ-OOK and PSK schemes operating over an atmospheric turbulence channel will be carried out.

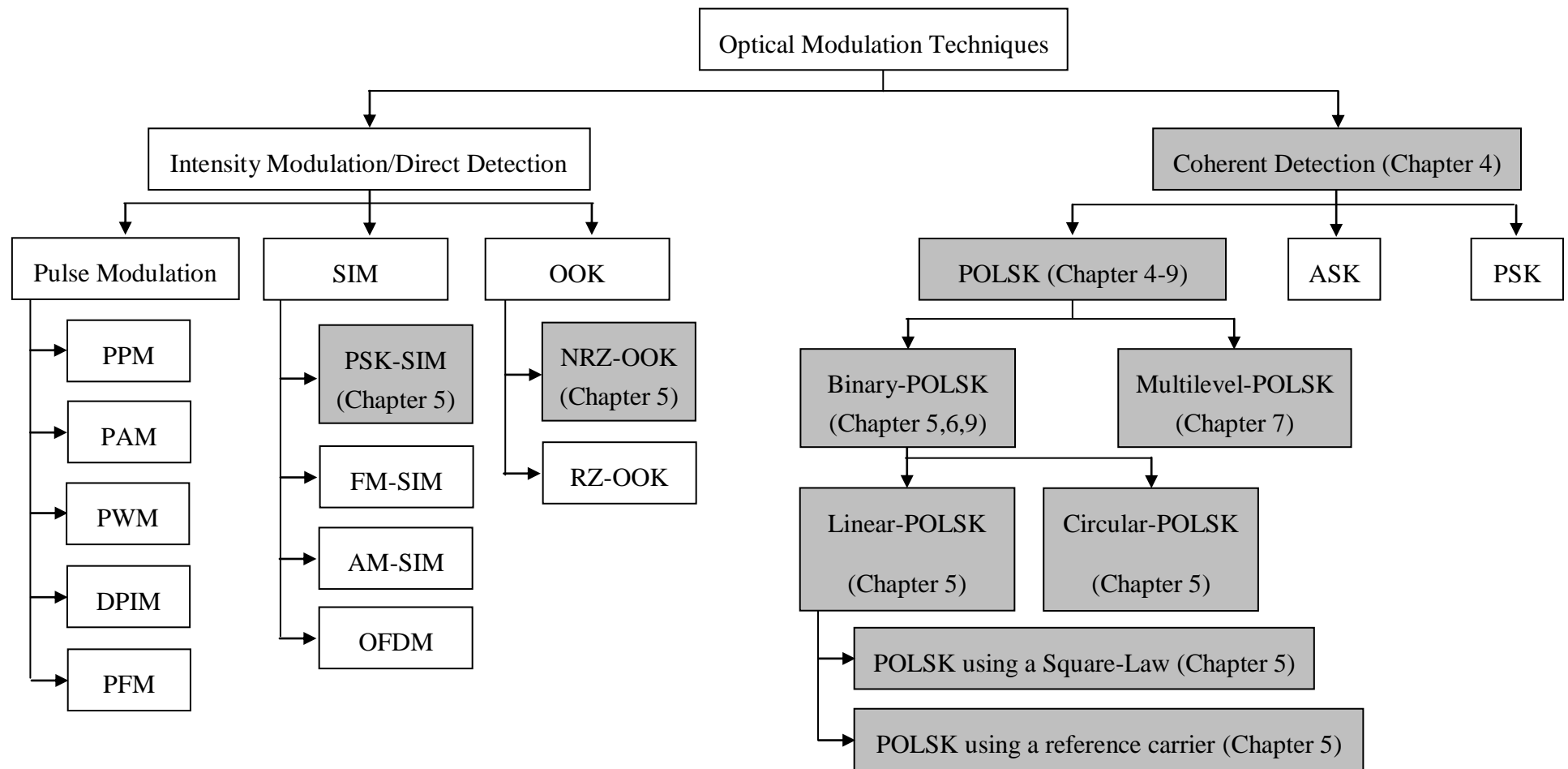


Fig. 4-1: Modulation tree. (OOK: on-off keying; NRZ-OOK: non-return-to-zero OOK; RZ-OOK: return-to-zero OOK; SIM: subcarrier intensity modulation; PSK-SIM: phase shift keying SIM; FM-SIM: frequency modulation SIM; AM-SIM: amplitude modulation SIM; PPM: pulse position modulation; PAM: pulse amplitude modulation; PWM: pulse width modulation; DPIM: digital pulse interval modulation; PFM: pulse frequency modulation; POLSK: polarisation shift keying; ASK: amplitude shift keying; PSK: phase shift keying).

In a single SIM scheme, the electric current to drive the transmitter is a radio frequency subcarrier of a higher frequency modulated by the original information, where the instantaneous power of the optical transmitter is proportional to the modulated signal [169]. The spectrum of a baseband signal is shifted to facilitate the transmission of the information signal. A DC bias is generally added to ensure that the signal amplitude is always positive. In single SIM, the PSK can be applied to modulate the carrier [166, 169-171].

Multiple subcarrier modulation (MSM) contains several digital or analogue signals on different electrical subcarriers, which are then used to intensity modulate the optical carrier signal [166, 171-173]. If the subcarriers are orthogonal, it is called orthogonal frequency division multiplexing (OFDM) [174]. MSM and OFDM schemes are attractive as the asynchronous multiplexing of different information streams is possible where only the desired information stream can be demodulated at the receiver. However, these modulation schemes suffer from the poor optical average power efficiency, which is caused by the high PAPR in the MSM electrical signal [87, 171, 174, 175]. The power reduction techniques for MSM have been investigated in [175, 176].

4.2 Optical Coherent Receiver

The block diagrams of a coherent system for the heterodyne and homodyne optical receivers are depicted in Fig. 4-2 and Fig. 4-3, respectively. In a heterodyne optical

receiver the local oscillator and the received carrier possess different optical frequencies [21, 177, 178]. However, the homodyne optical receiver is a type of degenerate heterodyne receiver in which two optical frequencies are the same [135, 177, 179-181]. In a coherent receiver, the received optical field is superimposed onto the optical local oscillator field by a PBS. The photodetector detects the sum of these two fields and provides an electric current proportional to the received optical power [135, 181].

4.2.1 Optical Heterodyne Detection Receiver

The optical heterodyne receiver is shown in Fig. 4-2. Both optical fields of the input signal $\vec{E}_r(t)$ and local oscillator signal $\vec{E}_{lo}(t)$ are linearly polarised along the \vec{x} polarisation. The optical field at the receiver input $\vec{E}_r(t)$ is superimposed onto the optical field $\vec{E}_{lo}(t)$ generated by an optical local oscillator by using a PBS. The frequency of signal $\vec{E}_r(t)$ differs from that of $\vec{E}_{lo}(t)$ by the desired IF. The current at the output of the photo-detector is proportional to the sum of the irradiance of $\vec{E}_r(t)$ and $\vec{E}_{lo}(t)$ and the information buried IF component [12, 21, 182].

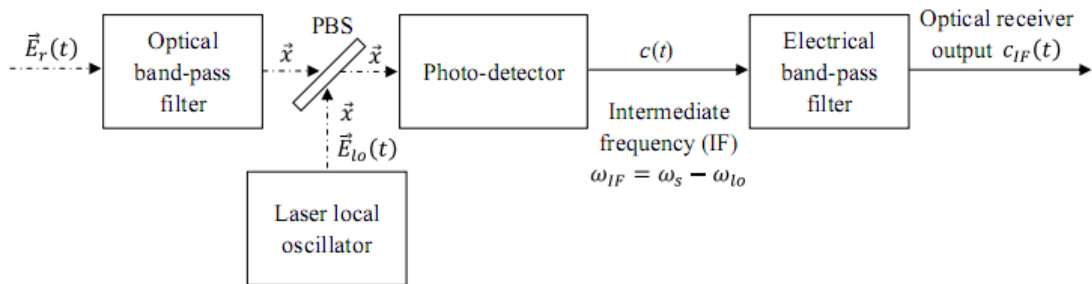


Fig. 4-2: A heterodyne detection receiver.

The electrical fields $\vec{E}_r(t)$ and $\vec{E}_{lo}(t)$ can be written as [69, 135]:

$$\vec{E}_r(t) = \sqrt{P_r} e^{i(\omega t + \varphi_r)} \cdot \vec{x}, \quad (4.1)$$

$$\vec{E}_{lo}(t) = \sqrt{P_{lo}} e^{i(\omega_{lo} t + \varphi_{lo})} \cdot \vec{x}, \quad (4.2)$$

where P_{lo} , ω_{lo} and $\varphi_{lo}(t)$ are the power, angular frequency and the phase noise of the local oscillator, respectively.

The receiver selects only the polarisation components of the received field that match the polarisation of the local oscillator, rejecting the others. It follows that the local oscillator will be assumed to be linearly polarised along the \vec{x} axis, and the information will be assumed to be encoded only in the \vec{x} polarisation of the received field.

The output current after the photo-detector is [69, 135]:

$$c(t) = \Re\{P_r + P_{lo} + 2\Re[\sqrt{P_r P_{lo}} e^{i(\omega_{IF} t + \varphi_{IF})}]\}, \quad (4.3)$$

where $\omega_{IF} = \omega - \omega_{lo}$ and $\varphi_{IF}(t) = \varphi_r(t) - \varphi_{lo}(t)$ are the frequency and phase noise of the intermediate signal, respectively. In (4.3) the first two terms are the baseband terms due to the received signal and local oscillator. The third term is the IF signal that can be separated by using a bandpass filter.

The bandwidth and the centre frequency of the bandpass electric filter are twice the symbol rate and ω_{IF} , respectively. Thus, the electric current $c_{IF}(t)$ is given as [69, 135]:

$$c_{IF}(t) = 2\Re\sqrt{P_r P_{lo}} \cos(\omega_{IF} t + \varphi_{IF}). \quad (4.4)$$

Therefore, the IF current depends on the received optical power, the angular frequency, and phase of the carrier signal. Each of these carrier parameters may be demodulated by the following electric processing circuit.

4.2.2 Optical Homodyne Detection Receiver

The homodyne receiver is illustrated in Fig. 4-3. The optical carrier and a local oscillator are set at the same frequency as the carrier and phase-locked to it. The optical mixing is performed by a PBS. The photodetector current $c(t)$ is given [35, 69, 135, 179]:

$$c(t) = \Re[P_r + P_{lo} + 2\sqrt{P_r P_{lo}} \cos(\varphi_r - \varphi_{lo})]. \quad (4.5)$$

The lowpass filter passes the signal and rejects the direct current components. The output current is given as [69, 135]:

$$c_{lp}(t) = 2\Re\sqrt{P_r P_{lo}} \cos(\varphi_r - \varphi_{lo}). \quad (4.6)$$

The carrier and local oscillator phase angles are set equal, which maximizes the signal current for intensity modulation of the carrier. Setting the local oscillator phase $\varphi_{lo} = \pi/2$ radians, the output signal from the local oscillator is proportional to φ_r ($\varphi_r \ll \pi/2$) for the phase modulation.

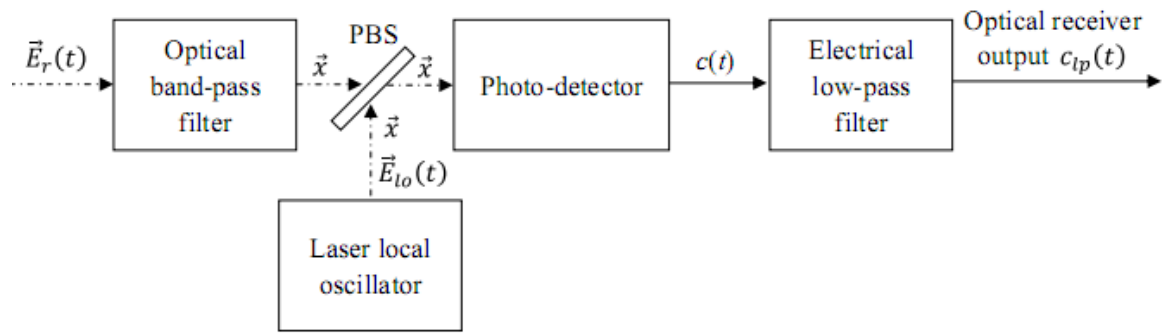


Fig. 4-3: A homodyne detection receiver.

4.2.3 Comparisons between Optical Coherent and Direct Detection

Receivers

In general, the coherent receiver offers the following features compared with the direct detection receiver [135, 178, 183-185]:

- i. A local oscillator (LO) with a sufficient power achieves the shot-noise limited receiver sensitivity. This is due to the signal gain offered by the LO induced shot noise being the dominant source.
- ii. An intrinsic frequency selectivity characteristic is based on the IF or the baseband stage. It is used to detect WDM signals at the electrical stage by an electrical filter.
- iii. A coherent receiver only selects the polarisation components of the received optical signal that match the polarisation of the local oscillator and rejects the others [69, 135].

- iv. Compared with the IM/DD system, the receiver sensitivity can be improved by using the phase detection, as the distance between symbols, expressed as phasors on the complex plane, is extended by the use of the phase information.
- v. Use of both bandwidth and power-efficient multilevel modulations that can be adopted for coherent optical communications by using phase modulation, such as the quadrature phase-shift keying (QPSK).
- vi. Coherent detection requires stringent synchronization and channel estimation.
- vii. Coherent receiver is more complex than IM/DD receiver.

In the OOK modulation scheme, the amplitude of the carrier varies in proportion to the amplitude of the modulation signal [157, 186]. On the other hand, the PSK scheme transmits the information by shifting the phase of the sinusoidal carrier [166]. The OOK scheme is one of the preferred modulation techniques used for FSO because of its good bandwidth efficiency and the simplicity of implementation [1, 36, 68, 157]. However the performance of the OOK with a fixed thresholding scheme is not optimal in a turbulence channel. The threshold level is required to vary in proportion to the irradiance fluctuation and noise, which is to apply an adaptive thresholding scheme at the receiver, thus increasing the system complexity.

The PSK technique requires no adaptive thresholding scheme and offers improved performance in the presence of turbulence [1, 9, 171]. The results reported by Gfeller *et al* showed that the PSK presented synchronization problems in a diffuse environment

where different paths for the transmitted energy existed. The angular modulation scheme is highly sensitive to the phase noise, thus requiring a complex synchronization at the receiver [42, 135, 187]. Compared to the OOK scheme, the binary PSK scheme requires twice the bandwidth and 1.5 dB more optical power [135]. Examples of FSO systems based on OOK and PSK can be found in [1, 135, 166, 171, 186].

Rather than using the traditional approach of modulating the amplitude, phase and frequency of the carrier signal, it is also possible to implement the modulation externally on the optical beam. By doing so another dimension such as polarisation states could be modulated in proportion to the amplitude of the modulating signal, thus it is named POLSK [111, 113, 116, 124, 168, 188]. The POLSK scheme has been proposed as an alternative modulation technique to both amplitude- and phase- based modulation schemes. The digital information is encoded in the SOP of the laser source [111-113, 168]. Stokes parameters are used to represent the SOP so the symbol constellation is scattered over a 3-D space [112]. The POLSK scheme offers high immunity to the laser phase noise [110, 112]; and maintains SOPs over a long propagation link [113, 114].

4.3 Polarisation Modulation

For a laser beam propagating over the atmospheric channel, the polarisation state is the most stable characteristic of all the parameters [111, 124, 189]. Both theoretical [190] and experimental [191] results have shown that the wave depolarisation is negligible in a

turbulence channel. Since the POLSK modulated systems show some advantages compared with other modulation formats, as discussed in the introduction, the investigation of polarisation modulated FSO communication systems through the atmospheric channel is of paramount importance [111, 124].

4.3.1 Polarised Waves

The field amplitudes as projected along the horizontal axis \vec{x} and vertical axis \vec{y} can be described using the parametric equations [111, 192]:

$$\vec{E}_x = A_x e^{j(\omega t - k\hat{z})} \cdot \vec{x}, \quad (4.7a)$$

$$\vec{E}_y = A_y e^{j(\omega t - k\hat{z} + \phi)} \cdot \vec{y}, \quad (4.7b)$$

where the variables A_x and A_y correspond to the amplitudes of the electric field projected onto the \vec{x} and \vec{y} axis, respectively, and ϕ denotes the phase difference between \vec{E}_x and \vec{E}_y , which govern the shape of the electric field. To describe the polarisation of an electric field using a single equation, (4.7) yields [192, 193]:

$$\frac{\vec{E}_x^2}{A_x^2} + \frac{\vec{E}_y^2}{A_y^2} - \frac{2\vec{E}_x\vec{E}_y}{A_x A_y} \cos\phi = \sin^2\phi. \quad (4.8)$$

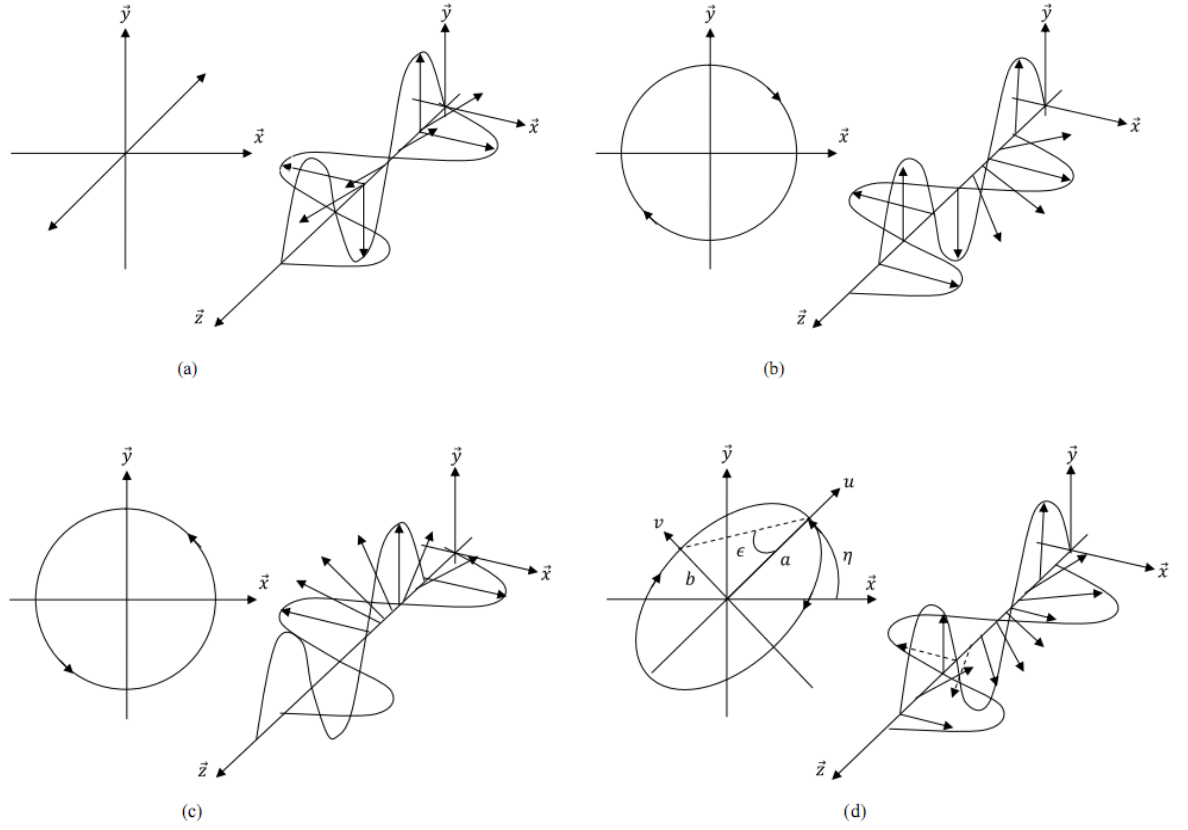


Fig. 4-4: Snapshots at a fixed time t of the electrical field vector of (a) linear polarised light, (b) right-hand circular polarised light, (c) left hand circular polarised light and (d) elliptical polarised light. a , major axis; b , minor axis; ϵ , ellipticity; η , azimuth.

Three general categories of polarisation states are: linear, circular and elliptical. The linearly polarised light is shown in Fig. 4-4. The light is linearly polarised along \vec{x} or \vec{y} axis if the component A_x or A_y is zero. When the phase difference ϕ equals zero or π , which means $A_y = \pm A_x$, the wave is linearly polarised at an offset angle of $\eta = \pm 45^\circ$ from the \vec{x} axis [111, 192]. If $\phi = \pm \pi/2$ and $A_x = A_y$, (4.8) is the equation of a circle and the wave is said to be circular polarised (see Fig. 4-4(b) and (c)). In the case of $\phi = +\pi/2$, the electric field vector at a fixed position \vec{z} rotates in a clockwise direction when viewed toward its propagation direction, which is also known as right-hand circular (RHC) polarised light (see Fig. 4-4(b)) [111, 192]. While the case of $\phi = -\pi/2$

corresponds to a counterclockwise rotation of the electric field vector and left-hand circular (LHC) polarised light (see Fig. 4-4(c)).

When the phase difference $\phi \neq 0, \pi$ or $\pi/2$ and $A_x \neq A_y$, though ϕ and the ratio A_x/A_y are constant, the wave is called elliptical polarised. Elliptical polarised light is shown in Fig. 4-4(d). A coordinate system (u, v) is used to define major and minor axes of elliptical polarised light with the elliptical equation expressed as:

$$\frac{u^2}{a^2} + \frac{v^2}{b^2} = 1, \quad (4.9)$$

where the major and minor axes of the ellipse, (a, b) , are on the (u, v) axes [111, 192].

The ellipticity ϵ defines the ratio of the minor to the major axis of the ellipsis and the rotation η is called the azimuth [111, 192]:

$$\tan \epsilon = \frac{b}{a}, \quad (4.10)$$

$$\begin{pmatrix} u \\ v \end{pmatrix} = \begin{pmatrix} \cos \eta & \sin \eta \\ -\sin \eta & \cos \eta \end{pmatrix} \begin{pmatrix} x \\ y \end{pmatrix}. \quad (4.11)$$

The Stokes vector (S_0, S_1, S_2, S_3) is another conventional description of the polarisation state and defined as [111],

$$S_0 = (A_x^2 + A_y^2)/2, \quad (4.12a)$$

$$S_1 = (A_x^2 - A_y^2)/2, \quad (4.12b)$$

$$S_2 = A_x A_y \cos \phi, \quad (4.12c)$$

$$S_3 = A_x A_y \sin \phi. \quad (4.12d)$$

The physical interpretations of the Stokes parameters are listed as follows [111]:

- S_0 represents the optical intensity.
- S_1 denotes the intensity difference between horizontal and vertical polarised components. For $S_1 > 0$, the electric field is horizontally polarised (i.e., for linear polarisation in the \vec{x} -direction); while for $S_1 < 0$, the electric field is vertically polarised (in the \vec{y} -direction). For a linearly polarised wave, a positive or negative S_1 corresponds to the polarisation in the \vec{x} -direction or \vec{y} -direction, respectively.
- A positive S_2 indicates $+45^\circ$ linear polarisation, while a negative S_2 indicates -45° linear polarisation.
- A positive S_3 indicates a RHC polarisation, while a negative S_3 indicates a LHC polarisation.

For a constant field power, the Stokes parameters can be considered as Cartesian coordinates of a point $P(S_1, S_2, S_3)$ lying on a sphere of radius S_0 which is called a Poincare sphere [111]. A point P on the sphere is completely identified by two angular coordinates $\{\eta, \epsilon\}$ with a fixed radius as shown in Fig. 4-5. The Stokes parameters are related to the angular coordinates $\{\eta, \epsilon\}$ [111, 135]:

$$S_1 = S_0 \cos 2\eta \cos 2\epsilon, \quad (4.13a)$$

$$S_2 = S_0 \sin 2\eta \cos 2\epsilon, \quad (4.13b)$$

$$S_3 = S_0 \sin 2\epsilon. \quad (4.13c)$$

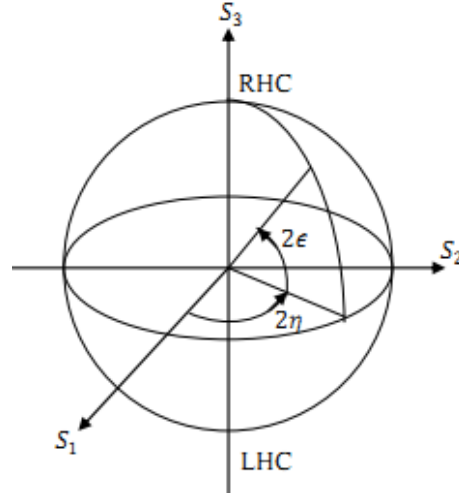


Fig. 4-5: Poincare sphere.

4.3.2 Polarisation Shift Keying Signals

The phase angles along the orthogonal axes are set equal for linear polarisation modulation, such that $\phi = 0$. Assuming the square of the amplitude directly provides the power and $A_x = A_y$, the optical power is constant and expressed as $A_x^2 = A_y^2 = P_t/2$, where P_t is the emitted optical power of the light. The field amplitude is set proportional to the modulating signal $m(t)$ [135, 193]:

$$\vec{E}_x(t) = \sqrt{P_t/2} \cos[K_{PL}m(t)]e^{j(\omega t)}, \quad (4.14a)$$

$$\vec{E}_y(t) = \sqrt{P_t/2} \sin[K_{PL}m(t)]e^{j(\omega t)}, \quad (4.14b)$$

where K_{PL} is a constant of proportionality dependent upon the physical modulation mechanism, and ω is the angular frequency of the optical signal, respectively.

For sine wave modulation with angular frequency of ω_m , the electric field equations are:

$$\vec{E}_x(t) = \sqrt{P_t/2} \cos[K_{PL}\cos(\omega_m t)]e^{j(\omega t)}, \quad (4.15a)$$

$$\vec{E}_y(t) = \sqrt{P_t/2} \sin[K_{PL} \cos(\omega_m t)] e^{j(\omega t)}. \quad (4.15b)$$

The linearly polarised system has a difficulty in detection when the transmitter or receiver rotates unpredictably, or the propagation medium induces random polarisation rotations. This problem can be solved by using the circular polarisation scheme [113, 124].

For an analog circular polarisation modulated system, the optical power of right and left circular polarisation is related to the amplitude of the information signal $m(t)$ [135, 193]:

$$C_R(t) = \frac{P_t}{2} [1 + m(t)], \quad (4.16a)$$

$$C_L(t) = \frac{P_t}{2} [1 - m(t)]. \quad (4.16b)$$

The carrier is completely right circularly polarised for $m(t) = 1$. The carrier is 25% right circularly polarised and 75% left circularly polarised for $m(t) = -0.5$. Because the carrier components $C_R(t)$ and $C_L(t)$ can be regarded as individual intensity modulated carriers, the frequency spectrum of a circularly polarised system is the same as that of an intensity modulated system. The carrier power is always transmitted in either the right or left polarisation state, while in an intensity modulation system only one-half the carrier power is transmitted on average. Therefore, when the same peak power is used, the circular polarisation modulation is inherently more efficient than intensity modulation.

4.3.3 Polarisation Modulator

The external binary polarisation modulator is made using the Lithium Niobate (LiNbO_3) MZI technique as shown in Fig. 4-6 [194, 195]. This MZI consists of two sections: a splitter which splits the input signals, followed by the waveguide to introduce a wavelength-dependent phase shift between the two arms. For simplicity, the following derivation does not take into account waveguide material losses or bend losses [196].

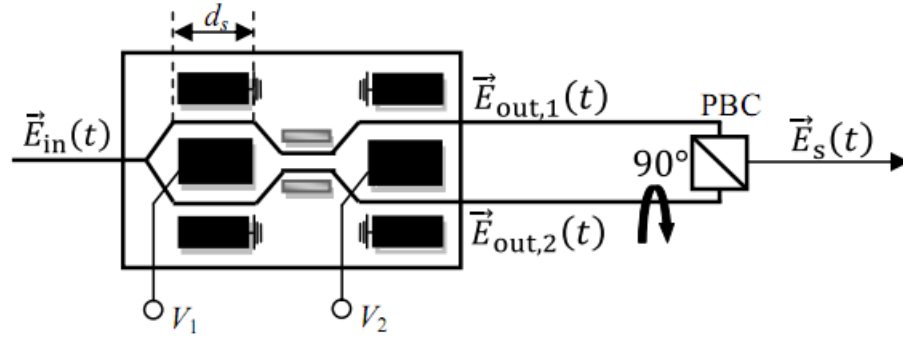


Fig. 4-6: Schematic of POLSK modulator.

The splitter of length d_s has the propagation matrix $\mathbf{M}_{\text{coupler}}$ expressed as:

$$\mathbf{M}_{\text{coupler}} = \begin{bmatrix} \cos \alpha_c d_s & -\sin \alpha_c d_s \\ \sin \alpha_c d_s & \cos \alpha_c d_s \end{bmatrix}, \quad (4.17)$$

where α_c is the coefficient. The signal $\vec{E}_{\text{in}}(t)$ enters into the waveguide and splits into two signals with a phase difference $\Delta\phi_c$ given by:

$$\Delta\phi_c = \frac{2\pi n_1}{\lambda} \ell - \frac{2\pi n_2}{\lambda} (\ell + \Delta\ell). \quad (4.18)$$

where ℓ is the path length in the waveguide. Note that the phase difference $\Delta\phi_c$ can arise either through a refractive index difference $n_1 \neq n_2$ or from a different path length $\Delta\ell$.

The propagation matrix $\mathbf{M}_{\Delta\phi_c}$ for the phase shifter with a given phase difference $\Delta\phi_c$ is expressed as:

$$\mathbf{M}_{\Delta\phi_c} = \begin{bmatrix} \exp(j\Delta\phi_c/2) & 0 \\ 0 & \exp(-j\Delta\phi_c/2) \end{bmatrix}. \quad (4.19)$$

The optical fields $\vec{E}_{\text{out},1}(t)$ and $\vec{E}_{\text{out},2}(t)$ from the two arms can be related to the input field \vec{E}_{in} through the following relationship,

$$\begin{bmatrix} \vec{E}_{\text{out},1}(t) \\ \vec{E}_{\text{out},2}(t) \end{bmatrix} = \mathbf{M} \begin{bmatrix} \vec{E}_{\text{in}}(t) \\ 0 \end{bmatrix}, \quad (4.20)$$

where \mathbf{M} is the matrix:

$$\begin{aligned} \mathbf{M} &= \mathbf{M}_{\Delta\phi_c} \cdot \mathbf{M}_{\text{coupler}} = \begin{bmatrix} \exp(j\Delta\phi_c/2) & 0 \\ 0 & \exp(-j\Delta\phi_c/2) \end{bmatrix} \begin{bmatrix} \cos\alpha_c d_s & -\sin\alpha_c d_s \\ \sin\alpha_c d_s & \cos\alpha_c d_s \end{bmatrix}, \\ &= \begin{bmatrix} \exp(j\Delta\phi_c/2)\cos\alpha_c d_s & -\exp(j\Delta\phi_c/2)\sin\alpha_c d_s \\ \exp(-j\Delta\phi_c/2)\sin\alpha_c d_s & \exp(-j\Delta\phi_c/2)\cos\alpha_c d_s \end{bmatrix}. \end{aligned} \quad (4.21)$$

Expressions (4.20) and (4.21) can be recombined yielding:

$$\begin{bmatrix} \vec{E}_{\text{out},1}(t) \\ \vec{E}_{\text{out},2}(t) \end{bmatrix} = \mathbf{M} \begin{bmatrix} \vec{E}_{\text{in}}(t) \\ 0 \end{bmatrix} = \begin{bmatrix} \exp(j\Delta\phi_c/2)\cos\alpha_c d_s \\ \exp(-j\Delta\phi_c/2)\sin\alpha_c d_s \end{bmatrix} \vec{E}_{\text{in}}(t). \quad (4.22)$$

The splitter considered here only splits the power equally for $2\alpha_c d_s = \pi/2$, so that (4.22) becomes:

$$\begin{bmatrix} \vec{E}_{\text{out},1}(t) \\ \vec{E}_{\text{out},2}(t) \end{bmatrix} = \mathbf{M} \vec{E}_{\text{in}}(t) = \frac{1}{\sqrt{2}} \begin{bmatrix} \exp(j\Delta\phi_c/2) \\ \exp(-j\Delta\phi_c/2) \end{bmatrix} \vec{E}_{\text{in}}(t). \quad (4.23)$$

As illustrated in Fig. 4-6 the driving voltages V_1 and V_2 are used to control the values of the length d_s and phase shift $\Delta\phi_c$, respectively [194]. Therefore, the linear polarisation

signal is generated by setting $\Delta\phi_c = 0, \pi$, while the circular polarisation signal is produced when $\Delta\phi_c = \pm\pi/2$. The voltage V_2 is expressed in the form of:

$$V_2 = V_0 + K_{PL} \cos(\omega_m t), \quad (4.24)$$

where V_0 is DC bias current.

4.4 Polarisation Fluctuations in a Turbulence Channel

The electric field traveling in the turbulence regime can be split into two components $\vec{E}_{x1}(t)$ and $\vec{E}_{y1}(t)$ with horizontal and vertical polarisation axes, respectively, in the plane of incidence. The polarisation angle is related to $\vec{E}_{x1}(t)$ and $\vec{E}_{y1}(t)$ with the following relationship [69, 189]:

$$\Xi = \tan^{-1} \left[\frac{\vec{E}_{x1}(t)}{\vec{E}_{y1}(t)} \right]. \quad (4.25)$$

At the output of the turbulence region, the electric field components become $\vec{E}_{x2}(t)$ and $\vec{E}_{y2}(t)$ due to the fluctuation of the refractive index of the propagation medium. The polarisation angle is changed as:

$$\Xi + \Delta\Xi = \tan^{-1} \left[\frac{\vec{E}_{x2}(t)}{\vec{E}_{y2}(t)} \right]. \quad (4.26)$$

An expression describing the change in the mean of the polarisation angle has been developed [69]. The RMS polarisation change in an atmospheric medium is:

$$\sqrt{[\Delta\Xi]^2} = 2\pi[\Delta n]^2 \left[\frac{L}{L_t} \right], \quad (4.27)$$

where $[\Delta n]^2$ is the mean square change in refractive index due to thermal variations, and L_t characterises the largest inhomogeneities of the turbulent medium.

The refractive index change is related to the altitude of observation, h , in metres by the relation [69]:

$$[\Delta n]^2 = 10^{-12} \exp \left\{ -\frac{h}{1600} \right\}. \quad (4.28)$$

For example, when the laser transmits over a low-altitude ($h \approx 0$) and a horizontal path of 10^4 m with a turbulence dimension of $L_t = 1$ m, the RMS change in polarisation angle, $\sqrt{[\Delta\Xi]^2}$, is in the order of 10^{-8} rad. Experimental results verified that polarisation fluctuations do not appear to be a problem for laser propagation over a turbulent atmosphere [69].

4.5 Outage Probability in a Lognormal Turbulence Channel

The performance of a communication system in a fading channel can be quantified by the average BER and the outage probability [1, 84]. The outage probability is defined as $P_e > P_e^*$, where P_e^* is a predetermined threshold BER. Alternatively, this probability corresponds to the SNR, $\gamma(P_r) < \gamma^*$, where $\gamma(P_r)$ and γ^* are the SNRs related to P_e and P_e^* , respectively. That is:

$$P_{out} = P(P_e > P_e^*) \equiv P(\gamma(P_r) < \gamma^*), \quad (4.29)$$

where γ^* is the average SNR in the absence of atmospheric turbulence for a given noise level.

The power margin, represented by the parameter m , is introduced to describe the extra power requirements which can also be viewed as the penalty introduced by the atmospheric turbulence. Invoking parameter m , the outage probability is expressed as:

$$\begin{aligned} P_{out} &= P(m\gamma(P_r) < \gamma^*) = \int_0^{P_0/m} \frac{1}{P_r \sqrt{2\pi}\sigma_l} \exp\left[-\frac{(\ln(P_r/P_0) + \sigma_l^2/2)^2}{2\sigma_l^2}\right] dP_r, \\ &= Q\left(\frac{1}{\sigma_l} \ln m - \frac{\sigma_l}{2}\right). \end{aligned} \quad (4.30)$$

An upper bound value for the outage probability is given by applying the Chernoff upper bound, $Q(x) \leq 0.5\exp(-x^2/2)$ into (4.30). The approximate power margin, m , is given as:

$$m \approx \exp\left(\sqrt{-2\sigma_l^2 \ln(2P_{out})} + \sigma_l^2/2\right). \quad (4.31)$$

The outage probability is plotted against the power margin at various levels of irradiance fluctuation in Fig. 4-7. The extra power of ~ 37 dBm is required to achieve an outage probability of 10^{-6} at $\sigma_l^2 = 0.1$. The value will increase to ~ 43 dBm and ~ 47 dBm corresponding to $\sigma_l^2 = 0.3$ and $\sigma_l^2 = 0.5$, respectively. To reduce the power margin, diversity techniques will be introduced in Chapter Six.

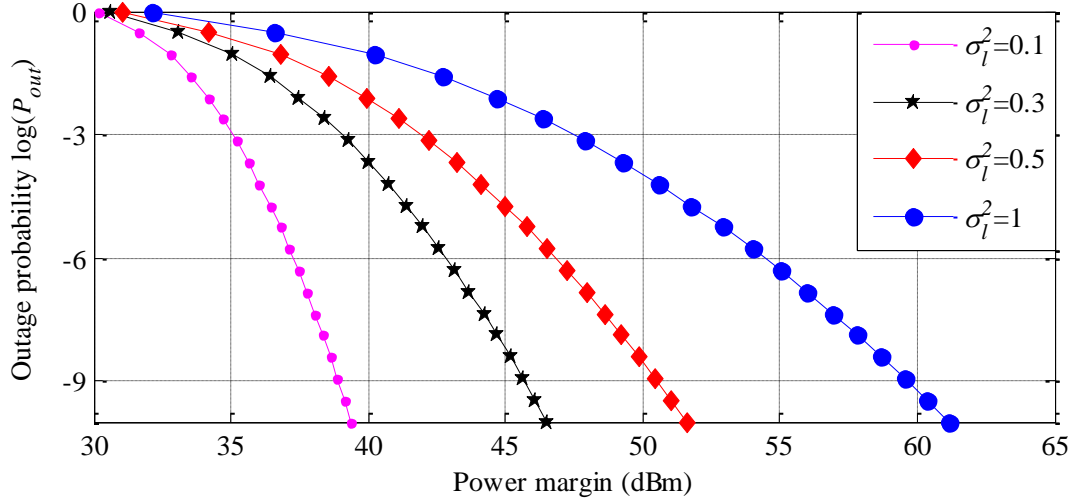


Fig. 4-7: Outage probability against the power margin for a lognormal turbulent atmospheric channel for $\sigma_l^2 = [0.1, 0.3, 0.5, 1]$.

4.6 Outage Probability in a Negative Exponential Turbulence

Channel

The outage probability in the fully developed speckle is obtained by following the approach discussed in Section 4.5:

$$P_{out} = P(m\gamma(P_r) < \gamma^*) = \int_0^{P_0/m} P_0^{-1} \exp[-P_r P_0^{-1}] dP_r. \quad (4.32)$$

The required power margin, m , to achieve a given P_{out} in the saturation regime is given by (4.33):

$$m = -\frac{1}{\ln(1 - P_{out})}. \quad (4.33)$$

The outage probabilities P_{out} in the weak ($\sigma_l^2 = 0.5$) and saturation turbulence regimes are plotted against the power margin, m , in Fig. 4-8. To achieve a P_{out} of 10^{-6} , an

additional power margin of ~ 43 dB is required in a saturation regime in comparison to that needed in the weak turbulence regime with $\sigma_I^2 = 0.5$.

For the outage probability below 10^{-6} , a further power margin will be required. The power margin required in the fully developed speckle regime suggests that a stable communication link in the saturation regime is extremely difficult due to the turbulence induced fading effect, which must be mitigated or compensated for by employing other techniques, such as channel coding and spatial diversity.

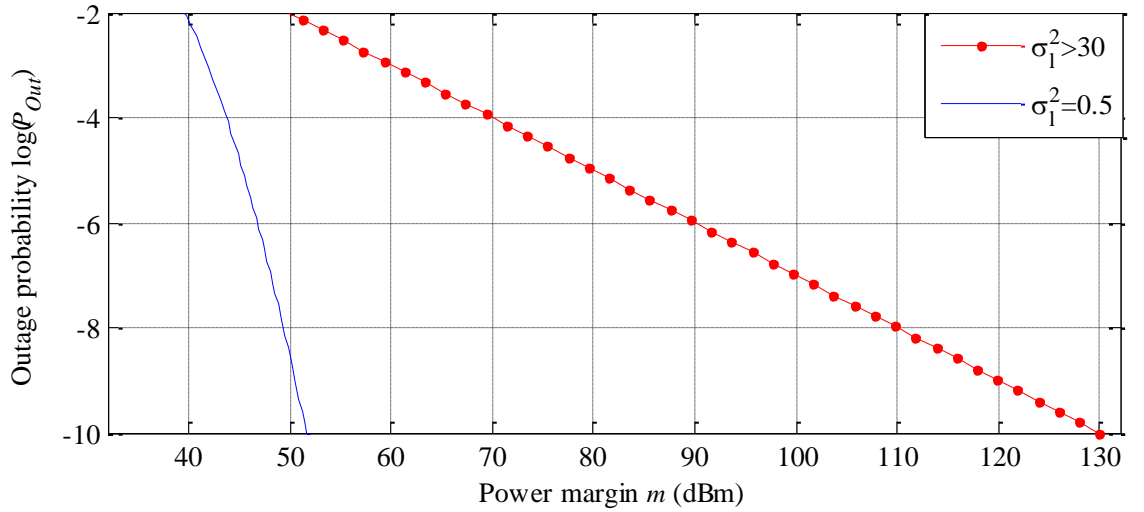


Fig. 4-8: The outage probability, P_{out} , against the power margin, m , in the saturation and weak turbulence regimes for $\sigma_I^2 = 0.5$.

4.7 Summary

In this chapter, the POLSK technique modulated an FSO communication link has been discussed, together with the analysis of the outage probabilities in the weak and

saturation turbulence regimes. The comparisons of the digital modulation techniques adopted for FSO in a turbulence channel suggest that there is always a trade-off between bandwidth efficiency, simplicity and power efficiency in the selection of modulation schemes. In the next chapter, the performance of POLSK-FSO in all turbulence regimes will be analysed.

Chapter Five

BPOLSK-FSO Systems in an Atmospheric Turbulence Channel

A number of modulation schemes in particular based on the IM/DD for FSO systems have been widely reported. However, the performance of intensity modulated schemes are highly sensitive to the turbulence fluctuation, thus an adaptive detection technique is required at the receiver to improve the link performance, such as OOK receiver using the adaptive threshold in an FSO turbulence channel [1, 197, 198]. Alternatively, a variant of POLSK schemes using external modulation have been adopted in [35, 116, 188, 189, 198, 199], where the state of polarisation (SOP) of a fully polarised propagating optical beam is considered in order to exploit the two orthogonal channels in FSO systems. However, in [200] it is shown that the coherent light beam may experience a degree of change in the polarisation while propagating through the channel. For optical beams, polarisation states are the most stable properties compared with the amplitude and phase

when propagating through a turbulent channel [113]. The experimental results show that the polarisation states can be maintained over a long propagation link [112]. In [121] it is shown that POLSK offers improved link performance in terms of the peak optical power by 3 dB but at the cost of increased system complexity compared with the OOK scheme. Additionally POLSK schemes are considerably insensitive to the laser source phase noise at the receiver, provided that the intermediate frequency (IF) filter bandwidth is large enough to avoid phase-to-amplitude noise conversion [119]. In [117] a polarisation modulated DD system to extract the Stokes parameters of the transmitted light for binary and multilevel transmissions has been proposed. A 4-level polarisation modulated DD system (with phase modulator) is reported in [116], whereas a coherent optical polarisation modulation scheme is outlined in [198].

In this chapter the performance of BPOLSK with the coherent heterodyne detection technique in the FSO turbulence channel will be investigated. The conditional and unconditional BER expressions will be derived. The frequency and phase noise of the IF component can be eliminated at the receiver, resulting in no error floor and no power penalty in the BER performance. Additionally, the higher transmission data rate can be achieved by employing the external modulation. The performance analysis will be based on the gamma-gamma channel which covers the turbulence regimes from weak to strong. Since the FSO link under consideration is LOS, the ISI due to the multipath propagation is not considered here. The noise (the background radiation, thermal noise and shot

noise) is modeled as an AWGN process. The error probabilities of heterodyne BPOLSK will be compared with OOK to show the advantages of polarisation modulated FSO link.

5.1 BPOLSK-FSO using the Square-Law Demodulation

5.1.1 System Configuration

The block diagram of the proposed BPOLSK system is illustrated in Fig. 5-1. The transmitter is composed of a single laser, a PBS, a polarisation beam combiner (PBC) and two external modulators. The external amplitude modulators are based on the LiNbO₃ MZIs. The emitted electric field of the optical carrier $\vec{E}_0(t)$, linearly polarised along $\pi/4$ with respect to the reference axis of the PBS, is split equally and is fed into two identical MZIs. At the output of each MZI, the optical signal will experience both constructive and destructive behavior depending on the phase differences of 0 and π , respectively. The outputs of MZIs are recombined using a PBC to form the BPOLSK signal. The electrical fields on the horizontal axis \vec{x} and the vertical axis \vec{y} represent the digital symbols ‘0’ and ‘1’, respectively.

The emitted optical field $\vec{E}_0(t)$ and the modulated optical field $\vec{E}_s(t)$ are given as [189]:

$$\vec{E}_0(t) = \sqrt{\frac{P_t}{2}} e^{i(\omega t + \varphi(t))} \{\vec{x} + \vec{y}\}, \quad (5.1a)$$

$$\vec{E}_s(t) = \sqrt{\frac{P_t}{2}} e^{i(\omega t + \varphi(t))} \{[1 - m(t)] \cdot \vec{x} + m(t) \cdot \vec{y}\}, \quad (5.1b)$$

where P_t , ω , and $\varphi(t)$ are the power, the angular frequency and the phase noise of the optical carrier, respectively.

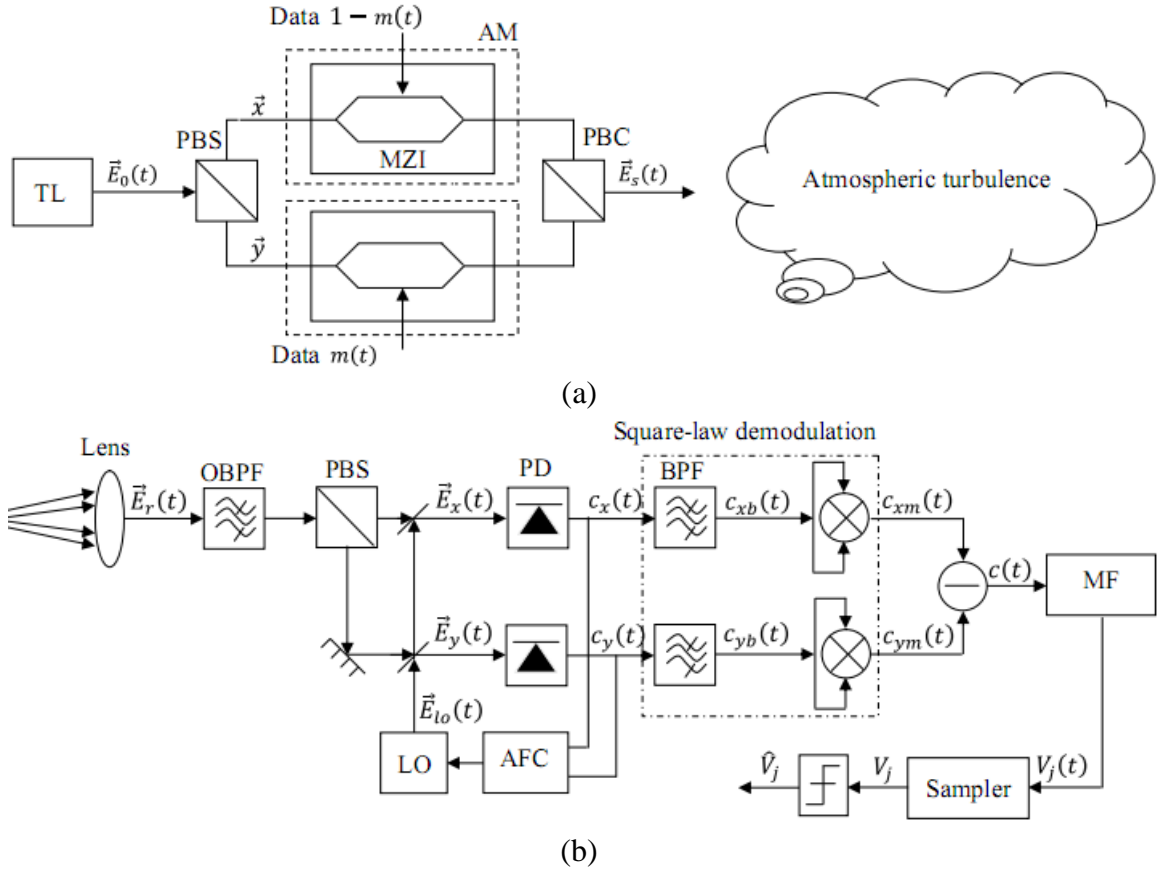


Fig. 5-1: Block diagram of the BPOLSK-FSO system using square-law demodulation: (a) the transmitter, and (b) the receiver. TL (transmitting laser), AM (amplitude modulation), AFC (automatic frequency control circuit), PD (photodiode), BPF (electric bandpass filter), MF (matched filter).

At the receiver a heterodyne scheme using the square-law demodulation is adopted, see Fig. 5-1(b). The highly sensitive PDs are located in the focal point of the large-aperture lens. An OBPF is placed after the optical lens at the entrance to the receiver. When the Sun is within the receiver's FOV, direct sunlight may cause link outages for periods of several minutes. To reduce the potential impact of the background light interference on the FSO link performance, the FOV and the bandwidth of the OBPF must be chosen carefully. For example, the OBPF with a bandwidth typically 1 nm is applicable. This is

because the OBPB's bandwidth depends on the linewidth of the infrared laser which has a narrow linewidth operation less than 1 nm.

The received signal $\vec{E}_r(t)$ can be viewed in both cases as two orthogonal amplitude modulated signals, related to the orthogonal components of the transmitted optical field.

The local oscillator laser source, linearly polarised at $\pi/4$, is identical to the transmitter laser. The received optical signal $\vec{E}_r(t)$ and the local oscillator signal $\vec{E}_{lo}(t)$ are expressed as [135, 189]:

$$\vec{E}_r(t) = \sqrt{\frac{P_r}{2}} e^{i(\omega t + \varphi_r(t))} \{ [1 - m(t)] \cdot \vec{x} + m(t) \cdot \vec{y} \}, \quad (5.2)$$

$$\vec{E}_{lo}(t) = \frac{\sqrt{P_{lo}}}{2} e^{i(\omega_{lo} t + \varphi_{lo}(t))} \{ \vec{x} + \vec{y} \}. \quad (5.3)$$

Both variables P_r and $\varphi_r(t)$ are time-variant statistics resulting from the turbulence fluctuation. The parameters P_{lo} , ω_{lo} and $\varphi_{lo}(t)$ are the power, angular frequency and phase noise of the optical field from the local oscillator, respectively.

The optical signal $\vec{E}_r(t)$ is split by the PBS and is mixed with the optical field of $\vec{E}_{lo}(t)$ thus resulting in:

$$\vec{E}_x(t) = \left\{ \sqrt{\frac{P_r}{2}} e^{i(\omega t + \varphi_r(t))} [1 - m(t)] + \frac{\sqrt{P_{lo}}}{2} e^{i(\omega_{lo} t + \varphi_{lo}(t))} \right\} \cdot \vec{x}, \quad (5.4a)$$

$$\vec{E}_y(t) = \left\{ \sqrt{\frac{P_r}{2}} e^{i(\omega t + \varphi_r(t))} m(t) + \frac{\sqrt{P_{lo}}}{2} e^{i(\omega_{lo} t + \varphi_{lo}(t))} \right\} \cdot \vec{y}. \quad (5.4b)$$

The optical fields are detected by two identical photodiodes with unit area. The output electric currents $c_x(t)$ and $c_y(t)$ are given as:

$$c_x(t) = \Re \left\{ \left(\sqrt{P_r/2} \right)^2 + \left(\sqrt{P_{lo}}/2 \right)^2 + 2 \operatorname{Re} \left[\left(\sqrt{P_r/2} \right) \left(\sqrt{P_{lo}}/2 \right) e^{i(\omega_{IF} t + \varphi_{IF}(t))} (1 - m(t)) \right] \right\} + n_x(t), \quad (5.5a)$$

$$c_y(t) = \Re \left\{ \frac{\left(\sqrt{P_r}/2\right)^2 + \left(\sqrt{P_{lo}}/2\right)^2 + 2\Re \left[\left(\sqrt{P_r}/2\right) \left(\sqrt{P_{lo}}/2\right) e^{i(\omega_{IF}t + \varphi_{IF}(t))} m(t) \right]}{2} \right\} + n_y(t), \quad (5.5b)$$

where \Re is the photodiode responsivity, $\omega_{IF} = \omega - \omega_{lo}$ and $\varphi_{IF}(t) = \varphi_r(t) - \varphi_{lo}(t)$ are the frequency and phase noise of the intermediate signal, respectively. $\Re[\]$ denotes the real part of a complex number.

The noise terms $n_x(t)$ and $n_y(t)$ are assumed to be statistically independent, and stationary Gaussian processes with a zero-mean and variance of σ_n^2 . Both noise terms are uncorrelated such that $\overline{n_x(t) \cdot n_y(t)} = 0$. The outputs of two identical optical detectors are applied to the AFC module which is a closed-loop circuit acting on the bias current. The control signal of AFC is derived from the IF signal. The working principle of AFC circuit is same as an PLL circuit for system synchronisation [135]. This is to compensate for slow-frequency fluctuations taking place in the local oscillator [184].

Detector outputs are also passed through ideal electric BPFs with a bandwidth and a center frequency of $B_{bp} = 2(R_s + k_F B_L)$ and ω_{IF} , respectively. R_s and B_L are the symbol rate and linewidth of the laser sources, respectively. The parameter k_F is chosen to pass the signal through the filter with a minimum distortion. The signals at the output of BPFs are given as:

$$c_{xb}(t) = \Re \sqrt{P_r P_{lo}} / 2 \cos(\omega_{IF}t + \varphi_{IF}(t)) [1 - m(t)] + n_x(t), \quad (5.6a)$$

$$c_{yb}(t) = \Re \sqrt{P_r P_{lo}} / 2 \cos(\omega_{IF}t + \varphi_{IF}(t)) m(t) + n_y(t). \quad (5.6b)$$

An ideal square-law demodulator consists of an electrical mixer, which is followed by a sampler and a threshold detector, is used to recover the information signal.

Since the optical field is linearly polarised and its power is unchanged, the Stokes parameters are expressed as [135]:

$$S_0 = |c_{xb}(t)|^2 + |c_{yb}(t)|^2 = \frac{\Re^2 P_r P_{lo}}{2} + n_0(t), \quad (5.7a)$$

$$S_1 = |c_{xb}(t)|^2 - |c_{yb}(t)|^2 = \frac{\Re^2 P_r P_{lo}}{2} [1 - 2m(t)] + n_1(t), \quad (5.7b)$$

$$S_2 = 2|c_{xb}(t)| \times |c_{yb}(t)| \cos(0) = n_2(t), \quad (5.7c)$$

$$S_3 = 2|c_{xb}(t)| \times |c_{yb}(t)| \sin(0) = n_3(t), \quad (5.7d)$$

where $\{n_i(t)\}_{i=0,1,2,3}$ represent noise contributions, which are independent of the received SOP and have the same variance. Note that the proposed BPOLSK refers only to the parameter S_1 . A digital symbol ‘0’ is assumed to have been received if S_1 is above the threshold level of zero and ‘1’ otherwise. Two orthogonal SOPs map onto opposite points at S_1 on the equator with respect to the origin in the Poincare sphere as depicted in Fig. 5-2.

The following hypotheses must be presumed in such a way that the quantum limit of the proposed receiver can thus be determined [69, 135, 201]:

- The power of the local oscillator is assumed to be sufficiently high;
- The responsivity of the photodiode is assumed to be equal to unity;
- Filters don’t cause any signal distortion and only limit the noise power and eliminate the undesired signal components;
- The photodiode and filters on different electronic branches at the receiver are assumed to be identical.

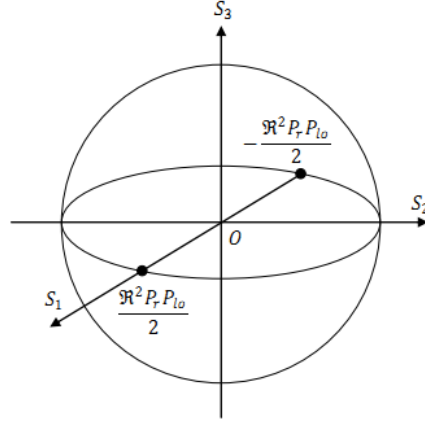


Fig. 5-2: SOPs at the output of the BPOLSK receiver.

5.1.2 Error Probabilities Analysis

Assuming independent and identically distributed (i.i.d.) data transmission, the total error probability P_{ec} is given by:

$$P_{ec} = \frac{1}{2}p(e|0) + \frac{1}{2}p(e|1) = p(e|0), \quad (5.8)$$

where $p(e|0)$ and $p(e|1)$ denotes the error rates of the transmission of a ‘0’ and a ‘1’, respectively.

The noise signals $n_x(t)$ and $n_y(t)$ in (5.6) can be expressed as [202, 203]:

$$n(t) = n^I(t)\cos(\omega_{IF}t + \varphi_{IF}(t)) - n^Q(t)\sin(\omega_{IF}t + \varphi_{IF}(t)), \quad (5.9)$$

where $n^I(t)$ and $n^Q(t)$ are the in-phase and quadrature components of the noise $n(t) \sim (0, \sigma_n^2)$, respectively.

Since i.i.d. transmission is assumed, for $m(t) = 0$, (5.6) is expressed as:

$$c_{xb}(t) = \left[\Re \sqrt{\frac{P_r P_{lo}}{2}} + n_x^I(t) \right] \cos(\omega_{IF}t + \varphi_{IF}(t)) - n_x^Q(t) \sin(\omega_{IF}t + \varphi_{IF}(t)), \quad (5.10a)$$

$$c_{yb}(t) = n_y^I(t) \cos(\omega_{IF}t + \varphi_{IF}(t)) - n_y^Q(t) \sin(\omega_{IF}t + \varphi_{IF}(t)). \quad (5.10b)$$

The electric currents at the output of the square-law demodulation become:

$$c_{xm}(t) = c_{xb}^2(t)$$

$$= \frac{1}{2} \left\{ \begin{aligned} & \left[\Re \sqrt{P_r P_{lo}/2} + n_x^I(t) \right]^2 [1 + \cos(2\omega_{IF}t + 2\varphi_{IF}(t))] \\ & + [n_x^Q(t)]^2 [1 - \cos(2\omega_{IF}t + 2\varphi_{IF}(t))] \\ & - 2\Re \sqrt{P_r P_{lo}/2} n_x^Q(t) \sin(2\omega_{IF}t + 2\varphi_{IF}(t)) \end{aligned} \right\}, \quad (5.11a)$$

$$c_{ym}(t) = c_{yb}^2(t)$$

$$= \frac{1}{2} \left\{ \begin{aligned} & [n_y^I(t)]^2 [1 + \cos(2\omega_{IF}t + 2\varphi_{IF}(t))] + [n_y^Q(t)]^2 \\ & + \left[[n_y^I(t)]^2 - [n_y^Q(t)]^2 \right] \cos(2\omega_{IF}t + 2\varphi_{IF}(t)) \end{aligned} \right\}. \quad (5.11b)$$

The transfer function of the MF is defined as:

$$h_{MF}(t) = \begin{cases} 1/\sqrt{T} & (0 \leq t \leq T) \\ 0 & (\text{otherwise}) \end{cases}, \quad (5.12)$$

where $h_{MF}(t)$ denotes the impulse response of the MF with a bandwidth of R_s . The currents $c_{xm}(t)$ and $c_{ym}(t)$ are fed into a subtractor followed by a MF. The electric signal $V_j(t)$ is expressed as [202]:

$$V_j(t) = \frac{1}{\sqrt{T}} \int_0^T [c_{xm}(t) - c_{ym}(t)] dt,$$

$$= \frac{1}{\sqrt{T}} \int_0^T \frac{1}{2} \left\{ \left[\Re \sqrt{P_r P_{lo}/2} + n_x^I(t) \right]^2 + [n_x^Q(t)]^2 - [n_y^I(t)]^2 - [n_y^Q(t)]^2 \right\} dt, \quad (5.13)$$

where $*$ represents the convolution operation. The noise terms are $(n_x(t), n_y(t)) \sim N(0, \sigma_n^2/2)$ because the bandwidth of the MF is reduced to half of the BPF.

Note that the intermediate phase noise disappears because of the square-law demodulation, thus illustrating BPOLSK insensitivity to the phase noise [199, 202]. It follows that the signal $V_j(t)$ is sampled at the symbol period $t = T$ to obtain the decision variable V_j . V_j is then compared with the zero threshold level yielding the signal \hat{V}_j , thus

leading to detection of the transition between two adjacent symbols, by which information is encoded.

An error occurs when $V_j < 0$ for the transmission of a ‘0’,

$$V_j = \frac{1}{2} \left\{ \left[\Re \sqrt{P_r P_{lo}} / 2 + n_x^I \right]^2 + [n_x^Q]^2 - [n_y^I]^2 - [n_y^Q]^2 \right\} < 0. \quad (5.14)$$

It follows that (5.14) can be rewritten as $\sqrt{[\Re \sqrt{P_r P_{lo}} / 2 + n_x^I]^2 + [n_x^Q]^2} < \sqrt{[n_y^I]^2 + [n_y^Q]^2}$.

Defining $V_x = \sqrt{[\Re \sqrt{P_r P_{lo}} / 2 + n_x^I]^2 + [n_x^Q]^2}$ and $V_y = \sqrt{[n_y^I]^2 + [n_y^Q]^2}$, the mean values are $\Re \sqrt{P_r P_{lo}} / 2$ and 0, respectively. Both variables have the same variance of $\sigma_n^2 / 2$. With $\omega \ll \omega_r$, PDFs of V_x and V_y can be described by the Rice and the Rayleigh probability functions, respectively [203]:

$$p(V_x) = \left\{ \frac{2V_x}{\sigma_n^2} I_0 \left(\frac{\Re \sqrt{P_r P_{lo}} / 2 V_x}{\sigma_n^2 / 2} \right) \exp \left[-\frac{V_x^2 + \Re^2 P_r P_{lo} / 2}{\sigma_n^2} \right] \right\}, \quad (5.15a)$$

$$p(V_y) = \frac{V_y}{\sigma_n^2 / 2} \exp \left(-\frac{V_y^2}{\sigma_n^2} \right), \quad (5.15b)$$

where I_0 is the zero order modified Bessel function of the first kind [203].

The conditional BER for $m(t) = 0$ can be derived as:

$$\begin{aligned} P_{ec} &= \int_0^\infty p(V_x) \left[\int_{V_y=V_x}^\infty p(V_y) dV_y \right] dV_x, \\ &= \int_0^\infty \left\{ \frac{2V_x}{\sigma_n^2} I_0 \left(\frac{\sqrt{\Re^2 P_r P_{lo}} / 2 V_x}{\sigma_n^2 / 2} \right) \exp \left[-\frac{(2V_x^2 + \Re^2 P_r P_{lo} / 2)}{\sigma_n^2} \right] \right\} dV_x. \end{aligned} \quad (5.16)$$

By invoking changes of variables $D = 2V_x / \sigma_n$ and $W = \sqrt{\Re^2 P_r P_{lo}} / 2 / \sigma_n$ and substituting into (5.16), P_{ec} now becomes:

$$P_{ec} = \frac{1}{2} e^{-W^2 / 2} \int_0^\infty D I_0(DW) e^{-(D^2 + W^2) / 2} dD. \quad (5.17)$$

Defining the Q -function as [203]:

$$Q(W, 0) = \int_0^{\infty} D I_0(DW) e^{-(D^2+W^2)/2} dD = 1. \quad (5.18)$$

The conditional error probability P_{ec} can be expressed in terms of the SNR as:

$$P_{ec} = \frac{1}{2} \exp\left(-\frac{W^2}{2}\right) = \frac{1}{2} \exp\left(-\frac{\Re^2 P_r P_{lo}}{4\sigma_n^2}\right) = \frac{1}{2} \exp\left(-\frac{\gamma}{2}\right), \quad (5.19)$$

where the electrical SNR at the input of the coherent demodulator is defined as $\gamma = \Re^2 P_r P_{lo} / 2\sigma_n^2$. This result is same as the BER expression for the binary frequency shift keying (BFSK) modulation technique [204]. With regard system sensitivity, both BPOLSK and BFSK techniques are almost the same.

Adopting the approach given in [1], the unconditional probability P_e is obtained by averaging (5.19) over the gamma-gamma distribution (3.23) given as:

$$\begin{aligned} P_e(P_r) &= \int_0^{\infty} P_{ec}(P_r) \cdot p_{gam}(P_r) dP_r, \\ &= \int_0^{\infty} \frac{1}{2} \exp\left(-\frac{\gamma(P_r)}{2}\right) \frac{2(\alpha\beta)^{(\alpha+\beta)/2}}{\Gamma(\alpha)\Gamma(\beta)} P_r^{\frac{\alpha+\beta}{2}-1} K_{\alpha-\beta}(2\sqrt{\alpha\beta P_r}) dP_r. \end{aligned} \quad (5.20)$$

5.1.3 Power Penalty Caused by Non-Ideal PBS

The PBS can be viewed as two ideal linear polarisers oriented orthogonally to each other. The non-ideal PBS results in an offset angle θ from the transmission axes of the linear polarised light as shown in Fig. 5-3. The electrical fields in \vec{x} and \vec{y} axes represent bits ‘0’ and ‘1’, respectively, which contributes to the power penalty incurred. Fig. 5-3 depicts the offset angle θ from \vec{x} axis of the linearly polarised light.

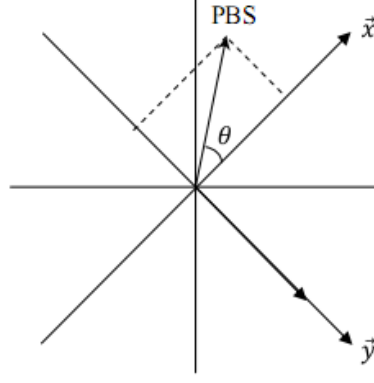


Fig. 5-3: An offset angle θ relatives to one of the transmission axes \vec{x} of the linear polarised light.

In this case, the bit '1' is detected without errors while bit '0' is not. The outputs from the PBS are given as:

$$\vec{E}_x(t) = \vec{E}_x(t)\cos\theta, \quad (5.21a)$$

$$\vec{E}_y(t) = \vec{E}_y(t) - \vec{E}_x(t)\sin\theta. \quad (5.21b)$$

Thus, the photo-currents generated by the photodiodes are:

$$c_{xb}(t) = \Re\sqrt{P_r P_{lo}/2} \cos(\omega_{IF}t + \varphi_{IF}(t))[\cos\theta - m(t)\cos\theta], \quad (5.22a)$$

$$c_{yb}(t) = \Re\sqrt{P_r P_{lo}/2} \cos(\omega_{IF}t + \varphi_{IF}(t))[m(t) + m(t)\sin\theta - \sin\theta]. \quad (5.22b)$$

The demodulated signal V_j at the output of the receiver is expressed as:

$$V_j = \frac{\Re^2 P_r P_{lo}}{2} [\cos 2\theta - 2m(t)\cos^2\theta]. \quad (5.23)$$

For $m(t) = 0$, $V_j = \Re^2 P_r P_{lo} \cos 2\theta / 2$, while for $m(t) = 1$, $V_j = -\Re^2 P_r P_{lo} / 2$. Since the offset angular error only reduces the signal power by a factor of $\cos 2\theta$ when '0' is transmitted, the conditional BER is given as:

$$P_{ec1} = \frac{1}{2}p(e|0) + \frac{1}{2}p(e|1) = \frac{1}{4}\exp\left(-\frac{\gamma\cos 2\theta}{2}\right) + \frac{1}{4}\exp\left(-\frac{\gamma}{2}\right). \quad (5.24)$$

In Fig. 5-4(a), the total offset angle of the transmission axes of both polarisers from SOP of the incoming light is equivalent to θ . The BER is calculated as:

$$\vec{E}_x(t) = \vec{E}_x(t)\cos\frac{\theta}{2} - \vec{E}_y(t)\sin\frac{\theta}{2}, \quad (5.25a)$$

$$\vec{E}_y(t) = \vec{E}_y(t)\cos\frac{\theta}{2} - \vec{E}_x(t)\sin\frac{\theta}{2}. \quad (5.25b)$$

Thus, the photo-currents generated by the photodiodes are:

$$c_{xb}(t) = \Re\sqrt{P_r P_{lo}/2} \cos(\omega_{IF}t + \varphi_{IF}(t)) \left\{ \cos\frac{\theta}{2} - m(t)\cos\frac{\theta}{2} - m(t)\sin\frac{\theta}{2} \right\}, \quad (5.26a)$$

$$c_{yb}(t) = \Re\sqrt{P_r P_{lo}/2} \cos(\omega_{IF}t + \varphi_{IF}(t)) \left\{ m(t)\cos\frac{\theta}{2} - \sin\frac{\theta}{2} + m(t)\sin\frac{\theta}{2} \right\}. \quad (5.26b)$$

The demodulated signal V_j at the output of the receiver is expressed as:

$$V_j = \frac{\Re^2 P_r P_{lo}}{2} [1 - 2m(t)] \cos\theta. \quad (5.27)$$

Since the offset angular error reduces the signal power by a factor of $\cos\theta$ for both ‘0’

and ‘1’, the conditional BER is expressed as:

$$P_{ec2} = \frac{1}{2}p(e|0) + \frac{1}{2}p(e|1) = \frac{1}{2} \exp\left(-\frac{\gamma \cos\theta}{2}\right). \quad (5.28)$$

In Fig. 5-4(b), the total offset angle is the same as θ . However, the orthogonality of the polarisers is preserved.

The BER can be derived as:

$$\vec{E}_x(t) = \vec{E}_x(t)\cos\frac{\theta}{2} + \vec{E}_y(t)\sin\frac{\theta}{2}, \quad (5.29a)$$

$$\vec{E}_y(t) = \vec{E}_y(t)\cos\frac{\theta}{2} - \vec{E}_x(t)\sin\frac{\theta}{2}. \quad (5.29b)$$

The photo-currents generated by the photodiodes are:

$$c_{xb}(t) = \Re\sqrt{P_r P_{lo}/2} \cos(\omega_{IF}t + \varphi_{IF}(t)) \left\{ \cos\frac{\theta}{2} - m(t)\cos\frac{\theta}{2} + m(t)\sin\frac{\theta}{2} \right\}, \quad (5.30a)$$

$$c_{yb}(t) = \Re\sqrt{P_r P_{lo}/2} \cos(\omega_{IF}t + \varphi_{IF}(t)) \left\{ m(t)\cos\frac{\theta}{2} - \sin\frac{\theta}{2} + m(t)\sin\frac{\theta}{2} \right\}. \quad (5.30b)$$

The demodulated signal at the output of the receiver is expressed as:

$$V_j = \frac{\Re^2 P_r P_{lo}}{2} [1 - 2m(t)] \cos\theta. \quad (5.31)$$

Therefore, the conditional error probability becomes:

$$P_{ec3} = \frac{1}{2}p(e|0) + \frac{1}{2}p(e|1) = \frac{1}{2} \exp\left(-\frac{\gamma \cos\theta}{2}\right). \quad (5.32)$$

According to (5.28) and (5.32), the system performances are the same for a non-orthogonal deviation of the transmission axes and for an orthogonality-preserving deviation of the transmission axes. This is because of the equal amount of the offset angle for both cases.

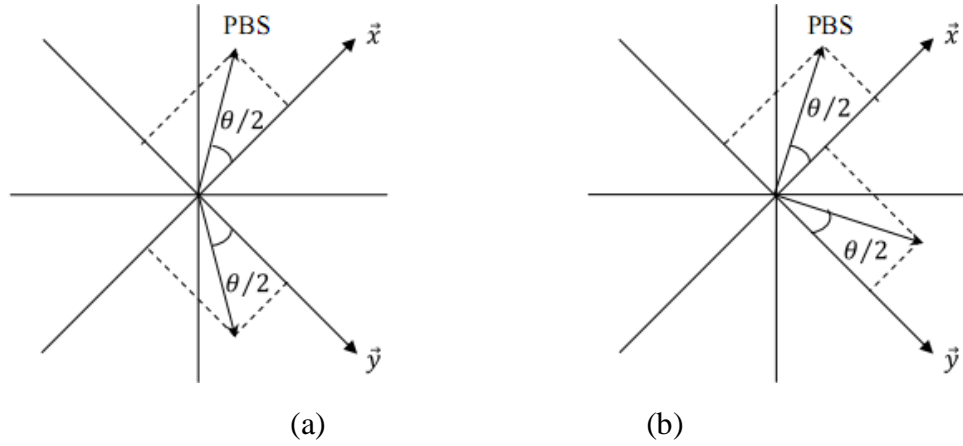


Fig. 5-4: An offset angle relative to one of the transmission axes of the linear polarised light: (a) A non-orthogonal deviation of the transmission axes, and (b) An orthogonality-preserving deviation of the transmission axes from the SOPs of the incoming light.

Using equations (5.24), (5.28) and (5.32), Fig. 5-5 illustrates the optical power penalty at the receiver to achieve a BER of 10^{-9} against a range of the offset angles relative to one or both transmission axes of the incident light. For the same offset angle θ , the power penalty is higher in the case of single deviation compared with equal deviation. For example, to achieve a BER of 10^{-9} at $\theta = 9^\circ$, the power penalties are ~ 1.4 dB and ~ 0.5 dB for the single and equal deviation, respectively. When $\theta = 15^\circ$, the single deviation suffers a power penalty of ~ 3.6 dB compared with the equal deviation. The power penalty required to achieve a BER of 10^{-9} increases with θ .

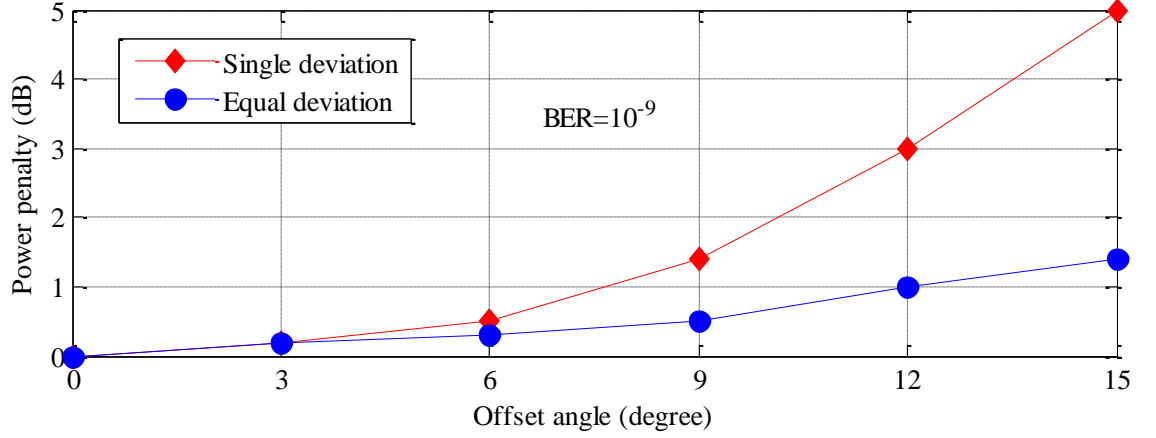


Fig. 5-5: Receiver sensitivity power penalty against the offset angle θ at a BER of 10^{-9} using (5.24), (5.28) and (5.32). (Single deviation: an offset angle relative to one of the transmission axes of the linearly polarised light; Equal deviation: an offset angle relative to both transmission axes of the linearly polarised light.)

5.2 BPOLSK-FSO with a Reference Carrier

In this section, a BPOLSK system using a reference carrier is proposed. Since the optical reference signal is transmitted at the orthogonal SOP through the turbulence channel, this scheme offers a number of advantages, including: no need for synchronization at the receiver; the frequency and phase noise of the IF component can be eliminated, which results no error floor and no power penalty.

5.2.1 System Configuration

Fig. 5-6 illustrates the block diagram of the proposed BPOLSK-FSO with a reference carrier. The transmitting laser beam is fed into the PBS. The laser beam is linearly polarised and has a $\pi/4$ polarisation with respect to the principle axes of the phase modulator [135, 189]. The $\pi/4$ polarisation of the input carrier is decomposed by the PBS into two equal components — \vec{x} and \vec{y} polarisations, while only the \vec{x} -component is

phase-modulated between 0 and π depending on the input data stream. The PM process is achieved by utilizing the effective refractive index of the waveguide that varies with the applied external voltage via a coated electrode. The phase modulator is a function of effective refractive index, the wavelength and the length of the electrode [135].

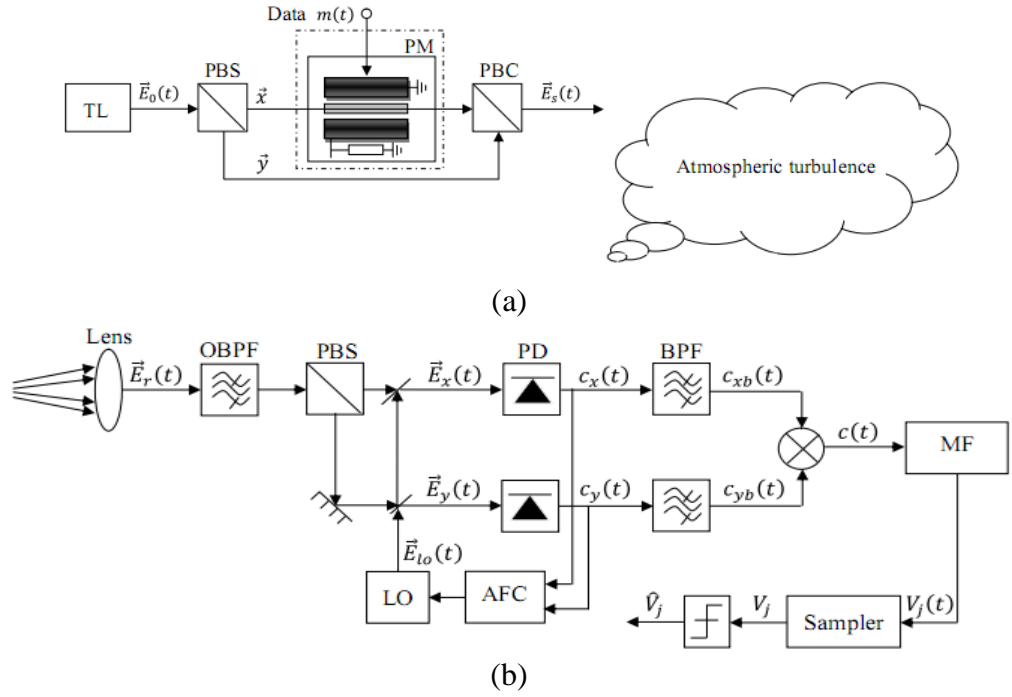


Fig. 5-6: Coherent BPOLSK-FSO transceiver: (a) the transmitter, and (b) the receiver. PM (phase modulation).

For a binary input data of '0', no voltage is applied to the phase modulator. Therefore, no phase shift is induced on the optical carrier; whereas for the input data of '1', a voltage of $1.5V_\pi$ (for the electro-optic coefficient ratio of 1/3) is applied to the phase modulator. The applied voltage induces a π phase shift in the \vec{x} -component and zero phase shifts in the \vec{y} -component. This leads to a $\pi/2$ rotation in the polarisation state of the optical carrier. Under these conditions, the binary data stream is encoded into two linear orthogonal SOPs with a constant envelope.

At the PBC output, the transmitted optical signal $\vec{E}_s(t)$ is expressed as:

$$\vec{E}_s(t) = \sqrt{\frac{P_t}{2}} e^{i(\omega t + \varphi(t))} \{e^{i\beta_x(t)} \cdot \vec{x} + \vec{y}\}, \quad (5.33)$$

where $\beta_x(t) = [0, \pi]$ is the phase difference between the two field components \vec{x} and \vec{y} .

The detection process is similar to that in Fig. 5-1, with the optical field for the local oscillator $\vec{E}_{lo}(t)$ defined in (5.3).

The received optical field $\vec{E}_r(t)$ is expressed as:

$$\vec{E}_r(t) = \sqrt{\frac{P_r}{2}} e^{i(\omega t + \varphi_r(t))} \{e^{i\beta_x(t)} \cdot \vec{x} + \vec{y}\}. \quad (5.34)$$

Assuming an electron is generated for every detected photon; outputs from two identical photodiodes with a unit detector area are filtered via ideal BPFs of which the bandwidth and center frequency are $B_{bp} = 2(R_s + k_F B_L)$ and ω_{IF} , respectively.

The electric currents $c_{xb}(t)$ and $c_{yb}(t)$ are expressed by:

$$c_{xb}(t) = \Re \sqrt{P_r P_{lo}/2} \cos(\omega_{IF} t + \beta_x(t) + \varphi_{IF}(t)) + n_x(t), \quad (5.35a)$$

$$c_{yb}(t) = \Re \sqrt{P_r P_{lo}/2} \cos(\omega_{IF} t + \varphi_{IF}(t)) + n_y(t). \quad (5.35b)$$

The noise terms $\{n_x(t), n_y(t)\} \sim N(0, \sigma_n^2)$ (given in (5.9)) are assumed to be statistically independent such that $\overline{n_x(t) \cdot n_y(t)} = 0$. This is because they are allocated within orthogonal SOPs. Applying (5.9), the electric currents $c_{xb}(t)$ and $c_{yb}(t)$ are processed by the square-law device to generate the output signal $c(t)$ expressed as:

$$c(t) = c_{xb}(t) \cdot c_{yb}(t), \quad (5.36)$$

$$= \frac{1}{2} \sqrt{\Re^2 P_r P_{lo}/2} \left\{ \begin{aligned} &\sqrt{\Re^2 P_r P_{lo}/2} [\cos(\beta_x(t)) + \cos(2\omega_{IF} t + 2\varphi_{IF}(t) + \beta_x(t))] \\ &+ [n_x^I(t) + n_y^I(t)] [\cos(2\omega_{IF} t + 2\varphi_{IF}(t)) + 1] \\ &- [n_x^Q(t) + n_y^Q(t)] \sin(2\omega_{IF} t + 2\varphi_{IF}(t)) \end{aligned} \right\}.$$

The electric signal fed into the threshold detector is given by:

$$\begin{aligned} V_j(t) &= \frac{1}{\sqrt{T}} \int_0^T c(t) dt, \\ &= \frac{1}{\sqrt{T}} \int_0^T \frac{1}{2} \sqrt{\Re^2 P_r P_{lo}/2} \left\{ \sqrt{\Re^2 P_r P_{lo}/2} \cos(\beta_x(t)) + n_x^l(t) + n_y^l(t) \right\} dt. \end{aligned} \quad (5.37)$$

where the noise $\{n_x^l(t), n_y^l(t)\} \sim N(0, \sigma_n^2/2)$ due to the bandwidth of the MF reduced to half of the BPF. A binary '0' is assumed to have been received if V_j is above the threshold level of zero and '1' otherwise. It is noteworthy that, under consideration of the multiplication demodulation process, the influence of the phase noise in the intermediate frequency component can be eliminated.

5.2.2 Error Probabilities Analysis

Given $m(t) = 0$ and $\beta_x(t) = 0$, the electric signal V_j is expressed as:

$$V_j = \frac{1}{2} \sqrt{\Re^2 P_r P_{lo}/2} \left\{ \sqrt{\Re^2 P_r P_{lo}/2} + n_x^l + n_y^l \right\}. \quad (5.38)$$

Given $z = \sqrt{\Re^2 P_r P_{lo}/2} + n_x^l(t) + n_y^l(t)$ and $z \sim N(\Re^2 P_r P_{lo}/2, \sigma_n^2)$, the PDF of z is $f(z)$, thus P_{ec} can be derived as:

$$P_{ec} = \int_{-\infty}^0 f(z) dz = \frac{1}{\sqrt{2\pi}\sigma_n} \int_{-\infty}^0 e^{-(z - \sqrt{\Re^2 P_r P_{lo}/2})^2 / 2\sigma_n^2} dz = \frac{1}{2} \operatorname{erfc} \left(\sqrt{\frac{\gamma}{2}} \right), \quad (5.39)$$

where the electrical SNR at the input of the coherent demodulator is defined as $\gamma = \Re^2 P_r P_{lo} / 2\sigma_n^2$.

Using the approach adopted in [1, 158], the link performance is evaluated under weak to strong turbulence regimes. The unconditional probability P_e (without the knowledge of

the channel state information) is obtained by averaging (5.39) over the gamma-gamma irradiance fluctuation statistics $p(P_r)$ (3.23) [172] to obtain the following:

$$\begin{aligned}
 P_e(P_r) &= \int_0^{\infty} P_{ec}(P_r) \cdot p_{gam}(P_r) dP_r , \\
 &= \int_0^{\infty} \frac{1}{2} \operatorname{erfc} \left(\sqrt{\frac{\gamma(P_r)}{2}} \right) \frac{2(\alpha\beta)^{(\alpha+\beta)/2}}{\Gamma(\alpha)\Gamma(\beta)} P_r^{\frac{\alpha+\beta}{2}-1} K_{\alpha-\beta}(2\sqrt{\alpha\beta P_r}) dP_r. \quad (5.40)
 \end{aligned}$$

5.3 Differential Circular Polarisation Shift Keying

5.3.1 System Configuration

The schematic of the DCPOLSK optical coherent transmitter is depicted in Fig. 5-7. The emitted optical field of the carrier is linearly polarised along $\pi/4$ with respect to the reference axis of the modulator, see Fig. 5-7(a). The differentially encoded information bits $m(t)$ are used to modulate the field phase of the laser in such a way that the field phase is equal to zero and π for transmission of a space and a mark, respectively.

Invoking $2\alpha_c d = \pi/2$ in (4.23), the electric field of the optical signal is given as:

$$\vec{E}_s(t) = \sqrt{\frac{P_t}{2}} e^{i(\omega t + \varphi(t))} \{ e^{i\vartheta/2} \cdot \vec{x} + e^{i-\vartheta/2} \cdot \vec{y} \}. \quad (5.41)$$

The left and right circular polarisations are produced by changing the field phase of $\vartheta = -\pi/2$ and $\pi/2$ with respect to the transmission of the differentially encoded space and mark, respectively.

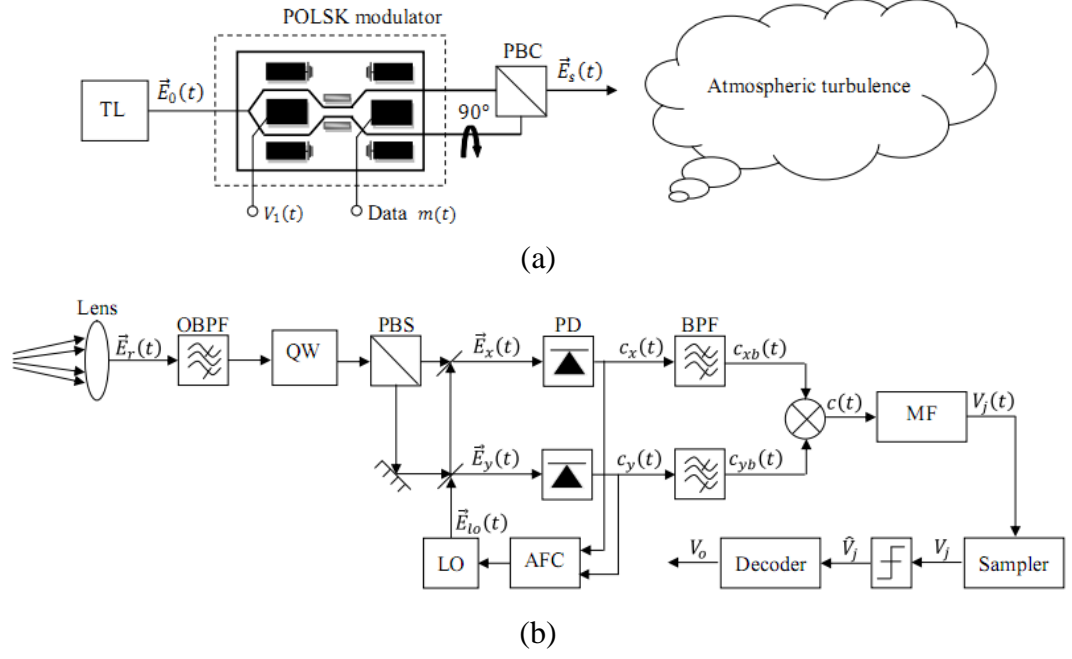


Fig. 5-7: Coherent DCPOLSK-FSO transceiver: (a) the transmitter, and (b) the receiver. QW (quarter wave retarder).

The block diagram of the heterodyne DCPOLSK receiver is illustrated in Fig. 5-7(b). The QW is fabricated using the birefringent materials and is used to alter the incoming light by one quarter of a wave out of phase from the other polarisation component. Therefore, a circularly polarised light passing through a QW becomes a linearly polarised light with polarisation axis along $-\pi/4$ and $\pi/4$ depending on which the polarisation component (\vec{x}, \vec{y}) is retarded [192]. The LO laser source, linearly polarised at $\pi/4$, is identical to the transmitter laser.

The received optical signal $\vec{E}_r(t)$ is written as:

$$\vec{E}_r(t) = \sqrt{\frac{P_r}{2}} e^{i(\omega t + \varphi_r(t))} \{e^{i(\vartheta/2)} \cdot \vec{x} + e^{i(-\vartheta/2)} \cdot \vec{y}\}. \quad (5.42)$$

After passing through the QW plate, the optical signal $\vec{E}_r(t)$ is split by the PBS and is mixed with the \vec{x} and \vec{y} components of $\vec{E}_{lo}(t)$ resulting in:

$$\vec{E}_x(t) = \left\{ \sqrt{\frac{P_r}{2}} e^{i[\omega t + \vartheta/2 + \pi/4 + \varphi_r(t)]} + \frac{\sqrt{P_{lo}}}{2} e^{i[\omega_{lo}t + \varphi_{lo}(t)]} \right\} \cdot \vec{x}, \quad (5.43a)$$

$$\vec{E}_y(t) = \left\{ \sqrt{\frac{P_r}{2}} e^{i[\omega t - \vartheta/2 - \pi/4 + \varphi_r(t)]} + \frac{\sqrt{P_{lo}}}{2} e^{i[\omega_{lo}t + \varphi_{lo}(t)]} \right\} \cdot \vec{y}. \quad (5.43b)$$

The optical fields are then detected by two identical photodiode and the outputs are passed through the electrical BPFs. The bandwidth and the center frequency of the BPFs are $B_{bp} = 2(R_s + k_F B_L)$ and ω_{IF} , respectively.

The expressions of the electrical currents $c_{xb}(t)$ and $c_{yb}(t)$ after passing through the BPFs on the \vec{x} and \vec{y} channels are given as:

$$c_{xb}(t) = \sqrt{\frac{\Re^2 P_r P_{lo}}{2}} \cos(\omega_{IF}t + \varphi_{IF}(t) + \vartheta/2 + \pi/4) + n_x(t), \quad (5.44a)$$

$$c_{yb}(t) = \sqrt{\frac{\Re^2 P_r P_{lo}}{2}} \cos(\omega_{IF}t + \varphi_{IF}(t) - \vartheta/2 - \pi/4) + n_y(t), \quad (5.44b)$$

where the noise terms $\{n_x(t), n_y(t)\} \sim N(0, \sigma_n^2)$.

The electric currents $c_{xb}(t)$ and $c_{yb}(t)$ are multiplied to generate the output electric current $c(t)$:

$$c(t) = c_{xb}(t) \cdot c_{yb}(t),$$

$$= \frac{1}{2} \sqrt{\Re^2 P_r P_{lo} / 2} \left\{ \begin{aligned} & \sqrt{\Re^2 P_r P_{lo} / 2} \left[\cos\left(\vartheta + \frac{\pi}{2}\right) + \cos(2\omega_{IF}t + 2\varphi_{IF}(t)) \right] \\ & + [n_x^I(t) + n_y^I(t)] [\cos(2\omega_{IF}t + 2\varphi_{IF}(t)) + 1] \\ & - [n_x^Q(t) + n_y^Q(t)] \sin(2\omega_{IF}t + 2\varphi_{IF}(t)) \end{aligned} \right\}. \quad (5.45)$$

It follows that the signal $c(t)$ is fed into the MF to be integrated over the symbol period T and sampled at time $t = T$ to obtain the decision variable V_j . V_j is then compared with the zero threshold level yielding the signal \hat{V}_{j_i} , thus leading to the detection of the

transition between two adjacent symbols, by which information is encoded. The output signal is given as:

$$\begin{aligned} V_j(t) &= \int_0^T c(t) dt, \\ &= \frac{1}{2} \sqrt{\Re^2 P_r P_{lo}/2} \left\{ \sqrt{\Re^2 P_r P_{lo}/2} \cos\left(\vartheta + \frac{\pi}{2}\right) + n_x^l(t) + n_y^l(t) \right\}. \end{aligned} \quad (5.46)$$

The noise components are $\{n_x^l(t), n_y^l(t)\} \sim N(0, \sigma_n^2/2)$. Note that the intermediate phase noise disappears due to the multiplication and filtering, thus illustrating DCPOLSK insensitivity to the phase noise.

5.3.2 Error Probabilities Analysis

Following the same procedure as in 5.2.2, an error occurs when $V_j < 0$ for transmission of a space with $\vartheta = -\pi/2$:

$$V_j = \frac{1}{2} \sqrt{\Re^2 P_r P_{lo}/2} \left(\sqrt{\Re^2 P_r P_{lo}/2} + n_x^l + n_y^l \right). \quad (5.47)$$

Defining the variable $z = \sqrt{\Re^2 P_r P_{lo}/2} + n_x^l + n_y^l$ and $z \sim N(\sqrt{\Re^2 P_r P_{lo}/2}, \sigma_n^2)$, the error rate before the code converter is thus expressed as:

$$P_{ec} = \frac{1}{\sqrt{2\pi}\sigma_n} \int_{-\infty}^0 e^{-\frac{(z - \sqrt{\Re^2 P_r P_{lo}/2})^2}{2\sigma_n^2}} dz = \frac{1}{2} \operatorname{erfc}\left(\sqrt{\frac{\gamma}{2}}\right). \quad (5.48)$$

where $\gamma = \Re^2 P_r P_{lo}/2\sigma_n^2$ is the SNR ratio at the demodulator output.

The decoder determines the changes between adjacent symbols. An error occurs if only one of two adjacent symbols is erroneous. Thus the error probability becomes:

$$P'_{ec} = 2P_{ec}(1 - P_{ec}) = \operatorname{erfc}\left(\sqrt{\frac{\gamma}{2}}\right) \left[1 - \frac{1}{2} \operatorname{erfc}\left(\sqrt{\frac{\gamma}{2}}\right) \right]. \quad (5.49)$$

Thus, considering the channel influence, the unconditional error rate is given as:

$$P_e(P_r) = \int_0^\infty \left\{ \operatorname{erfc} \left(\sqrt{\frac{\gamma(P_r)}{2}} \right) \left[1 - \frac{1}{2} \operatorname{erfc} \left(\sqrt{\frac{\gamma(P_r)}{2}} \right) \right] \right. \\ \left. \cdot \frac{2(\alpha\beta)^{\frac{\alpha+\beta}{2}}}{\Gamma(\alpha)\Gamma(\beta)} P_r^{\frac{\alpha+\beta}{2}-1} K_{\alpha-\beta}(2\sqrt{\alpha\beta P_r}) dP_r \right\} dP_r. \quad (5.50)$$

5.4 Comparison of BPOLSK, OOK and BPSK based FSO Links

In order to evaluate the BPOLSK modulated FSO systems operating over the turbulence channel, the error probabilities are compared with that of the OOK and coherent BPSK schemes under the same channel conditions. In the OOK modulated system, the PDF of the decision variable depends on the transmitted bit only through its average value and the error probability in the absence of turbulence is given as [1]:

$$P_{\text{OOK}} = p(0) \int_{i_{th}}^\infty \frac{1}{\sqrt{2\pi\sigma_n^2}} \exp\left(-\frac{i^2}{2\sigma_n^2}\right) di + p(1) \int_0^{i_{th}} \frac{1}{\sqrt{2\pi\sigma_n^2}} \exp\left[-\frac{(i - \Re P_r)^2}{2\sigma_n^2}\right] di. \quad (5.51)$$

where i_{th} denotes the threshold signal level, i represents the detected current with the receiver aperture size normalised to unity.

The OOK system conditioned on the received irradiance in the atmospheric turbulence modeled as gamma-gamma statistics is given as [1]:

$$P'_{\text{OOK}}(P_r) = p(0) \int_{i_{th}}^\infty \frac{1}{\sqrt{2\pi\sigma_n^2}} \exp\left(-\frac{i^2}{2\sigma_n^2}\right) di, \quad (5.52) \\ + p(1) \int_0^\infty \int_0^{i_{th}} \left\{ \frac{1}{\sqrt{2\pi\sigma_n^2}} \exp\left[-\frac{(i - \Re P_r)^2}{2\sigma_n^2}\right] \frac{2(\alpha\beta)^{\frac{\alpha+\beta}{2}}}{\Gamma(\alpha)\Gamma(\beta)} P_r^{\frac{\alpha+\beta}{2}-1} K_{\alpha-\beta}(2\sqrt{\alpha\beta P_r}) \right\} di dP_r.$$

In an atmospheric turbulence environment, the threshold level will vary with the irradiance fluctuation and the noise level. Therefore the threshold is no longer fixed at

half of the received irradiance. Since the transmission of zero pulses (for data ‘0’) is not subject to scintillation, the likelihood function Λ is derived by invoking the maximum posteriori symbol-by-symbol detection [205]:

$$\Lambda = \int_0^\infty \exp \left[\frac{-(i - \Re \sqrt{P_r P_{lo}})^2 - i^2}{2\sigma_n^2} \right] \frac{2(\alpha\beta)^{(\alpha+\beta)/2}}{\Gamma(\alpha)\Gamma(\beta)} P_r^{\frac{\alpha+\beta}{2}-1} K_{\alpha-\beta}(2\sqrt{\alpha\beta P_r}) dP_r. \quad (5.53)$$

Based on the antipodal nature of a coherent BPSK modulation technique, the threshold is fixed at a zero level, which is not affected by the irradiance fluctuation. In the coherent BPSK system, the PLL circuit is assumed to adequately track the phase changes due to the atmospheric turbulence and any phase error generated is solely due to the PLL. The phase tracking error not only introduces a power penalty at the receiver but also contributes to the minimum error probability, which is independent of the received optical power [135]. An exact analysis based on the nonlinear PLL is mathematically tractable.

Assuming a constant PLL tracking error within the symbol period T , the error probability can thus be deduced as [135, 203]:

$$P_{\text{BPSK}} = \int_0^{2\pi} \frac{1}{2} \operatorname{erfc}[\sqrt{\gamma} \cos(\Delta\varphi(t))] \frac{e^{r_l \cos(\Delta\varphi)}}{2\pi I_0(r_l)} d\Delta\varphi. \quad (5.54)$$

where $\gamma = \Re P_r P_{lo} / 2\sigma_n^2$ denotes the electric SNR per bit at the input of the coherent demodulator and $\Delta\varphi(t)$ is the phase tracking error due to the PLL. The parameter $\gamma_l = 1/\sigma_\Delta^2$ is the SNR of the PLL, and σ_Δ^2 is the phase noise variance.

Adopting the approach given in [158], the unconditional error probability $P'_{\text{BPSK}}(P_r)$ is given as:

$$P'_{\text{BPSK}}(P_r) = \int_0^\infty \int_0^{2\pi} \left\{ P_{\text{BPSK}} \cdot \frac{2(\alpha\beta)^{(\alpha+\beta)/2}}{\Gamma(\alpha)\Gamma(\beta)} P_r^{\frac{\alpha+\beta}{2}-1} K_{\alpha-\beta}(2\sqrt{\alpha\beta P_r}) \right\} d\Delta\phi dP_r. \quad (5.55)$$

Using (5.20), (5.40), (5.50), (5.52) and (5.55), the error probabilities of BPOLSK, OOK and BPSK schemes in the absence and presence of turbulence are depicted in Figs. 5-8 to 5-10, respectively. The values for α and β at any given regimes can be calculated with the corresponding values of σ_I^2 using (3.24) and are illustrated in Table 5.1.

Table 5.1: Turbulence parameters with respect to weak, moderate and strong regimes [149].

Parameter	Turbulence regime		
	Weak	Moderate	Strong
σ_I^2	0.2	1.6	3.5
α	11.6	4.0	4.2
β	10.1	1.9	1.4

Fig. 5-8 depicts the error probability against the normalized electric SNR for BPOLSK, BPSK and OOK schemes in an ideal channel. With no turbulence, to achieve a BER of 10^{-9} the SNR requirements are ~ 12.5 dB and ~ 18.5 dB for BPSK (with an ideal PLL) and OOK (with a fixed threshold of 0.5), respectively.

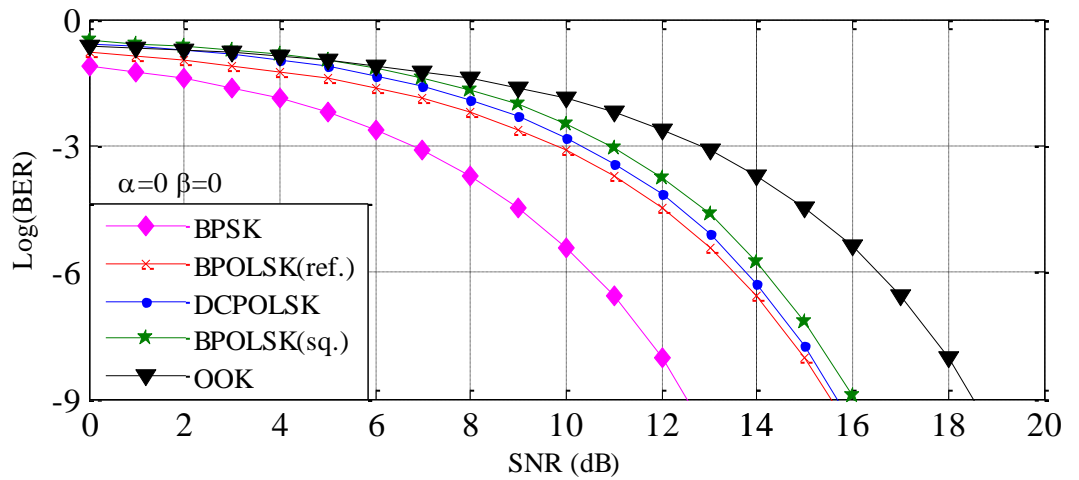


Fig. 5-8: Comparisons of BER performances of various schemes against the normalized electric SNR $E[\Re P_r P_{lo}] = 1$ in the absence of turbulence. (sq: BPOLSK-FSO using the square-law modulation; ref: BPOLSK-FSO with a reference carrier)

The SNR requirements for BPOLSK using different configurations have no evident differences, such that the SNRs of ~ 15.7 dB, ~ 15.5 dB and ~ 16 dB are needed for DCPOLSK and BPOLSK using a reference carrier and the square-law demodulation, respectively. The BPOLSK outperforms and under-performs OOK and BPSK by ~ 3 dB. Among all the BPOLSK systems discussed above, the receiver using the reference carrier offers the best performance. The error probability of BPOLSK in the following discussions will be only referred to that of the BPOLSK system using the reference carrier.

The BPOLSK scheme requires no carrier recovery circuit at the receiver and both the carrier and information signals suffer from the same phase noise. However, BPSK incurs penalties due to the phase tracking errors as depicted in Fig. 5-9.

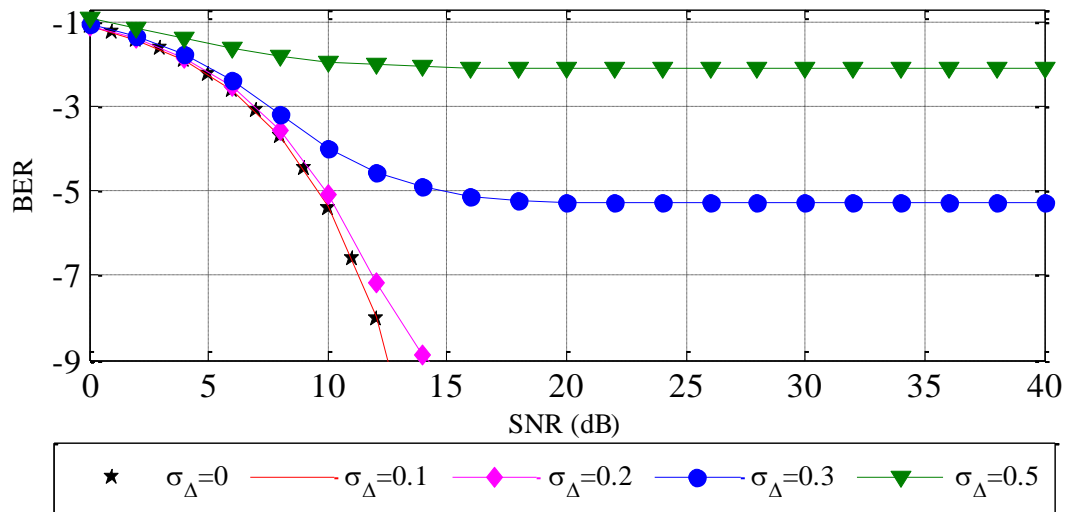


Fig. 5-9: BER against the SNR for coherent BPSK for a range of phase error variance $\sigma_\Delta = [0, 0.1, 0.2, 0.3, 0.5]$.

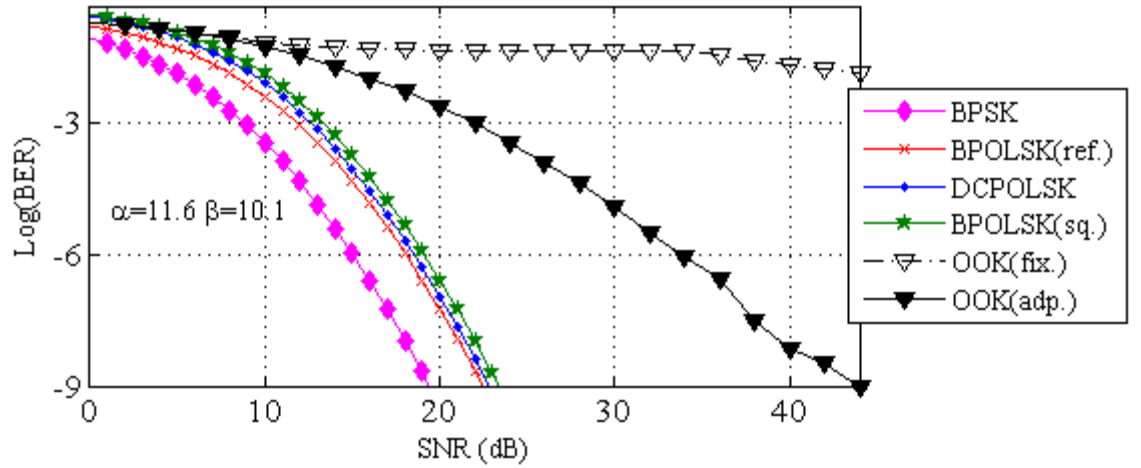
The PLL circuit based BPSK incurs penalties due to the phase tracking errors as shown in Fig. 5-9. When the phase error variance is small ($\sigma_\Delta = 0.1$), the power penalty can be

neglected since the degradation is not high. The performance degradation increases with the error variance. For higher values of variance ($\sigma_{\Delta} \geq 0.3$) the power penalty causes a significant shift in the BER floor. For example, in the case of $\sigma_{\Delta} = 0.3$ and 0.5 , the BER floor are equal to 5.4×10^{-6} and 7.7×10^{-3} , respectively.

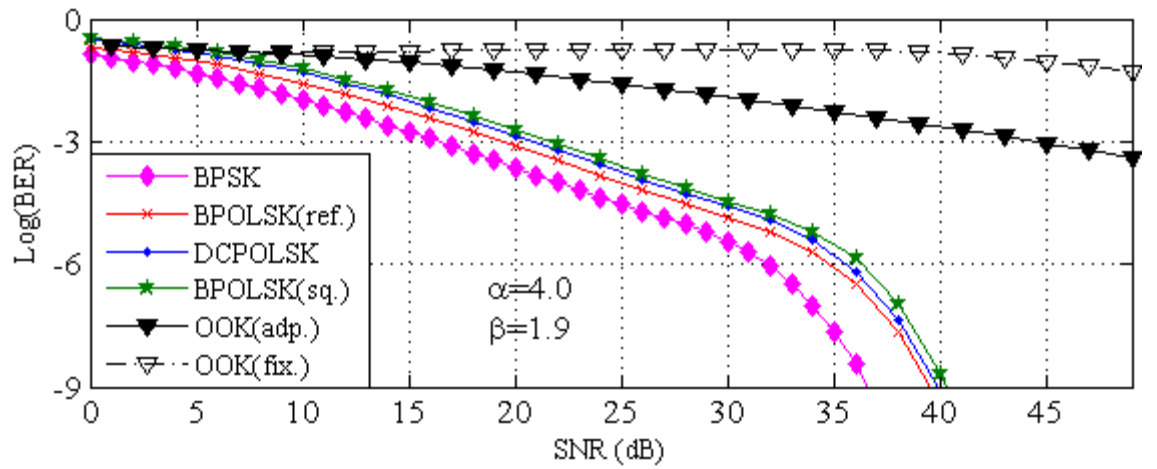
To compare the error probability with BPOLSK and OOK, the performances of BPSK without a phase tracking error in the atmospheric turbulence are depicted in Fig. 5-10. Irrespective of the modulation schemes, to achieve a fixed BER, the SNR requirement increases with the turbulence level and it is higher for lower values of BER at the same turbulence level as depicted in Fig. 5-10. For example, to achieve a BER of 10^{-6} in a weak turbulence regime, SNR requirements are ~ 15 dB, ~ 18 dB and ~ 33.8 dB for BPSK, BPOLSK and OOK schemes, respectively. To achieve a BER of 10^{-9} under the same channel condition, corresponding SNR values rise to ~ 19.5 dB, ~ 22.5 dB and ~ 44 dB, respectively. In a moderate regime to achieve a BER of 10^{-9} , SNR values further increase to ~ 36.5 dB and ~ 39.5 dB for BPSK and BPOLSK schemes, respectively. To reduce the BER of BPOLSK (using ref. and sq.) from 10^{-3} to 10^{-6} in the moderate turbulence regime, the additional required SNR is ~ 15 dB. Less SNR (~ 4.5 dB) is required for further reducing the BER to 10^{-9} . This is because the characters of $erfc(\cdot)$ and exponential functions.

OOK suffers higher BER floor levels in the moderate turbulence regime. For instance, using a SNR of 49 dB in the moderate turbulence regime, the BERs are 0.05 and 4×10^{-4} for fixed and adaptive threshold detections, respectively. For the ideal PLL

circuit without phase tracking errors, the BPSK system offers the best performance in terms of error probability followed by the BPOLSK scheme in the absence of turbulence. The results shown in Fig. 5-10 are valid because of the following reasons. Firstly, the BER curves for OOK-FSO and BPSK-FSO have the same trend as results reported in [1, 105, 166, 171, 206]. The coherent BPOLSK systems using different transceiver configurations applied in optical fibre have been theoretically and experimentally verified in [207-209]. The conditional BER expressions (without considering the channel effect) are the same as that reported in the common literature.



(a)



(b)

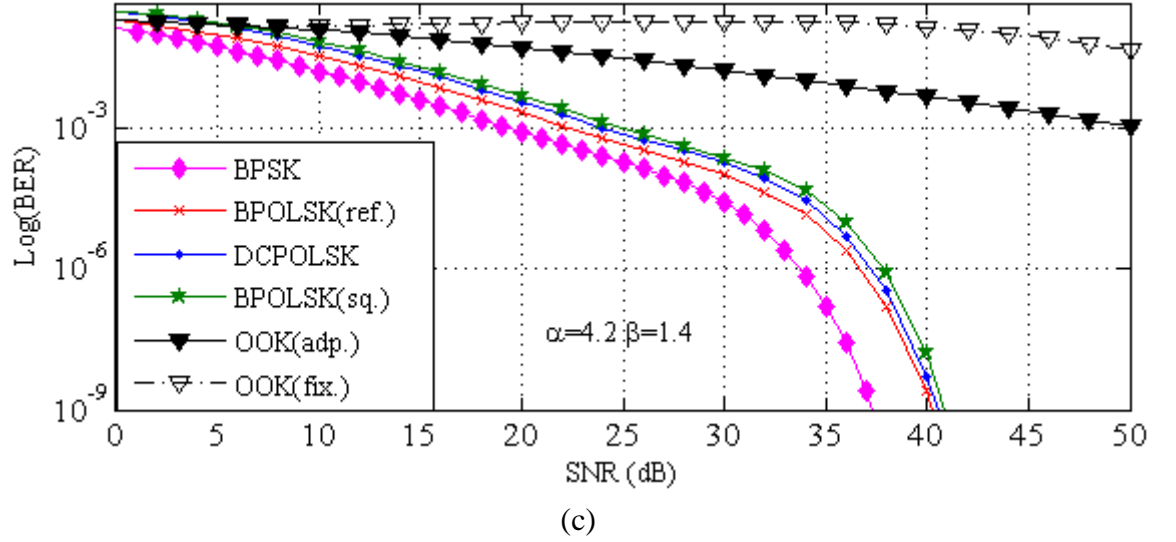


Fig. 5-10: Comparisons of BER performances of various modulation schemes against the normalized electric SNR $E[\Re P_r P_{lo}] = 1$ in (a) weak, (b) moderate and (c) strong turbulence regimes.

In the BPOLSK modulation format, the transmitted information is encoded into the SOPs. Because information is not carried by the signal instantaneous phase, the BPOLSK-FSO systems are the least sensitive to phase noise. The phase noise causes a sensitivity penalty mainly due to the broadening of the signal spectrum. A wide intermediate-frequency filter and a narrow-baseband filter can be applied at the receiver to limit this noise effect. For higher values of turbulence the BER performance deteriorates very rapidly for OOK with a fixed threshold level. The information encoded in the intensity of the carrier signal is much more prone to turbulence induced fluctuation. Information embedded into the phase or polarisation states are more robust to the atmospheric turbulence. However, using an adaptive threshold detection scheme we observe a considerable improvement in the BER performance even at higher values of turbulence.

5.5 Summary

In this chapter, the BER of BPOLSK modulated FSO have been presented and compared with the OOK and BPSK techniques across all turbulence regimes. Based on the results presented, the BPOLSK offers the highest immunity to the phase noise and is recommended in the atmospheric turbulence against the OOK (with fixed and adaptive threshold detection) modulated FSO systems, primarily because it does not exhibit a BER floor. For example, to achieve a BER of 10^{-9} in a moderate turbulence regime, the SNR requirement is ~ 39.5 dB for the BPOLSK scheme. For moderate turbulence regimes OOK suffers from high BER floors. For instance, for an SNR of 49 dB in a moderate regime, BERs are 4×10^{-4} and 0.05 for OOK with the fixed and adaptive threshold detections, respectively. The heterodyne BPSK modulated FSO systems are based on coherent optical detection and synchronous demodulation by an electrical PLL. However, the phase noise sensitivity of such coherent systems is considerable due to the presence of a PLL circuit. The power penalties caused by the atmospheric turbulence must be compensated for to guarantee a reliable communication link. One option would be to increase the transmitted optical power. However, this is only useful in the very weak turbulence regime and must meet the eye safety level. In the following chapter, the spatial diversity techniques combined with the BPOLSK system will be examined in the turbulent atmospheric channel.

Chapter Six

BPOLSK-FSO with Receiver Diversity Techniques

The performance impairments due to the temperature induced scintillation can be mitigated by adopting several approaches including aperture averaging, adaptive optics [80, 85, 166, 170, 181], diversity techniques [38, 98, 210, 211] and error control coding [43, 80, 212, 213]. To receive uncorrelated signals with the aperture averaging technique, the aperture size of the receiver must be much larger than the spatial coherence distance of the atmospheric turbulence (order of centimetres), which makes the aperture averaging not always achievable in FSO systems [105].

The adaptive optics approach based on the phase conjugation principle is used to reverse the wavefront deformation effect of the atmospheric turbulence [1, 3, 85, 101]. This scheme is mainly applied in deep space FSO systems as it significantly increases the system complexity and the implementation cost [85]. A superposition MIMO coding scheme for the transmission of unequally important sources in a point-to-multipoint system is proposed [214]. In this paper, for lower data rates, an Alamouti code is applied in order to maximize the performance for the receivers with poor channel qualities; while for higher data rates, the spatial multiplexing is applied at the receivers having with good channel conditions.

To circumvent the turbulence effects, the diversity techniques and error control coding schemes will be applied to the BPOLSK-FSO system. The performance analysis will be outlined in this and the following chapters. Linear combining techniques, including the maximum ratio combining (MRC) and the equal gain combining (EGC) will be considered. The atmospheric turbulence channel is modelled as the gamma-gamma distribution to predict the performance of short to very long FSO links. The results obtained for BPOLSK-FSO with the diversity technique and error control coding will be compared with BPOLSK-FSO using the reference carrier with a single detector and no channel coding as discussed in Chapter 5. The reason for this is that the BPOLSK system offers the best performance in comparison with other proposed BPOLSK-FSO systems in the turbulence channel. The results however can be easily extended to other BPOLSK systems.

6.1 Receiver Diversity Techniques

Receiver diversity techniques with their inherent redundancy provide an attractive approach to compensate for turbulence induced fading [38, 93, 98, 127, 211, 215]. By employing multiple receivers, the potential for temporary blockage of the laser beam due to obstructions (e.g., birds) mainly in urban areas can be significantly reduced. Apart from this, the receiver diversity combined with the wide divergence optical sources can be used to combat misalignment between transmitters and receivers and thus the requirement of an active tracking system can be avoided [45, 98, 131, 215].

In the aperture averaging technique, the single aperture size must be much larger than the irradiance spatial coherence distance [45, 87, 215, 216]. It offers significant performance improvement in the moderate and strong turbulence regimes [14, 45, 98, 215, 216]. For example, for the received power of -25 dBm in the weak turbulence regime, the BER decreases from 2×10^{-5} for a point receiver (with a diameter $D = 0$) to 10^{-8} for $D = 10$ cm. For the same received power in the moderate turbulence regime, the BER decreases from 10^{-4} for a 15 cm-diameter aperture to 10^{-6} for a 25 cm-diameter aperture. By increasing D from 15 cm to 30 cm in the strong turbulence regime, the BER decreases from 10^{-3} to 10^{-7} for a received power of -23 dBm [216]. It was also shown in [105] that the aperture averaging technique has a limitation to mitigate the scintillation effects. The limited SNR improvement can be obtained when the aperture size beyond a certain value. Additionally, increasing the aperture size also increases the capacity, which in turn reduces the data rate.

With the receiver diversity, a single receiver with a large FOV is replaced by a group of small surface area detectors with a narrow FOV that are positioned well within the received optical beam footprint [14, 98, 133]. The possibility of all the detectors suffering from deep fade simultaneously is much reduced. Moreover, the receiver diversity scheme allows higher data rate transmission due to the low capacitance of small area photodetectors [14, 98]. Additionally the diversity scheme limits the amount of background light from unwanted sources that impinges on the specific detector, which otherwise could be received by the single receiver with a wide FOV [98, 127, 133, 210, 211].

Employing multiple photodetectors can mitigate the turbulence induced fading in the received signal, thus leading to further improvement in the link error performance. To avoid any correlation in the received irradiance the detectors must be sufficiently spaced as shown in Fig. 6-1. Since the transverse correlation size ρ_0 of the laser radiation operating over the atmospheric turbulence channel is nearly a few centimetres, the parameter ρ_0 can be assumed to be greater than the spacing between the detectors [1, 14, 98, 103, 215]. The difference in the propagation delay across the receiver array would be negligible as the spacing between the photodiodes is much shorter than wireless link ranges [1, 210, 215]. The received optical power is assumed to be constant and time invariant during one symbol duration $T \ll \tau_0$, where the coherence time τ_0 of the atmospheric fluctuation is in the order of milliseconds [1, 127, 210].

The received signal from each branch is scaled by a gain factor $\{G_i\}_{i=1}^{\mathcal{N}}$ as illustrated in Fig. 6-1. The output of the combiner is the sum of the weighted and co-phased signals. Each receiver aperture size of \mathcal{N} -photodetector is $(1/\mathcal{N})^{\text{th}}$ of the aperture area of the single receiver. Accordingly, the background noise variance on each branch is proportional to the receiver aperture area, which is reduced by a factor of \mathcal{N} , whereas the thermal noise on each branch is not affected. For this reason, the AWGN noise variance on each branch will be σ_n^2/\mathcal{N} .

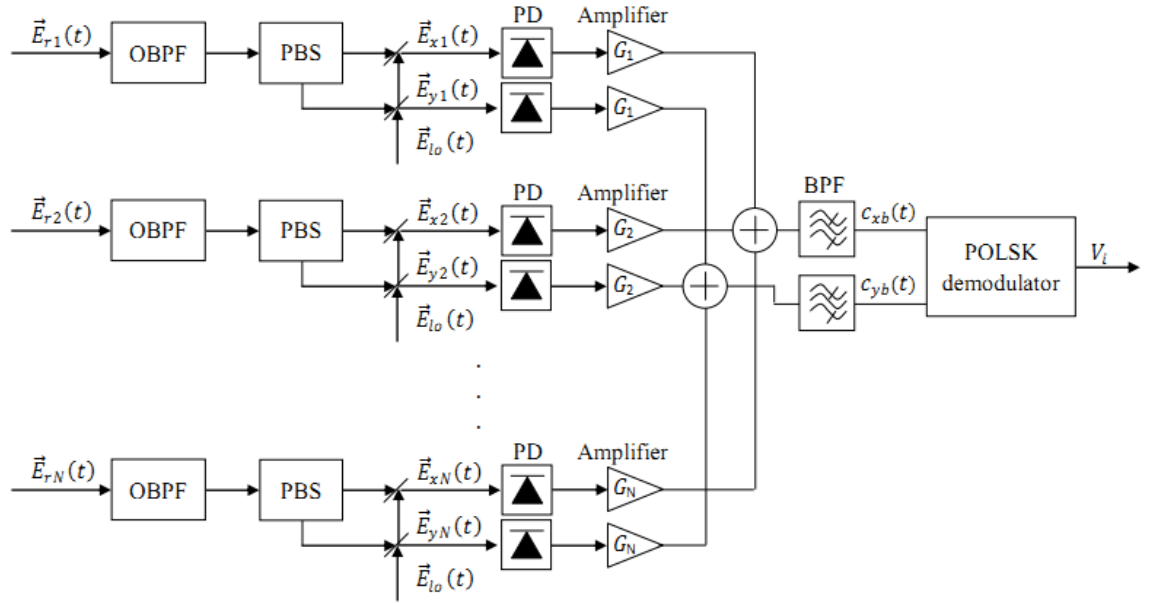


Fig. 6-1: Receiver diversity with \mathcal{N} - PDs.

For a background noise limited FSO link, the variance of the overall Gaussian noise with a zero mean becomes [1]:

$$\sigma_T^2 = \frac{1}{\mathcal{N}} \sum_{i=1}^{\mathcal{N}} G_i^2 \sigma_n^2, \quad (6.1)$$

where $i = 1, 2, 3, \dots, \mathcal{N}$.

Since the receiver diversity is applied in the BPOLSK-FSO system using the reference carrier signal, the individual received optical signal is given as:

$$\vec{E}_{ri}(t) = \sqrt{\frac{P_{ri}}{2}} e^{i(\omega t + \varphi_r(t))} \{e^{i\beta(t)} \cdot \vec{x} + \vec{y}\}. \quad (6.2)$$

The electric currents are scaled by a gain factor, $\{G_i\}_{i=1}^{\mathcal{N}}$, before being co-phased and coherently combined. The electric currents $\{c_{xb}(t), c_{yb}(t)\}$ from the combiner are given as:

$$c_{xb}(t) = \frac{\Re}{\mathcal{N}} \sum_{i=1}^{\mathcal{N}} G_i \sqrt{\frac{P_{ri} P_{lo}}{2}} \cos(\omega_{IF} t + \beta(t) + \varphi_{IF}(t)) + \sum_{i=1}^{\mathcal{N}} G_i n_{xi}(t), \quad (6.3a)$$

$$c_{yb}(t) = \frac{\Re}{\mathcal{N}} \sum_{i=1}^{\mathcal{N}} G_i \sqrt{\frac{P_{ri} P_{lo}}{2}} \cos(\omega_{IF} t + \varphi_{IF}(t)) + \sum_{i=1}^{\mathcal{N}} G_i n_{yi}(t). \quad (6.3b)$$

The optimum post detection electrical SNR γ_T at the BPOLSK demodulator input becomes:

$$\gamma_T(\vec{P}_r) = \frac{\Re^2 P_{lo} (\sum_{i=1}^{\mathcal{N}} G_i \sqrt{P_{ri}})^2}{2\mathcal{N} \sum_{i=1}^{\mathcal{N}} G_i^2 \sigma_n^2}, \quad (6.4)$$

where $\vec{P}_r = \sum_{i=1}^{\mathcal{N}} P_{ri}$. All the received optical power is assumed to be independent and obey the gamma-gamma distribution. The intermodulation distortion due to the inherent nonlinearity of the optical source has not been considered in (6.4).

Hypotheses are taken that all the received optical power is independent and all obey the gamma-gamma distribution. Therefore $p(\vec{P}_r)$ represents the joint PDF for \mathcal{N} -photodetector receiving uncorrelated signals, and is expressed as:

$$p(\vec{P}_r) = \prod_{i=1}^{\mathcal{N}} \int p(P_{ri}) dP_{ri}. \quad (6.5)$$

The system performance of the BPOLSK-FSO system employing the receiver diversity technique operating over the gamma-gamma turbulence channel can thus be evaluated from (6.4) and (6.5) using numerical integration since the resulting expression has no closed form solution. The receiver diversity generally consists of the following linear combining techniques: MRC, EGC and selection combining (SelC). The results obtained in [1] showed that the use of SelC in a single transmitter-multiple photodetector system results in no diversity gain in a very weak turbulence ($\sigma_t^2 \leq 0.2^2$) and it is therefore not recommended for use on a short link FSO system experiencing a weak irradiance fluctuation. In this work, only MRC and EGC receiver diversity techniques will be considered.

6.1.1 Maximum Ratio Combining (MRC)

In the MRC linear combiner scheme, the gain factor $\{G_i\}_{i=1}^{\mathcal{N}}$ is proportional to the received optical power. As the MRC linear combiner results in a maximum-likelihood receiver structure [1], it is optimal regardless of the fading statistics. However, the

received optical power level and phase on each branch has to be estimated prior to coherent combining, which makes it unsuitable for non-coherent demodulation schemes. Applying the Cauchy inequality [1, 217], $(\sum_{i=1}^N G_i \sqrt{P_{ri}})^2 \leq (\sum_{i=1}^N G_i^2)(\sum_{i=1}^N P_{ri})$, the $r_{\text{MRC}}(\vec{P}_r)$ is derived as:

$$\begin{aligned} \gamma_{\text{MRC}}(\vec{P}_r) &= \frac{\Re^2 P_{lo} (\sum_{i=1}^N G_i \sqrt{P_{ri}})^2}{2\mathcal{N} \sum_{i=1}^N G_i^2 \sigma_n^2} \leq \frac{\Re^2 P_{lo} (\sum_{i=1}^N G_i^2)(\sum_{i=1}^N P_{ri})}{2\mathcal{N} \sigma_n^2 \sum_{i=1}^N G_i^2}, \\ &= \frac{1}{\mathcal{N}} \left(\sum_{i=1}^N \frac{\Re^2 P_{lo} P_{ri}}{2\sigma_n^2} \right) = \frac{1}{\mathcal{N}} \left(\sum_{i=1}^N \gamma_i(P_r) \right). \end{aligned} \quad (6.6)$$

Therefore, the average SNR, $\vec{\gamma}_{\text{MRC}}$, is derived by averaging (6.6) over the turbulence statistics (6.5) which is given as:

$$\vec{\gamma}_{\text{MRC}} = \int \gamma_{\text{MRC}}(\vec{P}_r) p(\vec{P}_r) d\vec{P}_r. \quad (6.7)$$

The unconditional BER for the FSO system employing BPOLSK using the reference carrier signal with the receiver diversity is obtained by averaging the conditional error rate over the statistics of the gamma-gamma distribution (3.23):

$$P_{e\text{MRC}} = \int_0^\infty P_{ec}(\vec{P}_r) p(\vec{P}_r) d\vec{P}_r. \quad (6.8)$$

6.1.2 Equal Gain Combining (EGC)

In an EGC combiner, the knowledge of the phase on each branch is still required. Here, all received signals of x - and y - channels are combined coherently with equal weights of $\{G_{ci}\}_{i=1}^N = 1$ [1]. The γ_T for γ_{EGC} is given by:

$$\gamma_{\text{EGC}} = \frac{\Re^2 P_{lo}}{2\mathcal{N}^2 \sigma_n^2} \left(\sum_{i=1}^{\mathcal{N}} \sqrt{P_{ri}} \right)^2 = \frac{1}{\mathcal{N}^2} \left(\sum_{i=1}^{\mathcal{N}} \sqrt{\gamma_i(P_r)} \right)^2. \quad (6.9)$$

Following on from the previous section, the average SNR on each diversity branch and unconditional BER of a BPOLSK-FSO system with an array of photodetectors are given as (6.10) and (6.11), respectively:

$$\vec{\gamma}_{\text{EGC}} = \int \vec{\gamma}_{\text{EGC}}(\vec{P}_r) p(\vec{P}_r) d\vec{P}_r, \quad (6.10)$$

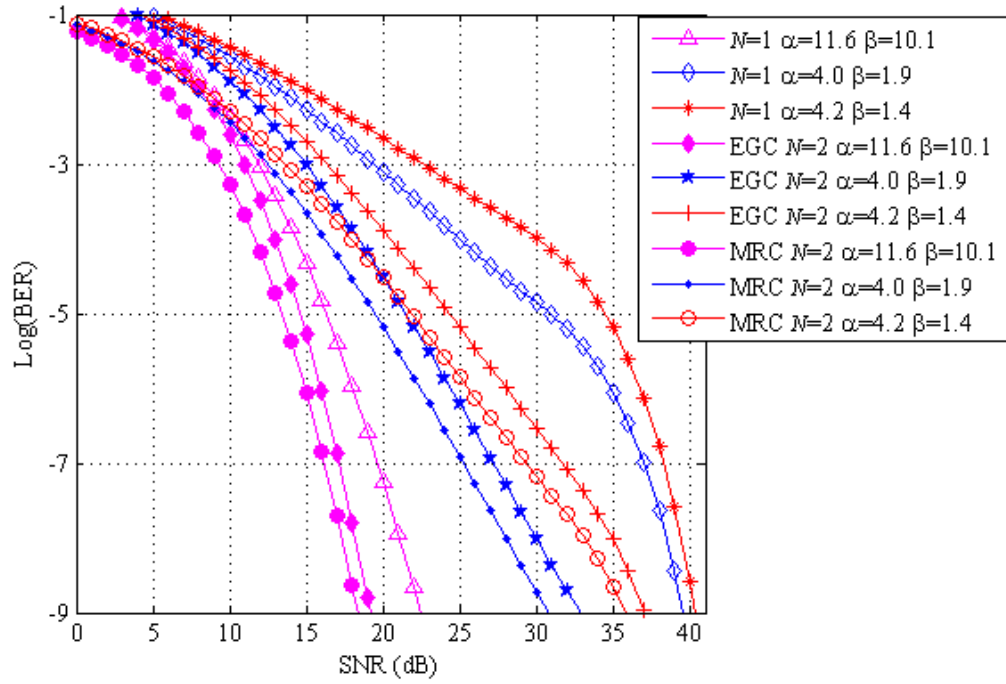
$$P_{e\text{EGC}} = \int_0^\infty P_{ec}(\vec{P}_r) p(\vec{P}_r) d\vec{P}_r. \quad (6.11)$$

6.1.3 Results and Discussions

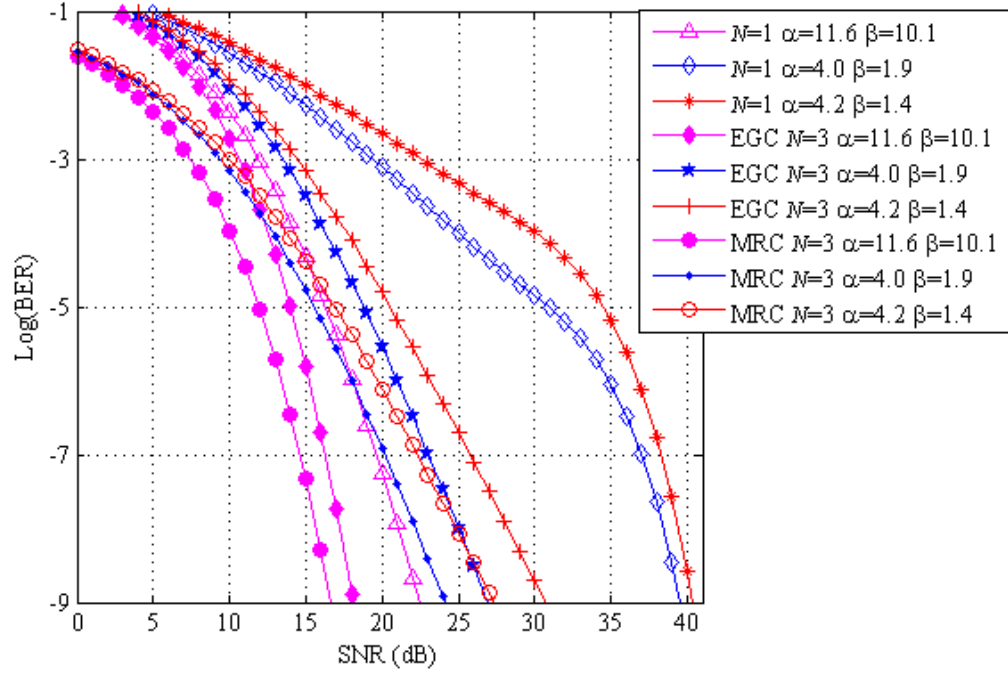
Using (6.8) and (6.11), the performance of the BPOLSK-FSO system employing the reference carrier signal with the receiver diversity in weak, moderate and strong turbulence regimes will be discussed in this section. The parameters representing each turbulence regime presented in Table 5.1 are used in this section. For the purpose of like-to-like comparison, the average optical signal power $E[\Re P_r P_{lo}]$ is normalized to the unity and the electric SNRs are made equal for the BPOLSK with EGC and MRC techniques.

In Figs. 6-2(a) and (b), the BER of BPOLSK-FSO employing the EGC and MRC techniques for a range of \mathcal{N} is plotted against the normalised SNR in the gamma-gamma channel covering all turbulence regimes. Compared with the results obtained with the single receiver given by (5.40), the advantage of using detector arrays for

mitigating the turbulence induced irradiance fluctuation is made evident. Fig. 6-2 shows that the optimum MRC outperforms the EGC diversity technique to achieve a fixed BER. For instance, to achieve a BER of 10^{-9} at various turbulence levels, the MRC offers a higher power gain (between ~ 1 dB and ~ 3 dB) than EGC for $\mathcal{N} = 2, 3$. The MRC results in a maximum-likelihood receiver which makes it the optimal regardless of the fading statistics [98, 218].



(a)



(b)

Fig. 6-2: Error probability of BPOLSK-FSO diversity with the EGC and MRC against the normalised SNR $E[\mathcal{R}P_r P_{lo}] = 1$ in the gamma-gamma channel for: (a) $\mathcal{N} = 1, 2$, and (b) $\mathcal{N} = 1, 3$.

By defining the SNR to achieve a BER of 10^{-9} with \mathcal{N} -detector at the turbulence level σ_l as, $\gamma_{\mathcal{N},\sigma_l}$, the spatial diversity gain can be represented as, $m_{\mathcal{N},\sigma_l} = \gamma_{1,\sigma_l} - \gamma_{\mathcal{N},\sigma_l}$. Fig. 6-2 also depicts that m_{2,σ_l} for the MRC combining scheme are ~ 4 , ~ 8.5 and ~ 4.5 dB in weak, moderate and strong turbulence regimes, respectively. When \mathcal{N} increases to 3, the corresponding values of m_{3,σ_l} increase to ~ 6 , ~ 15.5 and ~ 13 dB, respectively.

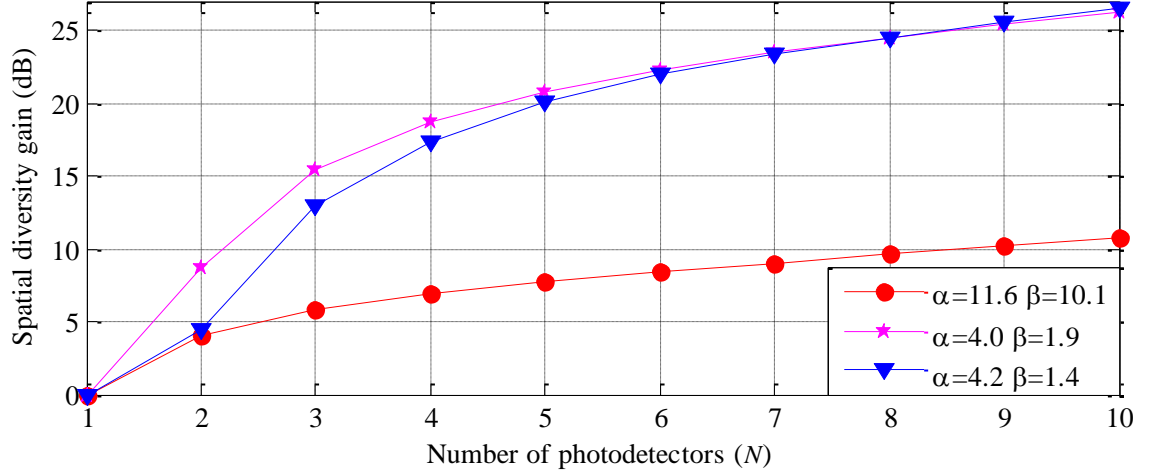


Fig. 6-3: Spatial diversity gain m_{N,σ_l} for the BPOLSK scheme employing MRC technique to achieve a BER of 10^{-9} against the number of photodetectors N with the normalised electric SNR $E[\Re P_r P_{lo}] = 1$ under all turbulence scenarios from weak to strong regimes.

The performance of spatial diversity gain is plotted against the number of photodetectors as shown in Fig. 6-3. For BPOLSK using MRC combining technique to achieve a BER of 10^{-9} , the spatial diversity gain $m_{N,\sigma_l} = \gamma_{1,\sigma_l} - \gamma_{N,\sigma_l}$ is plotted against the number of photodetectors N as illustrated in Fig. 6-3. The power gain in the strong turbulence regime is less than that in the moderate regime due to the fact that the deep fade results in a loss of spatial coherence of the laser radiation. However, when N increases to 10, the spatial diversity gain reaches up to ~ 26.5 dB in a strong turbulence regime. This is because adding more detectors will efficiently reduce the chance of a catastrophic fading from happening, but at the cost of increased system complexity.

Another observation from Fig. 6-3 is that when two detectors are used, the power gain is more than 3 dB for all turbulence regimes. Since the turbulence channel is modelled

as the gamma-gamma distribution, a diversity gain of 3 dB ($\mathcal{N} = 2$) is achievable in the Gaussian channel.

6.2 Performance of Received Signal Correlation and Outage

Probability

In the receiver diversity approach, the chance that multiple photodetectors suffer irradiance fading at the same time has been much reduced. However, the correlated irradiance fluctuations still cause observable power penalties. The performance analysis thus will be carried out using optimum EGC linear scheme operating over the lognormal turbulence channel; whereas other linear combining techniques and channel models can be easily adopted by extending the results in a similar manner. The conditional BER for the BPOLSK with the EGC combining scheme is given as:

$$P_{e\text{EGC}} = \frac{1}{2} \operatorname{erfc} \left(\sqrt{\frac{\gamma_{\text{EGC}}(\bar{P}_r)}{2}} \right) = \frac{1}{\pi} \int_0^{\frac{\pi}{2}} \exp \left(-\frac{\Re^2 P_{lo}}{4\mathcal{N}^2 \sigma_n^2 \sin^2 \phi} \left(\sum_{i=1}^{\mathcal{N}} \sqrt{P_{ri}} \right)^2 \right) d\phi, \quad (6.12)$$

where $\frac{1}{2} \operatorname{erfc}(x) = \frac{1}{\pi} \int_0^{\frac{\pi}{2}} \exp \left(-\frac{x^2}{2 \sin^2 \phi} \right) d\phi$.

The correlation coefficient $\rho(s)$ of an optical wave propagating over a turbulence channel can be expressed using Tatarski's infinite power series [95] and is given as:

$$\begin{aligned} \rho(s) = 1 - 2.36(2\pi s/\lambda L)^{5/6} + 1.71(2\pi s/\lambda L) - 0.024(2\pi s/\lambda L)^2 \\ + 0.00043(2\pi s/\lambda L)^4 + \dots \end{aligned} \quad (6.13)$$

where L is the link distance between the transmitter and receiver. Based on the results from [95], the correlation coefficient $\rho(\varsigma)$ against the spatial separation ς , is plotted in Fig. 6-4. It is shown that $\rho(\varsigma)$ is inversely proportional to ς for $\varsigma/\sqrt{\lambda L} < 1$, where $\rho_0 \approx \sqrt{\lambda L}$. The covariance matrix \mathcal{C}_χ is derived as [1, 95]:

$$\mathcal{C}_\chi = \begin{bmatrix} \sigma_\chi^2 & \cdots & \rho \frac{\varsigma_{12}}{\varsigma_{1N}} \sigma_\chi^2 \\ \vdots & \ddots & \vdots \\ \rho \frac{\varsigma_{12}}{\varsigma_{N1}} \sigma_\chi^2 & \cdots & \sigma_\chi^2 \end{bmatrix}, \quad (6.14)$$

where ρ is the correlation coefficient between two photodetectors with a spatial separation ς_{12} , ς_{ij} represents the spatial separation between photodetectors i and j , and $\sigma_\chi^2 = 0.25\sigma_l^2$.

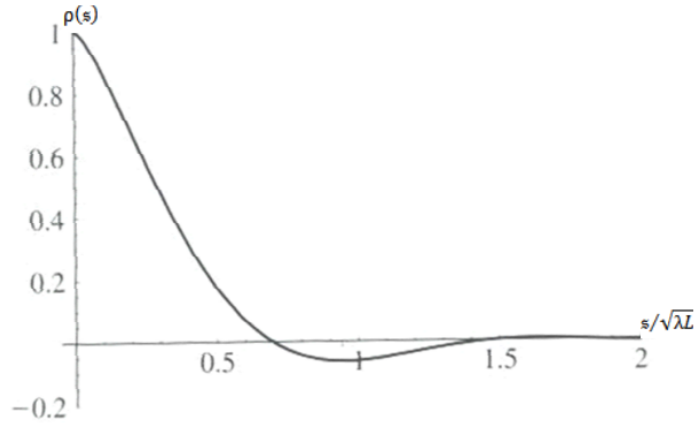


Fig. 6-4: Correlation coefficient $\rho(\varsigma)$ as a function of the transverse separation ς in a weak turbulent field [95].

The joint PDF of the received irradiance is obtained as [1, 95]:

$$p(P_{r1}, P_{r2} \cdots P_{rN}) = \frac{\exp(-\mathbb{X}\mathcal{C}_\chi^{-1}\mathbb{X}^T/8)}{2^N \prod_{i=1}^N I_i(2\pi)^{N/2} |\mathcal{C}_\chi|^{1/2}}, \quad (6.15)$$

where $\mathbb{X} = [\ln P_{r1}/P_{r0} \quad \ln P_{r2}/P_{r0} \quad \cdots \quad \ln P_{rN}/P_{r0}]$ is a row matrix.

The unconditional error probability is then given as [1, 95]:

$$P_e = \int P_{ec}(\bar{P}_r) p(P_{r1}, P_{r2} \cdots P_{rN}) d\bar{P}_r. \quad (6.16)$$

The effect of signal correlation on the error performance is shown in Fig. 6-5 using (6.14), (6.15) and (6.16) for $N = 2$, $\rho = [0, 0.1, 0.5, 0.8]$ and $\sigma_t^2 = 0.3$. For example, using two photodetectors to achieve a BER of 10^{-9} , the additional SNR caused due to increasing ρ from 0 to 0.5 is ~ 4 dB. Further increasing ρ to 0.8, ~ 4.5 dB additional SNR is required. Fig. 6-5 indicates that the increases signal correlation induces the power penalty. Therefore, in order to get the most of the spatial diversity technique, the photodetector separation must be greater than the spatial coherence length ρ_0 .

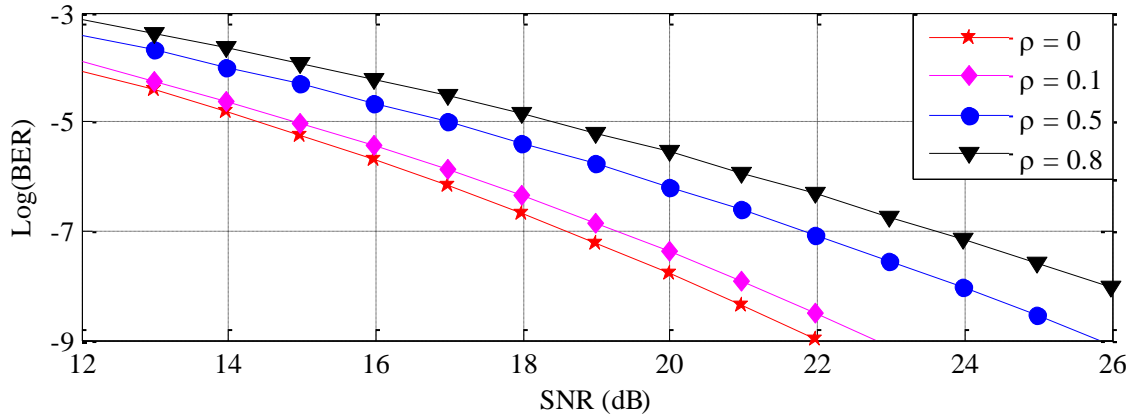


Fig. 6-5: Error probability of the BPOLSK-FSO with EGC at a range of correlation coefficients for $N = 2$ and $\sigma_t^2 = 0.3$.

With the spatial diversity receiver in a lognormal turbulence channel, the sum of N independent optical power is a lognormal variable and expressed as $Z = \sum_{i=1}^N P_{ri} =$

$\exp(\mathcal{U})$, where \mathcal{U} is normally distributed with mean μ_u and variance σ_u^2 [1, 103, 219].

In [1] the PDF of Z has been derived and is expressed as (6.17):

$$P(Z) = \frac{1}{\sqrt{2\pi\sigma_u^2}} \frac{1}{Z} \exp(-(\ln Z - \mu_u)^2 2^{-1} \sigma_u^{-2}), \quad (6.17)$$

$$\mu_u = \ln(\mathcal{N}) - \frac{1}{2} \ln(1 + (\exp(\sigma_l^2) - 1) \mathcal{N}^{-1}), \quad (6.18a)$$

$$\sigma_u^2 = \ln(1 + (\exp(\sigma_l^2) - 1) \mathcal{N}^{-1}). \quad (6.18b)$$

The outage probability with EGC spatial technique is expressed as

$P_{out} = P(P_{e\text{EGC}} > P_e^*) \equiv P(\gamma_{\text{EGC}}(\bar{P}_r) < \gamma^*)$. If the extra power margin to achieve a given P_{out} is represented by m_{EGC} and the average SNR in the absence of atmospheric turbulence is γ^* , therefore the outage probability can be expressed as:

$$P_{out} = Q\left((\ln(m_{\text{EGC}}/\mathcal{N}) + \mu_u) \sigma_u^{-1}\right). \quad (6.19)$$

To achieve a given P_{out} , m_{EGC} can be approximately derived by applying the Chernoff bound, $Q(x) \leq 0.5 \exp(-x^2/2)$, into (6.19), as:

$$m_{\text{EGC}} \approx \mathcal{N} \exp\left(\sqrt{-2\sigma_u^2 \ln(2P_{out})} - \mu_u\right). \quad (6.20)$$

The upper bound of the outage probability (6.20) and the exact solution given by (6.19) are illustrated in Fig. 6-6. The power margins based on the upper bound are ~ 0.2 and ~ 0.3 dBm more than that using the exact solution for $\sigma_l = 0.1, 0.3$, respectively. As the number of independent photodetector increases, the upper bound appears to become tighter. The diversity gain based on EGC combining for a given outage probability P_{out}

is given as (6.21), which is the ratio of the link margin without spatial diversity to that with the spatial diversity.

$$Gain = \frac{1}{\mathcal{N}} \exp \left(\sigma_l^2/2 + \mu_u + \sqrt{-2\sigma_l^2 \ln(2P_{out})} - \sqrt{-2\sigma_u^2 \ln(2P_{out})} \right). \quad (6.21)$$

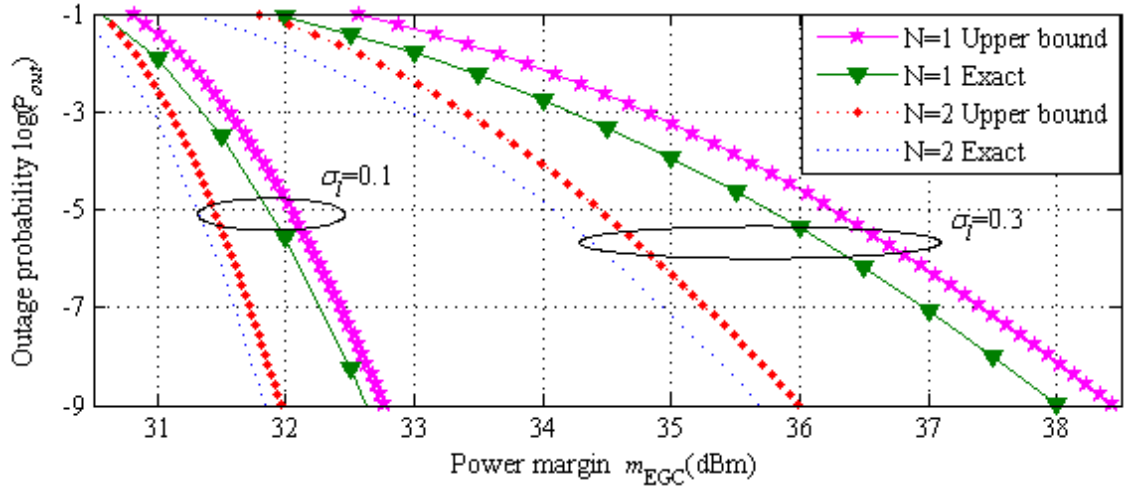


Fig. 6-6: The upper bound of the outage probability (6.20) and the exact solution (6.19) against the power margin with EGC spatial diversity in a weak turbulent atmospheric channel for $\sigma_l = [0.1, 0.3]$ and $\mathcal{N} = [1, 2]$.

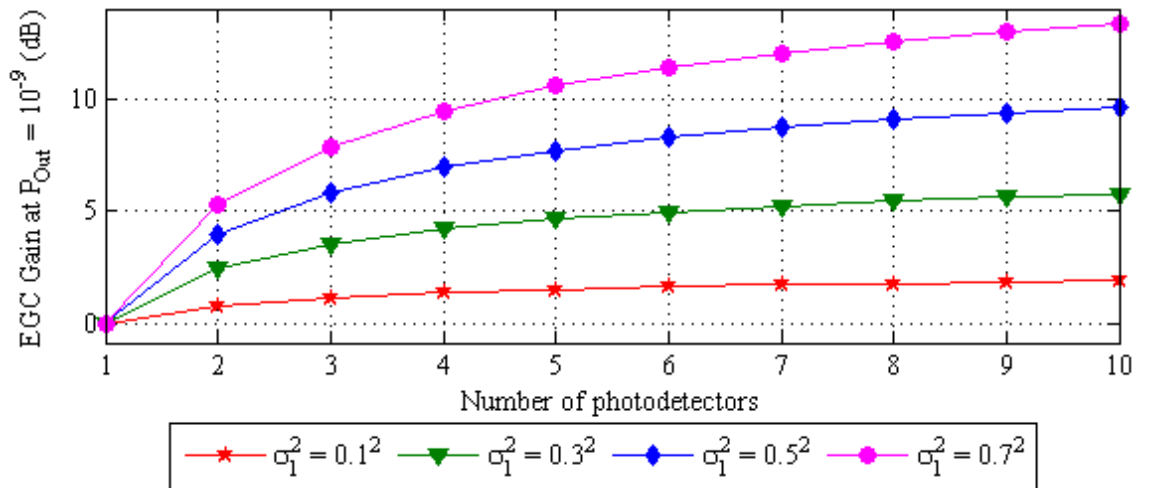


Fig. 6-7: EGC diversity gain against the number of photodetectors at P_{out} of 10^{-9} in a lognormal atmospheric channel with $\sigma_l^2 = [0.1^2, 0.3^2, 0.5^2, 0.7^2]$.

The diversity gain given by (6.21) to achieve a BER of 10^{-9} is plotted against the number of photodetectors for a range of the turbulence variance in Fig. 6-7. This figure indicates that a gain of ~ 4 dB is achievable using two photodetectors at $\sigma_t^2 = 0.5^2$. And the gain increases to ~ 6.5 dB with $\mathcal{N} = 4$. The plot starts to plateau for $\mathcal{N} > 4$, which indicates a reduction in the amount of gain for each additional photodetector.

6.3 Summary

The error performance and the outage probability for a BPOLSK-FSO employing the diversity receiver have been analysed in this chapter. The diversity receiver is used to combat the scintillation induced channel fading. The gamma-gamma and lognormal channel models have been considered. The details of error probability and achievable link margin using the EGC linear combining techniques have been outlined. Additionally, the power penalty caused by the received optical signal correlation on the error probability has been shown. For instance, to achieve a BER of 10^{-9} with $\mathcal{N} = 2$, the additional ~ 4 dB of SNR is required due to the increment of ρ from 0 to 0.5. The SNR value increases to ~ 4.5 dB when ρ further increases to 0.8. For the EGC linear combining to mitigate scintillation without overwhelming the complexity and cost, the reasonable number of independent photodetectors is between 2 and 4.

Chapter Seven

Multilevel POLSK FSO in the Gamma-Gamma Turbulence Channel

Various multilevel modulation formats have been proposed for optical transmission systems. Multilevel modulation schemes offer higher data rates than binary modulation formats using the state-of-the-art electronic and optoelectronic equipments [220-222]. Multilevel digital modulations like the PSK and the quadrature amplitude modulation (QAM) are commonly deployed in optical communications to encode multiple bits per symbol [221]. POLSK modulation can be combined with ASK and PSK and demodulated without the need for the dynamic polarisation control at the receiver by employing electrical multilevel detection schemes [189, 198, 199]. Though MPOLSK

has been studied for optical fibre communication systems where the fibre dispersion and noise are the impairment factors, no systematic study of such system in FSO links in the presence of the atmospheric turbulence has been carried out.

The performance impairments due to scintillation can be mitigated by adopting error control coding schemes [80, 212, 213]. The performances of coded IM/DD FSO links for the lognormal and gamma-gamma channel models under atmospheric turbulence have been investigated in [88, 94, 157]. Turbo and low density parity codes (LDPC) are more efficient and powerful coding schemes, which can be used to detect and correct burst errors caused by the scintillation [223, 224]. The LDPC coded subcarrier offers a coding gain of more than 20 dB compared with similarly coded OOK schemes in the atmospheric turbulence [225]. However, adding more redundant bits increases the processing delay and reduces the data throughput/user bandwidth as the overall block size of the outgoing data is increased [225].

This chapter studies the performance of the MPOLSK scheme in the presence of atmospheric turbulence for different modulation levels. The analytical SEP of the coherent heterodyne MPOLSK is carried out for a direct LOS FSO system. To mitigate the turbulence induced fading, convolutional coding and spatial diversity techniques will be also employed for the improvement in overall system performance. The upper SEP bounds are derived using the transfer function technique. The spatial diversity gain for a number of detectors is also determined for different turbulence levels.

The rest of the chapter is organized as follows: the performance analysis for the coherent 8-POLSK system combined with convolutional coding and spatial diversity technique will be given in Section 7.1; while the unconditional symbol error probability (SEP) for the MPOLSK-FSO system considering the penalty caused by the phase tracking error and turbulence effects will be derived in Section 7.2. Finally, the summary is made in Section 7.3.

7.1 Coherent Heterodyne 8-Polsk System

7.1.1 System Configuration

Fig. 7-1(a) illustrates the block diagram of the 8-POLSK transmitter. The TL beam is linearly polarised and has a $\pi/4$ polarisation with respect to the principle axis of the external PM. The output from TL ($\vec{E}_0(t)$) is decomposed by the PBS into two orthogonally polarised components, \vec{x} and \vec{y} with equal amplitudes. The amplitude and phase of the optical component polarised along the \vec{x} axis are modulated externally by the data stream $\{m_0(t), m_1(t), m_2(t)\}$ while the \vec{y} -component is used as the reference carrier which is transmitted with the modulated \vec{x} component. The applied voltage to the LiNbO₃ based external phase modulator is equal to either zero or V_π . The applied voltage V_π induces a π phase shift in the \vec{x} -component and a zero phase shift in the \vec{y} -component, thus leading to a $\pi/2$ rotation of the polarisation of the optical carrier.

The AM combined with the PM for the \vec{x} -component is described as an eight-level modulation scheme where the time axis is divided into symbol intervals. Each symbol is

associated with a value of the transmitted optical field which remains constant during a symbol interval.

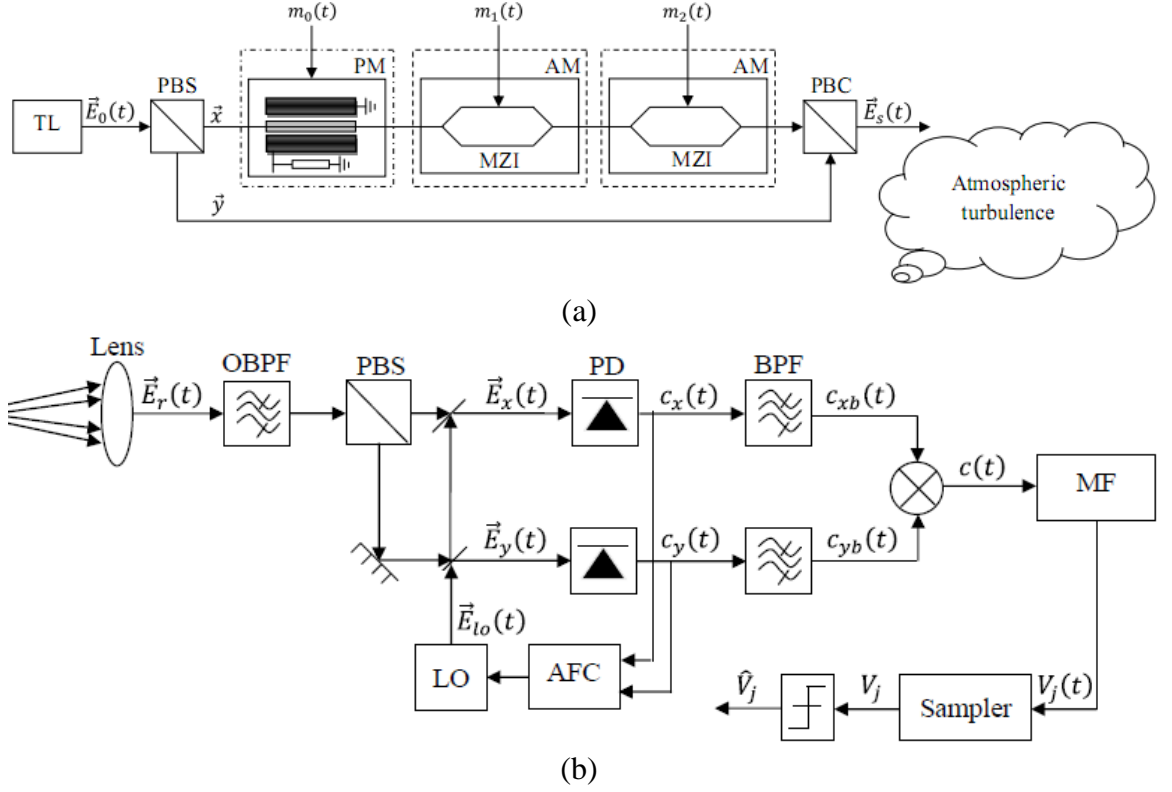


Fig 7-1: Coherent 8-POLSK-FSO transceiver: (a) the transmitter, and (b) the receiver.

Under these conditions, the transmitted optical field $\vec{E}_s(t)$ at the output of the PBC is expressed as:

$$\vec{E}_s(t) = \sqrt{\frac{P_t}{2}} e^{i[\omega t + \varphi(t)]} \{ \varepsilon e^{i\beta_x(t)} \cdot \vec{x} + \vec{y} \}, \quad (7.1)$$

where the PM function $\beta_x(t) \in [0, \pi]$ is for $m_0 \in [1, 0]$, and AM function $\varepsilon \in [1, 3, 5, 7]$ is for $\{m_1 m_2\} \in [10, 11, 01, 00]$, respectively.

Fig. 7-1(b) illustrates the block diagram of the proposed optical coherent heterodyne receiver. The optical field of the local oscillator $\vec{E}_{lo}(t)$ is linearly polarised at $\pi/4$ with respect to the receiver reference axes.

The received optical field $\vec{E}_r(t)$ following the optical lens is uncorrelated and can be expressed as:

$$\vec{E}_r(t) = \sqrt{\frac{P_r}{2}} e^{i(\omega t + \varphi_r(t))} \{ \varepsilon e^{i\beta_x(t)} \cdot \vec{x} + \vec{y} \}. \quad (7.2)$$

The received optical signal $\vec{E}_r(t)$ is split by the PBS into \vec{x} - and \vec{y} -components, which are then mixed with \vec{x} - and \vec{y} -components generated by the local oscillator, respectively.

Therefore, the decomposed orthogonally polarised components $\vec{E}_x(t)$ and $\vec{E}_y(t)$ with equal amplitudes are given as:

$$\vec{E}_x(t) = \left\{ \sqrt{\frac{P_r}{2}} \varepsilon e^{i[\omega t + \beta_x(t) + \varphi_r(t)]} + \frac{\sqrt{P_{lo}}}{2} e^{i[\omega_{lo} t + \varphi_{lo}(t)]} \right\} \cdot \vec{x}, \quad (7.3a)$$

$$\vec{E}_y(t) = \left\{ \sqrt{\frac{P_r}{2}} e^{i[\omega t + \varphi_r(t)]} + \frac{\sqrt{P_{lo}}}{2} e^{i[\omega_{lo} t + \varphi_{lo}(t)]} \right\} \cdot \vec{y}. \quad (7.3b)$$

Following optical-to-electrical conversion process, the signals $c_x(t)$ and $c_y(t)$ at the output of two identical PDs are expressed as [135]:

$$c_x(t) = \Re \left\{ \left| \sqrt{\frac{P_r}{2}} \varepsilon \right|^2 + \left| \frac{\sqrt{P_{lo}}}{2} \right|^2 + \sqrt{\frac{P_r P_{lo}}{2}} \varepsilon \cos[\omega_{IF} t + \beta_x(t) + \varphi_{IF}(t)] \right\} + n_x(t), \quad (7.4a)$$

$$c_y(t) = \Re \left\{ \left| \sqrt{\frac{P_r}{2}} \right|^2 + \left| \frac{\sqrt{P_{lo}}}{2} \right|^2 + \sqrt{\frac{P_r P_{lo}}{2}} \cos[\omega_{IF} t + \varphi_{IF}(t)] \right\} + n_y(t), \quad (7.4b)$$

where $n_{x,y}(t) \sim N(0, \sigma_n^2)$.

The electrical signals $c_x(t)$ and $c_y(t)$ are passed through the ideal BPF to reject the constant term and to limit the additive noise. The bandwidth of the BPF is expressed as

$B_{bp} = 2(R_s + k_F B_L)$ with the center frequency at ω_{IF} . The BPF in the lower branch has a very narrow bandwidth in order to only pass the carrier signal with negligible distortion. Therefore, the electrical currents at the output of BPFs are expressed as:

$$c_{xb}(t) = \sqrt{\frac{\Re^2 P_r P_{lo}}{2}} \varepsilon \cos[\omega_{IF} t + \beta_x(t) + \varphi_{IF}(t)] + n_{xb}(t), \quad (7.5a)$$

$$c_{yb}(t) = \sqrt{\frac{\Re^2 P_r P_{lo}}{2}} \cos[\omega_{IF} t + \varphi_{IF}(t)] + n_{yb}(t), \quad (7.5b)$$

where $\{n_{xb}(t), n_{yb}(t)\} \sim (0, \sigma_n^2)$ is the additive white Gaussian noise at the output of the BPF. The electric signal $c(t)$ is integrated over the symbol period T , and sampled at time $t = T$. Hence, the output of the correlation-type demodulator [203] is given by:

$$\begin{aligned} V_j(t) &= \frac{1}{\sqrt{T}} \int_0^T c_m(t) dt, \quad (7.6) \\ &= \frac{1}{\sqrt{T}} \int_0^T \frac{1}{2} \sqrt{\frac{\Re^2 P_r P_{lo}}{2}} \left[\sqrt{\frac{\Re^2 P_r P_{lo}}{2}} \varepsilon \cos(\beta_x(t)) + n_{xb}^I(t) + n_{yb}^I(t) \right] dt, \\ &= \frac{1}{2} \sqrt{\frac{\Re^2 P_r P_{lo}}{2T^2}} \left[\sqrt{\frac{\Re^2 P_r P_{lo}}{2}} \frac{1}{\sqrt{T}} \int_0^T \varepsilon \cos(\beta_x(t)) dt + \frac{1}{\sqrt{T}} \int_0^T n_{xb}^I(t) + n_{yb}^I(t) dt \right], \\ V_j &= \sqrt{\frac{\Re^2 P_r P_{lo}}{8}} \left[\sqrt{\frac{\Re^2 P_r P_{lo}}{2}} \varepsilon \cos(\beta) + n_{xb}^I + n_{yb}^I \right]. \quad (7.7) \end{aligned}$$

The noise variance is suppressed to half of its value at the output of the MF $\{n_{xb}^I, n_{yb}^I\} \sim N(0, \sigma_n^2/2)$. The decision rule which maximizes the correlation metrics is applied to determine the average probability of error. It follows that the detector compares the demodulator output V_j with seven threshold levels: $0, \pm \Re^2 P P_{lo}/2$,

$\pm \Re^2 P P_{lo}$, $\pm 3 \Re^2 P P_{lo}/2$. Therefore, a decision is made in favour of the amplitude level closest to V_j .

7.1.2 Error Probability Analysis

For equally probable signals, the decision rule which maximizes the correlation metrics is applied to determine the average probability of error. In other words the decision must be made by comparing V_j with different threshold levels and selecting the amplitude level. The average power for equiprobable coded 8-POLSK symbol is increased by a factor of 11/3 compared with the uncoded BPOLSK [226]. The average power per bit P_{av} in the coded 8-POLSK system must be reduced by a factor of 11/3:

$$P_{av} = \frac{\Re^2 P_r P_{lo}}{4 \log_2 8} \left[\frac{(1 + 1^2)}{2} + \frac{(1 + 3^2)}{2} + \frac{(1 + 5^2)}{2} + \frac{(1 + 7^2)}{2} \right] = \frac{11}{3} \Re^2 P_r P_{lo}. \quad (7.8)$$

The assumption is that all amplitude levels are equally likely a priori. Thus, an error is detected when $(n_{xb}^l + n_{yb}^l)$ exceeds one-half of the distance between adjacent amplitude levels. Therefore, the SEP is expressed as:

$$\begin{aligned} P_{sec} &= \frac{7}{8} P \left(|n_{xb}^l + n_{yb}^l| > \sqrt{\frac{\Re^2 P_r P_{lo}}{2}} \right) = \frac{7}{8} \frac{2}{\sqrt{2\pi\sigma_n^2}} \int_{\sqrt{\Re^2 P_r P_{lo}/2}}^{\infty} e^{-x^2/2\sigma_n^2} dx, \\ &= \frac{7}{8} \frac{2}{\sqrt{2\pi}} \int_{\sqrt{\Re^2 P_r P_{lo}/2\sigma_n^2}}^{\infty} e^{-x^2/2} dx = \frac{7}{4} Q \left(\sqrt{\frac{\Re^2 P_r P_{lo}}{2\sigma_n^2}} \right). \end{aligned} \quad (7.9)$$

The SEP expressed in (7.9) can also be expressed in terms of the average power per bit, which is:

$$P_{sec} = \frac{7}{4} Q \left(\sqrt{\frac{3P_{av}}{22\sigma_n^2}} \right) = \frac{7}{4} Q \left(\sqrt{\frac{3}{11}} \gamma \right). \quad (7.10)$$

where the electrical SNR at the input of the coherent demodulator is defined as $\gamma = P_{av}/2\sigma_n^2$. The alternative function form for the Gaussian-Q function is [157, 227]:

$$Q(x) = \frac{1}{\pi} \int_0^{\pi/2} \exp\left(-\frac{x^2}{2\sin^2\theta}\right) d\theta. \quad (7.11)$$

Substituting (7.10) into (7.11) and considering that the received signal is subjected to channel fading, the unconditional SEP for 8-POLSK in a gamma-gamma turbulence channel is given as:

$$P_e(P_r) = \frac{7}{4\pi} \int_0^{\pi/2} \left[\int_0^\infty \exp\left(\frac{-3\gamma(P_r)}{22\sin^2\theta}\right) \frac{2(\alpha\beta)^{\frac{\alpha+\beta}{2}}}{\Gamma(\alpha)\Gamma(\beta)} P_r^{\frac{\alpha+\beta}{2}-1} K_{\alpha-\beta}(2\sqrt{\alpha\beta P_r}) dP_r \right] d\theta. \quad (7.12)$$

The unconditional SEP (7.12) is derived for the uncoded 8-POLSK modulated FSO communication systems operating over the gamma-gamma turbulence channel. The unconditional SEP expression is the tool for the derivation of upper bounds on the error probability of the coded 8-POLSK communication system.

7.1.3 Maximum Likelihood Sequence Detection

In this section the performance of the 8-POLSK modulated FSO system with coherent detection operating over the gamma-gamma atmospheric turbulence channel is evaluated. For this purpose, the performance improvement by the error control coding and the spatial diversity will be also considered. However, the code should be short and simple in order to keep the complexity of this approach reasonably low.

The union upper bound on the average SEP with uniform error probability codes can be found as [157, 227]:

$$P_b \leq \frac{1}{\pi} \int_0^{\pi/2} \left[\frac{1}{k} \frac{\partial}{\partial \mathcal{M}} T(D(\theta), \mathcal{M})|_{\mathcal{M}=1} \right] d\theta. \quad (7.13)$$

where \mathcal{M} is an indicator taking into account the number of bits in error, $k = 1$ is the number of information bits per transmission, the transfer function $T(D(\theta), \mathcal{M})$ is in conjunction with the particular state diagram of a coded modulation, and $D(\theta)$ depends on the derived SEP. Here we have applied a convolutional code with the rate of $1/3$ ($k = 1$) and the constraint length of 3, as illustrated in Fig. 7-2 [203]. The function generators of the convolutional encoder are given as $g_1 = [100]$, $g_2 = [101]$ and $g_3 = [111]$.

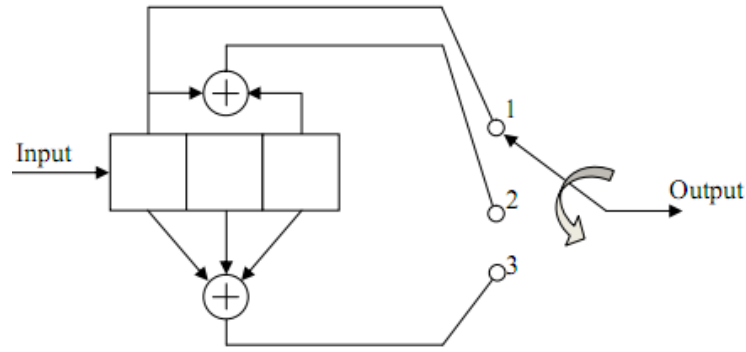


Fig. 7-2: Convolutional encoder.

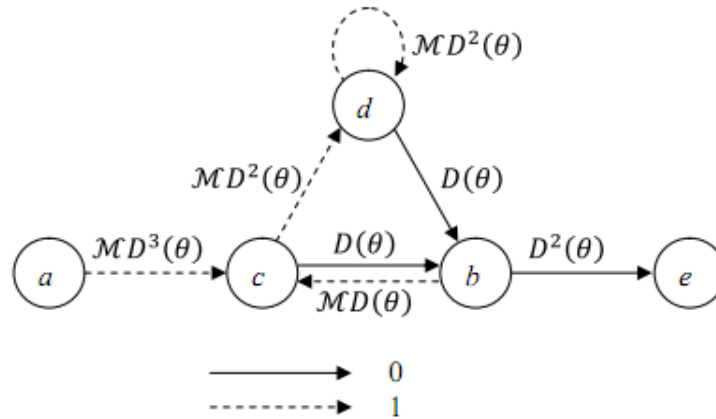


Fig. 7-3: State diagram for rate $1/3$ ($k = 1$) convolutional encoder.

The state diagram is shown in Fig. 7-3. It is important to demonstrate the method for obtaining the distance prosperities of a convolutional code. In Fig. 7-3, the branches of the state diagram are labelled as either $\{D^0, D^1, D^2, D^3\}$, where the exponent of D denotes the Hamming distance between the sequence of output bits corresponding to each branch and the sequence of output bits corresponding to the all-zero branch.

The four state equations derived from Fig. 7-3 are:

$$X_c = \mathcal{M}D^3(\theta)X_a + \mathcal{M}D(\theta)X_b, \quad (7.14a)$$

$$X_b = D(\theta)X_c + D(\theta)X_d, \quad (7.14b)$$

$$X_d = \mathcal{M}D^2(\theta)X_c + \mathcal{M}D^2(\theta)X_d, \quad (7.14c)$$

$$X_e = D^2(\theta)X_b, \quad (7.14d)$$

where $D(\theta)$ is defined based on the underlying SEP expression (7.12).

The transfer function is obtained by solving these equations for the ratio X_e/X_a :

$$T(D(\theta), \mathcal{M}) = \frac{D^6(\theta)\mathcal{M}}{1 - 2\mathcal{M}D^2(\theta)}. \quad (7.15)$$

Using (7.13) and (7.15), the SEP is thus obtained as:

$$P_b \leq \frac{7}{4\pi} \int_0^{\pi/2} \frac{D^6(\theta)}{(1 - 2D^2(\theta))^2} d\theta. \quad (7.16)$$

In this work, using the integrand of SEP expression given by (7.16), the approximation

$D(\theta)$ formula for the channels under consideration is:

$$D(\theta) = \int_0^\infty \exp\left(\frac{-3\gamma_{av}(P_r)}{22\sin^2\theta}\right) \frac{2(\alpha\beta)^{\frac{\alpha+\beta}{2}}}{\Gamma(\alpha)\Gamma(\beta)} P_r^{\frac{\alpha+\beta}{2}-1} K_{\alpha-\beta}(2\sqrt{\alpha\beta P_r}) dP_r. \quad (7.17)$$

7.1.4 Receiver Diversity Technique

Only MRC spatial diversity techniques are considered in this paper as the MRC linear combiner results in a maximum-likelihood receiver structure [227], which is optimal regardless of the fading statistics. The results for other linear combining techniques can also be obtained in a similar manner. Given Fig. 6-1, for a background noise limited FSO link, the variance of the overall Gaussian noise with a zero mean becomes:

$$\sigma_T^2 = \frac{1}{\mathcal{N}} \sum_{i=1}^{\mathcal{N}} G_i^2 \sigma_n^2. \quad (7.18)$$

The individual received optical signal is given as:

$$\vec{E}_{ri}(t) = \sqrt{\frac{P_{ri}}{2}} e^{i(\omega t + \varphi_r(t))} \{ \varepsilon e^{j\beta} \cdot \vec{x} + \vec{y} \}. \quad (7.19)$$

The outputs electric currents $\{c_{xbi}(t), c_{ybi}(t)\}$ from the combiner are given as:

$$c_{xbi}(t) = \frac{\Re}{\mathcal{N}} \sum_{i=1}^{\mathcal{N}} G_i \varepsilon \sqrt{\frac{P_{ri} P_{lo}}{2}} \cos(\omega_{IF} t + \beta + \varphi_{IF}(t)) + \sum_{i=1}^{\mathcal{N}} G_i n_{xi}(t), \quad (7.20a)$$

$$c_{ybi}(t) = \frac{\Re}{\mathcal{N}} \sum_{i=1}^{\mathcal{N}} G_i \sqrt{\frac{P_{ri} P_{lo}}{2}} \cos(\omega_{IF} t + \varphi_{IF}(t)) + \sum_{i=1}^{\mathcal{N}} G_i n_{yi}(t). \quad (7.20b)$$

The optimum post detection electrical SNR $r_{\text{MRC}}(\vec{P}_r)$ at the 8-POLSK demodulator input becomes:

$$r_{\text{MRC}}(\vec{P}_r) = \frac{\Re^2 P_{lo} (\sum_{i=1}^{\mathcal{N}} G_i \sqrt{P_{avi}})^2}{2\mathcal{N} \sum_{i=1}^{\mathcal{N}} G_i^2 \sigma_n^2}, \quad (7.21)$$

where $\vec{P}_r = \sum_{i=1}^{\mathcal{N}} P_{ri}$. All the received optical power is assumed to be independent and obey the gamma-gamma distribution. The received power level on every branch has to be estimated prior to the coherent summation.

The gain factor $\{G_i\}_{i=1}^{\mathcal{N}}$ is proportional to the received optical power. The overall noise is AWGN with a zero mean and variance σ_T^2 . Applying the Cauchy inequality [1, 217],

$(\sum_{i=1}^{\mathcal{N}} G_i \sqrt{P_{avi}})^2 \leq (\sum_{i=1}^{\mathcal{N}} G_i^2)(\sum_{i=1}^{\mathcal{N}} P_{avi})$, the $r_{\text{MRC}}(\vec{P}_r)$ is derived as:

$$\begin{aligned} \gamma_{\text{MRC}}(\vec{P}_r) &\leq \frac{\Re^2 P_{lo} (\sum_{i=1}^{\mathcal{N}} G_i^2) (\sum_{i=1}^{\mathcal{N}} P_{avi})}{2\mathcal{N} \sigma_n^2 \sum_{i=1}^{\mathcal{N}} G_i^2}, \\ &= \frac{\Re^2 P_{lo}}{\mathcal{N}} \left(\sum_{i=1}^{\mathcal{N}} \frac{P_{avi}}{2\sigma_n^2} \right) = \frac{1}{\mathcal{N}} \left(\sum_{i=1}^{\mathcal{N}} \gamma_{avi}(P_r) \right). \end{aligned} \quad (7.22)$$

Assuming that all the received optical power is independent and all obey the gamma-gamma distribution, therefore $p(\vec{P}_r)$ represents the joint PDF for \mathcal{N} -photodetector receiving uncorrelated signals, and is expressed as:

$$p(\vec{P}_r) = \prod_{i=1}^{\mathcal{N}} \int p(P_{ri}) dP_{ri}. \quad (7.23)$$

The system performance of the coded 8-POLSK FSO communication system operating over the gamma-gamma turbulence channel can thus be evaluated from (7.22) and (7.23) using the numerical integration since the resulting expression has no closed form.

Therefore, the unconditional SEP is derived as:

$$\begin{aligned} P_{e\text{MRC}}(\vec{P}_r) &= \frac{4}{7\pi} \int_0^{\pi/2} \left[\int_0^{\infty} \exp\left(\frac{-3\gamma_{\text{MRC}}(\vec{P}_r)}{22\sin^2\theta}\right) \frac{2(\alpha\beta)^{\frac{\alpha+\beta}{2}}}{\Gamma(\alpha)\Gamma(\beta)} \vec{P}_r^{\frac{\alpha+\beta}{2}-1} K_{\alpha-\beta}\left(2\sqrt{\alpha\beta\vec{P}_r}\right) d\vec{P}_r \right] d\theta. \end{aligned} \quad (7.24)$$

7.1.5 Results and Discussion

For the purpose of like-to-like comparison, the average optical signal power $E[\Re P_r P_{lo}]$ is normalized to unity. The values of α and β at any given regimes are previously presented

in Table 5.1. The SEP results in Fig. 7-4 are computed based on (5.40), (7.12) and (7.16) to allow comparisons of the performances of the uncoded and coded 8-POLSK as well as the BPOLSK scheme in the turbulence channel. The coded 8-POLSK and uncoded BPOLSK schemes have the same spectral efficiency of 1bit/symbol, for the uncoded and coded 8-POLSK, respectively. The performance of the convolutional coded 8-POLSK is made evident from Fig. 7-4. Compared with the BPOLSK scheme, the SEP performances deteriorate rapidly for the uncoded 8-POLSK scheme for all FSO scenarios under investigation. However, as revealed by the results under all turbulence assumptions, increasing SNR results in a relatively smaller change in the slope of SEP curves for the uncoded 8-POLSK scheme.

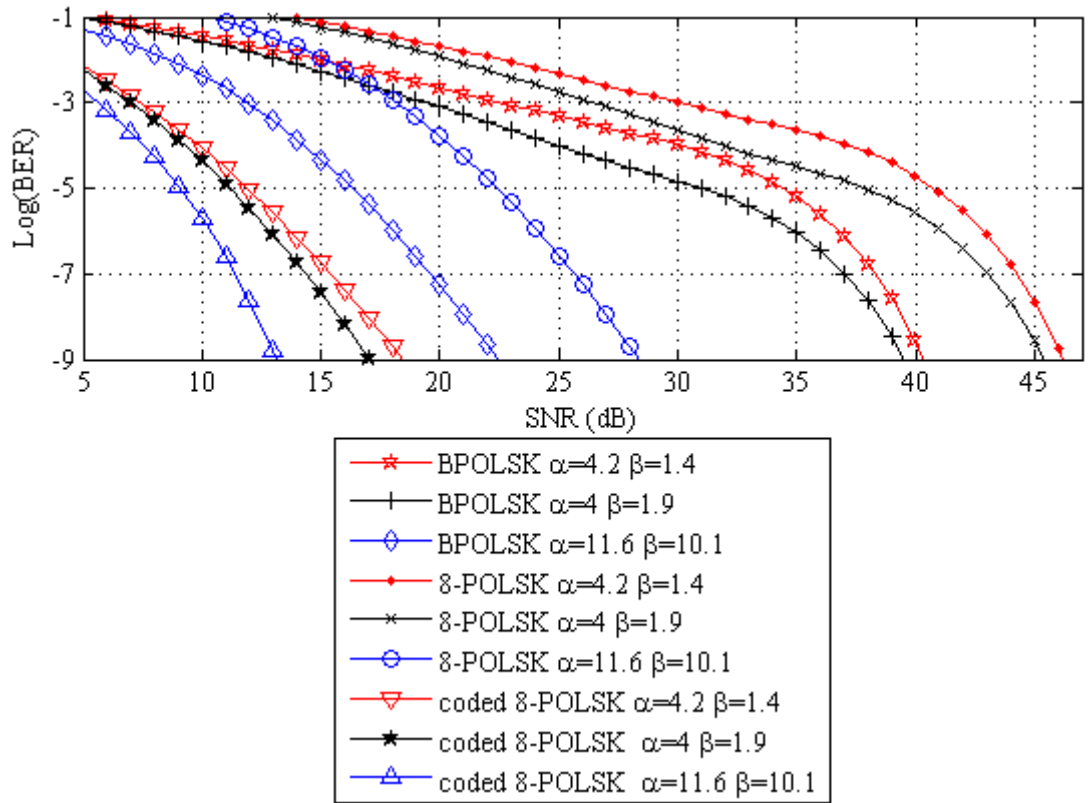


Fig. 7-4: Comparisons of SEP performances of coded 8-POLSK and uncoded BPOLSK (5.40), (7.13), (7.17) and (7.18) against the normalized electric SNR $E[\mathcal{R}P_r P_{l_o}] = 1$ in various turbulence levels.

The reduction in SNR for the coded 8-POLSK is achieved by the use of convolutional code in mitigating the effect of turbulence induced irradiance fluctuation. For example, to achieve a SEP of 10^{-9} , the SNR requirements are ~ 28.5 dB and ~ 13 dB for uncoded and coded 8-POLSK schemes, respectively in a weak turbulence regime. To achieve the same SEP performance in a moderate turbulence regime, the SNR increases to ~ 45.5 dB and ~ 17 dB, respectively. The coded 8-POLSK yields a very good SEP performance, which is achieved without the requirement of bandwidth expansion. It is not practical and even not feasible for many applications to increase the power margin in the link budget in order to eliminate the deep fades observed under turbulence. This motivates the employment of powerful scintillation-mitigation techniques, such as coding and/or diversity techniques.

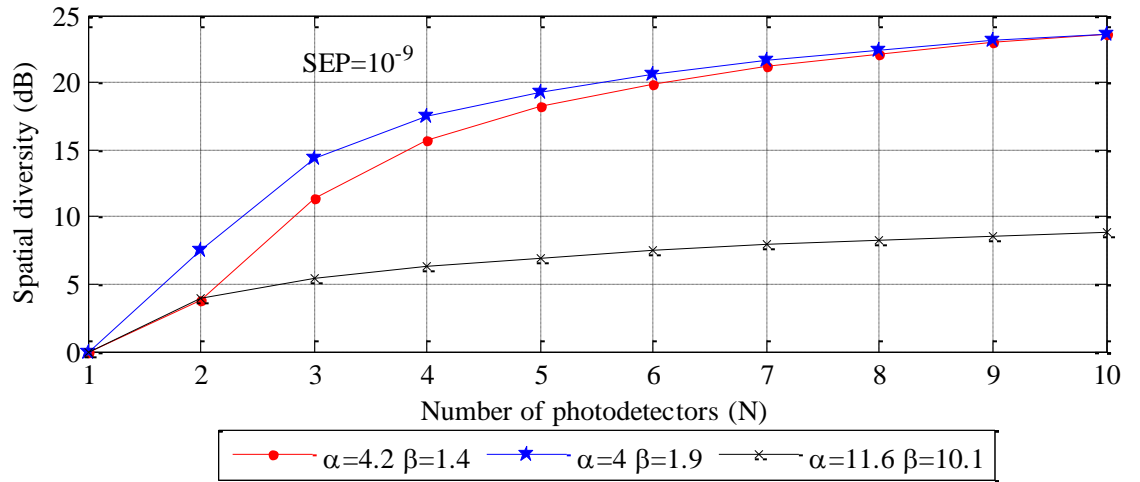


Fig. 7-5: Power gain for the 8-POLSK scheme employing MRC technique to achieve a SEP of 10^{-9} against the number of detectors with the normalized electric SNR $E[\mathcal{R}P_r P_{l_o}] = 1$ under all turbulence scenarios from weak to strong regimes.

Using (7.24) the spatial diversity gain $m_{\mathcal{N}, \sigma_l} = \gamma_{1, \sigma_l} - \gamma_{\mathcal{N}, \sigma_l}$ to achieve a SEP of 10^{-9} for the MRC technique is depicted in Fig. 7-5. The MRC technique ($\mathcal{N} = 4$) outperforms the

single receiver by ~ 6 dB, ~ 17.5 dB and ~ 15.5 dB, respectively in weak, moderate and strong turbulence regimes, respectively. The spatial diversity gain is more in the moderate turbulence regime than in the strong regime. This is because of the deep fades resulting from a loss of spatial coherence of the laser radiation. The gain reaches up to ~ 24 dB when ten detectors are used in a strong turbulence regime. The gain is higher in moderate and strong fading conditions since adding more detectors will efficiently reduce the chance of a catastrophic fading.

Another observation from Fig. 7-5 is that as the number of detectors (\mathcal{N}) increases, the spatial diversity gain starts to flatten out. For example, increasing the number of detectors from four to five only achieves ~ 1 dB, ~ 2 dB and ~ 2.5 dB more in $\gamma_{\mathcal{N},\sigma_l}$ from weak to strong turbulence regimes, respectively. Thus, the optimum number of the detectors is $2 \leq \mathcal{N} \leq 4$. As a consequence, the power gain is achieved with a rise in the system complexity and cost, thus the trade off between performance and cost. For applications where 100% link availability is a must, then employing larger number of photodetectors would be advantageous.

7.2 Coherent Heterodyne MPOLSK System

7.2.1 System Configuration

The schematic diagram of the MPOLSK optical coherent heterodyne transmitter is illustrated in Fig. 7-6(a). The laser beam is linearly polarised at an angle of $\pi/4$ with

respect to the transmitter reference axis. The linearly polarised beam is then launched into a PBS, which yields horizontal (\vec{x} -polarisation) and vertical (\vec{y} -polarisation) SOPs with equal amplitude and zero phase differences. Both orthogonally polarised components are amplitude and phase modulated synchronously before being fed into the PBC.

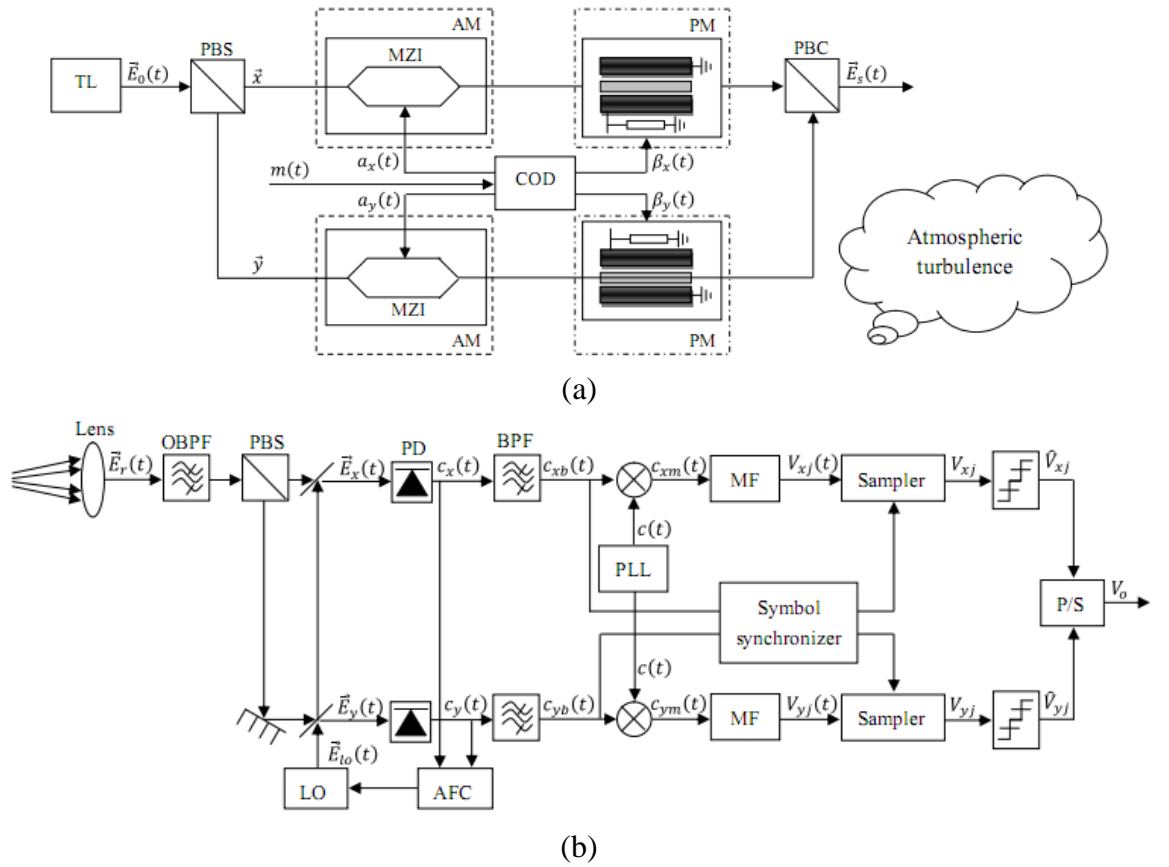


Fig. 7-6: Block diagram of the MPOLSK coherent heterodyne optical communication system: (a) the transmitter, and (b) the receiver. COD (encoder), P/S (parallel to serial converter).

The emitted optical field $\vec{E}_s(t)$ is thus given as:

$$\vec{E}_s(t) = \sqrt{\frac{P_t}{2}} e^{i(\omega t + \varphi(t))} \{a_x(t) e^{i\beta_x(t)} \cdot \vec{x} + i a_y(t) e^{-i\beta_y(t)} \cdot \vec{y}\}. \quad (7.25)$$

The modulation functions $a_x(t)$, $a_y(t)$, $\beta_x(t)$ and $\beta_y(t)$ are given by:

$$a_x(t) \cos(\beta_x(t)) = (2^{\ell} - 2^{\ell-1} - 1)d, \quad (7.26a)$$

$$a_y(t) \cos(\beta_y(t)) = (2^{\ell} - 2^{\ell-1} - 1)d, \quad (7.26b)$$

where ℓ is a positive integer and $\ell \in [1, M/2]$. The parameter d is half the distance between the adjacent symbols in one polarisation axis and M is the number of signal-points in the constellation. The PM functions $\beta_x(t), \beta_y(t) = [0, \pi]$ correspond to the transmission of a space and mark, respectively.

The proposed MPOLSK modulation format can be described as a two-dimensional multilevel AM in the orthogonal polarisation axes, such as $M = 2^{\ell+1}$. The transmitted field is constant over the symbol interval and each symbol is associated with a value of the optical field. The instantaneous transitions between the subsequent symbol intervals are assumed. The block diagram of the MPOLSK coherent heterodyne receiver is shown in Fig. 7-6(b). The background noise is limited by an ideal OBPF with a narrow bandwidth typically 1 nm. The received optical signal $\vec{E}_r(t)$ is expressed in the following form:

$$\vec{E}_r(t) = \sqrt{\frac{P_r}{2}} e^{i(\omega t + \varphi_r(t))} \{a_x(t) e^{i\beta_x(t)} \cdot \vec{x} + i a_y(t) e^{-i\beta_y(t)} \cdot \vec{y}\}, \quad (7.27)$$

where P_r and $\varphi_r(t)$ are the received optical power and phase noise of the laser carrier propagating through the atmospheric turbulence medium, respectively. Both parameters are time-variant statistical quantities due to the turbulence.

The electrical field of $\vec{E}_r(t)$ is split into \vec{x} and \vec{y} axes, which is then combined with the electrical field in \vec{x} and \vec{y} axes of LO. Thus, the optical fields $\vec{E}_x(t)$ and $\vec{E}_y(t)$ are given as:

$$\vec{E}_x(t) = \left\{ \sqrt{\frac{P_r}{2}} a_x(t) e^{i(\omega t + \beta_x(t) + \varphi_r(t))} + \frac{\sqrt{P_{lo}}}{2} e^{i(\omega_{lo} t + \varphi_{lo}(t))} \right\} \cdot \vec{x}, \quad (7.28a)$$

$$\vec{E}_y(t) = \left\{ \sqrt{\frac{P_r}{2}} a_y(t) e^{i(\omega t + \beta_y(t) - \frac{\pi}{2} + \varphi_r(t))} + \frac{\sqrt{P_{lo}}}{2} e^{i(\omega_{lo} t + \varphi_{lo}(t))} \right\} \cdot \vec{y}. \quad (7.28b)$$

After passing through two identical photo-detectors and electrical BPFs, the constant terms are filtered out and the additive noise is limited. BPFs are assumed to be ideal only passing IF signals without any distortions. The bandwidth and center frequency of BPFs are $B_{bp} = 2(R_s + k_F B_L)$ and ω_{IF} , respectively.

Electrical currents on \vec{x} and \vec{y} channels after BPFs are expressed as:

$$c_x(t) = \Re \sqrt{P_r P_{lo} / 2} a_x \cos(\beta_x(t)) \cos(\omega_{IF} t + \varphi_{IF}(t)) + n_x(t), \quad (7.29a)$$

$$c_y(t) = \Re \sqrt{P_r P_{lo} / 2} a_y \cos(\beta_y(t)) \sin(\omega_{IF} t + \varphi_{IF}(t)) + n_y(t). \quad (7.29b)$$

where $\omega_{IF} = \omega - \omega_{lo}$ and $\varphi_{IF}(t) = \varphi_r(t) - \varphi_{lo}(t)$ are the IF and phase noise, respectively. Note that $\sin(\beta_x(t), \beta_y(t)) = 0$ as $\{\beta_x(t), \beta_y(t)\} = \{0, \pi\}$. The noise terms $n_x(t)$ and $n_y(t)$ are assumed to be statistically independent and stationary AWGN with zero-mean and equal variance σ_n^2 . Assuming that the BPF filter bandwidth is larger than the IF linewidth to avoid the phase noise to the amplitude noise conversion, and also the square-law elements/multipliers being ideal the phase noise due to the laser LO source can be considered negligible.

The electric signals $c_x(t)$ and $c_y(t)$ are then multiplied with the local carrier signal $c_c(t)$ and $c_s(t)$ generated by the Costas-loop based PLL circuit:

$$c_c(t) = \cos(\omega_{IF}t + \varphi_{PLL}(t)), \quad (7.30a)$$

$$c_s(t) = \sin(\omega_{IF}t + \varphi_{PLL}(t)), \quad (7.30b)$$

where $\varphi_{PLL}(t)$ represents the estimation of $\varphi_{IF}(t)$.

The outputs of the mixers are passed through the identical MF to reject higher frequency components, with $V_{xj}(t)$ and $V_{yj}(t)$ expressed as:

$$\begin{aligned} V_{xj}(t) &= \int_0^T [c_x(t) \cdot c_c(t)] dt, \\ &= \Re\sqrt{P_r P_{lo}/2} a_x \cos(\beta_x(t)) \cos[\Delta\varphi(t)] + n'_x(t), \end{aligned} \quad (7.31a)$$

$$\begin{aligned} V_{yj}(t) &= \int_0^T [c_y(t) \cdot c_s(t)] dt, \\ &= \Re\sqrt{P_r P_{lo}/2} a_y \cos(\beta_y(t)) \cos[\Delta\varphi(t)] + n'_y(t), \end{aligned} \quad (7.31b)$$

where $\Delta\varphi(t) = \varphi_{IF}(t) - \varphi_{PLL}(t)$ is the phase tracking error.

Subsequently $V_{xj}(t)$ and $V_{yj}(t)$ are passed through a sampler at a sampling time $t = T$,

where T is the symbol period. The outputs are given by:

$$V_{xj} = \pm \Re\sqrt{P_r P_{lo}/2} a_x \cos(\Delta\varphi) + n'_x, \quad (7.32a)$$

$$V_{yj} = \pm \Re\sqrt{P_r P_{lo}/2} a_y \cos(\Delta\varphi) + n'_y, \quad (7.32b)$$

where $(n'_x, n'_y) \sim N(0, \sigma_n^2)$. The plus sign in \pm denotes the transmission of a space, and the minus sign represents a mark.

7.2.2 Symbol Error Probability with Ideal PLL

Since the structure of the MPOLSK receiver consists of two identical branches, the same expression for the SEP for a single-branch (\vec{x} -axis) also holds for the other branch. To determine the error probability for multilevel AM signals for a single-branch, the decision rule has to maximise the correlation metrics. In other words the decision must be made by comparing \hat{V}_{xj} with different threshold levels and selecting the amplitude level. Firstly, by assuming the phase tracking error $\Delta\varphi = 0$, the demodulation output is given as:

$$V_{xj} = \pm \Re \sqrt{P_r P_{lo}/2} a_x + n'_x, \quad (7.33)$$

where the noise variable $n'_x \sim (0, \sigma_n^2)$.

The average power per bit can be expressed as:

$$P_{av} = \frac{d^2 \Re^2 P_r P_{lo}}{2^{\ell} \cdot 2^{\ell}} \sum_{\ell=1}^{M/2} (2^{\ell} - 2^{\ell-1} - 1)^2 = \frac{d^2 \Re^2 P_r P_{lo}}{6^{\ell}} (2^{2\ell} - 1). \quad (7.34)$$

The assumption is that all amplitude levels are equally likely a priori. Thus, an error is detected when n'_x exceeds one-half of the distance between adjacent amplitude levels.

Therefore, the SEP is expressed as:

$$\begin{aligned} P_{ec} &= \left(\frac{2^{\ell} - 1}{2^{\ell}} \right) P \left(|n'_x| > \sqrt{\frac{d^2 \Re^2 P_r P_{lo}}{2}} \right) = \frac{2^{\ell} - 1}{2^{\ell-1}} \frac{1}{\sqrt{2\pi\sigma_n^2}} \int_{\sqrt{d^2 \Re^2 P_r P_{lo}/2}}^{\infty} e^{-x^2/2\sigma_n^2} dx, \\ &= \frac{2^{\ell} - 1}{2^{\ell-1}} \frac{1}{\sqrt{2\pi}} \int_{\sqrt{d^2 \Re^2 P_r P_{lo}/2\sigma_n^2}}^{\infty} e^{-x^2/2} dx = \frac{2^{\ell} - 1}{2^{\ell-2}} \operatorname{erfc} \left(\sqrt{\frac{d^2 \Re^2 P_r P_{lo}}{4\sigma_n^2}} \right). \end{aligned} \quad (7.35)$$

The SEP expressed in (7.35) can also be expressed in terms of the average power per bit, which is:

$$P_{ec} = \frac{2^k - 1}{2^{k-2}} \operatorname{erfc} \left(\sqrt{\frac{3kP_{av}}{2\sigma_n^2(2^{2k} - 1)}} \right) = \frac{2^k - 1}{2^{k-2}} \operatorname{erfc} \left(\sqrt{\frac{3k\gamma}{2^{2k} - 1}} \right). \quad (7.36)$$

The average electrical SNR per bit at the output of the demodulator is defined as $\gamma = P_{av}/2\sigma_n^2$. Thus, the SEP after the P/S converter can be approximately expressed as:

$$P_{P/S} = 1 - (1 - P_{ec})^2 \approx \frac{2^k - 1}{2^{k-3}} \operatorname{erfc} \left(\sqrt{\frac{3k\gamma}{2^{2k} - 1}} \right). \quad (7.37)$$

7.2.3 Performance Degradation due to Phase Tracking Error and

Atmosphere Turbulence

In this section we show further analysis on the impact of the phase tracking error $\Delta\varphi$ on the receiver performance. We have assumed that PLL can adequately track the phase changes due to the atmospheric turbulence and any phase error generated is solely due to the PLL. The phase tracking error not only introduces a power penalty at the receiver but also contributes to the minimum error probability, which is independent of the received optical power. Following the same procedures in section 7.2.2, $\Delta\varphi$ reduces the power level by a factor of $\cos(\Delta\varphi)$ [203]. An exact analysis based on the nonlinear PLL is mathematically tractable [203].

Under the hypothesis of a constant PLL tracking error within T , the error probability can thus be evaluated as [203]:

$$P_{PLL} = \int_0^{2\pi} \frac{2^{\ell} - 1}{2^{\ell-3}} \operatorname{erfc} \left(\sqrt{\frac{3\ell\gamma}{2^{2\ell} - 1} \cos^2(\Delta\varphi)} \right) \frac{e^{r_l \cos(\Delta\varphi)}}{2\pi I_0(r_l)} d\Delta\varphi, \quad (7.38)$$

where $I_0(\cdot)$ is the zeroth-order modified Bessel function. $\gamma_l = 1/\sigma_\Delta^2$ is the SNR of the PLL, and σ_Δ^2 is the phase noise variance. The integral in (7.38) provides the performance in the presence of $\Delta\varphi$ and must be evaluated numerically. To show the impairments of scintillation effects we have adopted the approach given in [1, 197, 226]. The unconditional SEP in the presence of turbulence is given by averaging the conditional SEP over the channel statistics as given by (7.39):

$$P_e(P_r) = \int_0^{2\pi} \int_0^\infty \frac{2^{\ell} - 1}{2^{\ell-3}} \operatorname{erfc} \left(\sqrt{\frac{3\ell\gamma}{2^{2\ell} - 1} \cos^2(\Delta\varphi)} \right) \frac{e^{r_l \cos(\Delta\varphi)}}{2\pi I_0(r_l)} p(P_r) dP_r d\Delta\varphi, \quad (7.39)$$

where $p(P_r)$ is the PDF of the gamma-gamma turbulence model (3.23).

7.2.4 Receiver Diversity Techniques

Given Fig. 6-1, for a background noise limited FSO link, the variance of the overall Gaussian noise with a zero mean becomes:

$$\sigma_T^2 = \frac{1}{\mathcal{N}} \sum_{i=1}^{\mathcal{N}} G_i^2 \sigma_n^2, \quad (7.40)$$

where $i = 1, 2, 3, \dots, \mathcal{N}$.

The weighted electric currents after the BPFs are given as:

$$\begin{aligned} c_{xb}(t) = \Re \mathcal{N}^{-1} \sum_{i=1}^{\mathcal{N}} G_i \sqrt{P_{ri} P_{lo}/2} a_x(t) \cos(\beta_x(t)) \cos(\omega_{IF} t + \varphi_{IF}(t)) \\ + \sum_{i=1}^{\mathcal{N}} G_i n_{xi}(t), \end{aligned} \quad (7.41a)$$

$$c_{yb}(t) = \Re \mathcal{N}^{-1} \sum_{i=1}^{\mathcal{N}} G_i \sqrt{P_{ri} P_{lo}/2} a_y(t) \cos(\beta_y(t)) \cos(\omega_{IF} t + \varphi_{IF}(t)) + \sum_{i=1}^{\mathcal{N}} G_i n_{yi}(t). \quad (7.41b)$$

The optimum post detection electrical SNR γ_T at the MPOLSK demodulator output is:

$$\gamma_T(\vec{P}_r) = \frac{d^2 \Re^2 P_{lo} (2^{2k} - 1) (\sum_{i=1}^{\mathcal{N}} G_i \sqrt{P_{ri}})^2}{6k\mathcal{N} \sum_{i=1}^{\mathcal{N}} G_i^2 \sigma_n^2}. \quad (7.42)$$

The weight $\{G_i\}_{i=1}^{\mathcal{N}}$ is proportional to the received optical power on each branch using the MRC technique so that the power level has to be estimated before being coherently combined. By applying the Cauchy inequality [217] (7.42) becomes:

$$\begin{aligned} \gamma_{\text{MRC}}(\vec{P}_r) &\leq \frac{d^2 \Re^2 P_{lo} (2^{2k} - 1) (\sum_{i=1}^{\mathcal{N}} G_i \sigma_n^2) (\sum_{i=1}^{\mathcal{N}} P_{ri} / \sigma_n^2)}{6k\mathcal{N} \sum_{i=1}^{\mathcal{N}} G_i \sigma_n^2}, \\ &= \frac{1}{\mathcal{N}} \left(\sum_{i=1}^{\mathcal{N}} \gamma_i(P_r) \right). \end{aligned} \quad (7.43)$$

It is assumed that the independently received optical power obeys the gamma-gamma distribution. The joint PDF $p(\vec{P}_r)$ for \mathcal{N} -detector receiving uncorrelated signals is given by:

$$p(\vec{P}_r) = \prod_{i=1}^{\mathcal{N}} \int p(P_{ri}) dP_{ri}. \quad (7.44)$$

7.2.5 Results and Discussion

In order to show the effect of turbulence and the PPL phase tracking error on the receiver sensitivity, we will investigate the SEP metric for different channel conditions. The values of α and β at any given regimes are previously presented in Table 5.1. Fig. 7-7

shows the predicted SEP performances against the electrical SNR for 8, 16 and 32 MPOLSK. Also shown is the SEP of 8MPOLSK against SNR for different phase tracking error variances σ_Δ . As expected, the modulation with higher number of constellation requires a larger SNR to achieve the same SEP. For example, the SNR requirements to achieve a SEP of 10^{-9} for 8POLSK, 16POLSK and 32POLSK are ~ 16.7 dB, ~ 21 dB and ~ 26 dB, respectively.

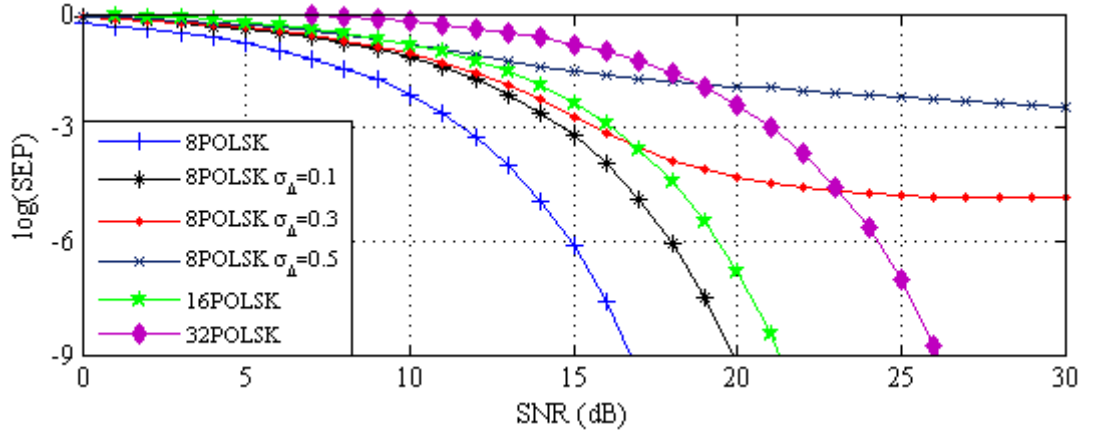


Fig. 7-7: SEP performances of 8POLSK (with the phase noise variance $\sigma_\Delta = [0.1, 0.3, 0.5]$), 16POLSK and 32POLSK schemes against the electrical SNR using a single detector in a non-turbulent channel.

The figure illustrates that MPOLSK is sensitive to phase tracking error and as phase tracking error increases, a high error floor is observed. The power penalty caused by the small phase tracking error variance $\sigma_\Delta \leq 0.1$ is ~ 3 dB. However, the error-floors of 1.3×10^{-5} and 3.4×10^{-3} are observed for $\sigma_\Delta = 0.3$ and 0.5 , respectively, which shows the high sensitivity of system to the phase tracking error. The SEP performance against the SNR for the 8POLSK, 16POLSK and 32POLSK modulation schemes using a single detector with an ideal PLL for all turbulence regimes are illustrated in Fig. 7-8.

The SNR requirement to achieve a fixed SEP increases as the turbulence level rises. It is observed that the power penalty due to the turbulence is almost identical for all levels. Electrical power penalties of ~ 7.5 dB, ~ 24.5 dB and ~ 25 dB are observed at SEP of 10^{-9} in weak, moderate and strong turbulence, respectively.

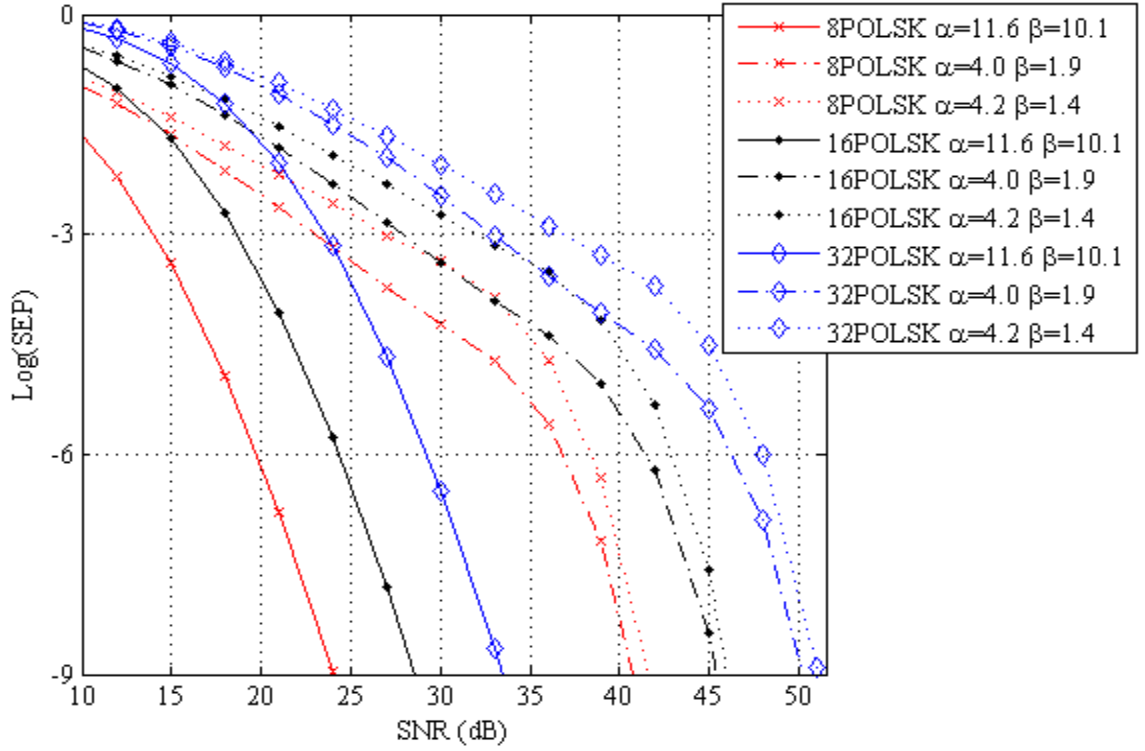


Fig. 7-8: The SEP performance of 8POLSK, 16POLSK and 32POLSK modulation schemes against the electrical SNR using a single detector and an ideal PLL in an atmospheric turbulence channel.

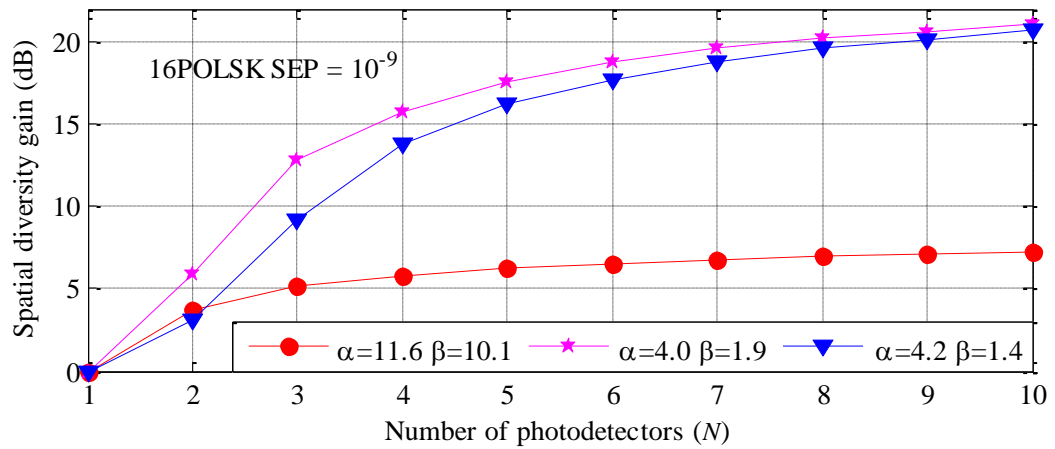


Fig. 7-9: The spatial diversity gain against the number of detector (N) for 16POLSK employing MRC in a turbulence channel to achieve a SEP of 10^{-9} .

Fig. 7-9 illustrates the spatial diversity gain $\gamma_{\mathcal{N},\sigma_l}$ against the number of photodetectors \mathcal{N} for 16POLSK using the MRC combining technique to achieve a SEP of 10^{-9} . For the same number of \mathcal{N} , the value of $\gamma_{\mathcal{N},\sigma_l}$ is the highest for the moderate turbulence regime followed by strong and weak turbulence regimes, respectively. The diversity gain in the strong turbulence regime is less than that in the moderate regime due to the fact that the deep fade results in a loss of spatial coherence of the laser radiation. There is a steep increment in $\gamma_{\mathcal{N},\sigma_l}$ for $2 \leq \mathcal{N} \leq 4$, which indicates optimum detectors number between two and four. For $\mathcal{N} > 4$, the diversity gain curves start to flatten out, reducing the gain per additional detector. When the receiver uses MRC technique with $\mathcal{N} = 4$ in weak, moderate and strong turbulence regimes, γ_{4,σ_l} are ~ 5.8 dB, ~ 15.8 dB and ~ 13.7 dB, respectively. Further increment in the diversity gain is observed for higher number of detectors with the maximum gain reaching ~ 21 dB at the moderate turbulence regime for $\mathcal{N} = 10$. This is because adding more detectors will efficiently reduce the chance of a catastrophic fading from happening, however at the cost of increased system complexity.

7.3 Summary

This chapter has outlined the theoretical analysis of two different coherent heterodyne MPOLSK-FSO communication systems operating over the gamma-gamma turbulence channel. To mitigate the turbulence induced fading the convolutional coding and the spatial diversity with the MRC technique have been applied. The upper SEP bound has been obtained using the transfer function. The SEP yields a very good performance, which is achieved without the need for increasing the SNR. For example, using the first

proposed coherent heterodyne 8-POLSK system to achieve a SEP of 10^{-9} in a weak turbulence regime, the SNR requirements are ~ 28.5 dB and ~ 13 dB for uncoded and coded 8-POLSK schemes, respectively. When the same system employs ten detectors, around 24 dB power gain is achievable in a strong turbulence regime. The spatial diversity with MRC technique ($\mathcal{N} = 4$) outperforms the uncoded 8-POLSK employing the single receiver by ~ 6 dB, ~ 17.5 dB and ~ 15.5 dB, respectively in weak, moderate and strong turbulence regimes. We also have shown that the spatial diversity offers increased link margin as the scintillation level rises.

For the second proposed MPOLSK-FSO system using PLL, the numerical analysis of SEP of 8, 16 and 32 POLSK was carried with the PLL phase tracking error showing the sensitivity of MPOLSK to the phase error. The comparative studies showed the power penalties of ~ 7.5 dB, ~ 24.5 dB and ~ 25 dB at SEP of 10^{-9} in weak, moderate and strong turbulence regimes, respectively. The MPOLSK receiver combined with the MRC technique offered improved error probability performance in turbulence conditions with the optimum number of detectors in the range of two to four. For the spatial diversity scheme with four detectors, diversity gains achieved were ~ 5.8 dB, ~ 15.8 dB and ~ 13.7 dB for 16POLSK in weak, moderate and strong turbulence regimes, respectively.

Chapter Eight

The Link Budget Analysis

In establishing a communication link an important issue is the link *power budget*, including the transmitter's power and all power losses experienced by the propagating optical beam. Losses encountered in an FSO link include the atmospheric channel loss, the geometric loss, the pointing loss and the optical loss caused by the imperfect optical elements (such as the lenses and mirrors). Other losses due to the component replacement or component ageing are also considered in the inclusion of link margin. The remaining power at the receiver largely determines the possible data transmission rate, which is influenced by the data format, the acceptable BER and various noise sources. The noise sources include the laser noise, the amplifier noise, excess noise in the receiver (e.g. Avalanche photo diode) and the background light.

The latter can readily suppressed with additional narrow-band optical filters, since the optical bandwidth of the laser is limited, whereas the background light frequency spectrum is usually very broad. To estimate the theoretical power limited link range of a terrestrial FSO system, receiver sensitivity will be determined based on the BER metric. The losses encountered while the laser beam propagating through the terrestrial channel will be examined in Section 8.1. Other losses due to the beam diverging, optical components, windows and pointing will be discussed in Section 8.2 and 8.3, respectively. The link budget equation will be derived in Section 8.4. And finally, the content in this chapter will be summarised in Section 8.5.

8.1 Atmospheric Transmission

The atmospheric transmittance at wavelength λ is described by the Beer-Lambert's law as [70, 130, 154]:

$$\tau(\lambda, L) = \frac{P_r}{P_t} = \exp[-\beta_T(\lambda)L], \quad (8.1)$$

where L is the transmission link (m), and $\beta_T(\lambda)$ is the attenuation coefficient, also called the extinction coefficient. $\beta_T(\lambda)$ is the sum of the absorption and scattering coefficients and is expressed as [36, 70, 129]:

$$\beta_T(\lambda) = \alpha_a(\lambda) + \beta_s(\lambda), \quad (8.2)$$

where $\alpha_a(\lambda)$ and $\beta_s(\lambda)$ are the absorption and the scattering coefficients, respectively. Since absorption is wavelength dependent and wavelengths used are based on the atmospheric transmission windows, the dominated factor in $\beta_T(\lambda)$ is the scattering and $\beta_T(\lambda) \cong \beta_s(\lambda)$.

Atmospheric scattering depends on the radius r of the particles present within the transmission channel. Considering the size parameter $X_0 = 2\pi r/\lambda$, the atmospheric scattering, when $X_0 \ll 1$, is known as the Rayleigh scattering [70, 228]; when $X_0 \approx 1$, it is referred to as the Mie scattering; and when $X_0 \gg 1$, it is best explained using diffraction theory (geometric optics). Various types of scatters encountered in the atmospheric channel are summarized in Table 8.1.

Table 8.1: Atmospheric scatters with their radius and the scattering process at $\lambda = 850$ nm [1].

Type	Radius (μm)	Size parameter X_0	Scattering process
Air molecules	0.0001	0.00074	Rayleigh
Haze particle	0.01 – 1	0.074 – 7.4	Rayleigh – Mie
Fog droplet	1 – 20	7.4 – 147.8	Mie – Geometrical
Rain	100 – 10000	740 – 74000	Geometrical
Snow	1000 – 5000	7400 – 37000	Geometrical
Hail	5000 – 50000	37000 – 370000	Geometrical

8.1.1 Rayleigh Scattering

Rayleigh scattering is the domain factor at lower wavelengths, which is caused by molecular size particles [70, 71, 136]. The attenuation coefficient $\beta_{\text{Rayleigh}}(\lambda)$ caused by the Rayleigh scattering is given by [34, 69, 139]:

$$\beta_{\text{Rayleigh}}(\lambda) = 0.827 N_p A_p^3 \lambda^{-4}, \quad (8.3)$$

where N_p represents the number of particles per unit volume in the transmission link, A_p denotes the cross-sectional area of a scattering particle and λ is the carrier wavelength [34, 139]. As the wavelength band of interest in FSO systems is between $0.5 \mu m$ to $2 \mu m$ and $\beta_{\text{Rayleigh}}(\lambda)$ is inversely proportional to λ^4 from (8.3), the Mie scattering is much stronger than the Rayleigh scattering in most practical cases [34, 138, 139].

8.1.2 Mie Scattering

Since the fog particles size is comparable to the propagating optical wavelength of interest in FSO systems ($0.5 \mu\text{m} - 2 \mu\text{m}$), this makes fog the major photo scattering particle and therefore Mie scattering becomes the dominant scattering process. The optical power loss due to the Mie scattering is high compared with to rain and snow induced losses. For a rainfall of 2.5 cm/hour a typical attenuation recorded is $\sim 6 \text{ dB/km}$ [1, 130, 229]. A light snow to blizzard will results in an attenuation of 3 dB/km to 30 dB/km , which is high compared to the rain [1, 71]. However, the link attenuation as high as 480 dB/km in the case of dense maritime fog conditions [230] and 130 dB/km in moderate fog conditions have been reported [231]. This level of attenuation certainly results in complete link failure or reduced link range to a few meters [232].

Mie scattering can be described as [138, 233]:

$$\beta_s(\lambda) = \frac{3.91}{V} \left[\frac{\lambda}{550} \right]^{-\delta}, \quad (8.4)$$

where V (km) represents the visibility range. It is defined as the distance that the parallel luminous beam propagates through the atmosphere channel until the optical intensity drops to 2% of its peak value. V can be therefore expressed in terms of $\beta_T(\lambda)$ and transmittance threshold \mathcal{T}_{th} as:

$$V = \frac{10 \log(\mathcal{T}_{th})}{\beta_T(\lambda)}. \quad (8.5)$$

The value of the \mathcal{T}_{th} of the atmospheric propagation path varies from 0.0077 to 0.06.

Widely used values of \mathcal{T}_{th} is 2% [234].

The parameter δ can be described by the well known Kim and/or Kruse models for a range of visibility given by (8.6) and (8.7), respectively [233, 235]:

$$\delta_{Kim} = \begin{cases} 1.6 & V > 50, \\ 1.3 & 6 < V < 50, \\ 0.16V + 0.34 & 1 < V < 6, \\ V - 0.5 & 0.5 < V < 1, \\ 0 & V < 0.5, \end{cases} \quad (8.6)$$

$$\delta_{Kruse} = \begin{cases} 1.6 & V > 50, \\ 1.3 & 6 < V < 50, \\ 0.585V^{1/3} & V < 6, \end{cases} \quad (8.7)$$

In the Kim model the fog attenuation is independent of the wavelength for $V < 500$ m.

The Kruse model was developed to take into account the wavelength effect.

The atmospheric transmission loss L_{Atmosp} is given as:

$$L_{Atmosp} = -10\log[e^{-\beta_s(\lambda)L}] = 4.343\beta_s(\lambda)L. \quad (8.8)$$

8.2 Beam Diverging Loss

One of the key advantageous of FSO links compared to the RF technology is its inherent security due to a very narrow propagating optical beam, which makes intrusion and detection more difficult. However, there is a down side with this and that is the beam will spread out as it propagates along the channel and only a fraction of the transmitted optical power can be collected at the receiver, thus the term beam divergence loss. A typical FSO communication link is shown in Fig. 8-1. Of course, high directionality is the best option, but it requires high precision in the alignment of the transmitter and receiver. The FSO links with an automatic tracking system are now commonly used for outdoor applications to ensure perfect alignment.

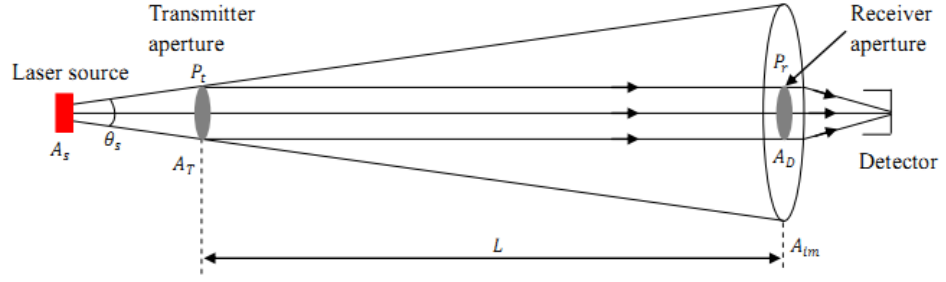


Fig. 8-1: AN FSO link showing beam divergence.

For a laser source, which is non-diffuse and small, the size of the received optical power is related to the diffraction at the transmitter aperture. As shown in Fig. 8-1, the ratio of the received power to the transmitted power is expressed as [1, 69]:

$$\frac{P_r}{P_t} = \frac{A_D}{A_{im}} = \frac{d_R^2}{(d_T + \theta_s L)^2}, \quad (8.9)$$

where d_T and d_R are the diameters of the transmitter and receiver, respectively. A_{im} is the size of the diffraction pattern, L is the link range, θ_s is the optical source divergence angle. A_T , A_D and A_s represent the aperture areas of the transmitter, receiver and the source, respectively.

The geometric loss L_{Geom} in dB is therefore obtained as:

$$L_{Geom} = -20 \log \left[\frac{d_R}{d_T + \theta_s L} \right]. \quad (8.10)$$

In a typical terrestrial FSO system with 1 km link length, the optical beam divergence, without tracking, is in the range of 2–10 mrad, which is equivalent to a beam spread of 2–10 m. With tracking the range is 0.05–1.0 mrad, which is equivalent to a beam spread of 5 cm to 1 m. Therefore for long range FSO systems using an optical source (preferably a laser) with a narrow beam size is the best option to minimum beam divergence, thus link availability. For short link FSO systems, optical sources with a wide divergence angle are employed with relatively straight forward alignment and no need for active tracking.

8.3 Losses due to Optical Components, Windows and Pointing

This part of power loss is caused due to the imperfect optical elements in the transmitter and receiver, including the absorption, scattering and reflection due to the lenses and mirrors in the system [36]. The optical loss L_{op} , depends on the characteristics and quality of the optical components. There is also additional power loss due to the windows installed in building. The pointing loss L_p occurs when the FSO link has non-perfect alignment due to building sway or strong wind effect. For long range FSO link the pointing loss can be relatively high [1, 69]. For example, for larger amount of misalignment ($\sigma_s/R_a = 3$ and $\omega_b/R_a = 10$ where σ_s is the pointing error displacement standard deviation at the receiver, ω_b is the beamwaist and R_a is the receiver aperture), ~ 55 dB electric SNR is required to achieve an average BER of 10^{-6} in strong turbulence regime [41]. However, in many applications with short links (< 1 km) pointing power loss can be neglected.

8.4 Link Budget Analysis

The received optical power $P_r(\lambda, L)$ (dBm) can be derived from the link budget analysis discussed above, which is expressed as:

$$P_r(\lambda, L) = P_t(\lambda, 0) - 4.343L\beta_s(\lambda) - L_{Geom} - L_{op} - L_p - L_M, \quad (8.11)$$

where the link margin L_M is the link margin to take into accounts any other losses due to rain and snow, the replacement of a faulty component, ageing of optical component etc.

The minimum acceptable value of received power required to achieve a specific level of

performance (i.e. BER, SNR) is referred to as the receiver sensitivity. It takes into account power penalties caused by use of a transmitter with worst-case values of extinction ratio, jitter, pulse rise times and fall times, optical losses, optical component aging, and measurement tolerances. It also depends on the noise level, the data rate, the modulation scheme and the scintillation level. The noise source could be one or a combination of the quantum shot noise, the thermal noise and the background radiation. Sensitivity usually takes into account worst-case operating and end-of-life conditions.

The specifications for the FSO link budget are shown in Table 8.2. These values adopted are based on the Kim model of atmospheric attenuation given in (8.6). The receiver sensitivities for the OOK and BPOLSK schemes are obtained from Figs. 5-8 and 5-10 and have been summarized in Table 8.3. Substituting values in Table 8.3 into (8.11), the link budget for the OOK-FSO and BPOLSK-FSO systems operating over the non-turbulent channel under a range of visibility values is shown in Fig. 8-2.

From Fig. 8-2, for the OOK-FSO operating at 155 Mbps in a channel with a visibility of 50 km, a link length of around 2 km is achievable at a 5 dB link margin. If the link margin increases to 10 dB, the link length reduces to about 1.1 km. For BPOLSK-FSO operating under the same conditions, the link lengths are ~ 2.3 km and ~ 1.3 km at 5 dB and 10 dB link margins, respectively.

Table 8.2: Specifications for the FSO link budget.

Parameter	Typical value
Modulation technique	On-Off keying/ BPOLSK
Transmitted power	14 dBm
Wavelength, λ	850 nm
Bit rate, R_b	155 Mbps
Transmitter aperture diameter, d_T	2.5 cm
Receiver aperture diameter, d_R	8 cm
Beam divergence, θ_s	2 mrad
Optical loss, L_{op}	1 dB
Pointing loss, L_p	1 dB
Load resistance, R_L	50 Ω
PIN photodetector responsivity, \mathfrak{R}	1
Operating temperature, T_e	300 K
Boltzmann constant, κ	1.38×10^{-23}

Table 8.3: Receiver sensitivity to achieve a BER of 10^{-9} based on OOK and BPOLSK.

Modulation scheme	Turbulence	SNR (required to achieve a BER of 10^{-9})	Receiver sensitivity
OOK	No turbulence	18.5 dB	- 27.2 dBm
BPOLSK	No turbulence	15.5 dB	-28.7 dBm

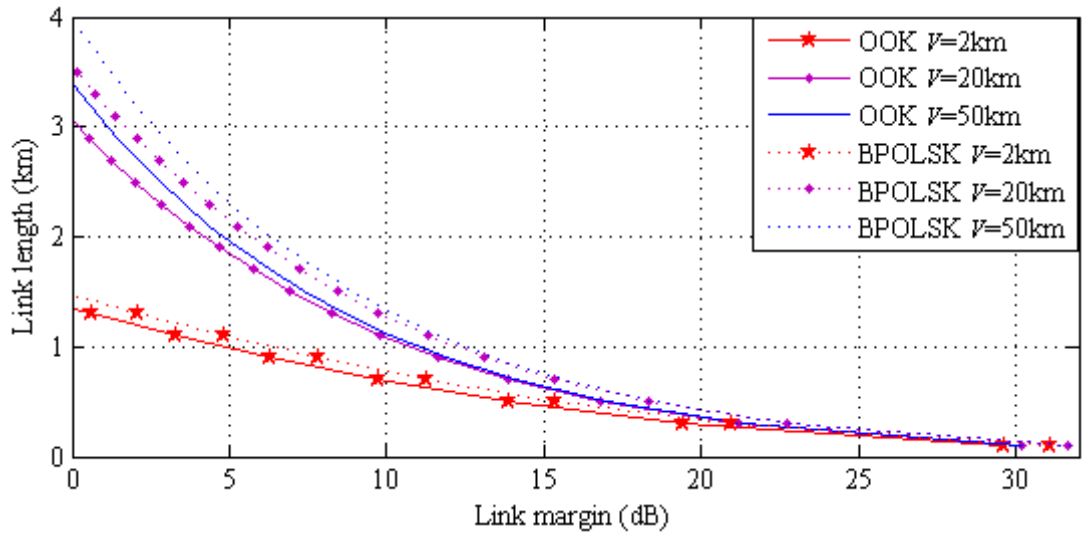


Fig. 8-2: Link range against the link margin for OOK and BPOLSK to achieve a BER of 10^{-9} in a non-turbulent FSO channel with visibility values $V = 2, 20$ and 50 km.

8.5 Summary

The link budget equation to obtain the achievable link length under a specified link margin at a certain data rate has been derived in this chapter. The power loss caused by various sources has been discussed. Additionally, the link length as a function of the link margin and receiver sensitivity for OOK and BPOLSK has been shown. For the OOK-FSO operating at 155 Mbps in a non-turbulent channel with a visibility of 50 km, the link lengths of around 2 km and 1.1 km are achievable at 5 dB and 10 dB link margins, respectively. For BPOLSK-FSO operating under the same conditions, the link lengths are ~ 2.3 km and ~ 1.3 km at 5 dB and 10 dB link margins, respectively.

Chapter Nine

Experimental Investigation of BPOLSK-FSO in a Turbulence Channel

In previous chapters the complete theoretical analysis of the proposed coherent POLSK-FSO systems in an atmospheric turbulence channel has been given. In a turbulence channel coherent detection schemes offer improved performance compared with IM-DD [135, 184]. The aim of this chapter is to experimentally investigate the performance of a linear BPOLSK scheme using DD scheme mainly because of its simple implementation. To demonstrate the advantages of BPOLSK-FSO using DD, the obtained results will be compared with the OOK scheme under same operating

conditions. To demonstrate fair comparison between BPOLSK and OOK signalling schemes, the parameters including the data rate and the intensity are kept the same.

Firstly, the experiment to assess the BPOLSK-FSO system performance is performed using the indoor atmospheric chamber (5.5 m in length) located in the ORCG Research Laboratory. Secondly, the long distance point-to-point communication is achieved by using multiple reflections of the laser beams between mirrors. An external interferometer is replaced by two intensity modulated laser sources with orthogonal SOPs. This new scheme is less complex compared to the existing techniques. Most of the polarisation modulators proposed so far are based on the LiNbO₃-based Mach Zehnder modulators [188]. However, those devices suffer from a 7.5 dB loss and their fabrications are more costly and complex. The remainder of this chapter is organized as follows: the descriptions of the experimental set-up for the BPOLSK-FSO with two communication distances (5.5 m and 27 m), including the discussions of results, are presented in Sections 9.1 and 9.2, respectively. The summary is given in Section 9.3.

9.1 BPOLSK-FSO Link using an Indoor Simulated Chamber

The experimental set-up for characterising the performance of the proposed BPOLSK-FSO system employing direct detection scheme using the indoor atmospheric chamber is shown in Fig. 9-1 and Fig. 9-2. Here direct detection is used instead of the coherent system to demonstrate the polarisation shift keying concept. The length of chamber is 5.5 m and the link span between the transmitter and receiver is 6 m. To

demonstrate the impact of turbulence on the link performance two received optical power levels (-16.8 dBm and -12.5 dBm) amplifier (TIA) were monitored and compared. All experimental parameters adopted are given in Table 9.1. The process was repeated by increasing the turbulence strength level within the chamber at the location T1 and keeping the ambient temperature at $\sim 20^\circ\text{C}$ at the location T3. The same procedure described above was applied to the OOK-FSO link with the same data rate and the turbulence strength for comparison. For like-to-like comparison with the OOK based FSO system, the average emitted optical power per laser source for BPOLSK was made equal to half the total transmitted power.

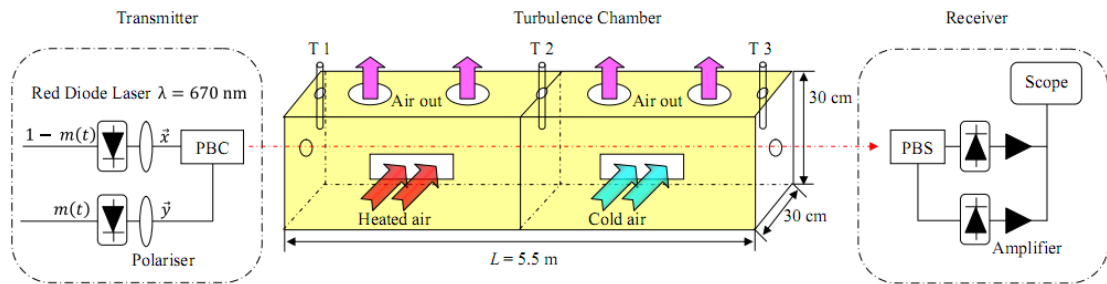
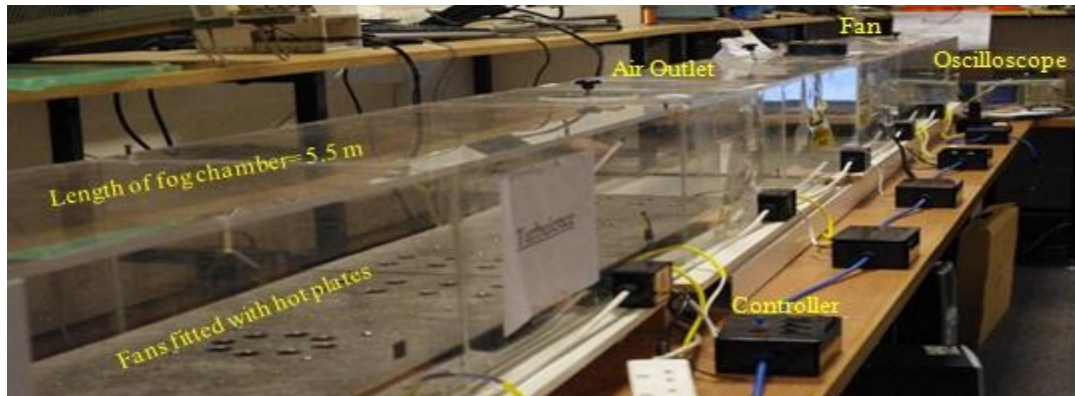


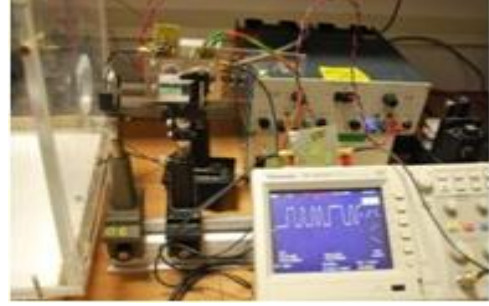
Fig. 9-1: BPOLSK-FSO experimental system block diagram to measure the atmospheric turbulence effect.



(a)



(b)



(c)

Fig. 9-2: BPOLSK-FSO link set-up (a) channel, (b) transmitter, and (c) receiver.

Table 9.1: Parameters of BPOLSK-FSO communication system.

Parameters		Values	Units
Laser			
- Wavelength λ		670	nm
- Bandwidth (-3 dB points)		50	MHz
- Power output		1	mW
- Divergence (full angle)		0.5	mrاد
- Beam size at transmitter		4.5×2.5	mm
- Output aperture		6.0	mm
Photodiode			
- Wavelength range		430 – 900	nm
- Responsivity		0.42 ($\lambda = 670$ nm)	
- Active area		15	mm ²
- Dark current		1	nA
AD8015 Trans-impedance Amplifier (TIA)			
- Bandwidth		240	MHz
- Optical sensitivity		-36 @155.52 Mbps	dBm
- Power supply		5	V
AD8042 Rail-To-Rail Amplifier			
- Bandwidth		160	MHz
Others			
- Bit rate		500	kbps
- Data length		2^{10}	
- Average optical received power		-16.8 dBm/-12.5 dBm	
- Modulation index		0.057	
- Losses	Polariser	2 dB	
	PBC	2 dB	
	PBS	2 dB	

Turbulence Chamber		
- Dimensions	$5.5 \times 0.3 \times 0.3$	m^3
- Wind speed	6.5	km/hr
- Temperature at T1	20, 30, 40, 50, 60	$^{\circ}\text{C}$
- Temperature at T3	~ 20	$^{\circ}\text{C}$

9.1.1 Transmitter

The schematic diagram of the transmitter is shown in Fig. 9-3. Two red lasers at $\lambda = 670 \text{ nm}$ were directly intensity modulated with the pseudo random binary sequence (PRBS) $m(t)$ with a length of 2^{10} at a data rate of 500 kbps. In fact any wavelengths within the 600-1550 nm range covering the entire optical wireless transmission band could be adopted as shown in Fig. 9-1. The polarisation states of the lasers were adjusted by two identical polarisers with the horizontal \vec{x} and vertical \vec{y} reference axes, respectively. The input light coinciding with the transmission axis of the polariser was linearly passed while the orthogonal component was completely removed. The orthogonally polarised optical beams were combined using a PBC to form the transmitted BPOLSK signal. The emitted optical signal is given as:

$$\vec{E}_s(t) = \sqrt{\frac{P_t}{2}} e^{i(\omega t + \varphi(t))} \left\{ \sqrt{1 - m(t)} \cdot \vec{x} + \sqrt{m(t)} \cdot \vec{y} \right\}. \quad (9.1)$$

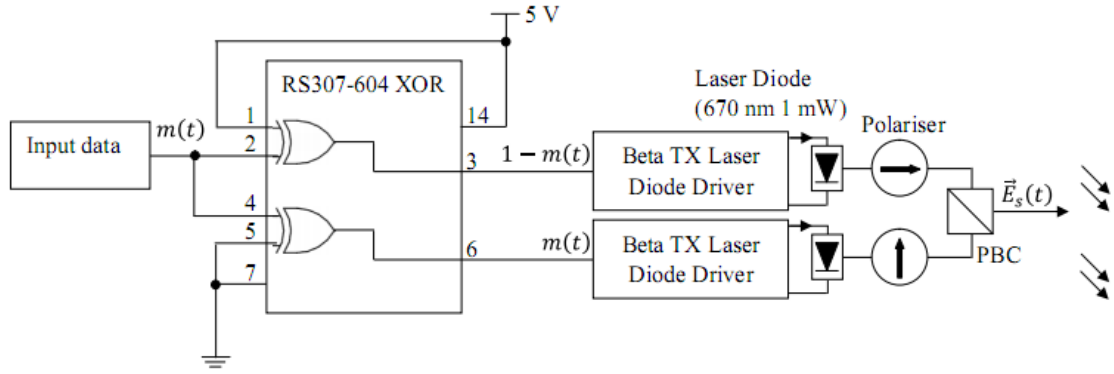


Fig. 9-3: The schematic diagram of the BPOLSK transmitter.

9.1.2 Turbulence Channel

A dedicated indoor atmospheric chamber of dimensions $5.5 \times 0.3 \times 0.3 \text{ m}^3$ width, length and height, respectively, was used to experimentally evaluate the performance of the BPOLSK-FSO link under a controlled atmospheric turbulence condition. The temperature gradient (a minimum of 6°C) and the wind speed were maintained to ensure the turbulence (i.e. scintillation) effects on the propagating laser beams within the chamber. The process was performed by blowing hot and cooler air at the speed of 6.5 km/hour into the chamber at transmitter and receiver ends, respectively, with the parameters given in Table 9.1. The cooler air temperature was maintained at $\sim 20^\circ\text{C}$ at the receiver end, whereas at the transmitter end the temperature could be maintained within the range of $20 - 60^\circ\text{C}$. A number of air vents were used to maintain a constant temperature gradient between the optical source and the photodetector.

The instantaneous temperature at different positions along the chamber was measured by three temperature sensors at T1, T2 and T3 as shown in Fig. 9-1. The wind velocity

within the chamber was maintained in the transversal direction of the propagating laser beams. The background ambient light was reduced to the barest minimum level by operating the whole experimental work in a dark room environment.

9.1.3 Receiver

The receiver structure for the proposed BPOLSK-FSO system is shown in Fig. 9-4. The optical fields were detected by two detector circuits. Each detector circuit consisted of a Series OSD15-5T PIN photodiode followed by an AD8015 TIA with parameters given in Table 9.1. The schematic diagram of the detector circuit is illustrated in Fig. 9-5.

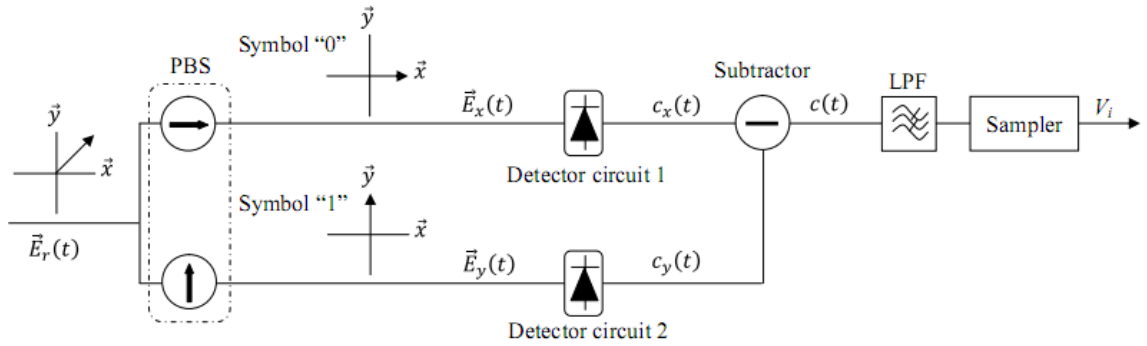


Fig. 9-4: The schematic of the optical receiver module. LPF (lowpass filter).

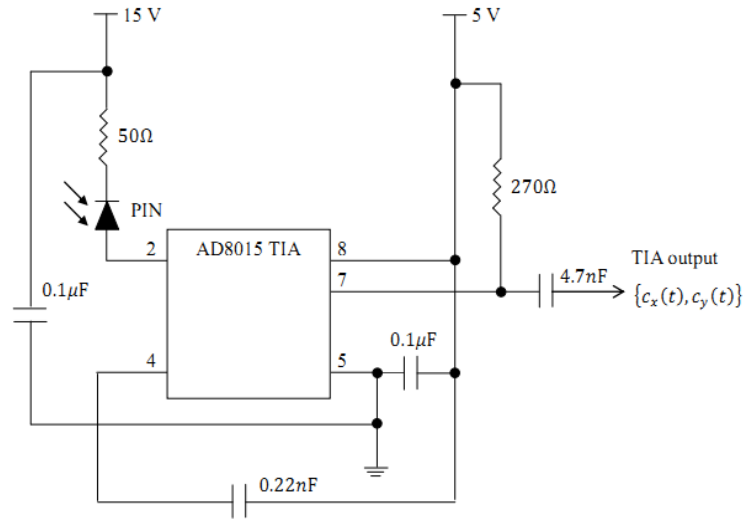


Fig. 9-5: AD8015 TIA based detector circuit schematic diagram.

The output signals from the detector circuits were fed into the AD8042 rail-to-rail amplifier based subtractor. The schematic diagram for the subtractor is shown in Fig. 9-6.

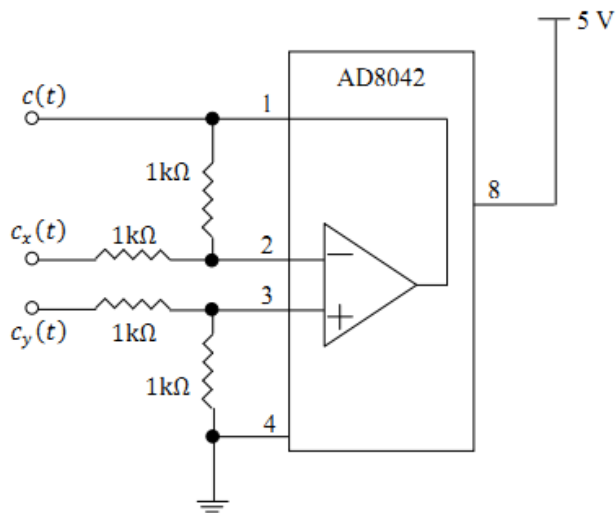


Fig. 9-6: AD8042 rail-to-rail amplifier based subtractor schematic diagram.

The received optical signal after passing through the turbulence chamber is given as:

$$\vec{E}_r(t) = \sqrt{\frac{P_r}{2}} e^{i(\omega t + \varphi_r(t))} \left\{ \sqrt{1 - m(t)} \cdot \vec{x} + \sqrt{m(t)} \cdot \vec{y} \right\}. \quad (9.2)$$

After passing through the PBS the optical signals with orthogonal SOPs are expressed as:

$$\vec{E}_x(t) = \sqrt{\frac{P_r}{2}} e^{i(\omega t + \varphi_r(t))} \sqrt{1 - m(t)} \cdot \vec{x}, \quad (9.3a)$$

$$\vec{E}_y(t) = \sqrt{\frac{P_r}{2}} e^{i(\omega t + \varphi_r(t))} \sqrt{m(t)} \cdot \vec{y}. \quad (9.3b)$$

The outputs of the photodetectors are given by [113]:

$$c_x(t) = \frac{\Re P_r}{2} [1 - m(t)] + n_x(t), \quad (9.4a)$$

$$c_y(t) = \frac{\Re P_r}{2} m(t) + n_y(t), \quad (9.4b)$$

where the system noise terms $n_{x,y}(t) \sim N(0, \sigma_n^2)$.

The instantaneous electric current at the output of the subtractor is defined as:

$$c(t) = c_x(t) - c_y(t) = \Re P_r / 2 [1 - 2m(t)] + n(t), \quad (9.5)$$

where the system noise terms $n(t) \sim N(0, \sigma_n^2)$.

The electric signal $c(t)$ is then applied to a LPF with the bandwidth equal to the bit rate,

with the output signal defined as:

$$V_i(t) = \frac{1}{\sqrt{T}} \int_0^T c(t) dt = \begin{cases} \Re P_r / 2 + n_{lp} & \text{for } m(t) = 0, \\ -\Re P_r / 2 + n_{lp} & \text{for } m(t) = 1, \end{cases} \quad (9.6)$$

where $h_{lp}(t)$ denotes the impulse response of the LPF and $n_{lp}(t) \sim N\{0, \sigma_n^2\}$ is the AWGN process. With the signal V_i being within the range of $\Re P_r/2$ and $-\Re P_r/2$ for the transmission of '1' and '0', respectively, so the threshold level is fixed at the zero level in this case.

Assuming independent and identically distributed transmission, the error probability is derived as:

$$P_{ec} = \frac{1}{\sqrt{2\pi\sigma_n^2}} \int_{-\infty}^0 e^{-\frac{(x-\Re P_r/2)^2}{2\sigma_n^2}} dx = \frac{1}{2} \operatorname{erfc}\left(\frac{\Re P_r}{2\sqrt{2}\sigma_n}\right). \quad (9.7)$$

The experimental BER is estimated by evaluating the statistical fluctuation in the received signal. The error rate can now be written as:

$$P_{ec} = \frac{1}{2} \operatorname{erfc}\left(\frac{Q}{\sqrt{2}}\right), \quad (9.8)$$

where $Q = \frac{|\mu_1 - \mu_0|}{\sigma_1 + \sigma_0}$, $|\mu_1 - \mu_0|$ presents the separation between the intensity levels of '1' and '0', corresponding to $|\mu_1 - \mu_0| = \Re P_r$, and $\sigma_1 + \sigma_0$ denotes the sum of the standard deviations of both intensities with $\sigma_1 = \sigma_0 \approx \sigma_n$.

The theoretical Q -factor ($\langle Q \rangle$) in the presence of turbulence is expressed as [236]:

$$\langle Q \rangle = \frac{Q_0}{\sqrt{\mu_{no}/\mu + \sigma_n^2 Q_0^2}}, \quad (9.9)$$

where Q_0 is the Q -factor in the absence of turbulence, μ and μ_{no} are the means received signal with and without turbulence, respectively.

In this chapter the BER is estimated by evaluating the statistical fluctuation of the received signal. Following the method in [1], the BER conditioned on the received irradiance for BPOLSK-FSO system transmitting through the turbulence channel is given as:

$$P_{\text{BPOLSK}}(P_r) = \frac{1}{2} \int_0^\infty \text{erfc}\left(\frac{Q(P_r)}{\sqrt{2}}\right) p(P_r) dP_r. \quad (9.10)$$

Its SNR expressed in terms of Q -factor is derived as $Q = \Re P_r / \sqrt{2} \sigma_n$ [237]. Note that the average optical power is half the value of the peak power for the OOK scheme, whereas for DD-BPOLSK the average and peak powers are the same.

9.1.4 Results

Experimentally obtained values for the Q -factors for BPOLSK and OOK schemes with two optical power levels (-16.8 dBm and -12.5 dBm) against the turbulence variances σ_t^2 are illustrated in Fig. 9-7, also shown are the predicted Q -factors using (9.9). The predictions are based on the measured Q -factor in the absence of turbulence. For all cases, the experimental and predicted plots show a very good agreement. The optical signal fluctuation caused by the turbulence leads to reduced Q -factor values for both modulation schemes. However, under the same turbulence strength, the effect on BPOLSK is less severe to compared with OOK with the same transmit optical power level. For example, for a turbulence variance σ_t^2 of 0.003 and the transmitted optical

power of -16.8 dBm, the values for Q -factor are ~ 11 and ~ 8.5 for BPOLSK and OOK, respectively.

For the same modulation schemes a higher transmission optical power level offers larger Q -factor values. For instance, for $\sigma_t^2 = 0.003$, Q -factors are ~ 11 and ~ 17 for the BPOLSK scheme with -16.8 dBm and -12.5 dBm of optical powers, respectively. As shown in Fig. 9-7 increasing the optical power has very little effect on the Q -factor when turbulence strength level is high.

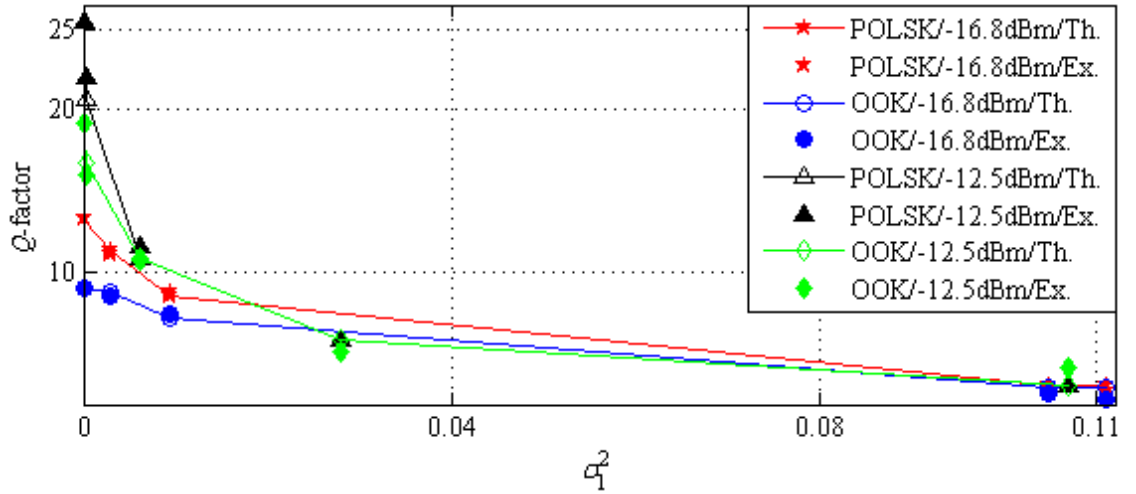


Fig. 9-7: Measured (Ex.) and theoretical (Th.) Q -factors for the BPOLSK and OOK (using peak power) modulation schemes with two transmit optical power levels (-16.8 dBm/-12.5 dBm) against the turbulence variances (σ_t^2).

9.2 BPOLSK-FSO using Direct Detection with Reflecting Mirrors

Using the chamber the maximum link span achieved without any reflection is ~ 6 m. To increase the link span there are two options: (i) multiple reflection within the chamber and (ii) multiple reflection between two reflecting mirrors. The former is quite

challenging to set up because of alignment of the laser beams, therefore the later is adopted for further investigation of the BPOLSK FSO link. Using two mirrors the link span is increased to 27 m. The comparative study of the BPOLSK has been carried out with respect to the OOK in a similar channel condition. The emitted optical power was -12.5 dBm and the received signal amplitude after TIA was 80 mV peak-to-peak for all modulation schemes for fair comparison. The data rate for both modulation schemes was kept at 2 Mbps.

9.2.1 Experimental Set-Up

The picture and diagram for BPOLSK-FSO system using two reflecting mirrors are shown in Fig. 9-8 and Fig. 9-9, respectively. The whole BPOLSK system was set up on the dedicated optical bench with the dimension of $1.5 \times 1.8 \text{ m}^2$ width and length, respectively. Two long mirrors of dimensions $0.004 \times 0.2 \times 1.4 \text{ m}^3$ thickness, width and length were positioned facing each other on the optical bench. Two red lasers at the wavelength of 670 nm were directly modulated with the PRBS data and their SOPs were adjusted by polarisers with horizontal and vertical polarisation axes, respectively.

The laser beams were collimated by convex and concave mirrors followed by the adjustable reflecting mirrors which were used to change the number of reflections between the fixed mirrors. The numbers of reflections achieved were 7 and 8 on the right hand side and left hand side reflecting mirrors, respectively. The spacing between adjacent reflection spots became larger due to the flat mirrors. The last reflection from

the left hand side mirror is collected by an adjustable concave mirror with a focal distance of 1.34 m and a diameter of 0.155 m. The reflected beam from the concave mirror with orthogonal SOPs is then passed through the PBS before being collected by two small area photodetectors.

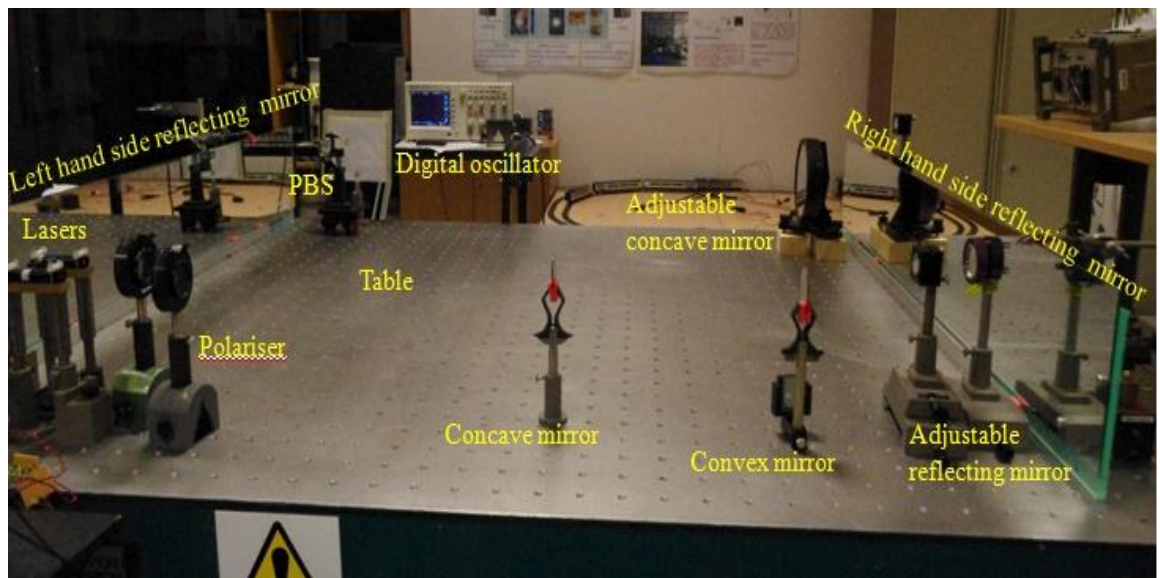


Fig. 9-8: BPOLSK-FSO with the link length of 27 m set-up picture.

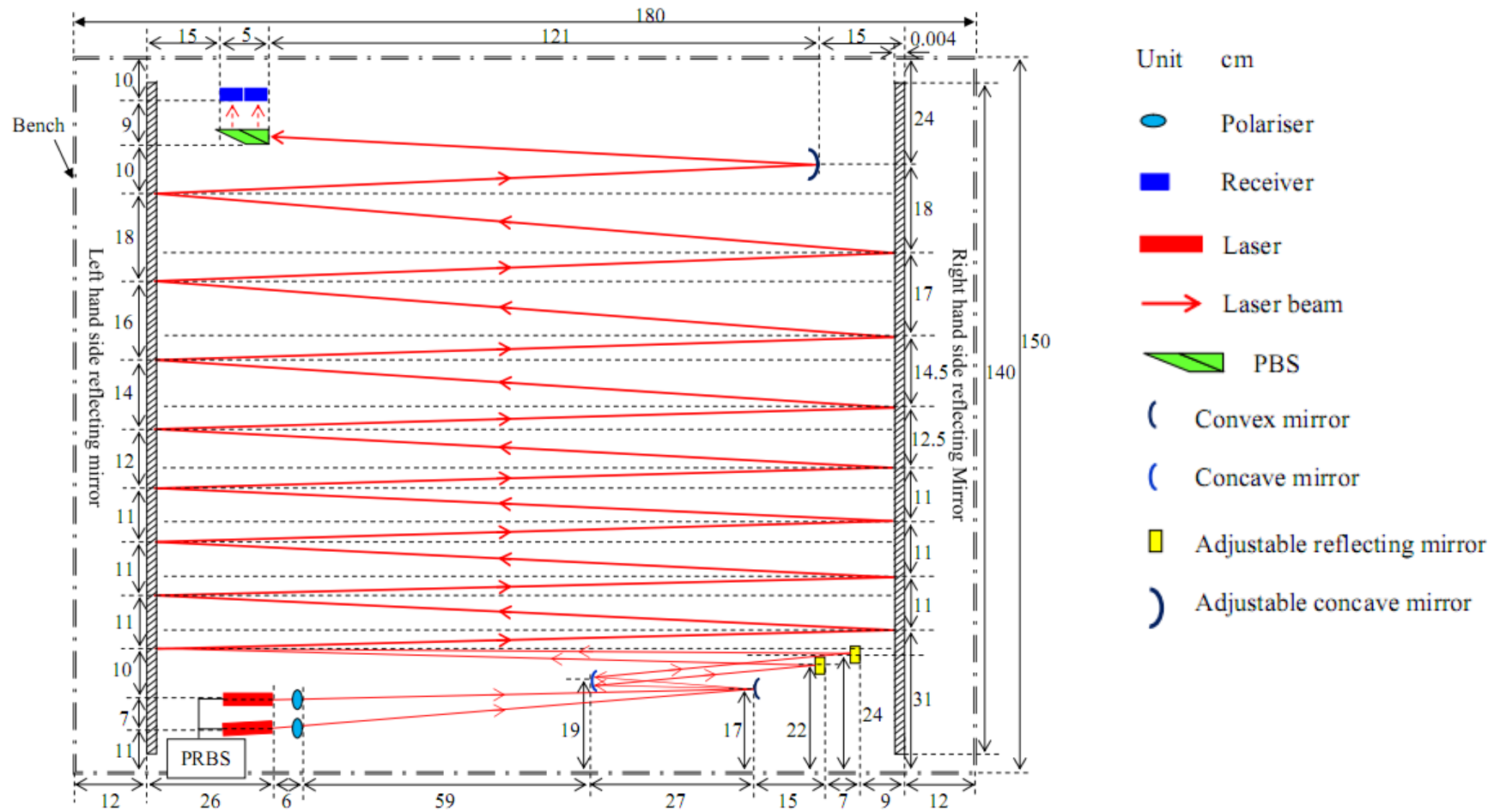


Fig. 9-9: BPOLSK-FSO with the link length of 27 m schematic diagram.

i Convex and concave mirrors

The convex and concave mirrors were used to reduce the beam divergence loss and to increase the received signal power at the receiver. The combination of the convex and concave mirrors configuration is illustrated in Fig. 9-10. The incident laser beams, which were parallel to the principal axis of the convex mirror with the focal length of 23 cm, are reflected divergently. Since the focus and the reflect surface are on the opposite side of the convex mirror, the laser beams pass through the focus by extending the reflected ray behind the convex mirror. The divergent laser beams from the convex mirror then incident on the concave mirror. The focal points of the convex and concave mirrors must be overlapped, so the reflected laser beams from the concave mirror are almost parallel.

The optical beam footprints of the first five reflection spots on the surface of fixed reflecting mirror are depicted in Fig. 9-11, thus illustrating the beam broadening with every reflection. The spot size has increased from 1 cm² to 3 cm², which is due to the beam divergence caused by the laser source and non-ideal mirrors.

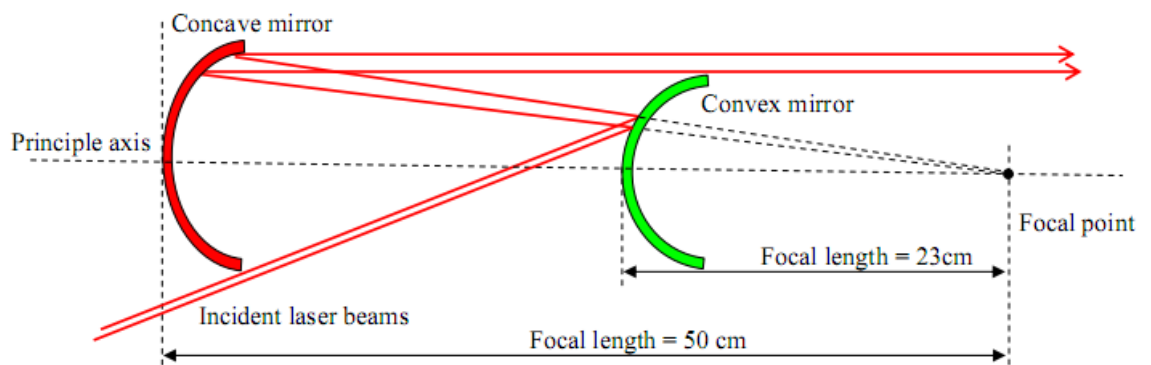


Fig. 9-10: Principle of the beam reflections between the convex and concave mirrors.

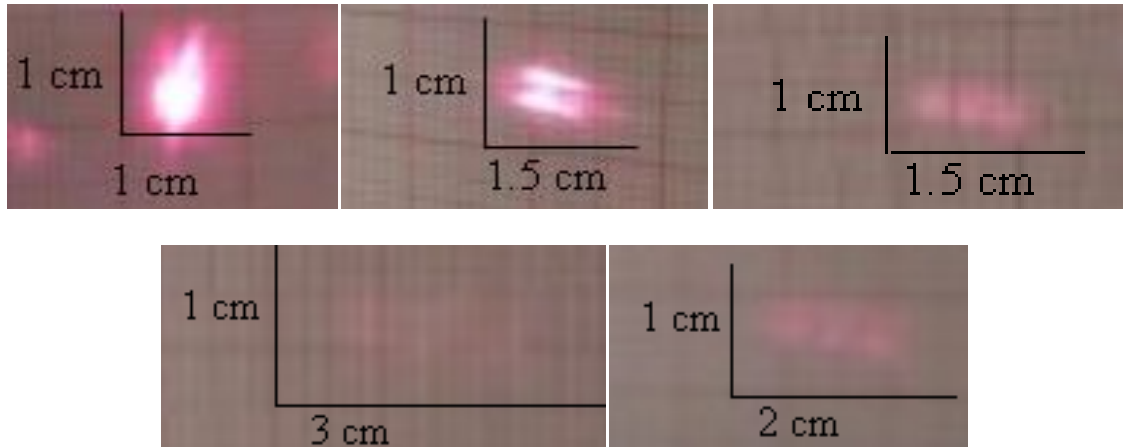


Fig. 9-11: Pictures of the first five reflection spots showing the laser beam divergence effects.

With turbulence the optical beam foot print fluctuated greatly covering an area of $6 \times 7 \text{ cm}^2$, which is far greater than the PBS surface area of $2 \times 2 \text{ cm}^2$, see Fig. 9-12. Therefore, it was almost impossible to focused the beam onto the PBS and then on to photodetectors for signal processing. Therefore, to overcome this problem and be able to focus the widely dispersive optical beams after a number of reflections, a concave mirror is used to collimate the incident laser beams and focus it on to the PBS, see Fig. 9-8 and Fig. 9-9. The adjustable concave mirror was placed 1.34 m (which is the focal length) in front of the PBS. The measured optical beam footprint of the collimated laser beam is 1 cm^2 much smaller than the non collimated beam.

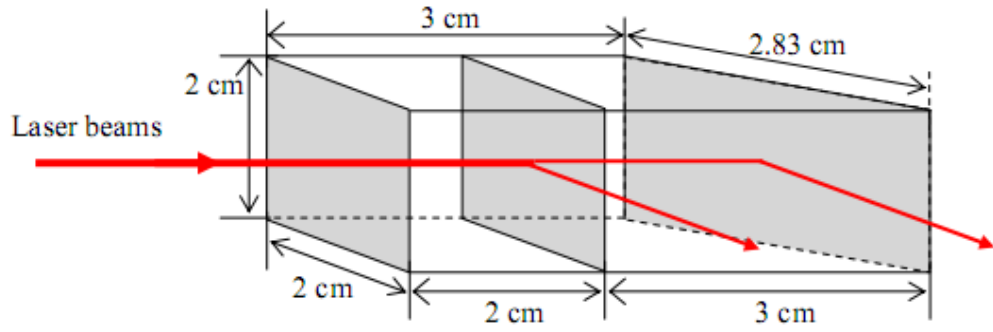


Fig. 9-12: Structure of the PBS.

ii *Turbulence channel*

The complete experimental parameters are given in Table 9.2. The temperature gradient and the wind speed are maintained to ensure the turbulence effect on the propagating reflecting laser beams between the two fixed mirrors. The process is repeated by increasing the turbulence strength level at the transmitter and receiver, respectively. The wind velocity is maintained in the transversal direction of the propagating laser beam. The background ambient light is reduced to a minimum level by operating the whole experimental in a dark room environment.

The output signal from the receiver is captured using a digital oscilloscope. The propagating optical signal is subjected to the atmospheric turbulence at a very low degree. The turbulence is introduced by using a fan blowing hot air across the reflected beams. Further signal processing is performed on the captured data from the digital oscilloscope using the Matlab software to calculate the Q -factor of the received signal. A LPF is used during signal processing to ensure that the overall noise bandwidth at the receiver is equal to the symbol rate.

Table 9.2: Experimental parameters for BPOLSK-FSO with the link length of 27 m.

Data type		PRBS – OOK-NRZ
Data rate		2 Mbps
Amplitude		80 mVpp
Received optical power level		-12.5 dBm
Sampling rate		500 M samples/s
Low pass filter	Type	Butterworth
	Order	4
	Bandwidth	2 MHz
Room temperature		24 °C
Turbulence simulation		
Heater position	Temperature °C	Wind Speed (m/s)
Transmitter	70/24	2.4
Transmitter	55/24	2.4
Transmitter	50/24	2
Transmitter	35/24	1
Receiver	24/80	2.7
Receiver	24/47	2
Receiver	24/40	1.4

9.2.2 Results

The experimental and the theoretical Q -factors using (9) against the turbulence variance for BPOLSK and OOK signaling schemes are depicted in Fig. 9-13. It shows that the experimental Q -factor matches the theoretical values for a range of turbulence variances. As the turbulence variance increases, the Q -factor decreases for both schemes due to the received signal fluctuation. For example, at $\sigma_l^2 = 0.02$, the experimental Q -factors are 5 and 5.5 for OOK and BPOLSK, respectively. When σ_l^2 increases to 0.03, the corresponding Q -factors become 4.6 and 5. This indicates that BPOLSK offers an optimum performance operating in turbulence channel, with a higher receiver complexity than the OOK.

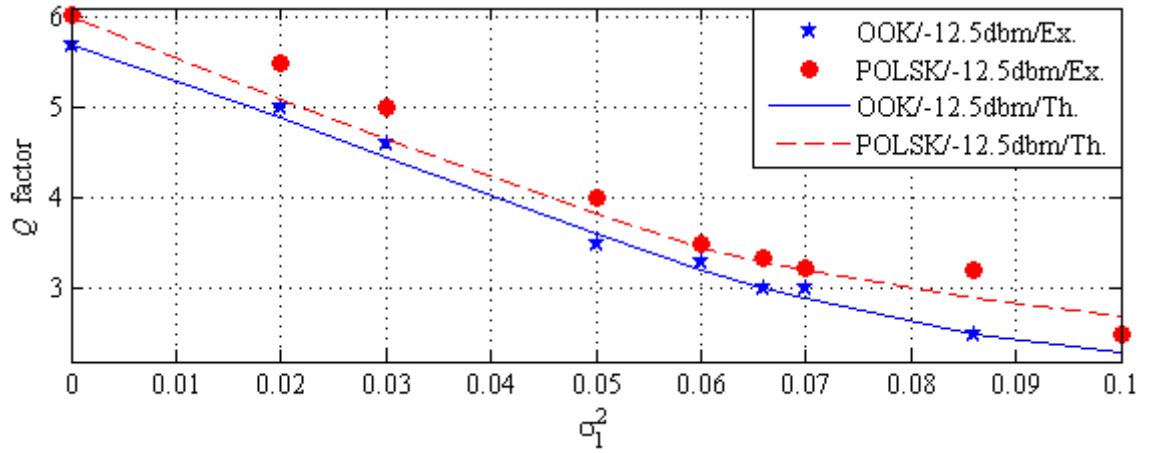
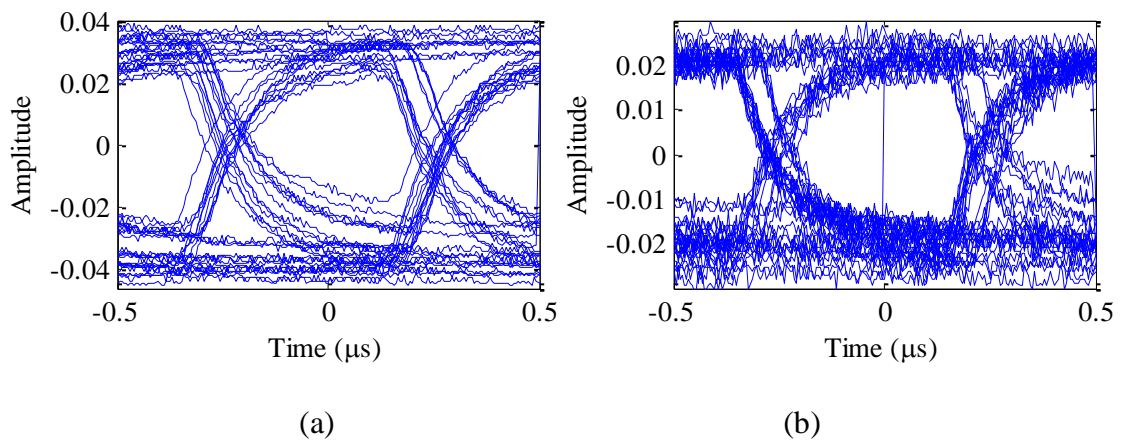


Fig. 9-13: Experimental (Ex.) and theoretical (Th.) Q -factors for the BPOLSK and OOK modulation schemes with the link length of 27 m against the turbulence variances (σ_l^2).

The measured eye-diagrams for the received signals are illustrated in Fig. 9-14. The height of eye-opening is smaller in the presence of turbulence due to the atmospheric turbulence induced signal intensity fluctuation. The height of eye-opening is bigger for BPOLSK signal compared with the OOK signal in the presence of turbulence, indicating that BPOLSK is less sensitive to the intensity fluctuation under the weak turbulence condition.



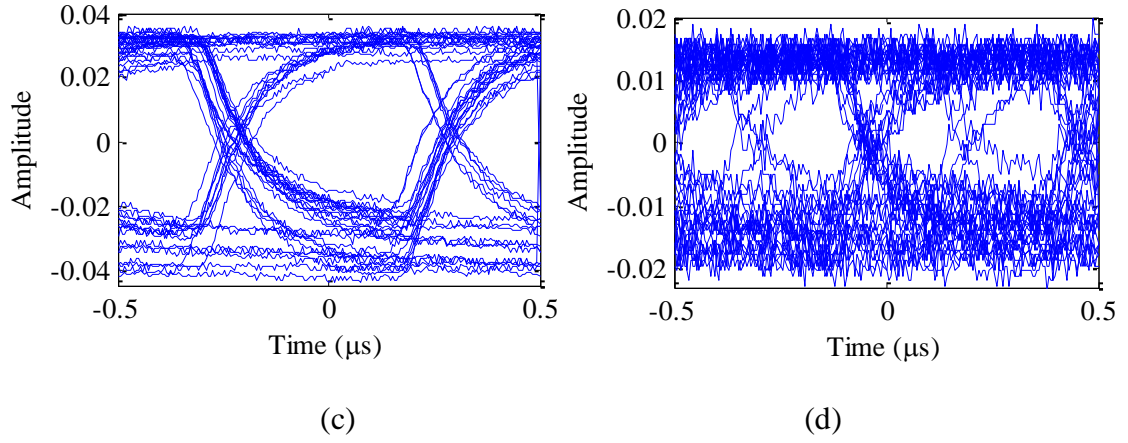
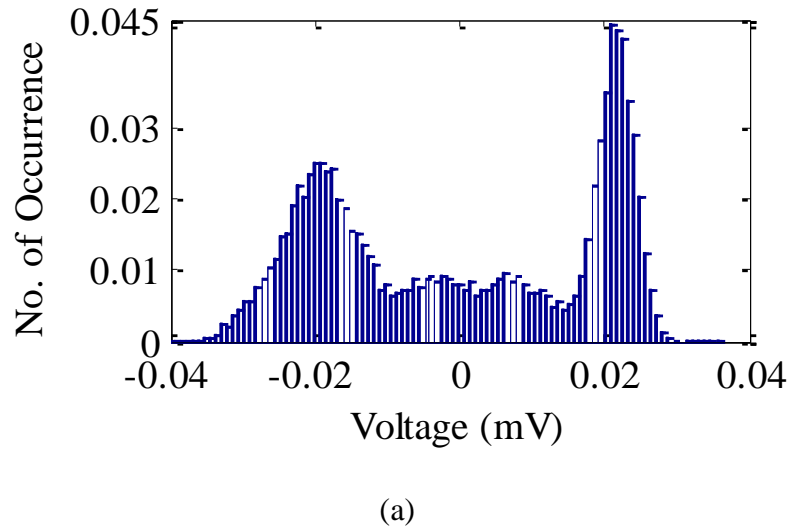
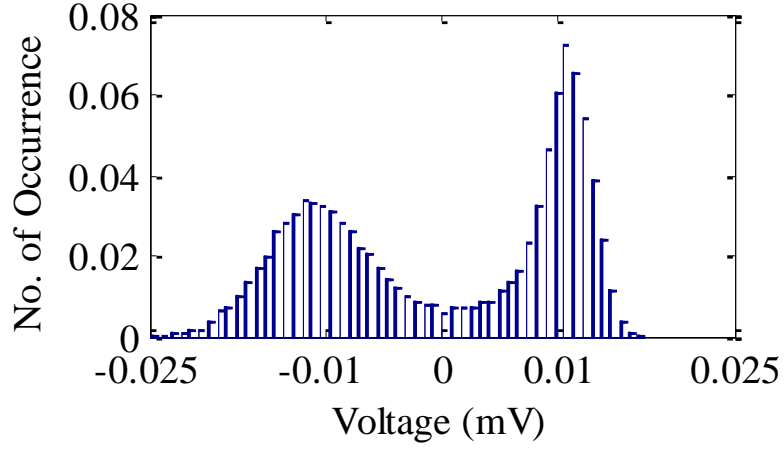


Fig. 9-14: Eye diagrams for the BPOLSK (a) without turbulence and (b) $\sigma_t^2 = 0.06$; and OOK (c) without turbulence and (d) $\sigma_t^2 = 0.06$.

The distributions of received signal level for '1' and '0' for BPOLSK and OOK schemes are depicted in Fig. 9-15. There is less signal overlapping in the presence of weak turbulence for the BPOLSK. In the case of OOK, the distance between received signal level for '1' and '0' is reduced by 50% compared with BPOLSK.





(b)

Fig. 9-15: Received signal distributions with turbulence variance of $\sigma_t^2 = 0.06$ for (a) BPOLSK and (b) OOK.

9.3 Summary

In this chapter, we have experimentally investigated the performance of the BPOLSK-FSO system with DD operating over 6 m and 27 m atmospheric turbulence channels. As a result of the underlying assumptions in the derivation, there is a close match between experimental and predicted Q -factors for the weak turbulence regimes for BPOLSK-FSO system. For comparison the predicted and analytical results for OOK (with peak and average power levels) have also been presented. We have shown that BPOLSK offers a slightly higher Q -factor values compared with OOK for the same transmit optical power and the turbulence variance. For example, when the link length is 6 m and the transmitted optical power is -16.8 dBm, the Q -factors are ~ 11 and ~ 8.5 for BPOLSK and OOK, respectively, with $\sigma_t^2 = 0.003$. Further experimental work has been performed using reflecting mirrors to assess the system performance with long link length. For example, when σ_t^2 is 0.03, the Q -factors are 4.6 and 5 for OOK and BPOLSK, respectively. This

indicates that BPOLSK offers an optimum performance operating in turbulence channel, with a higher receiver complexity than the OOK. The eye-diagrams for BPOLSK and OOK schemes have been illustrated. Comparing the height of eye-opening for BPOLSK and OOK schemes, BPOLSK is less sensitive to the intensity fluctuation under the weak turbulence condition. In the case of OOK, the distance between received signal level for '1' and '0' is reduced by 50% compared with BPOLSK.

Chapter Ten

Conclusions and Future Work

10.1 Conclusions

FSO technology is one of the most promising new technologies to deal with the bandwidth bottleneck that exists in access networks. FSO is a complementary technology to the RF offering a number of unique advantages, thus making it attractive for many applications both indoor and outdoor. This research work was aimed at investigating the performance of the coherent POLSK pre-modulated FSO system in an atmospheric turbulence channel with the view to understand its characteristics, limitations and performance. The aim was also to carry out comparison - with other systems such as OOK-FSO and BPSK-FSO.

To give the readers a brief overview about the FSO technology, its fundamentals, applications, features, and terminology, were reviewed in the Chapter Two. Optical detection methods as well as the noise sources at the receiver and their influences on the performances of the systems were also covered in this chapter. Concerning the atmospheric channel, both atmospheric attenuation and turbulence were also discussed. Chapter Three discussed the three mostly reported models for the irradiance fluctuation in the atmospheric turbulence, which is necessary to predict the reliability of an optical system operating in such an environment. The lognormal is mathematically tractable but only valid in the weak turbulence regime. Beyond the weak turbulence regime, the gamma-gamma model is more suitable but lacks the mathematical convenience. The negative exponential model is only used in the saturation regime.

In Chapter Four, the POLSK technique modulated an FSO communication link has been discussed, together with the analysis of the outage probabilities in the weak and saturation turbulence regimes. The comparisons of the digital modulation techniques adopted for FSO in a turbulence channel suggest that there is always a trade-off between bandwidth efficiency, simplicity and power efficiency in the selection of modulation schemes. In the next chapter, the performance of POLSK-FSO in all turbulence regimes will be analysed.

This research has focused on employing the POLSK scheme in the FSO turbulence channel to optimize the system performance. The coherent BPOLSK modulation scheme was selected and its error probabilities were analysed and compared with OOK and

BPSK schemes in the presence of the turbulence and noise in Chapter Five. The BPOLSK scheme is considerably insensitive to the laser phase noise at the receiver, which is based on the condition that the IF filter bandwidth was large enough to avoid the phase-to-amplitude noise conversion. Based on the results, POLSK was proposed for FSO links in the atmospheric turbulence channel.

The FSO link power penalties caused by the atmospheric turbulence must be compensated to guarantee a reliable communication link. One option was to increase the transmitted optical power. However, this is only useful in the very weak turbulence regime and must meet the eye safety requirement. Modulation schemes adopted must meet the emitted power requirement to ensure the power budget limitation and the eye safety regulations. The OOK-FSO system with a fixed threshold level in the presence of turbulence induced fading channel displayed increased BER performance. Therefore, it would be advantageous to adopt the optimum decision making scheme but at the cost of increased complexity. For instance, for an SNR of 49 dB in a moderate turbulence regime, the BERs are 0.05 and 4×10^{-4} for fixed and adaptive threshold detection schemes, respectively.

The heterodyne BPSK modulated FSO system is based on the coherent optical detection and the synchronous demodulation using an electrical PLL. However, the phase noise sensitivity of such coherent systems is considerably high due to the PLL circuit. For low values of phase error variance (e.g. $\sigma_{\Delta} = 0.1$), the power penalty can be neglected since the degradation is not high. However, for higher values of variance ($\sigma_{\Delta} \geq 0.3$) the power

penalty causes a significant shift in the BER floor. For example, in the case of $\sigma_{\Delta} = 0.3$ and 0.5, the BER floor are equal to 5.4×10^{-6} and 7.7×10^{-3} , respectively.

The error performance and the outage probability for a BPOLSK-FSO employing the diversity receiver were analysed in Chapter Six. The diversity receiver was used to combat the scintillation induced channel fading. The gamma-gamma and lognormal channel models were considered. The details of error probability and achievable link margin using the EGC techniques were outlined. Additionally, the power penalty caused by the received optical signal correlation on the error probability has been shown. For instance, to achieve a BER of 10^{-9} with $\mathcal{N} = 2$, additional 4 dB of SNR is required due to the increment of ρ from 0 to 0.5. The SNR value increases to ~ 4.5 dB when ρ further increases to 0.8. For the EGC linear combining scheme adopted to mitigate the scintillation without overwhelming the complexity and cost, the reasonable number of independent photodetectors is between 2 and 4.

Chapter Seven outlined the theoretical analysis of two different coherent heterodyne MPOLSK-FSO communication systems operating over the gamma-gamma turbulence channel. To mitigate the turbulence induced fading the convolutional coding and the spatial diversity with the MRC technique were considered. The upper SEP bound was obtained using the transfer function. For example, using the first proposed coherent heterodyne 8-POLSK system to achieve a SEP of 10^{-9} in a weak turbulence regime, the SNR requirements are ~ 28.5 dB and ~ 13 dB for uncoded and coded 8-POLSK schemes, respectively.

The spatial diversity with the MRC technique ($\mathcal{N} = 4$) outperforms the uncoded 8-POLSK employing a single receiver by ~6 dB, ~17.5 dB and ~15.5 dB, respectively in weak, moderate and strong turbulence regimes. It was also shown that the spatial diversity offers increased link margin as the scintillation level rises. For the second proposed MPOLSK-FSO system in Chapter Seven, the numerical analysis of SEP of 8, 16 and 32 POLSK was carried with the PLL phase tracking error showing the sensitivity of MPOLSK to the phase error. The comparative studies showed the power penalties of ~7.5 dB, ~24.5 dB and ~25 dB at SEP of 10^{-9} in weak, moderate and strong turbulence regimes, respectively. The MPOLSK receiver combined with the MRC technique offered improved error probability performance in turbulence conditions with the optimum number of detectors in the range of two to four. For the receiver with four detectors, diversity gains achieved were ~5.8 dB, ~15.8 dB and ~13.7 dB for 16POLSK in weak, moderate and strong turbulence regimes, respectively.

The link budget equation to obtain the achievable link length under a specified link margin at a certain data rate was derived in Chapter Eight. The power loss caused by various sources has been discussed. Additionally, the link length as a function of the link margin and the receiver sensitivity for OOK and BPOLSK have been shown. In Chapter Eight, for the OOK-FSO operating at a data rate of 155 Mbps in a non-turbulent channel with a visibility of 50 km, the link lengths of around 2 km and 1.1 km were achievable at 5 dB and 10 dB link margins, respectively. For BPOLSK-FSO operating under the same conditions, the link lengths are ~ 2.3 km and ~ 1.3 km at 5 dB and 10 dB link margins,

respectively. For BPOLSK-FSO operating under the same conditions, the link lengths increased to ~ 2.3 km and ~ 1.3 km at 5 dB and 10 dB link margins, respectively.

In Chapter Nine, the implementation and full system measurements of the proposed BPOLSK-FSO system with DD operating over a link span of 6 m and 27 m were investigated. As a result of the underlying assumptions in the derivation, it was shown that there is a close match between the experimental and predicted Q -factors for the weak turbulence regimes for the BPOLSK-FSO system. For comparison the predicted and analytical results for OOK (with peak and average power levels) were also presented. BPOLSK offers a slightly higher Q -factor values compared with OOK for the same transmit optical power and the turbulence variance. For example, when the link length is 6 m and the transmitted optical power is -16.8 dBm, the Q -factors are ~ 11 and ~ 8.5 for BPOLSK and OOK, respectively, with $\sigma_t^2 = 0.003$. For the BPOLSK-FSO system with a link length of 27 metres with $\sigma_t^2 = 0.03$, the Q -factors are 4.6 and 5 for OOK and BPOLSK, respectively.

10.2 Future Work

This research work has completed the objective and aims listed in Chapter One. However, the amount of time and work required to cover the comprehensive optical wireless communication area are out of the scope of this work. The following topics are suggested to further extend the research work reported in this thesis.

Hybrid FSO/RF communication using channel coding: The reliability of FSO communication system mainly depends on the atmospheric weather conditions, especially when the link is longer than 1 km. One of the biggest challenges is the attainment of 99.99 % link availability during all weather conditions. The hybrid FSO/RF link combined with the channel coding is one possible option as the RF system could be utilised as the back-up link but at a reduced data rate when the fog is moderate to high and the channel coding can also improve the system reliability.

Soft-switching hybrid FSO/RF links using field-programmable gate array (FPGA):

To switch the hybrid FSO/RF link, the current technique is based on the “hard-switching” or selection, which is based on the receiver feedback. In this method, only one medium can be used at a time, which makes it inefficient. A short-length channel code, such as the low-density parity-check (LDPC) or the Raptor code can be used as the “soft-switching” scheme for hybrid FSO/RF links. The FPGA could be used to implement the encoder and decoder at a high speed.

Modulation Schemes Combined with LDPC: LDPC is an advanced forward error correction (FEC) schemes. It is more efficient rather than RS and convolutional codes in the presence of strong turbulence or deep fog [238, 239].

Multipath Diversity: Wireless networks suffer signal fading due to multipath propagation, which can be mitigated by time-, frequency- or spatial diversity techniques. In the spatial diversity, multiple antennas can be equipped on the transmitters and/or

receivers, which is difficult to be implemented on a sensor node or a mobile terminal due to the size limitation and the hardware complexity.

Reference

- [1] W. O. Popoola, "Subcarrier intensity modulated free-space optical communication systems," in *School of Computing, Engineering and Information Sciences*. vol. Doctor of Philosophy Newcastle: University of Northumbria, September 2009, p. 264.
- [2] M. S. Awan, P. Brandl, E. Leitgeb, F. Nadeem, T. Plank, and C. Capsoni, "Results of an optical wireless ground link experiment in continental fog and dry snow conditions," *10th International Conference on Telecommunications 2009*, p. 45, June 2009.
- [3] A. Hashmi, A. Eftekhari, S. Yegnanarayanan, and A. Adibi, "Analysis of optimum adaptive optics systems for hybrid RF-wireless optical communication for maximum efficiency and reliability," *4th International Conference on Emerging Technologies, 2008*, pp. 62-67, 18-19 October 2008.
- [4] D. Killinger, "Free space optics for laser communication through the air," *Optics & Photonics News*, pp. 36-42, October 2002.
- [5] E. Ciaramella, Y. Arimoto, G. Contestabile, M. Presi, A. D'Errico, V. Guarino, and M. Matsumoto, "1.28 terabit/s (32x40 Gbit/s) WDM transmission system for free space optical communications," *IEEE Journal on Selected Areas in Communications* vol. 27 pp. 1639 - 1645, 2009.
- [6] A. G. Bell, "On the production and reproduction of sound by light," *American Journal of Sciences, Series 3*, vol. XX, pp. 305-324, October 1880.
- [7] C. Long, "Optical communication for the amateur," in '*Amateur Radio*' magazine Melbourne: Wireless Institute of Australia, January 1979, pp. 7-14.
- [8] F. E. Goodwin, "A review of operational laser communication systems," *Proceedings of IEEE*, vol. 58, pp. 1746-1752, October 1970.
- [9] H. Hemmati, "Deep space optical communications," in *Deep space communications and navigation series*, H. Hemmati, Ed. California: Wiley-Interscience; 1 edition, April 12 2006, p. 736.
- [10] Z. Sodnik, B. Furch, and H. Lutz, "Free-space laser communication activities in Europe: SILEX and beyond," *19th Annual Meeting of the IEEE Lasers and Electro-Optics Society 2006*, pp. 78-79, October 2006.
- [11] J. N. Pelton and A. U. M. Rae, "Global satellite communications technology and systems - an overview," *Journal Space Communications*, vol. 16, pp. 55-69, August 2000.
- [12] N. D. Chatzidiamantis, H. G. Sandalidis, G. K. Karagiannidis, and M. Matthaiou, "Inverse gaussian modeling of turbulence-induced fading in free-space optical systems," *Journal of Lightwave Technology*, vol. 29, pp. 1590-1596, 2011.
- [13] A. Bekkali, C. B. Naila, K. Kazaura, K. Wakamori, and M. Matsumoto, "Transmission analysis of OFDM-based wireless services over turbulent radio-on-FSO links modeled by gamma-gamma distribution," *IEEE Photonics Journal*, vol. 2, pp. 510-520, 2010.
- [14] R. Mesleh, H. Elgala, and H. Haas, "Optical spatial modulation," *IEEE/OSA Journal of Optical Communications and Networking*, vol. 3, pp. 234-244, 2011.
- [15] S. Hardy, "Free-space optics systems are finding their niches," *Lightwave*, pp. 33-36, December 2005.

- [16] C. P. Colvero, M. C. R. Cordeiro, G. V. d. Faria, and J. P. v. d. Weid, "Experimental comparison between far- and near infrared wavelengths in free space optical systems," *Microwave and Optical Technology Letters*, vol. 46, pp. 319-323, 20 August 2005.
- [17] R. Dennis, L. Mark, G. Ganesh, P. Bruce, and N. Gerald, "Optical wireless propagation: theory vs. experiment," *Proceedings of SPIE: Optical Wireless Communications III*, vol. 4214, pp. 38-45, 2001.
- [18] E. Korevaar, I. I. Kim, and B. McArthur, "Atmospheric propagation characteristics of highest importance to commercial free space optics," *Proceeding of SPIE*, vol. 4976, pp. 1-12, 2003.
- [19] D. Y. Song, J. W. Cho, Y. S. Hurh, J. H. Lim, D. W. Lee, and J. S. Lee, "4×10 Gb/s terrestrial optical free space transmission over 1.2 km using an EDFA preamplifier with 100 GHz channel spacing," *Optical Fiber Communication Conference, 2000*, vol. 3, pp. 142-144, 2000.
- [20] M. D'Amico, A. Leva, and B. Micheli, "Free-space optics communication systems: first results from a pilot field-trial in the surrounding area of Milan, Italy," *IEEE Microwave and Wireless Components Letters*, vol. 13, pp. 305-307, August 2003.
- [21] Y. Ma, S. C. Saha, A. L. Bernassau, and D. R. S. Cumming, "Terahertz free space communication based on acoustic optical modulation and heterodyne detection," *Electronics Letters*, vol. 47, pp. 868-870, 2011.
- [22] A. Biswas and W. H. Farr, "Detectors for ground based reception of laser communication from Mars. Lasers and electro-optics society," *The 17th Annual Meeting of the IEEE Lasers and Electro-Optics Society, 2004.*, vol. 1, pp. 74-75, 7-11 November 2004.
- [23] H. Tapse, D. K. Borah, and J. Perez-Ramirez, "Hybrid optical/RF channel performance analysis for Turbo codes," *IEEE Transactions on Communications*, vol. 59, pp. 1389-1399, 2011.
- [24] N. D. Chatzidiamantis and G. K. Karagiannidis, "On the distribution of the sum of gamma-gamma variates and applications in RF and optical wireless communications," *IEEE Transactions on Communications*, vol. 59, pp. 1298-1308, 2011.
- [25] M. Gregory and S. Badri-Hoeher, "Characterization of maritime RF/FSO channel," *International Conference on Space Optical Systems and Applications (ICSOS) 2011*, pp. 21-27, 2011.
- [26] P. Y. Zhou and F. Khan, "An introduction to millimeter-wave mobile broadband systems," *IEEE Communications Magazine*, vol. 49, pp. 101-107, June 2011.
- [27] I. I. Kim, B. McArthur, and E. Korevaar, "Comparison of laser beam propagation at 785 nm and 1550 nm in fog and haze for optical wireless communications," *SPIE Proceeding: Optical Wireless Communications III*, vol. 4214, pp. 26-37, 2001.
- [28] R. Arora, S. Seth, J. C. H. Poh, J. D. Cressler, A. K. Sutton, H. M. Nayfeh, G. L. Rosa, and G. Freeman, "Impact of Source/Drain contact and gate finger spacing on the RF reliability of 45-nm RF nMOSFETs," *2011 IEEE International Reliability Physics Symposium (IRPS)*, pp. 5A.6.1 - 5A.6.6, 10-14 April 2011.
- [29] H. Izadpanah, T. ElBatt, V. Kukshya, F. Dolezal, and B. K. Ryu, "High-availability free space optical and RF hybrid wireless networks," *IEEE Wireless Communications*, vol. 10, pp. 45-53, April 2003.
- [30] M. Bettayeb and S. F. A. Shah, "State of the art ultra-wideband technology for communication systems: a review," *Proceedings of the 2003 10th IEEE*

- International Conference on Electronics, Circuits and Systems, 2003*, vol. 3, pp. 1276-1279, 2003.
- [31] K. Kazaura, K. Omae, T. Suzuki, M. Matsumoto, E. Mutaungwa, T. Murakami, K. Takahashi, H. Matsumoto, K. Wakamori, and Y. Arimoto, "Performance evaluation of next generation free-space optical communication system," *IEICE Transaction of Electronics*, vol. E90-C, pp. 381-388, February 2007.
 - [32] K. Wang, A. Nirmalathas, C. Lim, and E. Skafidas, "High speed 4×12.5Gbps WDM optical wireless communication systems for indoor applications," *the National Fiber Optic Engineers Conference Optical Fiber Communication Conference and Exposition 2011*, pp. 1-3, 2011.
 - [33] Z. W. Xu, X. F. Cheng, Y. K. Yeo, L. Y. Zhou, X. Shao, and H. G. Zhang, "1.24-Tb/s hybrid SCM/WDM passive optical networks," pp. 1-3, 2011.
 - [34] S.-R. Moon, H.-K. Lee, and C.-H. Lee, "Automatic wavelength control method using Rayleigh backscattering for WDM-PON with tunable lasers," *Conference on Lasers and Electro-Optics (CLEO) 2011*, pp. 1-2, 2011.
 - [35] M. Sjödin, E. Agrell, P. Johannisson, G. W. Lu, P. A. Andrekson, and M. Karlsson, "Filter optimization for self-homodyne coherent WDM systems using interleaved polarization division multiplexing," *Journal of Lightwave Technology*, vol. 29, pp. 1219-1226, 2011.
 - [36] H. Willebrand and B. S. Ghuman, *Free space optics: enabling optical connectivity in today's network*: SAMS publishing: 1 edition, December 31, 2001.
 - [37] M. N. Khan and W. G. Cowley, "Signal dependent Gaussian noise model for FSO communications," *Australian Communications Theory Workshop 2011*, pp. 142-147, 2011.
 - [38] C. Abou-Rjeily, "On the optimality of the selection transmit diversity for MIMO-FSO links with feedback," *IEEE Communications Letters*, vol. 15, pp. 641-643, 2011.
 - [39] T. Plank, M. Czaputa, E. Leitgeb, S. S. Muhammad, N. Djaja, B. Hillbrand, P. Mandl, and M. Schonhuber, "Wavelength selection on FSO-links," *Proceedings of the 5th European Conference on Antennas and Propagation (EUCAP)*, pp. 2508-2512, 2011.
 - [40] I. Kim, R. Stieger, C. Moursund, J. A. Koontz, M. Barclay, P. Adhikari, J. Schuster, and E. Korevaar, "Wireless optical transmission of fast ethernet, FDDI, ATM, and ESCON protocol data using the TerraLink laser communication system," *Optical Engineering (1998)*, vol. 37, pp. 3143-3155, December 1998.
 - [41] W. Gappmair, S. Hranilovic, and E. Leitgeb, "OOK performance for terrestrial FSO links in turbulent atmosphere with pointing errors modeled by Hoyt distributions," *IEEE Communications Letters*, vol. 15, pp. 875-877, 2011.
 - [42] R. R. Iniguez, S. M. Idrus, and Z. Sun, *Optical wireless communications - IR for wireless connectivity*. London: Taylor & Francis Group, LLC, 2008.
 - [43] A. García-Zambrana, C. Castillo-Vázquez, and B. Castillo-Vázquez, "Rate-adaptive FSO links over atmospheric turbulence channels by jointly using repetition coding and silence periods," *Optics Express*, vol. 18, pp. 25422-25440, 2010.
 - [44] C. B. Naila, A. Bekkali, K. Wakamori, and M. Matsumoto, "Performance analysis of CDMA-based wireless services transmission over a turbulent RF-on-FSO channel," *Journal of Optical Communications and Networking IEEE/OSA*, vol. 3, pp. 475-486, 2011.
 - [45] Z. X. Wang, W. D. Zhong, S. N. Fu, and C. Lin, "Performance comparison of different modulation formats over free-space optical (FSO) turbulence links with

- space diversity reception technique," *IEEE Photonics Journal*, vol. 1, pp. 277-285, December 2009.
- [46] M. Chiani, A. Giorgetti, S. Minardi, E. Paolini., and M. Taormina, "Heterogeneous wireless/power line communication networks for energy metering and control," *Proceedings of the 34th International Convention MIPRO 2011*, pp. 624-628, 2011.
 - [47] A. Cataliotti, D. D. Cara, R. Fiorelli, and G. Tine, "Power-line communication in medium-voltage system: simulation model and onfield experimental tests," *IEEE Transactions on Power Delivery*, vol. 27, pp. 62-69, 2012.
 - [48] M. Bharathi and S. Ravishankar, "A combined correlation TDR and FDR procedure for Single Ended Loop topology estimation in DSL," *IEEE International Conference on Signal Processing, Communications and Computing (ICSPCC) 2011*, pp. 1-6, 2011.
 - [49] D. Acatauassu, F. Muller, and A. Klautau, "Capacity of MIMO DSL systems using 100 MHz measured channel data," *International Conference on Telecommunications 2009*, 2009.
 - [50] Z. Zhu, "A novel energy-aware design to build green broadband cable access networks," *IEEE Communications Letters*, vol. 15, pp. 887-889, 2011.
 - [51] Y.-S. Kim, D.-J. Choi, and J.-K. Pack, "Design and implementation of 4-channel upstream modulator in cable modem," *2011 International Conference on ICT Convergence (ICTC)*, pp. 681-682, 2011.
 - [52] C. F. Lam, "The road to scalable 1Gb/s FTTH access networks," *2011 37th European Conference and Exhibition on Optical Communication*, pp. 1-3, 2011.
 - [53] Z. A. El-Sahn, W. Mathlouthi, H. Fathallah, S. LaRochelle, and L. A. Rusch, "Dense SS-WDM over legacy PONs: smooth upgrade of existing FTTH networks," *Journal of Lightwave Technology*, vol. 28, pp. 1485-1495, 2010.
 - [54] K.-S. Chin, H.-T. Chang, and J.-A. Liu, "Design of LTCC wideband patch antenna for LMDS band applications," *IEEE Antennas and Wireless Propagation Letters*, vol. 9, pp. 1111-1114, 2010.
 - [55] M. Anastasopoulos, D. Petraki, and C. Hsiao-Hwa, "Secure communications in local multipoint distribution service (LMDS) networks," *IEEE Transactions on Wireless Communications*, vol. 8, pp. 5400-5403, 2009.
 - [56] D. Rajesh and P. K. Sahu, "Compact UWB notch filter parasitic microstrip antenna," *2011 International Workshop on Antenna Technology (iWAT)*, pp. 278-281, 2011.
 - [57] T.-Y. Lu and W.-Z. Chen, "A 3–10 GHz, 14 bands CMOS frequency synthesizer with spurs reduction for MB-OFDM UWB system," *IEEE Transactions on Very Large Scale Integration (VLSI) Systems*, vol. PP, pp. 1-11, 2011.
 - [58] J. Baliga, R. Ayre, K. Hinton, and R. S. Tucker, "Energy consumption in wired and wireless access networks," *IEEE Communications Magazine*, vol. 49, pp. 70-77, 2011.
 - [59] BuddeComm, "Global - Broadband - FTTH overview & statistics," May 2009.
 - [60] A. Nordbotten, "LMDS systems and their application," *IEEE. Communications Magazine*, vol. 38, pp. 150-154, 2000.
 - [61] R. C. Qiu, H. Liu, and X. Shen, "Ultra-wideband for multiple access communications," *IEEE Communications Magazine*, vol. 43, pp. 80-87, 2005.
 - [62] T. Kamalakis, T. Sphicopoulos, S. S. Muhammad, and E. Leitgeb, "Estimation of the power scintillation probability density function in free-space optical links by use of multicanonical Monte Carlo sampling," *Optics Letters*, vol. 31, pp. 3077-3079, November 2006.

- [63] D. Kedar and S. Arnon, "Optical wireless communication through fog in the presence of pointing errors," *Applied Optics*, vol. 42, pp. 4946-4954, August 2003.
- [64] N. H. M. Noor, A. W. Naji, and W. Al-Khateeb, "Theoretical analysis of multiple transmitters/receivers on the performance of free space optics (FSO) link," *IEEE International Conference on Space Science and Communication 2011*, pp. 291-295, July 2011.
- [65] D. Kedar and S. Arnon, "Urban optical wireless communication networks: the main challenges and possible solutions," *IEEE Communications Magazine*, vol. 42, pp. S2-S7, May 2004.
- [66] X. Zhu and J. M. Kahn, "Free-space optical communication through atmospheric turbulence channels," *IEEE Transactions on Communications*, vol. 50, pp. 1293-1300, August 2002.
- [67] S. Karp, R. M. Gagliardi, S. E. Moran, and L. B. Stotts, *Optical channels: fibers, cluds, water and the atmosphere*. New York: Plenum Press, 1988.
- [68] S. Bloom, E. Korevaar, J. Schuster, and H. Willebrand, "Understanding the performance of free-space optics," *Journal of Optical Networking*, vol. 2, pp. 178-200, June 2003.
- [69] W. K. Pratt, *Laser communication systems*. New York: John Wiley & Sons, Inc., 1969.
- [70] M. S. Khan, M. S. Awan, S. S. Muhammad, V. Kvicera, M. Grabner, C. Capsoni, E. Leitgeb, and P. Mandl, "Linearity in optical attenuations for free-space optical links in continental fog," *Proceedings of the 5th European Conference on Antennas and Propagation*, pp. 2504-2507, 2011.
- [71] M. S. Awan, P. Brandl, E. Leitgeb, F. Nadeem, L. Csugai-Horvath, and R. Nebuloni, "Transmission of high data rate optical signals in fog and snow conditions," in *Wireless VITAE 2009 Aalborg*, Denmark, 17-20 May 2009, pp. 702 - 706.
- [72] P. P. Smyth, P. L. Eardley, K. T. Dalton, D. R. Wisely, P. McKee, and D. Wood, "Optical wireless: a prognosis," *Proceeding of SPIE*, vol. 2601, pp. 212-225, 1995.
- [73] M. A. Bramson, *Infrared radiation: a handbook for applications*. New York: Plenum Press, 1968.
- [74] P. L. Eardley, D. R. Wisely, D. Wood, and P. McKee, "Holograms for optical wireless LANs," *IEE Proceedings - Optoelectronics*, vol. 143, pp. 365-369, December 1996.
- [75] E. Leitgeb, S. S. Muhammad, B. Flecker, C. Chlestil, M. Geghart, and T. Javornik, "The influence of dense fog on optical wireless systems, analysed by measurements in Graz for improving the link-reliability," *International Conference on Transparent Optical Networks 2006*, vol. 3, pp. 154-159, June 2006.
- [76] S. Bloom and W. S. Hartley, "The last-mile solution: hybrid FSO radio," *AirFiber, Inc.*, May 2002.
- [77] B. Flecker, E. Leitgeb, S. S. Muhammad, C. Chlestil, and M. Gebhart, "Results of attenuation measurements for optical wireless channels under dense fog conditions regarding different wavelengths," *SPIE proceedings*, vol. 6303, p. 63030P, 15 August 2006.
- [78] M. A. Naboulsi and H. Sizun, "Fog attenuation prediction for optical and infrared waves," *Optical Engineering*, vol. 23, pp. 319-329, 2004.

- [79] M. A. Al-Habash, L. C. Andrews, and R. L. Phillips, "Mathematical model for the irradiance probability density function of a laser beam propagating through turbulent media," *Optical Engineering*, vol. 40, pp. 1554-1562, August 2001.
- [80] I. B. Djordjevic, "Adaptive modulation and coding for free-space optical channels," *IEEE/OSA Journal of Optical Communications and Networking*, vol. 2, pp. 221-229, May 2010.
- [81] I. I. Kim, J. Koontz, H. Hakakha, P. Adhikari, R. Stieger, C. Moursund, M. Barclay, A. Stanford, R. Ruigrok, J. J. Schuster, and E. J. Korevaar, "Measurement of scintillation and link margin for the TerraLink laser communication system," *Wireless Technology and Systems: Millimeter Wave and Optical, Proceedings of SPIE*, vol. 3232, pp. 100-118, 23 January 1998.
- [82] J. C. Brandenburg and J. Q. Liu, "Optical signal detection in the turbulent atmosphere using p-i-n photodiodes," *IEEE Journal on Selected Areas in Communications*, vol. 27, pp. 1564-1571, December 2009.
- [83] I. I. Kim, M. Mitchell, and E. J. Korevaar, "Measurement of scintillation for free-space laser communication at 785 nm and 1550 nm," *Optical Wireless Communications II, Proceedings of SPIE*, vol. 3850, pp. 49-52, September 1999.
- [84] V. W. S. Chan, "Free-space optical communications," *IEEE Journal of Lightwave Technology*, vol. 24, pp. 4750-4762, December 2006.
- [85] A. K. Majumdar and J. C. Ricklin, *Free-space laser communications: principles and advances*. New York: NY: Springer, 2008.
- [86] A. Jurado-Navas and A. Puerta-Notario, "Generation of correlated scintillations on atmospheric optical communications," *IEEE/OSA Journal of Optical Communications and Networking*, vol. 1, pp. 452-462, 2009.
- [87] C. B. Naila, A. Bekkali, K. Kazaura, K. Wakamori, and M. Matsumoto, "Evaluating M-ary PSK multiple-subcarrier modulation over FSO links using aperture averaging," *Proceedings of the SPIE*, vol. 7814, pp. 78140V-78140V-11, August 2010.
- [88] X. Zhu and J. M. Kahn, "Performance bounds for coded free-space optical communications through atmospheric turbulence channels," *IEEE Transactions on Communications*, vol. 51, pp. 1233-1239, August 2003.
- [89] A. Khatoon, W. G. Cowley, and N. Letzepis, "Channel measurement and estimation for free space optical communications," *Australian Communications Theory Workshop (AusCTW) 2011*, pp. 112-117, 2011.
- [90] N. Letzepis and A. G. i. Fabregas, "Outage probability of the Gaussian MIMO free-space optical channel with PPM," *IEEE Transactions on Communications*, vol. 57, pp. 3682-3690, 2009.
- [91] A. Molisch, "Statistical description of the wireless channel," in *Wireless Communications - Edition 1*: Wiley-IEEE Press, 2011, pp. 69-99.
- [92] N. Beaulieu, "An extended limit theorem for correlated lognormal sums," *IEEE Transactions on Communications*, vol. PP, pp. 1-4, 2011.
- [93] C. Abou-Rjeily and A. Slim, "Cooperative diversity for free-space optical communications: transceiver design and performance analysis," *IEEE Transactions on Communications*, vol. 59, pp. 658-663, 2011.
- [94] M. Uysal, L. Jing, and Y. Meng, "Error rate performance analysis of coded free-space optical links over gamma-gamma atmospheric turbulence channels," *IEEE Transactions on Wireless Communications*, vol. 5, pp. 1229-1233, June 2006.
- [95] G. R. Osche, *Optical detection theory for laser applications*: Wiley, New Jersey, 2002.

- [96] L. C. Andrews, R. L. Philips, and C. Y. Hopen, *Laser beam scintillation with applications*: Bellingham: SPIE, 2001.
- [97] L. C. Andrews and R. L. Phillips, *Laser beam propagation through random media*. Bellingham: WA: SPIE, 1998.
- [98] M.-A. Khalighi, N. Schwartz, N. Aitamer, and S. Bourennane, "Fading reduction by aperture averaging and spatial diversity in optical wireless systems," *IEEE/OSA Journal of Optical Communications and Networking*, vol. 1, pp. 580-593, November 2009.
- [99] M. Abtahi, P. Lemieux, W. Mathlouthi, and L. A. Rusch, "Suppression of turbulence-induced scintillation in free-space optical communication systems using saturated optical amplifiers," *Journal of Lightwave Technology*, vol. 24, p. 4966, December 2006.
- [100] X. Zhu and J. M. Kahn, "Pairwise codeword error probability for coded free-space optical communication through atmospheric turbulence channels," *IEEE International Conference on Communications, 2001*, vol. 1, pp. 161-164, 11-14 June 2001.
- [101] J. E. Grave and S. Drenker, "Advancing free space optical communication with adaptive optics," *Lightwaveonline*, vol. 19, pp. 105-113, September 2002.
- [102] X. Zhu, J. M. Kahn, and J. Wang, "Mitigation of turbulence-induced scintillation noise in free-space optical links using temporal-domain detection techniques," *IEEE Photonics Technology Letters*, vol. 15, pp. 623 - 625, April 2003.
- [103] E. J. Lee and V. W. S. Chan, "Optical communication over the clear turbulent atmospheric channel using diversity," *IEEE Journal on Selected Areas in Communications* vol. 22, pp. 1896-1906, November 2004.
- [104] W. Huang, J. Takayanagi, T. Sakanaka, and M. Nakagawa, "Atmospheric optical communication system using subcarrier PSK modulation," *IEEE International Conference on Communications, 1993*, vol. 3, pp. 1597 - 1601, 23 - 26 May 1993.
- [105] L. Jia, J. Q. Liu, and D. P. Taylor, "Optical communication using subcarrier PSK intensity modulation through atmospheric turbulence channels," *IEEE Transactions on Communications*, vol. 55, pp. 1598-1606, August 2007.
- [106] I. Seto, T. Ohtsuki, H. Yshima, I. Sasase, and S. Mori, "Coherent optical polarization-shift-keying (PolSK) homodyne system using phase-diversity receivers," *Global Telecommunications Conference, 1991*, vol. 3, pp. 1601 - 1605, 2 - 5 December 1991.
- [107] M. Nazarathy and E. Simony, "Error probability performance of equi-energy combined transmission of differential phase, amplitude, and polarization," *Journal of Lightwave Technology*, vol. 25, pp. 249-260, January 2007.
- [108] S. Benedetto, R. Gaudino, and P. Poggiolini, "Performance of coherent optical polarization shift keying modulation in the presence of phase noise," *IEEE Transactions on Communications*, vol. 43, pp. 1603-1612 1995.
- [109] Z. Ghassemlooy, W. O. Popoola, and E. Leitgeb, "Free-space optical communication using subcarrier modulation in gamma-gamma atmospheric turbulence," *9th International Conference on Transparent Optical Networks, 2007*, vol. 3, pp. 156 - 160, 1 - 5 July 2007.
- [110] N. Chi, S. Yu, L. Xu, and P. Jeppesen, "Generation and transmission performance of 40 Gbit/s polarisation shift keying signal," *Electronics Letters*, vol. 41, pp. 547 - 549, 28 April 2005.
- [111] J. Grosinger, "Investigation of polarization modulation in optical free space communications through the atmosphere." vol. master: Technical University of Vienna, February 2008, p. 77.

- [112] M. M. Karbassian and H. Ghafouri-Shiraz, "Transceiver architecture for incoherent optical CDMA network based on polarization modulation," *Journal of Lightwave Technology*, vol. 26, pp. 3820-3828, 15 December 2008.
- [113] X. Zhao, Y. Yao, Y. Sun, and C. Liu, "Circle polarization shift keying with direct detection for free-space optical communication," *IEEE/OSA Journal of Optical Communications and Networking* vol. 1, pp. 307-312, September 2009.
- [114] A. A. M. Saleh, "An investigation of laser wave depolarization due to atmospheric transmission," *IEEE Journal of Quantum Electronics*, vol. 3, p. 256, June 1967.
- [115] X. Tang, Z. Ghassemloooy, S. Rajbhandari, W. O. Popoola, and C. G. Lee, "Coherent polarization shift keying modulated free space optical links over a gamma-gamma turbulence channel," *American Journal of Engineering and Applied Sciences*, vol. 4, pp. 520-530, Janary 2012.
- [116] E. Hu, Y. Hsueh, K. Wong, M. Marhic, L. Kazovsky, K. Shimizu, and N. Kikuchi, "4-level direct-detection polarization shift-keying (DD-PolSK) system with phase modulators," in *Proceedings of Optical Fiber Communication Conference and Exposition (OFC)*. vol. 2 Atlanta, USA, 23-28 March 2003, pp. 647- 649.
- [117] S. Betti, G. D. Marchis, and E. Iannone, "Polarization modulated direct detection optical transmission systems," *Journal of Lightwave Technology*, vol. 10, pp. 1985-1997, December 1992.
- [118] S. Benedetto, R. Gaudino, and P. Poggiolini, "Direct detection of optical digital transmission based on polarization shift keying modulation," *IEEE Journal on Selected Areas in Communications*, vol. 13, pp. 531-542 April 1995.
- [119] G. J. Foschini, L. J. Greenstein, and G. Vannucci, "Noncoherent detection of coherent lightwave signals corrupted by phase noise," *IEEE Transactions on Communications*, vol. 36, pp. 306-314, March 1988.
- [120] S. Benedetto and P. Poggiolini, "Theory of polarization shift keying modulation," *IEEE Transactions on Communications*, vol. 40, pp. 708-721, April 1992.
- [121] K.-S. Hou and J. Wu, "A differential coding method for the symmetrically differential polarization shift-keying system," *IEEE Transactions on Communications*, vol. 50, pp. 2042-2051, December 2002.
- [122] T. Yamashita, M. Morita, M. Shimizu, D. Eto, K. Shiratama, and S. Murata, "The new tracking control system for free-space optical communications," *2011 International Conference on Space Optical Systems and Applications (ICSOS)*, pp. 122-131, 2011.
- [123] X. Wu, P. Liu, and M. Matsumoto, "A study on atmospheric turbulence effects in full-optical free-space communication systems," *6th International Conference on Wireless Communications Networking and Mobile Computing 2010 (WiCOM)*, pp. 1-5, 2010.
- [124] S. A. J. Flórez, "Circular polarization and availability in free space optics (FSO) communication systems," *IEEE Latin-American Conference on Communications (LATINCOM) 2010*, pp. 1-6, 2010.
- [125] D. K. Hendraningrat, "Analysis of slot spectrum selection for long term evolution (LTE)," *2011 6th International Conference on TSSA*, pp. 267-270, 2011.
- [126] A. Andreescu, A. Ghita, A. A. Enescu, and C. Anghel, "Long term evolution primary synchronization algorithms," *2010 9th International Symposium on ISETC*, pp. 125-128, 2010.
- [127] M. Niu, J. Cheng, and J. F. Holzman, "Diversity reception for coherent free-space optical communications over K-distributed atmospheric turbulence channels,"

- IEEE Wireless Communications and Networking Conference (WCNC) 2010*, pp. 1-6, 2010.
- [128] A. C. Boucouvalas, "Editorial," *EURASIP Journal on Wireless Communications and Networking* 2005, vol. 2005, pp. 1-2, 2005.
 - [129] E. Dadrasnia, S. Ebrahimzadeh, and F. R. M. Adikan, "Influence of short range free space optical atmospheric attenuation in modulated radio signal," *The 2nd International Conference on Computer and Automation Engineering (ICCAE) 2010*, vol. 5, pp. 569-571, 2010.
 - [130] S. A. Zabidi, W. A. Khateeb, M. R. Islam, and A. W. Naji, "Investigating of rain attenuation impact on free space optics propagation in tropical region," *4th International Conference On Mechatronics 2011*, pp. 1-6, 2011.
 - [131] L. Peng, X. Wu, K. Wakamori, T. D. Pham, M. S. Alam, and M. Matsumoto, "Bit error rate performance analysis of optical CDMA time-diversity links over gamma-gamma atmospheric turbulence channels," *IEEE Wireless Communications and Networking Conference (WCNC) 2011*, pp. 1932-1936, 2011.
 - [132] J. Akella, M. Yuksel, and S. Kalyanaraman, "Multi-channel communication in free-space optical networks for the last-mile," *15th IEEE Workshop on Local & Metropolitan Area Networks*, 2007, pp. 43 - 48 10-13 June 2007
 - [133] A. Salehiomran and J. A. Salehi, "Spatial heterodyning optical code division multiple access technique for near-field free-space optical communication systems," *IEEE/OSA Journal of Optical Communications and Networking*, vol. 1, pp. 498-511 2009.
 - [134] W. S. Yu, J. S. Lai, H. B. Ma, and C. Zheng, "High-Efficiency DC–DC Converter With Twin Bus for Dimmable LED Lighting," *IEEE Transactions on Power Electronics*, vol. 26, pp. 2095-2100, 2011.
 - [135] S. Betti, G. D. Marchis, and E. Iannone, *Coherent optical communications systems*. New York: John Wiley & Son, Inc., 1995.
 - [136] R. M. Gagliardi and S. Karp, "The optical communication system," in *Optical Communications*, J. G. Proakis, Ed. New York: John Wiley & Sons, Inc, 1995, pp. 1-3.
 - [137] X. Liu, "Free-space optics optimization models for building sway and atmospheric interference using variable wavelength," *IEEE Transactions on Communications*, vol. 57, pp. 492-498, 2009.
 - [138] L. Hong and W. Xinmin, "Study of scattering characteristics of atmospheric aerosol particles based on infrared laser," *2011 Symposium on Photonics and Optoelectronics*, pp. 1-5, 2011.
 - [139] Z. Zhang, "Quantitative microplasma electron number density measurement by coherent microwave Rayleigh scattering," *IEEE Transactions on Plasma Science*, vol. 39, pp. 593-595, 2011.
 - [140] G. Keiser, *Optical communications essentials 1st ed.*: New York: McGraw-Hill Professional, 2003.
 - [141] T. S. Chu and M. J. Gans, "High speed infrared local wireless communication," *IEEE Communications Magazine*, vol. 25, pp. 4-10, 1987.
 - [142] J. J. G. Fernandes, P. A. Watson, and J. C. Neves, "Wireless LANs: Physical Properties of Infra-Red Systems vs. Mmw Systems," *IEEE Communications Magazine*, vol. 32, pp. 68-73, August 1994.
 - [143] M. Capelli-Schellpfeffer, "Signaling safety [electrical safety]," *IEEE Industry Applications Magazine*, vol. 17, p. 6, 2011.

- [144] L. Matthews and G. Garcia, *Laser and eye safety in the laboratory*: Institute of Electrical & Electronics Engineer, January 1995.
- [145] O. Bouchet, H. Sizun, C. Boisrobert, F. D. Fornel, and P. Favenec, *Free-space optics: propagation and communication*. London: ISTE Ltd, 2006.
- [146] J. M. Kahn and J. R. Barry, "Wireless infrared communications," *Proceedings of the IEEE*, vol. 85, pp. 265-298, 1997.
- [147] J. W. Goodman, *Statistical optics*. New York: Wiley-Interscience, January 18, 1985.
- [148] S. F. Clifford, "The classical theory of wave propagation in a turbulent medium," in *Laser Beam Propagation in the Atmosphere*, J. W. Strohbehn, Ed.: Springer-Verlag, 1978.
- [149] D. Chen, X. Z. Ke, and Q. Sun, "Outage probability and average capacity research on wireless optical communication over turbulence channel," *2011 10th International Conference on Electronic Measurement & Instruments (ICEMI)*, vol. 1, pp. 19-23, 2011.
- [150] A. Kolmogorov, "Turbulence," in *Classic Papers on Statistical Theory*, S. K. Friedlander and L. Topper, Eds. New York: Wiley-Interscience, 1961.
- [151] A. Kolmogorov, "The local structure of turbulence in incompressible viscous fluid for very large Reynold numbers," *Proceeding of Royal Society of London Series A- Mathematical and Physical*, vol. 434, pp. 9-13, 1991.
- [152] V. I. Tatarski, *Wave propagation in a turbulent medium*. (Translated by R.A. Silverman). New York: McGraw-Hill, 1961.
- [153] A. Ishimaru, *The beam wave case and remote sensing* vol. 25. New York: Springer-Verlag, 1978.
- [154] R. M. Gagliardi and S. Karp, *Optical communications, 2nd ed.* New York: John Wiley, 1995.
- [155] H. Hodara, "Laser wave propagation through the atmosphere," *Proceedings of the IEEE*, vol. 54, pp. 368-375, March 1966.
- [156] J. W. Strohbehn, "Line-of-sight wave propagation through the turbulent atmosphere," *Proceedings of the IEEE*, vol. 56, pp. 1301-1318, August 1968.
- [157] H. G. Sandalidis, "Coded free-space optical links over strong turbulence and misalignment fading channels," *IEEE Transactions on Communications*, vol. 59, pp. 669-674, 2011.
- [158] A. Jurado-Navas, A. Garcia-Zambrana, and A. Puerta-Notario, "Efficient lognormal channel model for turbulent FSO communications," *Electronics Letters*, vol. 43, pp. 178-179, February 2007.
- [159] H. Hemmati, "Interplanetary laser communications," *Optics and Photonics News*, vol. 18, pp. 22-27, November 2007.
- [160] S. G. Wilson, M. Brandt-Pearce, Q. Cao, and J. H. Leveque, "Free-space optical MIMO transmission with Q-ary PPM," *IEEE Transactions on Communications*, vol. 53, pp. 1402-1412 August 2005.
- [161] A. Garcia-Zambrana, "Error rate performance for STBC in free-space optical communications through strong atmospheric turbulence," *IEEE Communications Letters*, vol. 11, pp. 390 - 392, May 2007
- [162] J. H. Churnside and S. F. Clifford, "Log-normal Rician probability density function of optical scintillations in the turbulent atmosphere," *Journal of Optical Society of America*, vol. 4, pp. 1923-1930, October 1987.
- [163] L. C. Andrews and R. L. Phillips, "I-K distribution as a universal propagation model of laser beams in atmospheric turbulence," *Journal of Optical Society of America*, vol. 2, pp. 160-163, 1985.

- [164] G. Parry and P. N. Pusey, "K distributions in atmospheric propagation of laser light," *Journal of Optical Society of America*, vol. 69, pp. 796-798, 1979.
- [165] S. F. Clifford and R. J. Hill, "Relation between irradiance and log-amplitude variance for optical scintillation described by the K distribution," *Journal of Optical Society of America*, vol. 71, pp. 112-114, 1981.
- [166] N. D. Chatzidiamantis, A. S. Lioumpas, G. K. Karagiannidis, and S. Arnon, "Adaptive subcarrier PSK intensity modulation in free space optical systems," *IEEE Transactions on Communications*, vol. 59, pp. 1368-1377, May 2011.
- [167] C.-A. Yeh and Y.-S. Lai, "Digital pulsewidth modulation technique for a synchronous buck DC/DC converter to reduce switching frequency," *IEEE Transactions on Industrial Electronics*, vol. 59, pp. 550-561, 2012.
- [168] M. Selmi, C. Gosset, M. Noelle, P. Ciblat, and Y. Jaouen, "Block-wise digital signal processing for PolMux QAM/PSK optical coherent systems," *Journal of Lightwave Technology*, vol. 29, pp. 3070-3082, 2011.
- [169] J. J. Yu, Z. Dong, X. F. Tang, W. Jian, Y. Xia, S. Shi, S. H. Fan, and G. K. Chang, "Generation of 432Gb/s single-carrier optical signal by format conversion from QPSK to 16QAM," *2011 and the National Fiber Optic Engineers Conference Optical Fiber Communication Conference and Exposition (OFC/NFOEC)*, pp. 1-3, 2011.
- [170] H. Samimi and P. Azmi, "Performance analysis of adaptive subcarrier intensity-modulated free-space optical systems," *IET Optoelectronics*, vol. 5, pp. 168-174, 2011.
- [171] N. D. Chatzidiamantis, A. S. Lioumpas, G. K. Karagiannidis, and S. Arnon, "Optical wireless communications with adaptive subcarrier PSK intensity modulation," *2010 IEEE Global Telecommunications Conference GLOBECOM 2010*, pp. 1-6, 2010.
- [172] E. Bayaki, R. Schober, and R. K. Mallik, "Performance analysis of MIMO free-space optical systems in gamma-gamma fading," *IEEE Transactions on Communications*, vol. 57, pp. 3415-3424, November 2009.
- [173] Y. Zhao, X. Yu, X. Zheng, I. T. Monroy, and H. Zhang, "Generalized tensor analysis model for multi-subcarrier analog optical systems," *Journal of Lightwave Technology*, vol. PP, 2011.
- [174] J. Karout, E. Agrell, and M. Karlsson, "Power efficient subcarrier modulation for intensity modulated channels," *Optics Express*, vol. 18, pp. 17913-17921, 2010.
- [175] J. Ilic and T. Strohmer, "Average power reduction for MSM optical signals via sparsity and uncertainty principle," *IEEE Transactions on Communications*, vol. 58, pp. 1505-1513, 2010.
- [176] W. Kang and S. Hranilovic, "Power reduction techniques for multiple-subcarrier modulated diffuse wireless optical channels," *IEEE Transactions on Communications*, vol. 56, pp. 279-288, 2008.
- [177] A. Baylón-Fuentes, P. Hernández-Nava, I. E. Zaldívar-Huerta, J. Rodríguez-Asomoza, A. García-Juárez, and G. Aguayo-Rodríguez, "Microwave signal generation based on optical heterodyne and its application in optical telecommunication system," *21st International Conference on Electrical Communications and Computers 2011*, pp. 334-338, 2011.
- [178] F. Constantin, "Phase-coherent heterodyne detection in the terahertz regime with a photomixer," *IEEE Journal of Quantum Electronics*, vol. PP, p. 1, 2011.
- [179] S. K. Ibrahim, S. Sygletos, R. Weerasuriya, and A. D. Ellis, "Real-time self-heterodyne coherent receiver for BPSK signals using feed-forward carrier extraction," *Conference on Lasers and Electro-Optics 2011*, pp. 1-2, 2011.

- [180] H. P. Forstner, M. Ortner, and L. Verweyen, "A fully integrated homodyne upconverter MMIC in SiGe:C for 60 GHz wireless applications," *2011 IEEE 11th Topical Meeting on Silicon Monolithic Integrated Circuits in RF Systems (SiRF)*, pp. 129-132, 2011.
- [181] S. L. Zhang, L. Xu, P. Y. Kam, C. Y. Yu, J. Chen, and T. Wang, "A performance investigation of adaptive phase estimations in coherent optical communications," *IEEE Photonics Technology Letters*, vol. 23, pp. 462-464, 2011.
- [182] J. K. Fischer, R. Ludwig, L. Molle, C. Schmidt-Langhorst, C. C. Leonhardt, A. Matiss, and C. Schubert, "High-speed digital coherent receiver based on parallel optical sampling," *Journal of Lightwave Technology*, vol. 29, pp. 378-385, 2011.
- [183] G. F. Li, "Recent advances in coherent optical communication," *Advances in Optics and Photonics I*, pp. 279-307, 2009.
- [184] K. Kikuchi, *Coherent optical communication systems*: Elsevier Inc., 2008.
- [185] S. Adhikari, S. L. Jansen, M. Alfiad, B. Inan, V. A. J. M. Sleiffer, A. Lobato, P. Leoni, and W. Rosenkranz, "Self-coherent optical OFDM: An interesting alternative to direct or coherent detection," *13th International Conference on Transparent Optical Networks 2011*, pp. 1-4, 2011.
- [186] S. Farugue, "Application of orthogonal on-off keying (O3K) based optical CDMA in free space laser communication," *4th Annual Canopus Fly by Wireless Workshop (FBW) 2011*, p. 1, 2011.
- [187] D. Zaccarin, D. Angers, and T. H. Huynh, "Performance analysis of optical heterodyne PSK receivers in the presence of phase noise and adjacent channel interference," *Journal of Lightwave Technology*, vol. 8, pp. 353-366, March 1990.
- [188] A. Yi, L. Yan, B. Luo, W. Pan, and J. Ye, "All optical signal regeneration in polarization-division-multiplexing systems," *IEEE Photonics Journal*, vol. 3, pp. 703-712, 2011.
- [189] G. D. Xie, F. X. Wang, A. Dang, and H. Guo, "A novel polarization-multiplexing system for free-space optical links," *IEEE Photonics Technology Letters*, vol. 23, pp. 1484-1486, 2011.
- [190] J. Strohbehn and S. Clifford, "Polarization and angle-of-arrival fluctuations for a plane wave propagated through a turbulent medium," *IEEE Transactions on Antennas and Propagation*, vol. 15, pp. 416-421, May 1967.
- [191] D. H. Hohn, "Depolarisation of a laser beam at 6328 Angstrom due to atmospheric transmission," *Applied Optics*, vol. 8, pp. 367-369, February 1969.
- [192] E. Collett, *Polarized light: fundamentals and applications*. New York: Marcel Dekker, Inc., 1993.
- [193] D. Clarke and J. F. Grainger, *Polarized light and optical measurement (monographs in natural philosophy)* vol. 35. Oxford: Pergamon Press; 1st edition, 1971.
- [194] S. Benedetto and P. T. Poggiolini, "Multilevel polarization shift keying: optimum receiver structure and performance evaluation," *IEEE Transactions on Communications*, vol. 42, pp. 1174-1186, April 1994.
- [195] S. Benedetto, A. Djupsjobacka, B. Lagerstrom, R. Paoletti, P. Poggiolini, and G. Mijic, "Multilevel polarization modulation using a specifically designed LiNbO3 device," *IEEE Photonics Technology Letters*, vol. 6, pp. 949-951, August 1994.
- [196] G. Keiser, *Optical fiber communications: Third Edition*. Boston: McGRAW-HILL International Editions 2000.
- [197] A. O. Aladeloba, A. J. Phillips, and M. S. Woolfson, "Improved bit error rate evaluation for optically pre-amplified free-space optical communication systems in turbulent atmosphere," *IET Optoelectronics*, vol. 6, pp. 26-33, February 2012.

- [198] X. Tang, Z. Ghassemlooy, S. Rajbhandari, W. O. Popoola, and C. G. Lee, "Coherent optical binary polarisation shift keying heterodyne system in the free-space optical turbulence channel," *IET Microwaves, Antennas & Propagation*, vol. 5, p. 1031, June 2011.
- [199] N. Cvijetic, D. Y. Qian, J. J. Yu, Y. K. Huang, and T. Wang, "Polarization-multiplexed optical wireless transmission with coherent detection," *Journal of Lightwave Technology*, vol. 28, pp. 1218-1227, 2010.
- [200] D. F. V. James, "Changes of polarization of light beams on propagation in free space," *The Journal of the Optical Society of America A*, vol. 11, pp. 1641-1643, 1994.
- [201] M. M. Matalgah and R. M. Radaydeh, "Hybrid frequency-polarization shift-keying Modulation for optical transmission," *Journal of Lightwave Technology*, vol. 23, pp. 1152-1163, March 2005.
- [202] L. Y. L. Andy, Y. K. Chan, S. F. Chien, A. H. You, and T. S. Guan, "40 Gbit/s polarization modulation in ultra-long haul transmission systems by using optical phase conjugators," *EICE Electronics Express*, vol. 1, pp. 386 - 391, 2006.
- [203] J. G. Proakis, *Digital communications 4th ed.* New York: McGraw-Hill Series in Electrical and Computer Engineering, 2001.
- [204] R. Calvani, R. Caponi, F. Delpiano, and G. Marone, "An experiment of optical heterodyne transmission with polarization modulation at 140 Mbit/s bitrate and 1550 nm wavelength," *GLOBECOM '91*, pp. 1587-1591, 2-5 December 1991
- [205] I. I. Kim, E. Woodbridge, V. Chan, and B. R. Strickland, "Scintillation measurements performed during the limited-visibility lasercom experiment," in *SPIE Proceedings Series* vol. 3266 San Jose, CA, USA, 1998, pp. 209 - 220.
- [206] W. O. Popoola and Z. Ghassemlooy, "BPSK subcarrier intensity modulated free-space optical communications in atmospheric turbulence," *Journal of Lightwave Technology*, vol. 27, pp. 967-973, April 2009.
- [207] I. Seto, T. Ohtsuki, H. Yshima, I. Sasase, and S. Mori, "Coherent optical polarization-shift-keying (PolSK) homodyne system using phase-diversity receivers," *Global Telecommunications Conference 1991*, vol. 3, pp. 1601-1605, 1991.
- [208] R. Calvani, R. Caponi, F. Delpiano, and G. Marone, "An experiment of optical heterodyne transmission with polarization modulation at 140 Mbit/s bitrate and 1550 nm wavelength," *GLOBECOM 91*, pp. 1587-1591, December 1991
- [209] E. Dietrich, B. Enning, R. Gross, and H. Knupke, "Heterodyne transmission of a 560 Mbit/s optical signal by means of polarisation shift keying," *Electronics Letters*, vol. 23, pp. 421-422, April 1987.
- [210] A. Ashok, M. Gruteser, N. Mandayam, and K. Dana, "Characterizing multiplexing and diversity in visual MIMO," *45th Annual Conference on Information Sciences and Systems (CISS) 2011*, pp. 1-6, 2011.
- [211] S. Ahmed, "Soft metrics and EXIT chart analysis of noncoherent MFSK with diversity reception in Rician fading channel," *IEEE Transactions on Wireless Communications*, vol. 10, pp. 1692-1696, 2011.
- [212] F. Xu, M. A. Khalighi, P. Caussé, and S. Bourennane, "Channel coding and time-diversity for optical wireless links," *Optics Express*, vol. 17, p. 872, January 2009.
- [213] A. Molisch, "Channel coding and information theory," in *Wireless Communications, Second Edition*: Wiley-IEEE Press, 2011, pp. 277-317.

- [214] S.-H. Chang, M. Rim, P. C. Cosman, and L. B. Milstein, "Superposition MIMO coding for the broadcast of layered sources," *IEEE Transactions on Communications*, vol. 59, pp. 3240-3248, 2011.
- [215] A. Molisch, "Diversity," in *Wireless Communications-Edition 1*: Wiley-IEEE Press, 2011, pp. 249-275.
- [216] C. B. Naila, A. Bekkali, K. Kazaura, and M. Matsumoto, "BPSK intensity modulated free-space optical communications using aperture averaging," *International Conference on Photonics (ICP) 2010*, pp. 1-5, 2010.
- [217] I. S. Gradshteyn and I. M. Ryzhik, *Table of integrals, series, and products*, 5th ed. London: Academic Press, Inc., 1994.
- [218] W. O. Popoola, Z. Ghassemlooy, J. I. H. Allen, E. Leitgeb, and S. Gao, "Free-space optical communication employing subcarrier modulation and spatial diversity in atmospheric turbulence channel," *IET Optoelectronics*, vol. 2, pp. 16-23, February 2008.
- [219] R. L. Mitchell, "Permanence of the log-normal distribution," *Journal of the Optical Society of America*, vol. 58, pp. 1267-1272, 1968.
- [220] N. Avlonitis, E. M. Yeatman, M. Jones, and A. Hadjifotiou, "Multilevel amplitude shift keying in dispersion uncompensated optical systems," *IEE Proceedings Optoelectronics*, vol. 153, pp. 101-108 2006
- [221] T. Tokle, M. Serbay, J. B. Jensen, Y. Geng, W. Rosenkranz, and P. Jeppesen, "Investigation of multilevel phase and amplitude modulation formats in combination with polarization multiplexing up to 240 Gb/s," *IEEE Photonics Technology Letters*, vol. 18, pp. 2090-2092, 2006.
- [222] Y. Han and G. Li, "Theoretical sensitivity of direct-detection multilevel modulation formats for high spectral efficiency optical communications," *IEEE Journal of Selected Topics in Quantum Electronics*, vol. 12, pp. 571-580, 2006.
- [223] H. Tapse and D. K. Borah, "Performance of regular low density parity check codes over hybrid optical/RF channels," *IEEE GLOBECOM 2008*, pp. 1-6, 2008.
- [224] I. B. Djordjevic, S. Denic, J. Anguita, B. Vasic, and M. A. Neifeld, "LDPC-coded MIMO optical communication over the atmospheric turbulence channel," *Journal of Lightwave Technology*, vol. 26, pp. 478-487, 2008.
- [225] I. B. Djordjevic, B. Vasic, and M. A. Neifeld, "LDPC coded OFDM over the atmospheric turbulence channel," *Optics Express*, vol. 15, pp. 6336-6350, 2007.
- [226] X. Tang, Z. Ghassemlooy, S. Rajbhandari, W. O. Popoola, C. G. Lee, E. Leitgeb, and V. Ahmadi, "Free-space optical communication employing polarization shift keying coherent modulation in atmospheric turbulence channel," *Proceeding of the 7th Symposium on Communication Systems, Networks and Digital Signal Processing 2010*, pp. 663-668, July 2010.
- [227] M. K. Simon and M.-S. Alouini, *Digital communication over fading channels 2nd edition*: Wiley, 2005.
- [228] D. R. Bates, "Rayleigh scattering by air," *Planetary space Science*, vol. 32, pp. 785-790, 1984.
- [229] I. I. Kim and E. Korevaar, "Availability of free space optics and hybrid FSO/RF systems," *Proceedings of SPIE: Optical Wireless Communications IV*, vol. 4530, pp. 84-95, 2001.
- [230] M. Gebhart, E. Leitgeb, S. S. Muhammad, B. Flecker, C. Chlestil, M. A. Naboulsi, H. Sizun, and F. D. Fornel, "Measurement of light attenuation in dense fog conditions for optical wireless links," *SPIE proceedings*, vol. 589, 2005.

- [231] S. S. Muhammad, B. Flecker, E. Leitgeb, and M. Gebhart, "Characterization of fog attenuation in terrestrial free space links," *Journal of Optical Engineering*, vol. 46, p. 066001, June 2007.
- [232] M. S. Awan, E. Leitgeb, Marzuki, M. S. Khan, F. Nadeem, and C. Capsoni, "Evaluation of fog attenuation results for optical wireless links in free space," *IEEE International Workshop on Satellite and Space Communications*, 2008, pp. 112-116, 2008.
- [233] M. Grabner and V. Kvicera, "Fog attenuation dependence on atmospheric visibility at two wavelengths for FSO link planning," *2010 Loughborough Antennas and Propagation Conference (LAPC)*, pp. 193-196, 2010.
- [234] WMO-No.8, *Guide to meteorological instruments and methods of observation (seventh edition)*. Geneva, Swetzerland: World Meteorological Organisation, 2008.
- [235] F. Nadeem, M. S. Khan, and E. Leitgeb, "Optical wireless link availability estimation through Monte Carlo simulation," *Proceedings of the 2011 11th International Conference on Telecommunications (ConTEL)*, pp. 345-350, 2011.
- [236] L. C. Andrews, R. L. Phillips, and C. Y. Hopen, *Laser beam sintillation with applications*: SPIE Optical Engineering Press, 2001.
- [237] S. V. Kartalopoulos, *Optical bit error rate: an estimation methodology*. United States of America: Wiley-IEEE Press, October 2004.
- [238] A. Eslami, S. Vangala, and H. Pishro-Nik, "Hybrid channel codes for efficient FSO/RF communication systems," *IEEE Transactions on Communications*, vol. 58, pp. 2926-2938, 2010.
- [239] B. Barua and D. Barua, "Analysis the performance of a LDPC coded FSO system with Q-ary pulse-position modulation," *2011 3rd International Conference on ICCRD*, vol. 1, pp. 339-343, 2011.